AN INVESTIGATION OF THE OZONE ACTIVITY AND SELECTIVITY OF Ni/Sb-SnO_2 ANODES IN AQUEOUS ACID ELECTROLYTE

A thesis submitted by

AJCHARA IMKUM

For the degree of Doctor of Philosophy

School of Chemical Engineering and Advanced Materials,
Newcastle University, Newcastle upon Tyne, United Kingdom

September 2011

Preface

Declaration

I hereby declare that the work embodies in this thesis entitled "**An Investigation of the Ozone Activity and Selectivity of Ni/Sb-SnO_2 Anodes in Aqueous Acid Electrolyte**" is the result of investigations carried out in the School of Chemical Engineering and Advanced Materials and the school of Natural Sciences, University of Newcastle, United Kingdom between September 2007 and June 2011 under the supervision of Professor Paul A. Christensen.

Extracts from this work has been accepted for publication in the following journals.

1. Christensen, P. A., W. F. Lin, H. Christensen, **A. Imkum**, J. M. Jin, G. Li and C. M. Dyson, "Room Temperature, Electrochemical Generation of Ozone with 50% Current Efficiency in 0.5 M Sulfuric Acid at Cell Voltages < 3V," *Ozone Science & Engineering* 31(4):287-293 (2009).
2. Christensen, P. A., and **A. Imkum**, "The Inhibition of Ozone Generation at Ni/Sb-SnO_2 Electrodes in High Solution Concentrations of Ozone," *Ozone Science & Engineering in press* (2011).

Poster Presentations

1. Pure and Applied Chemistry International Conference 2009 (PACCON 2009), "Electrochemical Generation of Ozone in 0.5 M Sulphuric Acid at Room Temperature and Cell Voltages < 3.0 V with up to 50% Current Efficiency, 14-16 January 2009, Department of Chemistry, Faculty of Science, Naresuan University, Phitsanulok, Thailand.

Oral Presentations

1. Electrochem 2008 Conference, "Electrochemical Generation of Ozone with up to 50% Current Efficiency in 0.5 M Sulphuric Acid at Room Temperature and Cell Voltages < 3.0 V," 16-17 September 2008, Department of Chemistry, University of Liverpool, Liverpool, United Kingdom.

2. The 2009 CEAM Post Graduate Student Research Conference, "Electrochemical Generation of Ozone with Higher Current Efficiency in Sulphuric Solution at Room Temperature and Small Cell Voltages," 16-17 April 2009, School of Chemical Engineering and Advanced Materials, University of Newcastle, Newcastle, United Kingdom.
2. Electrochem 2009 Conference, "Development of Anodes for Electrochemical Ozone Generation," 16-17 September 2009, School of Chemistry, University of Manchester, Manchester, United Kingdom.
3. The 2010 CEAM Post Graduate Student Research Conference, "Anode Development for Electrochemical Ozone Generation," 14-15 April 2010, School of Chemical Engineering and Advanced Materials, University of Newcastle, Newcastle, United Kingdom.

Acknowledgements

I wish to deeply biggest thank to my lovely supervisor and his family, Professor Dr. Paul Andrew Christensen for his inspiring guidance, large enthusiasm and help through out this work and my life in Newcastle. It has been a privilege to work with him. I also would like to thank Dr. Wen feng Lin, Dr. Ashleigh Fletcher, Professor Dr. Tom Curtis, Professor Dr. Keith Scott and Professor Dr. Geoffrey Kelsall for their help and valuable advice.

I must to big thank the Clarizon Ltd, Dr. Clive M. Dyson, Dr Henriette Christensen, Dr. David Hodgson, Amanda Graham, Rob Kevan, Dr. Jiamei Jin for the collaboration, supporting and their kindly assistance.

I would like to take this opportunity to thank my present colleagues, David Molyneux, Khalid Zakalia, Nutchapon Chiarasumran, Dr. Taner Yonar, Dr. Panagiotis Moussas, Dr. Xiaoteng Liu, Daniel Lawrence and also to the past members of PAC research group, Dr. Fei Li, Dr. Rachel Cambell, Xiayoi Xu, Dr. Shuihua Tang, Dr. Guohua Li, Dr Rui Yang, Dr Jalal Basiri Parsa, Renato Garcia Freitas, Ricardo Garcia Baquero, Christopher Brown, for their help, encouragement and fruitful discussions. The biggest thanks go to Douglas Linares Moya, the first favorite colleague in the laboratory for their encouragement, friendship and kindly assistance in Newcastle.

I would like to thank everyone, the staff and students in the School of Chemistry and school of Chemical Engineering and Advanced Materials and the Newcastle University for all their helpful suggestions and kindly assistance. Thanks also to technicians in the mechanical and glass blowing workshops for building and maintaining the equipment used in my work.

I would also like to take this opportunity to thank Robin Ingleton, Store Supervisor at School of Chemistry, Pauline Carrick at Advanced Chemical and material Analysis (ACMA) in Newcastle University And I also thank Dr. Adrain Boatwright at Centre for Surface Chemical Analysis (CSCA), Dr. David Scurr at Laboratory of Biophysics and

Surface Analysis (LBSA) at Nottingham University and Dr. Martin Hogarth at Johnson Matthey for their advice and assistance.

I must thank the Royal Thai Government for providing the scholarship throughout this project and supporting my living expense in the United Kingdom. And many thanks to all my Thai friends at Newcastle and around the United Kingdom in the past and present for their help and making my staying enjoyable in the United Kingdom.

I must to big thank my parents, my older sister, my nice, my nephew, my brother-in law, my relatives and my friends, my teachers, my colleagues for their love, support and encouragement throughout my education. And also big thank to my lovely boyfriend and his family for his concerning and giving love to me.

'To my parents and family'

Ajchara Imkum

Abstract

Ozone is finding increasingly wider application across a range of industries, from semiconductor manufacture to water treatment. In principle, electrochemical ozone generation is capable of producing very high concentrations of ozone both in the gas phase and directly into solution, in contrast to Cold Corona Discharge, the present, most generally applied ozone technology.

The aim of the work described in this thesis was to develop highly active and selective anodes for the generation of ozone based on Ni and Sb-doped SnO_2: Ni/Sb-SnO_2.

Each step of the synthesis of Ni/Sb-SnO_2-coated Ti mesh anodes was investigated in detail and the electrodes so produced characterized by SEM and EDX, and their activity and selectivity determined using UV-Vis spectroscopy.

Anodes with ozone current efficiencies of up to 50% in aqueous acidic electrolyte were developed, and efficiencies of *ca.* 30-40% were calculated routinely. However, such impressive efficiencies were derived only when operating the electrochemical cells in single pass mode. When the ozonated electrolyte was injected into the inlet of the electrochemical cell in order to generate gas phase ozone, efficiencies <10% were determined. Such an effect of ozone in solution inhibiting the ozone generating reaction, has not been determined with other electrocatalysts, and suggests that the mechanism of ozone evolution at Ni/Sb-SnO_2 anodes is novel. This inhibiting effect of ozone was investigated in detail and it was concluded that dissolved ozone was displacing a key intermediate or intermediates.

Anode durability is a key issue, particularly when using aqueous acid. It was found that some anodes showed high stability, whilst others activated very quickly. When deactivation occurred was found to be due to physical loss of catalyst and/or etching. A key strategy with respect to the former challenge was to coat the Ti mesh with an Electro Deposited Inter Layer (EDIL), to protect the Ti from oxidation as this would lead to the

formation of TiO_2 and spalling of the catalyst layer. The methodology employed was implemented initially by collaborators in Hong Kong University and based on precedent literature. In essence, etched Ti mesh was held at cathodic potentials in ethanolic solutions of $SbCl_3$ and $SnCl_4$; this was reported to produce a protective EDIL containing Sn and Sb. However, it was shown that, no Sn deposited, under the conditions employed. Furthermore, there was no evidence that the EDIL was effective with respect to durability and, indeed, the electrodeposition step introduced significant variability into the catalyst coating process. The reason why some catalysts were durable and others very short lived remains unclear; however, it was postulated that the former involved Ni as NiOOH.

A strategy based on the addition of Au to prevent structural change of the SnO_2 and/or passivation of the SnO_2 surface was investigated. Unfortunately, no beneficial effect (in terms of durability, activity or ozone selectivity) was derived.

The scale up of the synthesis of the Ni/Sb-SnO_2 anodes from 6.25 cm^2 to 35.0 cm^2 was achieved successfully. Preliminary experiments with an industrial collaborator suggested the technology is transferable.

Preliminary experiments using a prototype water/air cell gave very promising current efficiencies (up to 22%) and showed a major design flaw in the prototype in terms of the compression of the anode/Nafion/cathode membrane electrode assembly.

Contents

Table of contents **Pages**

Table of contents **Pages**

Table of contents **Pages**

Table of contents **Pages**

List of Tables **Pages**

Chapter 1 : Introduction

Chapter 2 : Experimental

Chapter 3 : System development & the recycle problem

Chapter 4 : The evolution of the anode synthesis

List of Tables **Pages**

Chapter 5 : Anode durability

List of Tables **Pages**

Chapter 6 : Scale up

List of Tables **Pages**

List of schemes

Table of Figures **Pages**

Chapter 1 : Introduction

Chapter 2 : Experimental

Table of Figures **Pages**

Chapter 3 : System development and the recycle problem

Table of Figures **Pages**

Table of Figures **Pages**

Table of Figures **Pages**

Table of Figures **Pages**

Table of Figures **Pages**

Chapter 4 : The evolution of the anode synthesis

Table of Figures **Pages**

Table of Figures **Pages**

Table of Figures **Pages**

Table of Figures **Pages**

Chapter 5 : Anode durability

Table of Figures **Pages**

Table of Figures **Pages**

Table of Figures **Pages**

Table of Figures **Pages**

Chapter 6 : Scale up

Table of Figures **Pages**

Table of Figures **Pages**

Table of Figures **Pages**

Index of Nomenclatures, Greek symbols and Acronyms

Nomenclature	Name	Unit
A	Absorbance	
A	Electrode area	cm^2
Å	Ångstroms, 10^{-10} m	Å
A_g	Steady state gas phase ozone absorbance	
A_s	Steady state dissolved ozone absorbance	
b.p.	Boiling point	°C
C	Concentration	mol dm^{-3}
C_{Red}^{O}	Bulk concentration of reduction species	mol cm^{-3}
C_{Ox}^{O}	Bulk concentration of oxidation species	mol cm^{-3}
C_{Red}^{S}	Surface concentration of reduction species	mol cm^{-3}
C_{Ox}^{S}	Surface concentration of oxidation species	mol cm^{-3}
D_{ox}	Diffusion coefficient of product	cm^2 s^{-1}
D_{H2}	Diffusion coefficient of H_2	cm^2 s^{-1}
C_t	Contact time	mg min dm^{-3}
E^o	Standard Reduction Potential	V
F	Faraday constant/ 96485 C mol^{-1}	C mol^{-1}
I	Current	A
j	Current density	A cm^{-2}
j_0	Exchange current density	A cm^{-2}
j_{Cath}	Current density at the cathode	A cm^{-2}
j_{An}	Current density at the anode	A cm^{-2}
$j_{L,Cath}$	Limiting current density at the cathode	A cm^{-2}
$j_{L,An}$	Limiting current density at the anode	A cm^{-2}
k_f	Forward rate constant	
k_r	Reverse rate constant	
l	Distance	cm
m	Mass of reactant	g, kg
m.p.	Melting point	°C

Nomenclature	Name	Unit
MW	Molecular weight	g mol^{-1}
P	Pressure	kPa, atm
Q	Electric charge	C
R	Gas constant, 8.3145 J mol^{-1} K^{-1}	J mol^{-1} K^{-1}
R	Electric resistance	Ω cm^2
R_{elec}	Resistance of electrolyte	Ω cm^2
R_{Nafion}	Resistance of Nafion	Ω cm^2
R_f	Roughness factor	
t	Time	second,minute
T	Temperature	ºC, K
V	Volume of the electrochemical reactor	cm^3
V	Cell voltage	V
V_{cell}	Potential difference between anode and cathode	V
V_a	Anode gas volume	cm^3
V_c	Cathode gas volume	cm^3
V_m	Molar volume	cm^3
V_{O2}	Volume of O_2	cm^3
V_{gas}	Volume of gas	cm^3
$V_{a,app}$	Apparent anode gas volume	cm^3
W	Energy	W
x	The medium of thickness	mm, cm

Greek symbol	**Name**	**Unit**
β_C	Cathodic transfer coefficient	
β_A	Anodic transfer coefficient	
λ	Wavelength	nm
κ	Conductivity	Ω^{-1} cm^{-1}
Ω	Units of resistance	Ω cm^2
f	Flow rate	cm^3 min^{-1}

Greek symbol	Name	Unit
f	F/RT (the frequency of rotation in hertz	V^{-1}
ℓ	Path length	cm
n	Mole of substance	mol
η	Overpotential	V
η_c	Overpotential at the cathode	V
η_a	Overpotential at the anode	V
ε	Extinction coefficient	$dm^3\ mol^{-1}\ cm^{-1}$
ε_g	Extinction coefficient of gas	$dm^3\ mol^{-1}\ cm^{-1}$
ε_s	Extinction coefficient of solution	$dm^3\ mol^{-1}\ cm^{-1}$
Φ	Efficiency	%
Φ^e	Fractional current efficiency	%
Φ^e_{O3}	Fractional current efficiency of ozone	%
Φ^e_{O2}	Fractional current efficiency of O_2	%
Φ^e_{True}	Actual current efficiency	%
Φ^e_{App}	Apparent current efficiency	%
ϕ_c	Inner Galvani potential at the cathode	V
ϕ_a	Inner Galvani potential at the anode	V
$\delta\phi$	Inner Galvani potential difference	V
$\delta\phi_c$	Inner Galvani potential difference at the cathode	V
$\delta\phi_a$	Inner Galvani potential difference at the anode	V
δ_N	Diffusion layer thickness	cm

Acronyms	Name
Abs	Absorbance
An	Anode
BDD	Boron Doped Diamond
Cath	Cathode
CC	Catalyst coating

Acronyms	Name
CHA	Concentric Hemispherical Analyser
Elec.	Electrolyte
DC	Direct Current
DLD	Delay Line Detector
Exp.	Experiment
ED	Electrodeposition
EDIL	Electro Deposition Inter Layer
EDX	Energy Dispersive X-ray analysis
EXAFS	Extend X-ray Absorption Fine Structure
Fig.	Figure
FAT	Fixed Analyser Transmission
FDA	Food and Drug Association
g	Gram
GAC	Granular Activated Carbon
GCMS	Gas Chromatography Mass Spectrometry
GDE	Gas Diffusion Electrode
GDL	Gas Diffusion Layer
hrs	Hours
MEA	Membrane Electrode Assembly
MCL	Maximum Contaminant Level
mins	Minutes
NHE	Normal Hydrogen Electrode
PEM	Poly Electrolyte Membrane
PSU	Power Supply Unit
PTFE	Poly Tetra Fluoro Ethylene
s	Second
SCE	Saturated Caramel Electrode
SEM	Scanning Electron Microscope
SHE	Standard Hydrogen Electrode

Acronyms	Name
Sol.	Solution
TEM	Transmission Electron Microscopy
ToF-SIMS	Time-of-flight Secondary Ion Mass Spectrometry
THM	Trihalomethane
UHV	Ultra High Vacuum
UV-Vis	Ultraviolet-Visible
XPS	X-ray Photoelectron Spectrometry
XRD	X-ray Diffraction

Chapter 1 Introduction

1. Introduction

This thesis concerns the development of active and selective anode catalysts for the electrochemical generation of ozone.

1.1 The properties of ozone

1.1.1 Physical properties

Ozone is an allotropic form of oxygen (b.p.-111.9 ºC) and is a pale blue gas at room temperature [1]. It was discovered by a Dutch physicist, Van Marum, in 1785 during experiments on electric discharge through air. The molecule is triangular with a bond angle of 116.8 º [2] and bond length of 0.1278 nm. In terms of valence bond theory, the structure of the ozone molecule is a resonance hybrid of four canonical forms, shown schematically in fig. 1.1.

The general properties of ozone are shown in table 1.1.

Property	Unit	Value
Molecular weight	g	48.0
Boiling point	ºC	-111.9 ± 0.3
Melting point	ºC	-192.5 ± 0.4
Latent heat of vaporization at 111.9 ºC	kJ/kg	14.90
Liquid density at -183 ºC	kg/m^3	1574
Vapor density at 0 ºC and 1 atm	g/mL	2.154
Solubility in water at 20.0 ºC	mg/L	12.07
Vapor pressure at -183 ºC	kPa	11.0
Vapor density compared to dry air at 0 ºC and 1 atm	Unitless	1.666
Specific volume of vapor at 0 ºC and 1 atm	m^3/kg	0.464
Critical temperature	ºC	12.1
Critical pressure	kPa	5532.3

Table 1.1 The physical of properties of ozone [3].

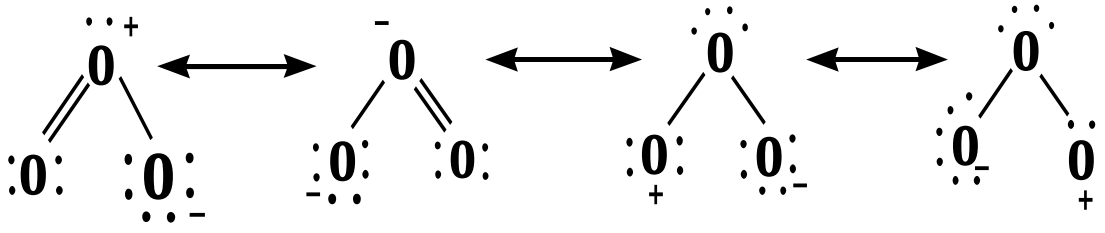

Figure 1.1 The structure of the ozone molecule [4].

Ozone is thermally unstable and explosive in all three phases in the 'pure' form. In the gas phase, ozone decomposes and this process is sensitive to light, the presence of trace organic and inorganic species, etc. [1]. The half life of 1 mol% pure gaseous ozone in oxygen at 25ºC [5] is 19.3 years. In the aqueous phase, the rate and mechanism of ozone decomposition depends upon pH [6][7][8][9] and the presence of other organic and inorganic species such as bicarbonate ion, a radical scavenger [10]. In "pure" water, the mechanism of ozone decay generally quoted is that of Weiss [8][11]:

Initiation

$O_3 + OH^- \rightarrow HO_2 + O_2^{\cdot -}$	$k = 7.0 \times 10^1\ M^{-1}\ s^{-1}$	(1.1)
$H_2O \leftrightarrow H^+ + OH^-$	$k_f = 5.0 \times 10^{-4}\ s^{-1}$	(1.2)
($pK_w = 14$)	$k_r = 5.0 \times 10^{10}\ M^{-1}\ s^{-1}$	(1.3)
$O_3 + HO_2^{\cdot -} \rightarrow OH^{\cdot} + O_2^{\cdot -} + O_2$	$k = 2.2 \times 10^6\ M^{-1}\ s^{-1}$	(1.4)
$H_2O_2 \leftrightarrow HO_2^{\cdot -} + H^+$	$k_f = 1.25 \times 10^{-1}\ s^{-1}$	(1.5)
($pK_{a,H2O2} = 11.6$)	$k_r = 5.0 \times 10^{10}\ M^{-1}\ s^{-1}$	(1.6)
$HO_2^{\cdot} \leftrightarrow O_2^{\cdot -} + H^+$	$k_f = 7.9 \times 10^5\ s^{-1}$	(1.7)
($pK_{a,HO2^{\cdot}} = 4.8$)	$k_r = 5.0 \times 10^{10}\ M^{-1}\ s^{-1}$	(1.8)
$O_3 + O_2^{\cdot -} \rightarrow O_3^{\cdot -} + O_2$	$k = 1.6 \times 10^9\ M^{-1}\ s^{-1}$	(1.9)
$HO_3^{\cdot} \leftrightarrow O_3^{\cdot -} + H^+$	$k_f = 3.7 \times 10^4\ s^{-1}$	(1.10)
($pK_{a,HO3^{\cdot}} = 6.1$)	$k_r = 5.2 \times 10^{10}\ M^{-1}\ s^{-1}$	(1.11)

Propagation

$HO_3^{\cdot} \rightarrow OH^{\cdot} + O_2$	$k = 1.1 \times 10^5\ s^{-1}$	(1.12)
$OH^{\cdot} + O_3 \rightarrow HO_4^{\cdot}$	$k = 2.0 \times 10^9\ M^{-1}\ s^{-1}$	(1.13)
$HO_4^{\cdot} \rightarrow HO_2^{\cdot} + O_2$	$k = 2.8 \times 10^4\ s^{-1}$	(1.14)
$2HO_4^{\cdot} \rightarrow H_2O_2 + 2O_3$	$k = 5.0 \times 10^9\ M^{-1}\ s^{-1}$	(1.15)
$HO_4^{\cdot} + HO_3^{\cdot} \rightarrow H_2O_2 + O_2 + O_3$	$k = 5.0 \times 10^9\ M^{-1}\ s^{-1}$	(1.16)
$CO_2 + H_2O \rightarrow HCO_3^- + H^+$	$k_f = 2.1 \times 10^4\ M^{-1}\ s^{-1}$	(1.17)
($pK_{a,CO2} = 6.37$)	$k_r = 5.0 \times 10^{10}\ M^{-1}\ s^{-1}$	(1.18)
$HCO_3^- \leftrightarrow CO_3^{2-} + H^+$	$k_f = 2.8\ s^{-1}$	(1.19)
($pK_{a,HCO3-} = 10.25$)	$k_r = 5.0 \times 10^{10}\ M^{-1}\ s^{-1}$	(1.20)
$CO_3^{2-} + OH^{\cdot} \rightarrow CO_3^{-} + OH^-$	$k = 3.7 \times 10^8\ M^{-1}\ s^{-1}$	(1.21)
$HCO_3^- + OH^{\cdot} \rightarrow HCO_3 + OH^-$	$k = 8.0 \times 10^6\ M^{-1}\ s^{-1}$	(1.22)
$HCO_3 \leftrightarrow CO_3^- + H^+$	$k_f = 1.3 \times 10^1\ s^{-1}$	(1.23)
($pK_{a,HCO3} = 9.6$)	$k_r = 5.0 \times 10^{10}\ M^{-1}\ s^{-1}$	(1.24)

Termination

$2CO_3^- \rightarrow CO_2 + CO_4^{2-}$	$k = 2.0 \times 10^7\ M^{-1}\ s^{-1}$	(1.25)
$CO_3^- + O_2 \rightarrow CO_3^{2-} + O_2$	$k = 4.0 \times 10^8\ M^{-1}\ s^{-1}$	(1.26)
$CO_3^- + O_3^{\cdot -} \rightarrow CO_3^{2-} + O_3$	$k = 6.0 \times 10^7\ M^{-1}\ s^{-1}$	(1.27)
$CO_3^- + HO_2^{\cdot -} \rightarrow CO_3^{2-} + HO_2^{\cdot}$	$k = 5.6 \times 10^7\ M^{-1}\ s^{-1}$	(1.28)
$CO_3^- + H_2O_2 \rightarrow HCO_3^- + HO_2^{\cdot}$	$k = 8.0 \times 10^5\ M^{-1}\ s^{-1}$	(1.29)
$CO_3^- + OH^{\cdot} \rightarrow CO_2 + HO_2^-$	$k = 3.0 \times 10^9\ M^{-1}\ s^{-1}$	(1.30)

The solubility of ozone varies with temperature, pH and ionic strength. At 0 ºC in pure water at pH 3.5 and atmospheric pressure it is 1.06 g dm^{-3}, compared to *ca.* 0.06 g dm^{-3} for O_2 at 0 ºC [1][12][13]. The solubility of ozone in water as a function of pH may be found in references [14][15].

Ozone is a toxic gas with an unpleasant and irritating odour (Greek: “ozein” “to smell”); the odour threshold of ozone varies between individuals but most people can smell it at concentrations of 0.01 to 0.05 ppm in air [1], which is well below the limit for general comfort. The toxicity of ozone is related mostly to its powerful oxidizing properties. Overexposure to ozone has been associated with both acute and chronic effects such as chest pain, coughing and irritation of the respiratory system. Ozone exposure has also been shown to cause chronic asthma and other respiratory diseases [1].

A summary of physiological effects of ozone is presented in table 1.2.

Concentration(ppm)	**Description of effects**
0.003-0.01	Threshold of odor perception by average person in clean air.
0.02-0.04	Representative average total oxidant concentrations in major US cities 1964.
0.1	*Recommended exposure limit.* Eye, nose and throat irritation often experienced.
0.2-0.5	Reduced dark adaptation and alteration of extra-ocular muscle balance occurs after several hours exposure.
0.5	Nausea and headache sometimes occur. Extended exposure can cause pulmonary oedema and enhanced susceptibility to respiratory infections (both bacterial and viral).
1.0	10 minutes exposure typically reduces desaturation rate of oxyhaemoglobin in the lung.
1-2	Chronic exposure (one year for 6 hours per day) at this level has resulted in bronchiolitis and bronchitis in animals. 2 hour exposure can cause headache, chest pain and dryness of respiratory tract and a reported 20% reduction in timed vital capacity of the lung.
1.5-2	Exposure for 2 hours typically results in cough, substernal pain and excessive sputum.

Concentration(ppm)	Description of effects
5-25	Experimentation showed that 3 hour exposure at 12 ppm was lethal for rats and 25 ppm was lethal for guinea pigs. Humans (welders) exposed to 9 ppm developed pulmonary oedema. Their chest X-rays were normal in 2-3 weeks, but 9 months later they still exhibited fatigue and exertional dyspnoea (laboured respiration).
50	30 minute exposure may be fatal.

Table 1.2 A summary of the symptomatic and clinical effects of ozone at various concentrations [16].

1.1.2 Chemical Properties

Ozone is a powerful oxidant, as may be seen in table 1.3 [17][18], with a standard reduction potential of 1.51 V *vs.* the Normal Hydrogen Electrode (NHE), and is also an excellent disinfectant. Because of these properties, the most important application of ozone is in the treatment of drinking water which began in Europe in 1903 [1].

In general, ozone is useful for a number of other applications in which it may be categorized as a: (1) bactericide; (2) viricide and (3) powerful chemical oxidant.

1.1.3 Ozone as a bactericide and viricide

Ozone, like chlorine, is a strong oxidizing agent with bactericidal properties; however unlike chlorine, the use of ozone does not cause changes in pH [19].

The bactericidal properties of ozone are detailed in a number of publications covering both laboratory and pilot scale operation [20]. Chlorine is believed to attack enzymes inside the cells of micro-organisms after diffusing through the cell wall [20]. In contrast, ozone attacks the cell wall directly and causes lysis; much lower concentrations of ozone are required for disinfection compared to chlorine and other disinfectants [20]. Ozone is believed to be an effective viricide, finding application in swimming pools to protect the public from viral illnesses [20].

Species	Half Reaction	Standard Reduction Potential/V *vs.* NHE[a]
Fluorine (F_2)	$F_2(g) + 2H^+(aq) + 2e^- \rightarrow 2HF(aq)$	3.05
Hydroxyl radical ($OH^{\cdot}$)	$OH^{\cdot} + H^+ + e^- \rightarrow H_2O$	2.38
Atomic oxygen (O)	$O(g) + 2H^+(aq) + 2e^- \rightarrow H_2O(l)$	2.43
Molecular oxygen (O_2)	$O_2(g) + 4H^+(aq) + 4e^- \rightarrow 2H_2O(l)$	1.23
Ozone (O_3)	$O_3(g) + 6H^+(aq) + 6e^- \rightarrow 3H_2O(l)$	1.51
Hydrogen peroxide (H_2O_2)	$H_2O_2(aq) + 2H^+(aq) + 2e^- \rightarrow 2H_2O(l)$	1.76
Per-hydroxyl radical ($HOO^{\cdot}$)	$O_2^- + H_2O \rightarrow HO_2 + OH^-$	1.70
Permanganate (MnO_4^-)	$MnO_4^-(aq) + 4H^+(aq) + 3e^- \rightarrow MnO_2(s) + 2H_2O(l)$	1.70
Hypobromous acid (HBrO)	$HBrO(aq) + H^+(aq) + 2e^- \rightarrow Br^-(aq) + H_2O(l)$	1.34
Chlorine dioxide (ClO_2)	$ClO_2(g) + H^+(aq) + e^- \rightarrow HClO_2(aq)$	1.19
Hypochlorous acid (HClO)	$2HClO(aq) + 2H^+(aq) + 2e^- \rightarrow Cl_2(g) + 2H_2O(l)$	1.63
Hypoiodous acid (HIO)	$HIO(aq) + 2H^+(aq) + 2e^- \rightarrow I^-(aq) + H_2O(l)$	0.99
Chlorine (Cl_2)	$Cl_2(g) + 2e^- \rightarrow 2Cl^-(aq)$	1.36
Bromine (Br_2)	$Br_2(g) + 2e^- \rightarrow 2Br^-(aq)$	1.09
Iodine (I_2)	$I_2(s) + 2e^- \rightarrow 2I^-(aq)$	0.54

[a]NHE = Normal Hydrogen Electrode.

Table 1.3 Standard Reduction Potentials of common oxidants [17][18].

1.2 The Applications of Ozone

The global market for chemical agents in the water, wastewater and food (*e.g.* bleaching of flour) sectors was $32bn in 2007 [21][22] and ozone is making significant inroads into these and other sectors, such as the semiconductor industry. Ozone is regarded as a 'clean' chemical agent. It has received FDA approval for application in the food industry and, as was discussed above, is finding increasing application in water treatment [23] as a result of its ability to kill chlorine-resistant pathogens such as *Cryptosporidium parvum* [24][25] and its green credentials. More recently, concerns over the presence of micro pollutants in water and wastewater such as endocrine disrupting chemicals [26][27][28] and pharmaceuticals [29][30] have increased attention on the application of ozone.

Ozone is employed in water treatment for taste and odor control, color and metal ion (*e.g.* ferric and manganic) removal, etc. [20].

In terms of the oxidation process in the context of water treatment, chlorine use can lead to undesirable disinfection by-products (DBPs) by reacting with naturally occurring (humic) matter to form, for example, haloacetic acids and trihalomethanes (THMs). Ozone oxidizes dissolved species in a different way to chlorine, initially breaking down to O_2 and O* (active atomic oxygen) according to [31]:

$$O_3 \rightarrow O_2 + O^* \tag{1.31}$$

The O* is the active agent which oxidizes any solution species. In contrast, chlorine dissolves in water to form 'free chlorine', HOCl [20]:

$$Cl_{2(aq)} + H_2O \rightarrow HOCl + Cl^- + H^+ \tag{1.32}$$

The impact of these different first steps maybe judged by comparing the C_t values of the two oxidants. The C_t value is the contact time, in mg min dm^{-3}, required for 99% inactivation of a particular micro-organism at 5 ºC [31][32], and a comparison of C_t values for various micro-organisms and disinfectants is shown in table 1.4.

It can be seen that ozone has the advantage over free chlorine. The C_t values are much lower, allowing more water to be processed within a specific amount of time and showing that ozone is more efficient than chlorine [32]. In addition, chlorine treatment is not effective against *e.g. G. lamblia* and *Cryptosporidium* when compared to alternative oxidants such as ozone (O_3) and chlorine dioxide (ClO_2) [31]. Chlorine dioxide, like O_3, is an effective bactericide/viricide.

Microorganism	**C_t values of disinfectant / mg min dm^{-3}**			
	Free chlorine (pH 6-7)	**Preformed chloramine (pH 8-9)**	**Chlorine dioxide (pH 6-7)**	**Ozone (pH 6-7)**
E. coli	0.034-0.05	95-180	0.4-0.75	0.02
Polio 1	1.1-2.5	770-3740	0.2-6.7	0.1-0.2
Rotavirus	0.01-0.05	3810-6480	0.2-2.1	0.006-0.06
Phage f2	0.08-0.18	-	-	-
G. lamblia cysts	47->150	-	26	0.5-0.6
G. muris cysts	30-630	1400	7.2-18.5	1.8-2.0
Cryptosporidium	7200	-	78	5-10

Table 1.4 C_t values of various disinfectants and microorganisms [31][32].

Ozone does have the disadvantage that, when Br^- is present (*e.g.* in ballast water treatment [20]), bromate is generated:

$$O_3 + Br^- \rightarrow O_2 + OBr^- \quad (1.33)$$

$$O_3 + OBr^- \rightarrow O_2 + BrOO^- \rightarrow 2O_2 + Br^- \quad (1.34)$$

$$O_3 + 2Br^- + OH^- \rightarrow HOBr + BrO_3^- \qquad pKa = 8.86 \text{ at } 20\ ^oC \quad (1.35)$$

Bromate is a highly toxic substance that causes irreversible renal failure, deafness, and death and has been linked to renal tumors in rats. The American, Canadian and European environmental protection agencies have designated 10 µg/L as the Maximum Contaminant Level (MCL) of BrO_3^- in drinking water [20][33].

Ozone is employed widely in water treatment throughout Europe, and is becoming more popular in the USA. However, for some years, there has been concerned that ozone can react with humic matter (*i.e.* the naturally-occurring organic material in untreated water) particularly in surface waters to form "oxidation byproducts" such as quinones and

organic peroxides [34]. These byproducts are potentially harmful [35][36]; however, in comparison to chlorine dioxide and chlorine, ozone produces less mutagenic byproducts and may even reduce the mutagenicity of water [37].

Ozone is unstable, and hence is generated at the place of application by an electronic discharge process, typically Cold Corona Discharge or CCD [3], through a flowing stream of air or (ideally) oxygen. The resulting air/ozone or oxygen/ozone mixtures then have to be contacted with the water to be treated such that the ozone dissolves efficiently [38]. A schematic diagram of a typical ozone system for water treatment is shown in fig. 1.2 [39].

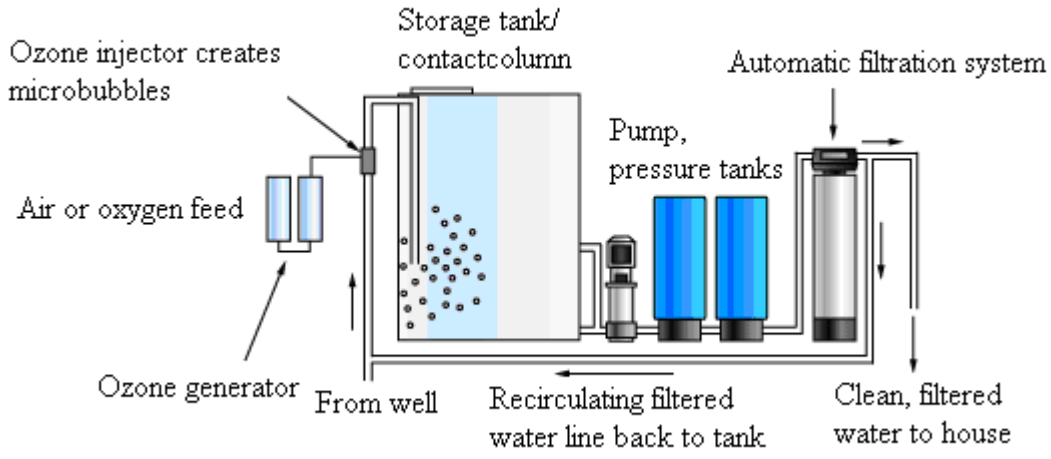

Figure 1.2 A schematic diagram of a typical ozone generator for water treatment [39].

As may be seen from table 1.3, ozone is the most powerful oxidant employed directly in water treatment. At low pH, ozone will attack organic substances directly; but under conditions of high pH, or in the presence of Fe(II) or humic substances, it will decompose spontaneously [37] according to:

$$HO^- + O_3 \rightarrow HO_2^{\cdot} + O_2^- \qquad (1.36)$$

$$HO_2^{\cdot} \rightarrow H^+ + O_2^- \qquad (1.37)$$

$$O_2^- + O_3 \rightarrow O_2 + O_3^- \quad (1.38)$$

$$O_3^- + H^+ \rightarrow HO_3^\cdot \quad (1.39)$$

$$HO_3^\cdot \rightarrow O_2 + OH^\cdot \quad (1.40)$$

$$OH^\cdot + O_3 \rightarrow HO_2^\cdot + O_2 \quad (1.41)$$

The decomposition step at high pH results in the generation of hydroxyl radicals, an even more powerful oxidizing agent than ozone, other organics such as phenol are more reactive towards molecular ozone at low pH [37].

Hydroxyl radicals are second only to fluorine in oxidation potential and have been shown to be effective both in the detoxification (organic removal) and disinfection of water [37].

Ozonation used in conjunction with Granular Activated Carbon (GAC) is considered as the polishing step for the removal of odours, taste and micropollutants prior to disinfection of drinking water [17]. No evidence has been found of trihalomethane (THM) destruction by ozonolysis; however, ozonation of water prior to chlorination has been found to reduce THM formation by oxidizing the THM precursors [40].

1.3 Advanced Oxidation Processes

Treatment methods that operate *via* the generation of OH radicals are termed Advanced Oxidation Processes or AOPs [17]. Hydroxyl radicals are extremely short lived, oxidizing dissolved organics initially by hydrogen abstraction. Hydroxyl radicals are nonselective in their mode of attack, able to operate at normal temperature and pressures, and are capable of oxidizing almost all reduced organic materials, without restriction to specific classes or groups of compounds, as compared to other oxidants [3]. Advanced oxidation processes differ from other common treatment processes (such as ion exchange [37] or air stripping) because pollutants are degraded rather than

concentrated or transferred into a different phase. Because secondary waste species are not generated, there is no need to dispose of, or regenerate, materials [37].

$$OH^{\cdot} + RH \rightarrow R^{\cdot} + H_2O \quad (1.42)$$

$$R^{\cdot} + O_2 \rightarrow RO_2^{\cdot} \rightarrow \rightarrow \quad (1.43)$$

The peroxyl radicals initiate thermal chain reactions which lead to oxidative degradation and, ultimately, to the formation of CO_2, H_2O and inorganic salts (mineralisation) [41].

The AOPs involving O_3 in use on the commercial scale [3][17] are O_3/UV, $O_3 + H_2O_2$ and $O_3 + H_2O_2$/UV, and these are listed, with other non-ozone AOPs for comparison, in table 1.5.

Ozone-based processes	**Non-ozone-based processes**
Ozone at elevated pH (8 to >10)	H_2O_2 + UV
Ozone + UV_{254} (also applicable in the gas phase)	H_2O_2 + UV + ferrous salts (Fenton's reagent)
Ozone + H_2O_2	Electron-beam irradiation
Ozone + UV_{254} + H_2O_2	Electrohydraulic cavitation
Ozone + TiO_2	Ultrasonics
Ozone + TiO_2 + H_2O_2	Nonthermal plasmas
Ozone + electron-beam irradiation	Pulsed corona discharges
Ozone + ultrasonics	Photocatalysis (UV + TiO_2) Gamma radiolysis Catalytic oxidation Supercritical water oxidation

Table 1.5 Examples of the Advanced Oxidation Processes used to produce hydroxyl radicals [37]. UV_{254} is 254 nm UV light.

1.3.1 O_3 + UV and H_2O_2 + UV

Hydroxyl radicals can be generated by the UV photolysis ($\lambda < 310$ nm) of ozone, H_2O_2 and $H_2O_2 + O_3$. Typically, commercially available lamps emitting at $\lambda_{max} = 254$ nm are employed [3][37]:

$$O_3 \xrightarrow{h\nu = 254\ nm} O_2 + O \quad (1.44)$$

in wet air:

$$O + H_2O \rightarrow 2\ OH^{\cdot} \quad (1.45)$$

in water:

$$2\ OH^{\cdot} \rightarrow H_2O_2 \quad (1.46)$$

$$H_2O_2 \xrightarrow{h\nu = 254\ nm} 2\ OH^{\cdot} \quad (1.47)$$

Due to the production of H_2O_2 as a reactive intermediate, direct photolysis of O_3 is not cost effective [3][37].

1.3.2 O_3 + H_2O_2

The combination of ozone and hydrogen peroxide ("Peroxone" [41]) accelerates the production of OH radicals through the decay of the O_3 [40][43][44], and is regarded as a relatively low cost AOP [44]. The process was discovered by Staehelin and Hoigne in 1982 [43] and the mechanism is now believed to be [44]:

$$HO_2^- + O_3 \rightarrow HO_5^- \quad (1.48)$$

$$HO_5^- \rightarrow HO_2^{\cdot} + O_3^{\cdot -} \quad (1.49)$$

$$HO_2^{\cdot} \rightarrow O_2^{\cdot -} + H^+ \quad (1.50)$$

$$O_2^{\cdot -} + O_3 \rightarrow O_3^{\cdot -} + O_2 \quad (1.51)$$

$$O_3^{\cdot -} \rightarrow O_2 + O^{\cdot -} \quad (1.52)$$

$$O^{\cdot -} + H_2O \rightarrow OH + OH^- \quad (1.53)$$

The rate of decay of O_3 is pH sensitive, decreasing by a factor of 10 per unit increase in pH; it is also pH sensitive due to (unwanted) scavenging of OH radicals by HCO_3^-.

1.3.3 Comparison of AOPs with conventional water treatment technologies

There are two primary disadvantages in the application of ozone and hydrogen peroxide-based AOPs.

(1) The installation and maintenance of ozone generators and UV lamps are costly, and such AOPs are relatively expensive compared to conventional methods of water treatment (see [17] and references therein). It is believed that the cost of the AOP approach will be reduced when these methods are adopted more widely. In addition, combining AOPs with other processes, particularly GAC, will make the process more competitive and effective.

(2) Radical traps such as bicarbonate ions have been shown to decrease the rate of organic destruction, and hence pretreatment may be required to reduce high bicarbonate levels by lowering the pH of the waste stream prior to the application of the UV/O_3 process [43].

The advantages and disadvantages of the established and emerging water treatments are summarized in table 1.6.

Oxidation/ Treatment	Objective of Treatment	Advantages	Disadvantages
Chlorine	- Primary disinfectant. enhances flocculation/ sedimentation processes. - Removal of color and odour. - Control of manganese. - Control of biofouling.	- Simple addition procedure. - Persistent residual. - Long history of use. - Cheap.	- Production of chlorinated by-products (Trihalomethanes). - Taste and odor problems possible. - pH influences effectiveness.
Chlorine Dioxide	- Disinfectant. - Control of iron and manganese. - Control of taste and odour. - Oxidation of natural and synthetic organics. - Control of biofouling.	- Relatively persistent residual. - No THM formation. - No pH effect.	- Total organic halogen (TOX) formation. - ClO_2 and ClO_3 by-products. - On-site generation required. - Hydrocarbon odours possible.
Ozone	- Disinfectant. - Destruction of THM precursors. - Oxidation of natural and synthetic organics. - Aid to color removal and flocculation. - Control of biofouling.	- Usually no THM or TOX formation. - No taste or odor problems. - Some by-products biodegradable. - Little pH effect. - Coagulant aid.	- Short half-life. - Installation cost of an ozone generator; (on-site generation required). - Energy intensive. - Some by-products biodegradable-enhancing biofouling. - Complex generation and addition. - Corrosive. - $OH^{\cdot}$ action inhibited by naturally-occuring bicarbonate.
Hydrogen peroxide/ ozone	- Disinfection. - Destruction of THM precursors. - Oxidation of natural and synthetic organics. - Control of biofouling. - Aid to color removal and flocculation.	- Improved ozone efficiency. - Easy application for existing ozone facilities. - Removal of micropollutants when used inconjuction with GAC. - No taste or odor problems.	- See above

Oxidation/ Treatment	Objective of Treatment	Advantages	Disadvantages
AOPs	- Disinfection. - Destruction of THM precursors. - Control of biofouling. - Oxidation of natural and synthetic organics.	- Destruction of THM precursors. - Easy application for existing ozone facilities. - Removal of micropollutants when used inconjuction with GAC. - No taste or odor problems.	- Bicarbonate radical scavengers. - Installation cost of ozone generator and UV lamps.
Granular Activated Carbon (GAC)	- Removal of THM and TOX precursors. - Removal of tastes and odours. - Removal of organic and synthetic organics.	- Effective treatment. - Carbon can be re-activated.	- Cost of reactivation. - Reactivation pollution. - Decreasing adsorption activity with use. - Phase transfer method: -pollutant disposal still remains.
Air stripping	- Removal of organic and synthetic organics. - Removal of dissolved gases. - Removal of taste and odor-causing compounds, and volatile organics compounds (VOCs). - Oxidation of iron and manganese.	- Effective treatment. - Relatively inexpensive.	- Phase transfer method. - Introduction of VOCs into the atmosphere.
Incineration	- Ultimate sludge disposal method.	- Effective method. - Hazardous waste disposal.	- Cost of construction and operation. - Energy intensive. - Products of incomplete combustion.
Lagoons	- Sludge dehydration prior to landfill: -non-hazardous waste disposal.	- Short-term basis-economic solution. - On-site treatment.	- Ample land requirement well away from dwellings. - Favorable climatic conditions. - Potential environmental and health hazards.
Landfill	- Ultimate sludge disposal method: -hazardous and non-hazardous waste disposal.	- Effective method.	- Potential environmental and health hazards. - Land availability.

Oxidation/ Treatment	Objective of Treatment	Advantages	Disadvantages
Land spreading	- Ultimate sludge disposal method:-non-hazardous waste disposal.	- Effective method.	- Potential environmental and health hazards. - Adsorption capacity of the soil. - Climatic conditions.

Table 1.6 The advantages and disadvantages of established and emerging treatments for water[3]

1.4 The electrochemical generation of ozone

Ozone was first identified as a distinct chemical compound by Schönbein in work that commenced with his observation that the electrolysis of water produced an odour at the anode identical to that from an electric arc [45]. Schönbein's acquisition of a Grove cell, which was able to deliver a much higher current than his previous apparatus, led to his proposal that the odour was due to a distinct chemical [46] which he named "ozone" [47]. There is a nice circularity in the acquisition of the Grove cell by Schönbein in the mid-19th century being so critical to the discovery of ozone and the use of air cathodes in electrochemical ozone cells in the 21st century (see, for example, [48]). For an in-depth review of Schönbein's work see [49]. The molecular formula of ozone was determined by Andrews and Tait in 1860 [50], only after which could the compound be determined quantitatively.

The electrolysis of water is generally believed to produce ozone *via* a 6-electron process [4][51]:

$$3H_2O \rightarrow O_3 + 6H^+ + 6e^- \qquad E° = +1.51\ V \qquad (1.54)$$

As E° for the oxidation of water to oxygen is somewhat lower, +1.23 V [18]:

$$2H_2O \rightarrow O_2 + 4H^+ + 4e^- \qquad E° = +1.23\ V \qquad (1.55)$$

oxygen is always produced simultaneously with ozone ([4] and references therein).

The solubility of ozone in acidic solutions is generally accepted as being up to *ca.* 10x that of O_2 [1][14][15] *i.e.* the saturation solubility at 0 °C and 1 atm is 22 mM.

14.1 The cell configurations employed in the electrochemical generation of ozone

The types of cell employed in the electrochemical generation of O_3 reflect those generally employed in electrolysis.

In the simplest cell configuration, the electrodes are immersed directly in the electrolyte [52] and the gases evolved at anode and cathode are allowed to mix. Professor Chan in Hong Kong University employed a small UV-Vis cuvette cell in his initial work, and this is dealt with in detail below. Separated cells employ an inert separator such as glass [52][53][54], wetted Teflon [53][55] or Nafion [56][57] and the anode and cathode gases are vented separately. As it is generally believed that ozone efficiency increases with decreasing pH [25][51], acidic electrolytes are generally employed; however, a number of studies have been reported using aqueous electrolytes at near neutral pH [58][59][60][61][62] with ozone current efficiencies of 5-12%.

Zero gap, filter-press or Membrane Electrolyte Assembly (MEA)-based cells employ a membrane (typically Nafion) as the electrolyte, with the anode and cathode being pressed tightly against the membrane. If water is fed to a Pt-based cathode (*e.g.* Pt or Pt/Ti mesh), hydrogen is evolved as the cathode reaction [63][64][65][66][67][68][69]. In contrast, if an air breathing cathode is employed (*i.e.* Pt particles deposited upon porous carbon in a gas diffusion electrode), oxygen is reduced to water at the cathode [48][70] which is a safer system, especially for domestic applications. There are also a number of reports on variations of the zero gap cell, *e.g.* feeding humidified O_2 to a gas diffusion cathode to generate H_2O_2 [71] using an air breathing cathode/Nafion "half MEA" separated from the anode by acidic electrolyte [55] and a spiral wound MEA-based cell [72].

In general, electrochemical ozone generation is carried out either in single pass/flow operation [70] or in batch recycle mode [63]. In the former case, ozone is generated in both gas and liquid phases continuously, in the latter, once saturation of the anode solution has taken place, all the ozone produced is released into the gas phase.

1.4.2 The effect of temperature on the electrochemical generation of ozone

It was realised very early in the research on electrochemical ozone generation that low temperatures favoured higher ozone current efficiencies at Pt and Pt-based electrodes [52][53][73][74][75], an observation later confirmed using other anode materials; *e.g.* PbO_2 [76][77][78] and carbon [55]. However, some authors have reported that ozone efficiency at PbO_2 decreases with decreasing temperature, *e.g.* [69][79]. Early workers took great care to cool the anode as it was generally believed that the anode temperature, rather than that of the electrolyte, was critical [52][53][75][76], and that gas bubbles could affect heat transfer [53][76][80][81][82].

Briner, Haefeli and Paillard [73] electrolysed a 5.0 M H_2SO_4 eutectic solution using a Pt anode, obtaining a maximum current efficiency of 8.5% at -67 °C. Putnam et al. [52] obtained a maximum current efficiency of 19.4% by electrolysing a 30% $HClO_4$ solution at -50 °C using a Pt anode; however, they found significantly lower efficiencies using H_2SO_4 at temperatures down to -62 °C, in contrast to the results reported by Briner and co-workers. Interestingly, Putnam et al. analysed the ozone evolved from their cells by liquefaction and measurement of the boiling point; an interesting COSHH form indeed. In general, ozone efficiency falls dramatically as the temperature approaches room temperature when Pt anodes are employed [52][53][83].

Low temperatures are often employed in conjunction with fluorine-containing anions to obtain high ozone current efficiencies [76][84][85][86]; this is generally believed to be due to the ability of small amounts of F^- to raise the oxygen overpotential [76] and was first reported in 1950 by Hickling and Hill, [87], although it has also been postulated that F^- stabilises the coverage of singlet oxygen at PbO_2, enhancing the production of O_3 [54]. Thus, PbO_2 at 0 ºC typically exhibits current efficiencies of 10-12% in the absence

of specialist anions, this increases up to *ca.* 20% in the presence of PF_6^- at the same temperature [76]. Foller and Kelsall [55] reported a current efficiency of 45% using glassy carbon electrodes at -5 ºC in 62 wt% HBF_4. However, the very high concentration of HBF_4 employed required that it was especially synthesised and also resulted in intermittent passivation of the electrode which could only be reversed by periodic switching to open circuit potential. F^--doping of PbO_2 anodes to inhibit O_2 evolution and hence improve ozone current efficiency has also been employed see, for example, the work by Amadelli et al. [88], who obtained a maximum current efficiency of *ca.* 8% at 25 ºC in 1 M H_2SO_4, using PbO_2 anodes formed by electroldeposition from solutions containing 0.01 M NaF. Higher F^- concentrations in the electrodepostion solution caused the ozone efficiency to decrease, reaching 1% at 40 mM NaF. The latter observation was interpreted by the authors as higher F^--doping of PbO_2 facilitating the formation of persulfate ions at the expense of O_3.

The primary effect of increasing temperature on electrochemical ozone generation is generally accepted to be to increase the decomposition of O_3, at least at Pt anodes; this was first postulated by Fisher and co-workers in 1907 [80][82]. In more recent papers and reviews of electrochemical ozone generation at a variety of anodes, this theory has remained unchallenged [4][51][54][57][76][78][84][89][90][91].

1.4.3 The anode material

The anodes employed for electrochemical generation fall into two time periods: ≤ 1982 and > 1982. Up to 1982, the only anode materials that had been investigated were Pt and PbO_2 ([76] and references therein), and then only in aqueous acid electrolytes. After 1982, Pt ceased to be of interest (with one exception, see [92]) and, whilst β-PbO_2 continues to be employed (see, for example, [69][93] alternative materials have been investigated, including glassy carbon [55], Ni/Sb-SnO_2 [25], IrO_2-Nb_2O_5 [86][94], tantalum oxide [95], TiO_2 [96][97] and Boron Doped Diamond (BDD) [56][68][72][98][99][100].

It is generally accepted that the most active of the α and β forms of PbO_2 is the latter [78]. A comparison of ozone evolution at 0 °C at PbO_2 anodes gives a fairly accurate view of the general activity of this material. In the absence of added F^- or fluoride-containing electrolytes, the current efficiencies observed at PbO_2 are *ca.* 3-10% at current densities of *ca.* 1.0 A cm^{-2} in aqueous H_2SO_4 or $HClO_4$ [51][54][76][85]. In 7.3 M HPF_6, an efficiency of *ca.* 50% was observed by Foller and Tobias [76], whilst addition of NaF increased current efficiency to 21% [85] or 10% [54].

IrO_2-Nb_2O_5 showed a very low ozone current efficiency at 0 °C in 3.0 M H_2SO_4, *ca.* 1% [94], rising to *ca.* 12% at 800 mA cm^{-2} in the presence of 0.03 M KPF_6. Using a layered anode formed on Si and exposing TiO_2 to the 0.01 M $HClO_4$ solution, Kitsuka et al. [97] have reported a current efficiency of *ca.* 9% at 50 mA cm^{-2} and 15 °C. Tantalum oxide-based anodes have shown a current efficiency of *ca.* 12% at room temperature and 200 mA cm^{-2} using model tap water at neutral pH.

In terms of very active and selective anodes capable of current efficiencies of ≥ 30% at room temperature and using conventional aqueous electrolytes, there are, to date, only two anodes using Boron Doped Diamond (BDD) electrodes as the anode and cathode in a zero gap cell, Kraft et al. [100] observed a current efficiency of *ca.* 24% at 20 °C for the electrolysis of deionised water. Further, Arihara and co-workers [68] obtained current efficiencies up to 47% using a zero gap cell employing a BDD anode and Pt cathode, at 25 °C, a cell voltage of 19 V and 53 mA cm^{-2}. However, electrolysis of acidic electrolyte using a BDD anode has been reported as giving O_3 at a current efficiency of only 'a few percent' at ambient temperature. In fact, it is not clear that ozone is an expected major product at BDD anodes [56]. The second highly selective anode material is Ni/Sb-SnO_2 and, as this material is the focus of the work in this thesis, is described in detail below.

In 2004, Prof K. Y. Chan of Hong Kong University [101] reported (incorrectly) that his group had generated ozone from 0.64 cm^2 Sb-SnO_2 Ti foil electrode in 0.1 M $HClO_4$ in a UV-Vis cuvette electrochemical cell, see fig 1.3, with a maximum current efficiency of

15% at cell voltages < 3 V. In a second paper [25] it was reported that the activity of the anodes reported in the first publication was due to adventitious Ni. This latter paper detailed the preparation of Ni/Sb-SnO_2 electrodes and reported a maximum current efficiency of 35%, again using the UV-Vis cuvette cell shown in fig. 1.3. There had been one previous report of ozone generation at Sb-SnO_2/Ti mesh by Foller and Tobias in 1982 [76]; the authors reported a maximum current efficiency of *ca.* 4% in 5.0 M H_2SO_4 at 0 ºC, which was short lived, due to dissolution of the electrode. Otherwise, Sb-SnO_2 electrodes are generally considered not to be ozone active. In general, Sb-SnO_2 anodes supported on Ti are associated with the direct, electrochemical oxidation of organics [102]. Hence, the production of very high O_3 activity at low cell voltages under ambient conditions and in a simple electrolyte through the addition of small amounts of Ni to Sb-SnO_2 is truly remarkable, and could not have been predicted. Further, all the anode materials discussed above are essentially 'inactive', relying upon high oxygen overpotentials to generate ozone. Ni/Sb-SnO_2 would seem to be the first 'active' anode with an active site specifically to facilitate ozone generation.

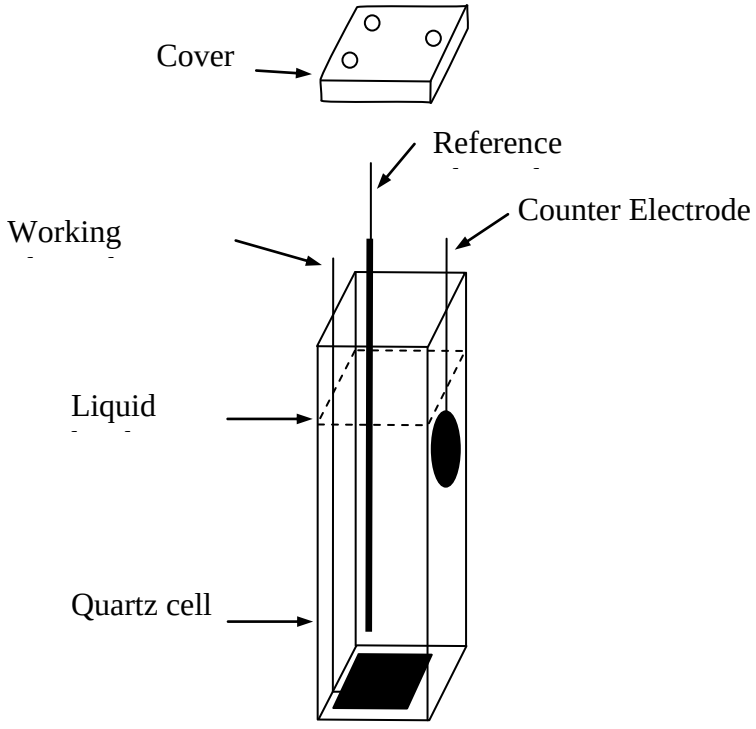

Figure 1.3 A schematic drawing of the electrolysis UV cell showing the arrangement of the working electrode, reference electrode, and the counter electrode [25].

The Chan group has only reported the very high ozone current efficiencies using small (0.64 cm^2) anodes and an important objective of the work reported in this theses was to develop active and selective Ni/Sb-SnO_2 anodes on the larger scale.

In general, at PbO_2 anodes, current efficiency increases essentially, linearly with current density [90] before levelling out and becoming independent [63][64][65][67][69][76]; typically, the current density at which this change occurs is *ca.* 1.0 A cm^{-2}, but this value depends upon the electrolyte composition [76]. Exceptions to this observation are Onda and co-workers [66] and Awad [93], both groups observe current efficiency to go through a maximum, around 1.0 A cm^{-2} and 1.5-2.0 mA cm^{-2} (respectively), before decreasing.

Boron doped diamond anodes show similar behaviour to PbO_2, with current efficiency becoming independent of current density [68] and also showing a clear maximum [100]. TiO_2 [23], Pt [25][26], C [12] and TaO_x [27] show increasing current with current density. IrO_2-Nb_2O_5 shows an onset current density for ozone evolution that varies with IrO_2 content [24]. Ni/Sb-SnO_2 electrodes show a clear maximum [25][48].

1.4.4 The effect of electrolyte

Until recently, the large majority of work on electrochemical ozone generation has focused on acid electrolytes, presumably due to the generally-held belief that ozone efficiency decreases as the pH rises. However, there have been few studies on the effect of the anion on ozone efficiency in acid solution. By far the most comprehensive work on this was reported by Foller and Tobias in 1982 [76]. The authors found a linear relationship between ozone current efficiency in 2.0 M acid at 0 °C using β–PbO_2 anode and the "composite electronegativity" of the anions. The composite electronegativity was obtained by summing the tabulated electronegativities of the individual atoms of the anion.

The data were rationalised in terms of a model, the essence of which remains in place to date, in which one of the active intermediates in the formation of O_3 is the adsorbed

oxygen atom. Quite simply, anion and oxygen coverage are competitive, with the former determined by the electronegativity of the anion: the more electronegative the less adsorption takes place. Thus, at high anion coverage, the free energy of adsorption of $O^{\cdot}$ is too low and the activation energy for $O^{\cdot}_{\mathbf{a}} + O^{\cdot}_{\mathbf{a}} \rightarrow O_{\mathbf{2}}$ is so low that O_3 does not have time to form. Conversely, too little anion adsorption causes the O atoms to be bound too tightly. However, the authors also commented that, due to the evolution of gas, the free energy of adsorption of the O atom would actually assume a broad range of values. An ideal anion coverage, specific for a particular electrolyte and anode material, would then produce the maximum possible ozone efficiency for that combination. Anions such as F^- that are non-adsorbing may never show such a maximum in efficiency as 'optimum' surface coverage is never reached. The authors also postulated that F^- could inhibit the discharge of water (to O_2) by hydrogen bonding to the H atoms of water in the Inner Helmholtz Layer.

There does not appear to be any detailed later studies on the effect of anion adsorption on electrochemical ozone generation in acid solution; studies in acid electrolyte focus primarily on the effect of F^- or F-containing electrolytes *e.g.* [4][54][78][85][94]. Da Silva and co-workers [54] re-iterate the postulate of Foller and Tobias [76] that F^- stabilises the coverage of adsorbed oxygen atoms as well as inhibiting the oxygen evolution reaction.

With respect to the effect of common acid electrolytes on ozone current efficiency, this appears, as expected, to depend upon the anode material, thus Franco et al. [103] found that the ozone current efficiency at a β–PbO_2 anode was 3.5% in 6.0 M $HClO_4$ compared to 2.9% in 3.0 M H_2SO_4. Y. H. Wang et al. [25] determined a current efficiency of *ca.* 35% in 1.0 M H_2SO_4 and *ca.* 32% in 1.0 M $HClO_4$ at a Ni/Sb-SnO_2 anode. At -50 °C at a Pt anode, Putnam et al. [52] the current efficiency was *ca.* 20% in 30% $HClO_4$ and *ca.* 6% in 28% H_2SO_4. However, Kotz and Stucki [85] determined a complex dependence of ozone efficiency at 1 A cm^{-2} when using 3.0 M $HClO_4$, H_2SO_4 and H_3PO_4 as a function of temperature. Ozone efficiency at fixed current density generally goes through a maximum as the concentration of the acid electrolyte is increased [25][76].

Most of the papers in the electrochemical ozone literature concern ozone generation using either aqueous acid electrolytes or, to a lesser extent, using Nafion as an (acidic) polymer electrolyte membrane, (Nafion is also commonly employed as the cell separator in the former studies). Few studies reported work in neutral electrolyte, *e.g.* [90][104].

More recently, work has been reported using imitation tap water, aimed at the potential application of electrochemical ozone generation in water treatment [58][59]. Feng et al. [90] obtained ozone current efficiencies of 6% and *ca.* 14% using β-PbO_2 anodes without and with Fe doping, respectively, in pH 7.5 phosphate buffer at 10 °C. El-Shal et al. [104] derived a maximum current efficiency of 7% at PbO_2 in pH 7 phosphate buffer. Kaneda and co-workers have studied anodes based on tantalum oxide in imitation tap water, *i.e.* Millipore water containing added Na^+, Ca^{2+}, K^+ and Mg^{2+} salts to a conductivity of 160 μs cm^{-1} [58][59]. The authors derived a maximum ozone current efficiency of *ca.* 12%, comparable to that derived by Feng et al. using Fe-doped β-PbO_2 [90]. To date, there has been no attempts to discuss the implications of such high ozone efficiencies obtained in neutral solution.

The third, and final, electrolyte type employed in electrochemical ozone generation is the solid polymer electrolyte, or polymer electrolyte membrane, typically Nafion. The earliest of such zero gap cells employed Pt as the cathode, with deionised water fed to both anode and cathode; O_2 + O_3 being produced at the anode and hydrogen at the cathode, and this remains the most common configuration of such cells [63][64][65][66][67][68][69][84]. Commercial systems, "Membrel" -type electrolysers, are available based on β–PbO_2 powder anodes and Pt cathodes [63], and β–PbO_2 remains the most generally employed anode in such systems [63][64][65][66][67][69][84]. Current efficiencies for ozone generation using such cells at temperatures around 25 °C are typically 5 to 20% at cell voltage 4.0 to 5.0 V. In contrast (as stated above), using a Boron Doped Diamond (BDD) anode Arihara and co-workers obtained a maximum current efficiency of 47% albeit at a cell voltage of 19.0 V. Kraft reported an ozone current efficiency of 24% using BDD electrodes as anode

and cathode, again at a relatively high cell voltage (8.0 V at 0.5 A to 23.0 V at 5.0 A with the optimum efficiency determined at *ca.* 1.3 A.

Nishiki and co-workers [72] reported a maximum current efficiency of 13% at a current of 0.75 A and *ca.* 16.0 V using a BDD rod (2.0 mm diameter) wound with a Nafion strip and stainless steel wire cathode rather than the usual planar geometry. The ozonated water so produced was used to treat skin complaints in dogs. Other variations of the zero gap configuration include the work by Okada and Naya [92] who employed a polyethylene terephthalate felt separator between the Nafion membrane and Pt mesh cathode in order to prevent degradation of the Nafion on the cathode side of the cell due to transport of Pt particles from the Pt mesh anode to the cathode. As the cathode was no longer in contact with the Nafion membrane dilute NaCl or Na_2SO_4 was employed as the catholyte. The authors reported a current efficiency of 20% at room temperature; a remarkably high value for Pt.

Another variation of the zero gap, or of the more standard acid electrolyte, approach was reported by Foller and Kelsall [55]. This is a remarkable study for several reasons: (1) it was one of the first to employ an air breathing cathode (air depolarized) as in a fuel cell; (2) the maximum current efficiency obtained was 45% using a glassy carbon anode, albeit in highly concentrated (corrosive, expensive) HBF_4 at -5 °C; (3) the paper presents a thoroughgoing analysis of the engineering aspects of the electrochemical reactors employed. One of the two reactors employed in the study utilized two air-breathing cathodes between which were cooled, tubular glassy carbon electrodes immersed in the aqueous HBF_4 electrolyte. The authors employed an air cathode following the work of the Permelec Electrode Corporation who incorporated such an air cathode into Membrel-type cell [105] and obtained current efficiencies of *ca.* 16% at a cell voltage of *ca.* 2.3 V. Such an arrangement removes the challenges associated with hydrogen gas management, lowers the cell voltage ($E°_{(O2/H2O)}$ = +1.23 V *vs.* NHE *vs.* $E°_{(H+/H2)}$ = 0 V *vs.* NHE) and decreases thermal management problems. Professor K. Y. Chan has reported two studies on zero gap cells employing air breathing cathodes [48][70] and Ni/Sb-SnO_2 anodes supported on Ti mesh. The first paper concerned a single cell comprising a Membrane

Electrode Assembly, formed by hot pressing the anode, Nafion membrane and air breathing cathode. The anode had a geometric area of 24.0 cm^2. A maximum current efficiency of *ca.* 15% was determined at a cell voltage of 2.0 V and current of 312.0 mA. The later paper concerned the development of larger electrodes (8.0 cm x 13.0 cm) and the assessment of a 4-cell stack. Using a single MEA, the authors derived a maximum current efficiency of *ca.* 17% at 2.0 A and cell voltage of 3.0 V. The four cell stack gave a maximum efficiency of 21.7% at an individual cell voltage of 3.3 V. Thus, in general, MEA-based zero gap cells using Pt or air breathing cathodes based on Pt on porous carbon give current efficiencies ≤ *ca.* 20%, the exception being the work of Arihara et al. [68][99].

1.5 Mechanism

The gas phase reaction:

$$(O^{\cdot})_{(g)} + O_2 \rightarrow O_3 \qquad (1.54)$$

is well known [106] to proceed with low activation energy, and the role of atomic oxygen as a key intermediate to O_3 has hence long been postulated (see, for *e.g.*, [76][85]). Initially, dissolved O_2 was believed to be the other reactants [63][65][85]. Stucki and co-workers employed a pressured membrel electrolyzer, [89] to investigate the possible role of dissolved O_2, but found that pressure had no effect upon current efficiency, an observation they rationalised in terms of the reactions:

$$(O)_{ads} + O_{2(g)} \xrightarrow{k_1} O_{3(g)} \qquad (1.55)$$

$$(O)_{ads} + O_{3(g)} \xrightarrow{k_2} O_{2(g)} \qquad (1.56)$$

Increasing the pressure increases O_3 and O_2 but decreases $(O)_{ads}$, hence the ratio of the two reaction rates (1.55) and (1.56) remains unchanged.

Reactions (1.55) and (1.56) show another generally held view that $(O^{\cdot})_{ads}$ is common to both O_2 and O_3 formation. It is now generally accepted that adsorbed O_2 is the active intermediate, along with $(O^{\cdot})_{ads}$ and/or $(OH^{\cdot})_{ads}$ [65][84][90], and that the discharge of water is the rate determining step [84].

The most commonly accepted, general mechanism for electrochemical ozone generation is that put forward by Da Silva and co-workers [78][4]:

$$(H_2O)_{ads} \rightarrow (OH^{\cdot})_{ads} + H^+ + e^- \quad (1.57)$$

$$(OH^{\cdot})_{ads} \rightarrow (O^{\cdot})_{ads} + H^+ + e^- \quad (1.58)$$

$$(O^{\cdot})_{ads} \rightarrow [1-\theta](O^{\cdot})_{ads} + \theta(O^{\cdot})^*_{ads} \ (0 < \theta < 1) \quad (1.59)$$

$$[1-\theta](2O^{\cdot})_{ads} \rightarrow [1-\theta](O_2)_{ads} \quad (1.60)$$

$$[1-\theta](O_2)_{ads} \rightarrow [1-\beta].[1-\theta](O_2)_{ads} + \beta[1-\theta](O_2)^*_{ads} \ (0 < \beta < 1) \quad (1.61)$$

$$[1-\beta].[1-\theta](O_2)_{ads} \rightarrow O_2\uparrow \quad (1.62)$$

$$\theta(O^{\cdot})^*_{ads} + \beta[1-\theta](O_2)^*_{ads} \rightarrow [\theta + \beta(1-\theta)](O_3)_{ads} \quad (1.63)$$

$$[\theta + \beta(1-\theta)](O_3)_{ads} \rightarrow O_3\uparrow \quad (1.64)$$

"θ" and "β" represent the surface coverage by oxygen species while "*" represent the fractional surface coverage leading to O_3.

1.6 Research objectives

The aim of the research reported in this thesis was to develop an electrochemical cell capable of injecting ozone directly into water having no added electrolyte (*e.g.* tap water) at a cell voltage <3.0 V and at an ozone concentration of ≥3 ppm.

The objectives of the research to achieve the aim were: (1) to reproduce the synthesis of Ni/Sb-SnO_2 anodes developed by Prof. Chan's group in Hong Kong; (2) optimize the synthesis of the electrodes with respect to the selective generation of ozone in acid solution as a step to achieving the aim of ozone generation in neutral water; (3) develop an in-situ UV-Vis spectroscopic analysis, and calibrate this approach against complementary methods, *e.g.* iodometry. (4) characterizse the anodes using appropriate analytical techniques (*e.g.* I/V methods, SEM, EDX). (5) Develop and optimize a scale up synthesis of active and selective anodes. (6) Develop methodology to produce Membrane Electrode Assemblies (MEAs) to allow the electrochemical production of ozone in water without added electrolyte, and optimize. The target energy consumption is that typically reported for Cold Corona Discharge (CCD) of 18 kWh kg^{-1}.

It should be noted that the project was sponsored by Clarizon Ltd and hence the scientific strategy employed was tempered with the commercial development required by the sponsor.

1.7 References

1. Seidel, A., *Kirk-Othmer Encyclopaedia of Chemical Technology*. 5th Edition, Vol. 17, New Jersey: John Wiley and Sons Inc., p. 768-822 (2006).
2. Tramborubo, R., S. N. Ghosh, C. A. Burrus Jr. and W. Gordy, "The Molecular Structure, Dipole Moment, and g Factor of Ozone from Its Microwave Spectrum," *The Journal of Chemical Physics* 21(5): 851-855 (1953).
3. Tchobanoglous, G., F. L. Burton and H. D. Stensel, *Wastewater Engineering, Treatment and Reuse.* 4th Edition, New York: McGraw-Hill, p. 1286-1295 (2004).
4. Da Silva, L. M., M. H. P. Santana and J. F. C. Boodts, "Electrochemistry and Green Chemical Processes: Electrochemical Ozone Production," *Quimica Nova* 26(6): 880-888 (2003).
5. Benson, S. W., and A. E. Axworthy, "Mechanism of the Gas Phase, Thermal Decomposition of Ozone," *The Journal of Chemical Physics* 26(6): 1718-1726 (1957).
6. Weiss, J., "Investigations on the Radical HO_2 in Solution," *Transactions of the Faraday Society* 31: 668-681 (1935).
7. Kilpatrick, M. L., C. C. Herrick and M. Kilpatrick, "The Decomposition of Ozone in Aqueous Solution," *Journal of the American Chemical Society* 78(9): 1784-1789 (1956).
8. Bühler, R. E., J. Staehelin and J. Hoigné, "Ozone Decomposition in Water Studied by Pulse Radiolysis. 1. HO_2/O_2^- and HO_3/O_3^- as Intermediates," *The Journal of Physical Chemistry* 88: 2560-2564 (1984).
9. Staehelin, J., R. E. Bühler and J. Hoigné, "Ozone Decomposition in Water Studied by Pulse Radiolysis. 2. OH and HO_4 as Chain Intermediates," *The Journal of Physical Chemistry* 88(24): 5999-6004 (1984).
10. Staehelin, J., and J. Hoigné, "Decomposition of Ozone in Water in the Presence of Organic Solutes Acting as Promoters and Inhibitors of Radical Chain Reactions," *Environmental Science and Technology* 19(12): 1206-1213 (1985).

11. Lim, S. W., and C. E. D. Chidsey, "Role of O_3 and $OH^{\cdot}$ Radicals in Ozonated Aqueous Solution for the Photoresist Removal of Semiconductor Fabrication," *Ozone Science and Engineering* 27: 139-146 (2005).
12. Streng, A. G., "Tables of Ozone Properties," *Journal of Chemical and Engineering Data* 6(3): 431-436 (1961).
13. Battino, R., *Oxygen and Ozone. IUPAC Solubility Series*. Volume 7, 519, Oxford: Pergamon (1981).
14. Smedt, F. De, S. De Gendt, M. M. Heyns and C. Vinckier, "The Application of Ozone in Semiconductor Cleaning Processes, The Solubility Issue," *Journal of The Electrochemical Society* 148(9): G487-493 (2001).
15. Levanov, A. V., I. V. Kuskov, E. E. Antipenko and V. V. Lunin, "The Solubility of Ozone in Aqueous Solutions of Sulfuric, Phosphoric, and Perchloric Acids," *Russian Journal of Physical Chemistry A* 82(7): 1126-1131 (2008).
16. Guidance Note EH38 from the Health and Safety Executive, *"*Ozone: Health Hazards and Precautionary Measures," *Environmental Hygiene Series* 38: 1-4 (1983).
17. Christensen, P. A., and G. M. Walker, *Opportunities for the UK in Solar Detoxification.* University Newcastle upon Tyne, Newcastle upon Tyne (1996).
18. Bard, A. J., R. Parsons and J. Jordan, *Standard Potentials in Aqueous Solution*. New York and Basel: International Union of Pure and Applied Chemistry, p. 321-339 (1985).
19. Cheremisinoff, N. P., *Handbook of Water and Wastewater Treatment Technologies.* Boston: Butterworth-Heinemann, p. 454-495 (2002).
20. White, G. C., *Handbook of Chlorination and Alternative Disinfectants.* 4th Edition, New York: John Wiley and Sons Inc., p. 1203-1261 (1999).
21. Bcc Research., Ozone Generation: Technologies, Markets and Players. Retrieved 13th November, 2010, from World Wide Web http://www.bccresearch.com/report/CHM044B.html.
22. Freedonia, *Products-Non-Chemical Water Treatment to 2009: Ozone Generation Equipment Demand in Water Treatment*. Internal Report (2004)**.**

23. Meunier, L., S. Canonica and U. V. Gunten, "Implications of Sequential Use of UV and Ozone for Drinking Water Quality," *Water Research* 40: 1864-1876 (2006).
24. Kim, J. H., M. S. Elovitz, U. V. Gunten, H. M. Shukairy and B. J. Mariñas, "Modeling Cryptosporidium Parvum Oocyst Inactivation and Bromate in a Flow-Through Ozone Contactor Treating Natural Water," *Water Research* 41: 467-475 (2007).
25. Wang, Y. H., S. Cheng, K. Y. Chan and X. Y. Li, "Electrolytic Generation of Ozone on Anotimony- and Nickel- Doped Tin Oxide Electrode," *Journal of The Electrochemical Society* 152(11): D197-D200 (2005).
26. Ning, B., N. Graham, Y. Zhang, M. Nakonechny and M. G. El-Din, "Degradation of Endocrine Disrupting Chemicals by Ozone/AOPs," *Ozone: Science and Engineering* 29(3): 153-176 (2007).
27. Uchiyama, T., H. Kobayashi, H. T. Znad, M. Tokumura, Y. Kawase, "Dynamic Performance of Ozonation Treatment for Nonionic Surfactants (Polyoxyethylene Alkyl Ether) in a Bubble Column Reactor," *Ozone Science and Engineering* 29(1): 65-72 (2007).
28. Ikehata, K., N. J. Naghashkar, M. G. El-Din, "Degradation of Aqueous Pharmaceuticals by Ozonation and Advanced Oxidation Processes: A Review," *Ozone: Science and Engineering* 28(6): 353-414 (2006).
29. Hua, H., E. R. Bennett and R. J. Letcher, "Ozone Treatment and the Depletion of Detectable Pharmaceuticals and Atrazine Herbicide in Drinking Water Sourced from the Upper Detroit River, Ontario, Canada," *Water Research* 40: 2259-2266 (2006).
30. Buffle, M. O., J. Schumacher, E. Salhi, M. Jekel and U. V. Gunten, "Measurement of the Initial Phase of Ozone Decomposition in Water and Wastewater by Means of a Continuous Quench-Flow System: Application to Disinfection and Pharmaceutical Oxidation," *Water Research* 40: 1884-1894 (2006).

31. Gordon, G., and B. Bubnis, "Environmentally Friendly Methods of Water Disinfection: The Chemistry of Alternative Disinfectants," *Progress in Nuclear Energy* 37(1-4): 37-40 (2000).
32. Bicknell, D. L., and R. K. Jain, "Ozone Disinfection of Drinking Water-Technology Transfer and Policy Issues," *Environmental Engineering and Engineering and Policy* 3(1-2): 55-66 (2002).
33. Haag, W. R., and J. Hoigné, "Kinetics and Products of the Reactions of Ozone with Various Forms of Chlorine and Bromine in Water," *Ozone Science and Engineering* 6(2): 103-114 (1984).
34. Glaze, W. H., "Reaction Productions of Ozone: A Review," *Environmental Health Perspectives* 69: 151-157 (1986).
35. Fielding, M., J. H., C. D. Watts, C. Corless, N. J. D. Graham and R. Perry, *Water Research Centre* 127 (1987).
36. Reynolds, G., N. Graham, R. Perry and R. G. Rice, "Aqueous Ozonation of Pesticides: A Review," *Ozone Science and Engineering* 11(4): 339-382 (1989).
37. William, P. E. F., *Water Quality and Treatment-A Handbook of Community Water Supplies, American Water Works Association.* New York: McGraw-Hill (1990).
38. Kogelschatz, U., B. Eliasson and M. Hirth, "Ozone Generation from Oxygen and Air: Discharge Physics and Reaction Mechanisms," *Ozone Science and Engineering* 10(4): 367-377 (1988).
39. Excel water Technologies Instrument. Retrieved 13th November, 2010, from World Wide Web http://www.excelwater.com/eng/b2c/ozone.php.
40. Mallevialle, J., I. H. Suffet and U. S. Chan, *Influence and Removal of Organics in Drinking Water.* London: Lewis Publishers, p. 207-217 (1992).
41. Legrini, O., E. Oliveros and A. M. Braun, "Photochemical Process for Water Treatment," *Chemical Reviews* 93(2): 671-698 (1993).
42. Pocostales, J. P., M. M. Sein, W. Knolie, C. V. Sonntag and T. C. Schmidt, "Degradation of Ozone-Refractory Organic Phosphates in Wastewater by Ozone and Ozone/Hydrogen Peroxide (Peroxone): The Role of Ozone Consumption by

Dissolved Organic Matter," *Environmental Science and Technology* 44(21): 8248-8253 (2010).

43. Staehelin, J., and J. Holgné, "Decomposition of Ozone in Water: Rate of Initiation by Hydroxide Ions and Hydrogen Peroxide," *Environmental Science and Technology* 16: 676-681 (1982).
44. Merényi, G., J. Lind, S. Naumov and C. V. Sonntag, "Reaction of Ozone with Hydrogen Peroxide (Peroxone Process): A Revision of Current Mechanistic Concepts Based on Thermokinetic and Quantum-Chemical Considerations," *Environmental Science and Technology* 44: 3505-3507 (2010).
45. Schönbein, C. F., *Ber. Verh. Nat. Ges. Basel.* 4: 58 (1838-40).
46. Schönbein, C. F., *Philos. Mag. (III)* 17: 293 (1840).
47. Schönbein, C. F., C. R. Hebd., *Seances Acad. Sci. Ser. C*, 10: 706 (1840).
48. Wang, Y. H., S. Cheng and K. Y. Chan, "Synthesis of Ozone from Air *via* a Polymer-Electrolyte-Membrane Cell with a Doped Tin Oxide Anode," *Green Chemistry* 8: 568-572 (2006).
49. Rubin, M. B., *Bull. Hist. Chem.*, 26 (2001) 40.
50. Andrews, T. and P. G. Tait, *Philos. Trans. Roy. Soc.*, London 150: 113 (1860).
51. Da Silva, L. M., D. V. Franco, J. C. Forti, W. F. Jardim and J. F. C. Boodts, "Characterisation of a Laboratory Electrochemical Ozonation System and Its Application in Advanced Oxidation Process," *Journal of Applied Electrochemistry* 36(5): 523-530 (2006).
52. Putnam, G. L., R. W. Moulton, W. W. Fillmore and L. H. Clark, "Electrolytic Ozone," *Journal of The Electrochemical Society* 93(5): 211-221 (1948).
53. Seader, J. D. and C. W. Tobias, "Ozone by Electrolysis of Sulfuric Acid," *Industrial and Engineering Chemistry* 44(9): 2207-2211 (1952).
54. Da Silva, L. M., L. A. D. Faria and J. F. C. Boodts, "Electrochemical ozone production: Influence of the Supporting Electrolyte on Kinetics and Current Efficiency," *Electrochemica Acta* 48: 699-709 (2003).
55. Foller, P. C., and G. H. Kelsall, "Ozone Generation *via* the Electrolysis of Fluoboric Acid Using Glassy Carbon Anodes and Air Depolarized Cathodes," *Journal of Applied Electrochemistry* 23(10): 996-1010 (1993).

56. Michaud, P. A., M. Panizza, L. Ouattara, T. Diaco, G. Foti and Ch. Comninellis. "Electrochemical Oxidation of Water on Synthetic Boron-Doped Diamond Thin Film Anodes," *Journal of Applied Electrochemistry* 33: 151-154 (2003).
57. Kim, J. and G. V. Korshin, "Examination of in situ Generation of Hydroxyl Radicals and Ozone in a Flow-Through Electrochemical Reactor," *Ozone: Science and Engineering*, 30: 113-119 (2008).
58. Kaneda, K., M. Ikematsu, Y. Koizumi, H. Minoshima, T. Rakuma, D. Takaoka and M. Yasuda, "Ozone Generation by a TaOx and Pt Composite Insulator-Coated Ti Electrode," *Electrochemical and Solid-State Letters* 8(6): J13-J16 (2005).
59. Award, M. I., S. Sata, K. Kaneda, M. Ikematsu, T. Okajima and T. Ohsaka, "Ozone Electrogeneration at a High Current Efficiency Using a Tantalum Oxide-Platinum Composite Electrode," *Electrochemistry Communication* 8(8): 1263-1269 (2006).
60. Graves, J. E., D. Pletcher, R. L. Clarke and F. C. Walsh, "The Electrochemistry of Magnéli Phase Titanium Oxide Ceramic Electrodes Part II: Ozone Generation at Elbonex and Ebonex/Lead Dioxide Anodes," *Journal of Applied Electrochemistry* 22: 200-203 (1992).
61. Wen, T. C. and C. C. Chang, *Journal of the Electrochemical Society* 9: 2764 (1993).
62. Kaneda, K., M. Ikematsu, M. Iseki, D. Takaoka, T. Higuchi, T. Hattori, T. Tsukamoto and M. Yasuda, *Chemistry Letters* 34(10): 1320-1321 (2005).
63. Stucki, S., G. Theis, R. Kötz, H. Devantay and H. J. Christen, "In Situ Production of Ozone in Water Using a Membrel Electrolyzer," *Journal of The Electrochemical Society* 132(2): 367-371 (1985).
64. Tatapudi, P., and J. M. Fenton, "Synthesis of Ozone in a Proton Exchange Membrane Electrochemical Reactor," *Journal of the Electrochemical Society* 140(12):3527-3530 (1993).
65. Beaufils, Y., C. Comninellis and P. Bowen, "Preparation and Characterisation of Ti/IrO2/Pb Electrodes for ozone Production in a SPE Electrochemical Cell," *ICHEME Symposium Series* 145: 191-200 (1999).

66. Onda, K., T. Ohba, H. Kusunoki, S. Takezawa, D. Sunakawa and T. Araki, "Improving Characteristics of Ozone Water Production With Multilayer Electrodes and Operating Conditions in a Polymer Electrolyte Water Electrolysis Cell," *Journal of the Electrochemical Society* 152(10): D177-D183 (2005).
67. Han, S. D., J. D. Kim, K. S. Myung, R. K. Rana and K. C. Singh, "Electro-chemical production of ozone using water electrolysis cell of solid polymer electrolyte (SPE)," *Indian Journal of Chemical Technology* 13: 156-161 (2006).
68. Arihara, K., C. Terashima and A. Fujishima, "Electrochemical Production of High-Concentration Ozone-Water Using Freestanding Perforated Diamond Electrodes," *Journal of the Electrochemical Society* 154(4): E71-E75 (2007).
69. Da Silva, L. M., D. V. Franco, L. G. Sousa and I. C. Goncalves, "Characterization of an Electrochemical Reactor for the Ozone Production in Electrolyte-Free Water," *Journal of Applied Electrochemistry* 40: 855-864 (2010).
70. Cui, Y. H, Y. H. Wang, B. Wang, H. H. Zhou, K. Y. Chan and X. Y. Li, "Electrochemical Generation of Ozone in a Membrane Electrode Assembly Cell with Convective Flow," *Journal of the Electrochemical Society* 156(4): E75-E80 (2009).
71. Tatapudi, P. and J. M. Fenton, *Journal of Electrochemical Society* 141: 1174 (1994).
72. Nishiki, Y., N. Kitaori and K. Nakamuro, "Performances of Small-Sized Generator of ozone-Dissolved Water Using Boron-Doped Diamond Electrodes," *Ozone: Science and Engineering* 33: 114-120 (2011).
73. Briner, E., R. Haefeli and H. Paillard, *Helv. Chim. Acta* 20: 1510 (1937).
74. Briner, E., and A. Yalda, *Helv. Chim. Acta* 25: 1188 (1942).
75. Lash, E. I., R. D. Hornbeck, G. L. Putnam and E. D. Boelter, "Production of ozone with Refrigerated Anodes," *Electrochemical and Solid-State Letters* 98(4): 134-137 (1951).
76. Foller, P. C., and C. W. Tobias, "The Anodic Evolution of Ozone," *Journal of Electrochemical Society* 129(3):506-515 (1982).

77. Amadelli, R., A. D. Battisti, D. V. Girenko, S. V. Kovalyov and A. B. Velichenko, "Electrochemical Oxidation of *trans*-3,4-dihdroxycinnamic Acid at PbO_2 Electrodes: Direct Electrolysis and Ozone Mediated Reactions Compared," *Electrochemica Acta* 46: 341-347 (2000).
78. Da Silva, L. M., L. A. D. Faria and J. F. C. Boodts, "Green Processes for Environmental Application. Electrochemical Ozone Production" *Pure Applied Chemistry* 73(12): 1871-1884 (2001).
79. Velichenko, A. B., R. Amadelli, A. Benedetti, D. V. Girenko, S. V. Kovalyov and F. I. Danilov, "Electrosynthesis and Physicochemical Properties of PbO_2 Films," *Journal of the Electrochemical Society* 149(9): C445-C449 (2002).
80. Fischer, F. and K. Massenez, *Z. Anorg. Chem.* 52: 202 (1907).
81. Mazza, B., P. Pedeferri and G. Re, "Hydrodynamic Instabilities in Electrolytic Gas Evolution," *Electrochemica Acta* 23: 87-93 (1978).
82. Fischer, F. and K. Bendixsohn, *Z. Anorg. Chem.* 61: 13 (1909).
83. Baleji, J. and M. Thumova, Collect. Czech. Chem. Commun. 39: 3409 (1974).
84. Babak, A. A., R. Amadelli, A. De Battisti and V. N. Fateev, "Influence of Anions on Oxygen/Ozone Evolution on PbO_2/*spe* and PbO_2/Ti Electrodes in Neutral pH Media," *Electrochimica Acta* 39(11-12): 1597-1602 (1994).
85. Kotz, E. R., and S. Stucki, "Ozone and Oxygen Evolution on PbO_2 Electrodes in Acid Solution," *Journal of Electronalysis Chemistry* 228: 407-415 (1987).
86. Santana, M. H. P., L. A. Faria and J. F. C. Boodts, "Effect of preparation Procedure of IrO_2-Nb_2O_5 anodes on surface and Electrocatalytic Properties," *Journal of Applied Electrochemistry* 35: 915-924 (2005).
87. Hickling A. and S. Hill, "Oxygen Overvoltage Part III.-A Note on the Standard Potentials of the Hydroxyl Radical and Atomic Oxygen," *Transaction Faraday Society* 46: 557-559 (1950).
88. Amadelli, R., L. Armelao, A. B. Velichenko, N. V. Nikolenko, D. V. Girenko, S. V. Kovalyov and F. I. Danilov, "Oxygen and ozone Evolution at Fluride Modified Lead Dioxide Electrodes," *Electrochemica Acta* 45: 713-770 (1999).

89. Stucki, S., H. Baumann, H. J. Christen and R. Kötz, "Performance of a Pressurized Electrochemical Ozone Generator," *Journal of Applied Electrochemistry* 17: 773-778 (1987).
90. Feng, J. and D. C. Johnson, "Electrocatalysis of Anodic Oxygen-Transfer Reactions," *Journal of the Electrochemical Society* 141(10): 2708-2711 (1994).
91. Franco, D. V., W. F. Jardim, J. F. C. Boodts and L. M. D. Silva, "Electrochemical Ozone Production as an Environmentally Friendly Technology for Water Treatment," *Clean* 36(1): 34-44 (2008).
92. Okada, F. and K. Naya, "Highly Efficient and Long-Lifetime Ozone Water Production System Realized Using a Felt Separator," *Journal of the Electrochemical Society* 156(8): E125-E131 (2009).
93. Awad, M. I. and M. M. Saleh, "Electrochemical Generation of Ozone at PbO2-Loaded Platinum Screens," *Journal of Sold State Electrochemistry* 14(10): 1877-1883 (2010).
94. Santana, M. H. P., L. A. D. Faria and J. F. C. Boodts, "Investigation of the Properties of Ti/[IrO_2-Nb_2O_5] Electrodes for Simultaneous Oxygen Evolution and Electrochemical ozone Production, EOP," *Electrochemica Acta* 49(12): 1925-1935 (2004).
95. Kaneda, K., M. Ikematsu, M. Iseki, D. Takaoka, T. Higuchi, T. Hattori, T. Tsukamoto and M. Yasuda, "Si/TiO_X/Pt/TaO_X Electrodes Fabricated by Sputtering for Electrochemical Ozone Generation," *Japanese Journal of Applied Physics* 45: 6417-6419 (2006).
96. Kitsuka, K., K. Kaneda, M. Ikematsu, M. Iseki, K. Mushiake and T. Ohsaka, "Ex Situ and In Situ Characterization Studies of Spin-Coated TiO_2 Film Electrodes for the Electrochemical Ozone Production Process," *Electrochemica Acta* 55(1): 31-36 (2009).
97. Kitsuka, K., K. Kaneda, M. Ikematsu, M. Iseki, K. Mushiake and T. Ohsaka, "n-Type TiO_2 Thin Films for Electrochemical Ozone Production," *Journal of the Electrochemical Society* 157(2): F30-F34 (2010).

98. Katsuki, N., E. Takahashi, M. Toyoda, T. Kurosu and M. Lida, "Water Electrolysis Using Diamond Thin-Film Electrodes" *Journal of the Electrochemical Society* 145(7): 2358-2362 (1998).
99. Arihara, K., C. Terashima and A. Fujishima, "Application of Freestanding Perforated Diamond Electrodes for Efficient Ozone-Water Production," *Electrochemical and Solid-State Letters* 9(8): D17-D20 (2006).
100. Kraft, A., M. Stadelmann, M. Wünsche and M. Blaschke, "Electrochemical Ozone Production Using Diamond Anodes and a Solid Polymer Electrolyte," *Electrochemistry Communications* 8: 883-886 (2006).
101. Cheng, S. A., and K. Y. Chan, "Electrolytic Generation of Ozone on an Antimony-Doped Tin Dioxide Coated Electrode," *Electrochemical and Solid State Letter* 7(3): D4-D6 (2004).
102. Lozano, B. C., Ch. Comninellis and A. De Battisti, "Service Life of Ti/SnO_2-Sb_2O_5 Anodes," *Journal of Applied Electrochemistry* 27(8): 970-974 (1997).
103. Franco, D. V., L. M. Da Silva, W. F. Jardim, J. F. C. Boodts, "Influence of the Electrolyte Composition on the Kinetics of the Oxygen Evolution Reaction and Ozone Production Processes," *Journal Brazilian Chemical Society* 17(4): 746 – 757 (2006).
104. W.El-Shal et al., Desalination 99: 149 (1994).
105. Katoh, M., Y. Nishiki and S. Nakamatsu, "A Study on Electrochemical Ozone Generator Using Oxygen Gas Diffusion Cathode," *Meeting of the Japan Electrochemical Society*, April (1992).
106. Eliasson, B. and U. Kogelschatz, "Electron impact dissociation in Oxygen," *Journal of Physics B: Atomic and Molecular Physics.* 19: 1241-1247 (1986).

Chapter 2 Experimental

2. Experimental

Table 2.1 and 2.2 list the chemicals, materials and equipment used during the work reported in this thesis, along with purity and suppliers. All the chemicals were used as received unless otherwise stated.

2.1 Chemicals and materials

Reagents / Materials	Formula	Analysis	Supplier
Tin (IV) chloride pentahydrate	$SnCl_4.5H_2O$	Puriss min 98%	Riedel-de Haën
Antimony (III) chloride	$SbCl_3$	A.C.S. reagent 99%	Sigma-Aldrich
Nickel(II)chloride hexahydrate	$NiCl_2.6H_2O$	A.C.S. reagent	Sigma-Aldrich
Oxalic acid	$(COOH)_2$	98%	Sigma-Aldrich
Gold (III) chloride hydrate	$HAuCl_4.xH_2O$	99.99% metal	Sigma-Aldrich
Dihydrogen hexachloroplatinate (IV) hexahydrate	$H_2PtCl_6.6H_2O$	99.9 %	Alfa Aesar, A John Matthey
Acetone	CH_3COCH_3	Puriss	Fluka
Hydrochloric acid	HCl	Puriss min 37%	Riedel-de Haën
Sulfuric acid	H_2SO_4	Puriss 95-97%	Fluka
Ethanol	C_2H_5OH	Puriss	Fluka
Millipore water	H_2O	18.2 MΩ.cm	Millipore
Hydrogen peroxide	H_2O_2	Puriss, 35%	Riedel-de Haën
Potassium chloride	KCl	> 99.5%	Fluka
Potassium Ferrocyanide	$K_4Fe(CN)_6.3H_2O$	Analytical Reagent, 99%	Hopkin and Williams Ltd
Nafion® perfluorinated ion-exchange resin	$C_7HF_{13}O_5S\ .C_2F_4$	5wt % in a mixture of lower aliphatic alcohols and H_2O	Sigma-Aldrich
Sodium Hydroxide	NaOH	Puriss	Riedel-de Haën
Platinum mesh, 0.25 mm, 20 x 20 mm	Pt	99.9%	Goodfellow

Reagents / Materials	**Formula**	**Analysis**	**Supplier**
Titanium mesh, 20 feet	Ti	20%	Dexmet, USA
Titanium wire, diameter 0.25mm	Ti	99.6%	Goodfellow
Nafion 117 membrane	$C_7HF_{13}O_5S\ .C_2F_4$	0.41 x 1.23 m	DuPont Corp. USA
Celgard 2400, 25 μm thick microporous polypropylene membrane	$(C_3H_6)_n$	41% porosity, 0.043 μm pore size	Celgard USA
Polyethylene tubing	$(C_2H_4)_n$	7.0 mm x 10.5 mm	Portex 800/012/425/800
Anti-bumping granules 250g	Al_2O_3	Grains de ponce, Siedesteine	BDH
Calomel Reference Electrode,	Ag/AgCl/ 4M KCl		SH Scientific

Table 2.1 List of chemicals and materials employed in the work reported in this thesis.

Equipment	**Supplier**
UV/VIS 200 nm FF Concave Holographic Spectrometer EEP 2000C	Stellar Net Inc.
Xenon Flash Lamp Module, 11-28 V DC(1 A)	Hamamatsu
UV/VIS Spectrometer and software, Astranet Systems	Astranet Systems Limited, Cambridge, United Kingdom
MasterFlex Digital Standard Pump L/S™ Console Drive, model 7519-06 cartridge pump	Cole-Palmer
Flow meter system, WU series	Cole-Palmer
TSX 1820P Programmable DC PSU (TTi), 18 V, 20 A	Tektronix
Hameg HM 7044 Power supply	Hameg Instrument
Air admiral air pump	Cole-Palmer
Potentiostat/Galvanostat version 4.9 and General Purpose Electrochemical System Program (GPES)	Windsor Scientific
Precision DC Power supply, TS3022S, 30V-2A	Thandar
Hot surface heating press	Chauffante Elcometer
Ultrasonic bath, 2510	Branson
Oven, model N6C	Genlab Ltd. Thermal Engineers
Furnace, Carbolite Type 301, MC16-GB-C-1, Eurotherm 301 controller	Barlword Scientific

Equipment	Supplier
Stirrer Bar, PC-351	Corning
Magnetic Stirrer CB 162	Stuart
Ceramic Boat	Shenzhen Jinghui Electronics Co. Ltd.
Thermometer76 mm immersion,	Fisherbrand
Analytical balance, model R 20	Oertling
Bunsen burner	Amal
Heating press (Presse Chauffante)	Ecometer

Table 2.2 List of equipment employed in the work reported in this thesis.

2.2 The anodes

The ozone anodes were initially fabricated *via* a paint brush coating method developed by Prof K. Y. Chan in Hong Kong University [1]; this coating procedure was modified significantly during the period covered by this thesis, and the development of the synthesis will be described in Chapter 4; hence only a basic summary of the initial coating process is given below. As the brush method was rapidly replaced by dip-coating, the latter is described.

Titanium was chosen as a substrate as its use as a support for SnO_2-based anodes is well documented in the literature, see for example: [1][2][3][4][5], Ti mesh substrates of dimensions 0.8 cm x 0.8 cm, 2.5 cm x 2.5 cm and 7.0 cm x 5.0 cm were employed.

Taking the fabrication of a 2.5 cm x 2.5 cm anode as typical (see fig. 2.1): each Ti mesh was cut to produce a 2.5 cm x 2.5 cm section which was then pressed in a Chauffante Elcometer press at room temperature and 1000 N for 5 minutes to flatten out any protrusions. The tip of a 4.0 cm length of 0.5 mm diameter. Ti wire was flattened with a hammer and spot-welded to the mesh (scale = low, %weld 40 weld = 1) such that the wire ran along the middle of the mesh in firm contact with its entire length.

Each mesh + wire was weighed and the mass recorded, after which the meshes were degreased by wiping with a tissue soaked in acetone, followed by thorough washing with Millipore Milli-Q water (18 MΩ cm) and then ultrasonication in Millipore Milli-Q water for 5 minutes.

The Ti meshes were then boiled in 10 wt.% oxalic acid (20 g in 200 ml Millipore Milli-Q water) for at least 30 minutes, *i.e.* until the solution took on a brownish tinge. The solution was allowed to cool to room temperature after which the meshes were washed with copious amounts of Millipore Milli-Q water. They were then placed in fresh Millipore Milli-Q water in a beaker immersed in an ultrasonic bath for 10 minutes, the water replaced and the procedure repeated until no oil/grease was observed on the surface of the water. The meshes were then dried in a 60 ºC oven for 1 hour by placing in a beaker with the meshes uppermost, in the oven. The meshes were then weighed and their masses recorded.

2.2.1 Electrodeposition

The electrodeposition solution consisted of 0.5 M $SnCl_4.5H_2O$ and 0.05 M $SbCl_3$ in 500 ml ethanol, *i.e.* to give a Sn:Sb molar ratio of 10:1. The Pt/Ti cathodes and Ti mesh anode were both immersed in the electrodeposition solution. The Ti mesh was clamped *via* its connecting wire, and held vertically in 200 ml of the electrodeposition solution, co-facial to a Pt-coated Ti mesh (see fig. 2.2). The Ti mesh was then connected to the (-) {black} pole of a TTi TSX 1820P programmable DC power supply and a Pt/Ti mesh, one either side of the Ti mesh, to the (+) {red} pole. The initial potential of the anode and cathode were not determined. Deposition was initiated at a current density of 6.40 mA cm^{-2} (0.04 A) for 25 minutes (the voltage across the cell was typically 4.23 V).

Following electrodeposition, each Ti mesh was washed thoroughly with Millipore Milli-Q water and placed in a beaker with the meshes uppermost, and allowed to dry at room temperature for 1 hour. The meshes were then weighed and the masses recorded.

The Ti mesh electrodes were placed in an oven, in a beaker with the meshes uppermost, at 100 ºC for 15 minutes. The meshes were removed and immediately laid horizontally in a silica boat and placed in a furnace pre-heated to 520 ºC for 2 hours. The furnace was switched off, the meshes removed and allowed to cool for 1 minute before commencing dip-coating.

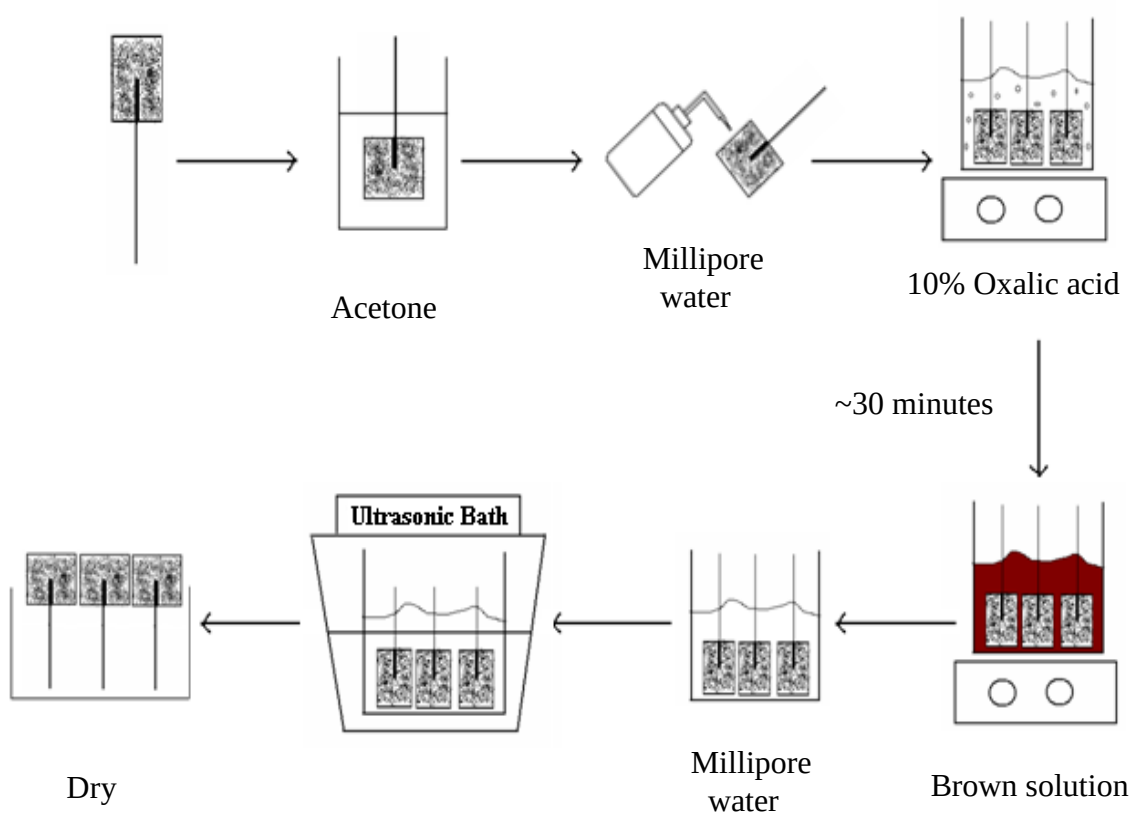

Figure 2.1 Schematic representation of the procedure involved in cleaning and etching.

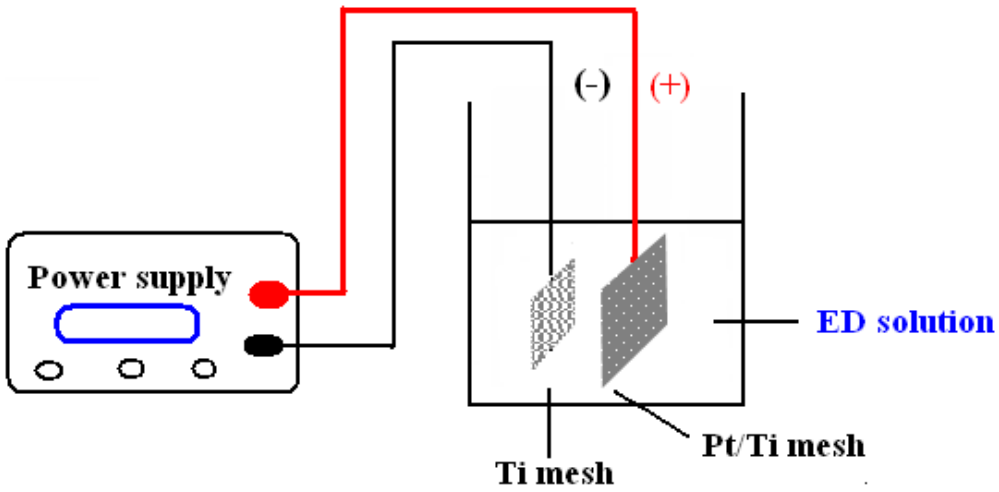

Figure 2.2 Schematic representation of the electrodeposition step.

2.2.2 Catalyst coating

The catalyst coating solution consisted of $SnCl_4.5H_2O$, $SbCl_3$ and $NiCl_2.6H_2O$ in the molar ratio 500:8:x where x = 1 in the Hong Kong University recipe; for the latter, 35.0 g, 0.365 g and 0.0475 g, respectively, of the reactants were placed in 100 ml ethanol in a 100 ml volumetric flask and shaken thoroughly to dissolve. The solution was poured into a beaker. Each 6.25 cm^2 mesh electrode was dip-coated with catalyst solution. The electrodes were then placed in a beaker (mesh uppermost) and transferred to an oven at 100 ºC for 15 minutes after which they were removed, laid horizontally in a furnace boat and placed in a furnace pre-heated to 520 ºC. The furnace was switched off before admitting the meshes. It was then turned on and allowed to attain 520 ºC again (*ca*. 5 minutes) and the meshes heated for 20 minutes. The boat + mesh electrodes were then removed, the meshes allowed to cool for 1 minute and the coating repeated. The coating, oven and furnace steps were repeated 18 times. The final (20^{th}) coating was heated in the furnace for 75 minutes at 520 ºC. After every 5 coats, the anodes were weighed. The cool mesh electrodes were then weighed and the masses recorded.

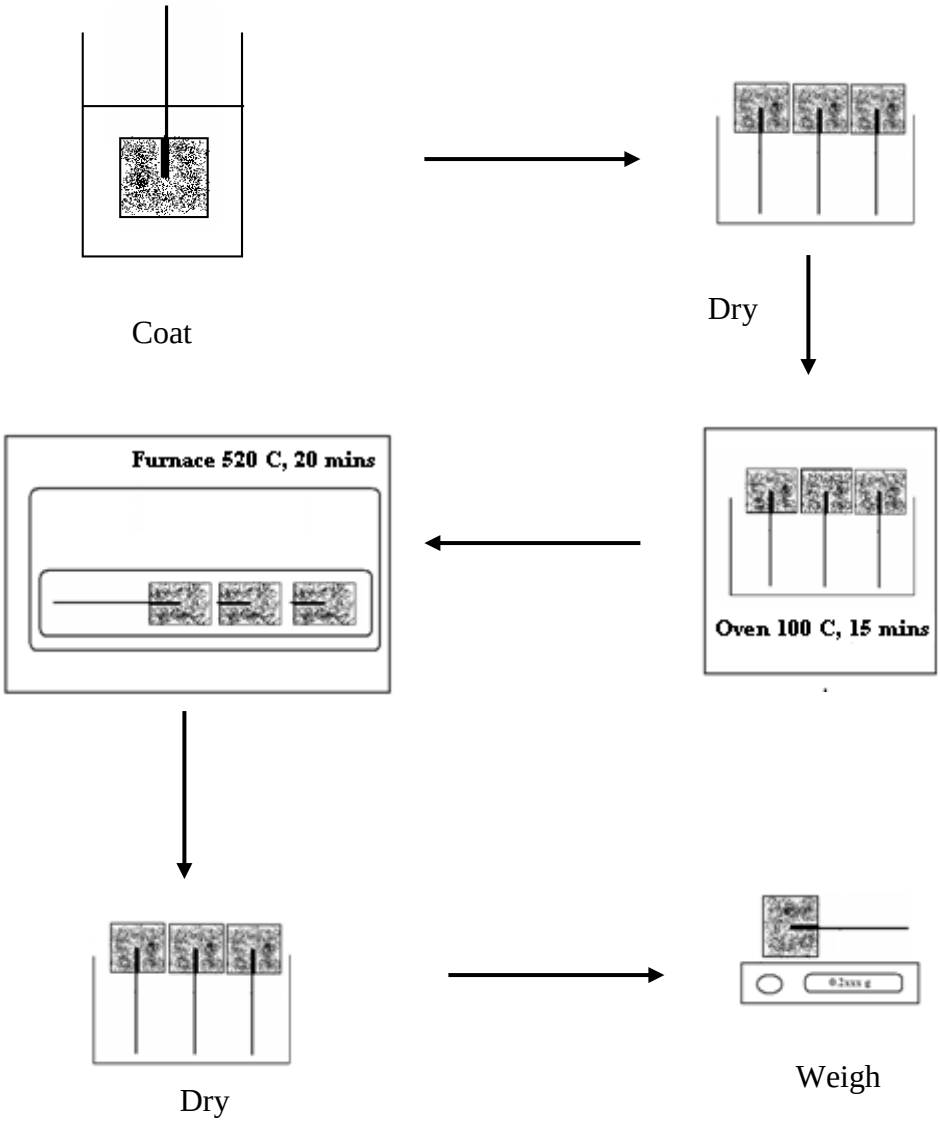

Figure 2.3 Schematic representations of the procedure involved in dip-coating.

The 7.0 cm x 5.0 cm anodes were made for use in the polycarbonate cells (see section 2.4) and were spot welded into a titanium frame once the mesh was coated with catalyst. Thus, a 8.0 cm x 5.0 cm Ti mesh was cleaned and degreased etc as described above, see fig. 2.4. Two titanium wires there then spot-welded on see fig 2.4 (a).

Following electrodeposition and coating, the meshes were trimmed, removing the wires, to 7.0 cm x 5.0, and spot-welded into a titanium frame, figs. 2.4 (g) and (h).

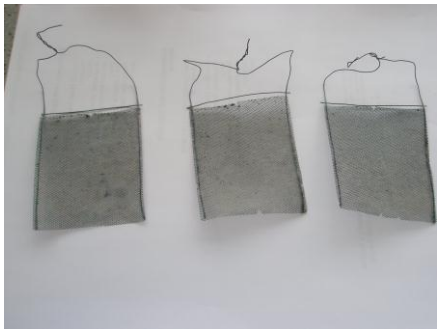

(a)

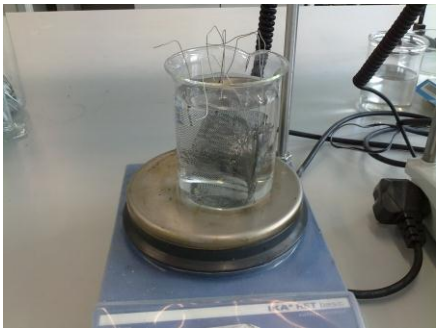

(b)

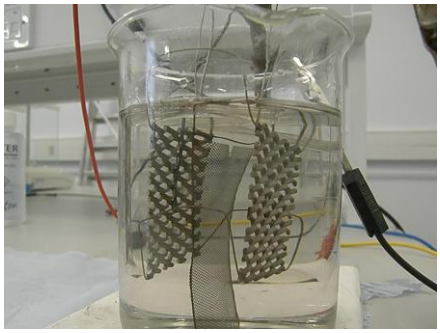

(c)

(d)

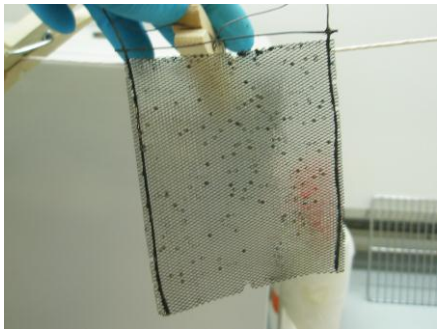

(e)

(f)

(g)

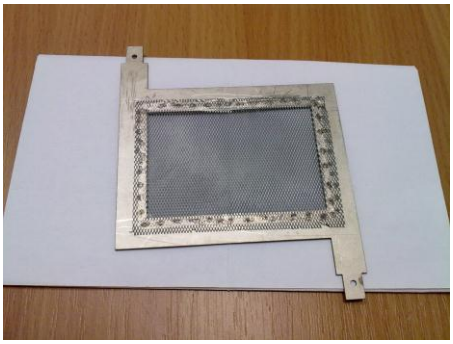

(h)

Figure 2.4 Photographs of (a) 8.0 cm x 5.0 cm Ti mesh with Ti wire on (b) cleaning, (c) electrodeposition, (d) coating, (e) drying, (f) heating, (g) 7.0 cm x 5.0 Ti mesh after cutting and (h) 7.0 cm x 5.0 Ti mesh in a titanium frame.

2.3 Power supplies and pumps

The DC power supplies employed in the work reported in this thesis were a TTi TSX 1820P DC PSU and a Hameg HM 7044 PSU, see figs 2.5 (a) and (b), respectively.

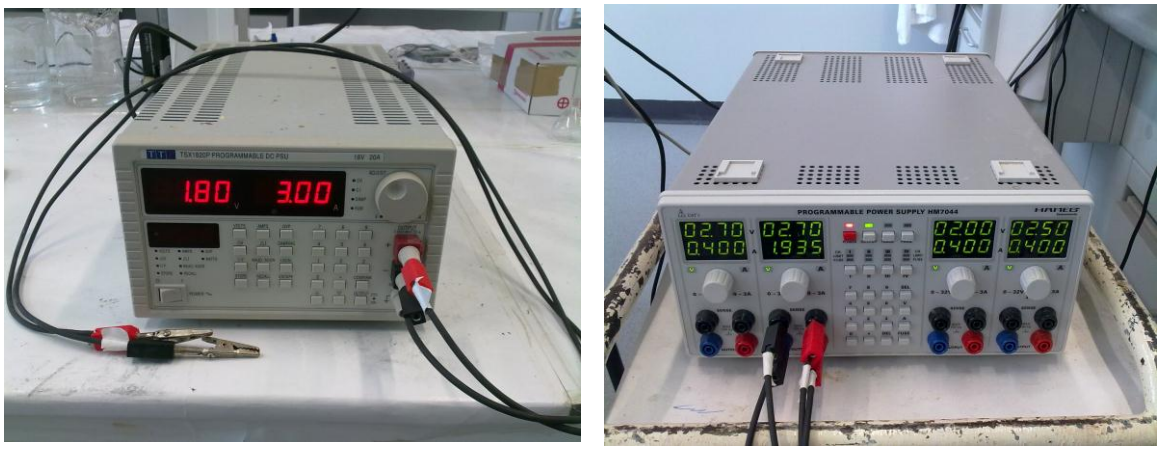

(a) *(b)*

Figure 2.5 Photographs of the (a) TTi and (b) Hameg power supply units.

The pump most commonly employed was a Masterflex L/S with an 'Easyload II' 77200-60 tubing cassette, see fig. 2.6.

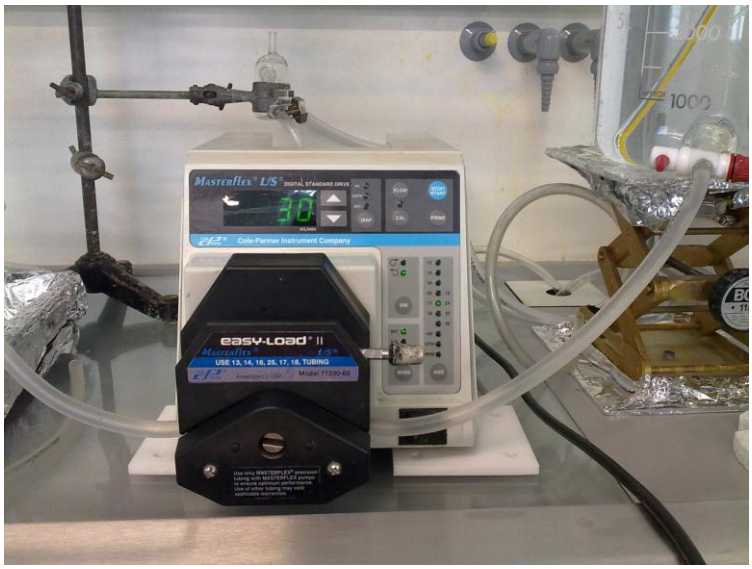

Figure 2.6 Photograph of the Masterflex pump.

2.4 The electrochemical cells

Two types of electrochemical cell were employed: glass (area exposed to electrolyte = 6.0 cm x 4.0 cm) and polycarbonate, depending upon whether 2.5 cm x 2.5 cm or the 'framed' electrodes, respectively were being tested. The most commonly employed was the glass cell.

The glass cell comprised two Pyrex glass halves of oval section having ground glass flanges. The sections were clamped together on either side of the Nafion or Celgard membrane, sealing being achieved by means of silicone O-rings between the ground glass flanges and membrane. The volume of each half of the cell was *ca.* 100 cm^3. 0.5 M H_2SO_4 was employed as the anolyte and catholyte, which were kept separate by the membrane; the later was stationary and supplied from a glass reservoir *via* polyethylene tubing (Portex 800/012/425/800 7.0 mm x 10.5 mm), see fig. 2.7. The counter electrode (cathode) was a 5.0 cm x 5.0 cm platinised Ti mesh, and the cell voltage across the ozone anode and Pt/Ti cathode was controlled with a TTi TSX 1820P or Hameg HM 7044 power supply unit. All experiments were conducted at room temperature, 20-25 ºC.

Figure 2.7 Photograph of the glass electrochemical cell.

The polycarbonate cell was designed to allow both 'standard' electrolysis (acid anolyte and acid catholyte) or (with slight modifications) electrolysis with a membrane/electrode assembly (MEA). A photograph of a polycarbonate cell is shown in fig 2.8 (a), and a schematic representation in fig. 2.8 (b).

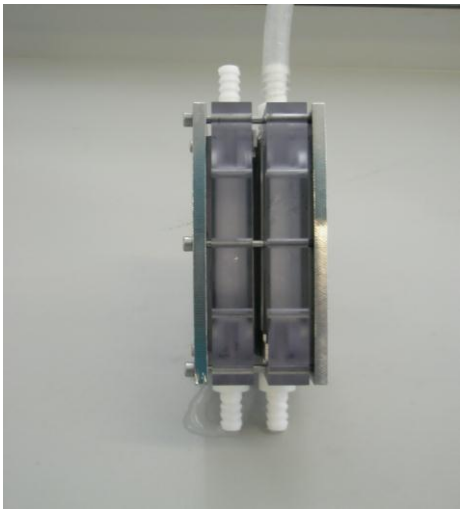

(a)

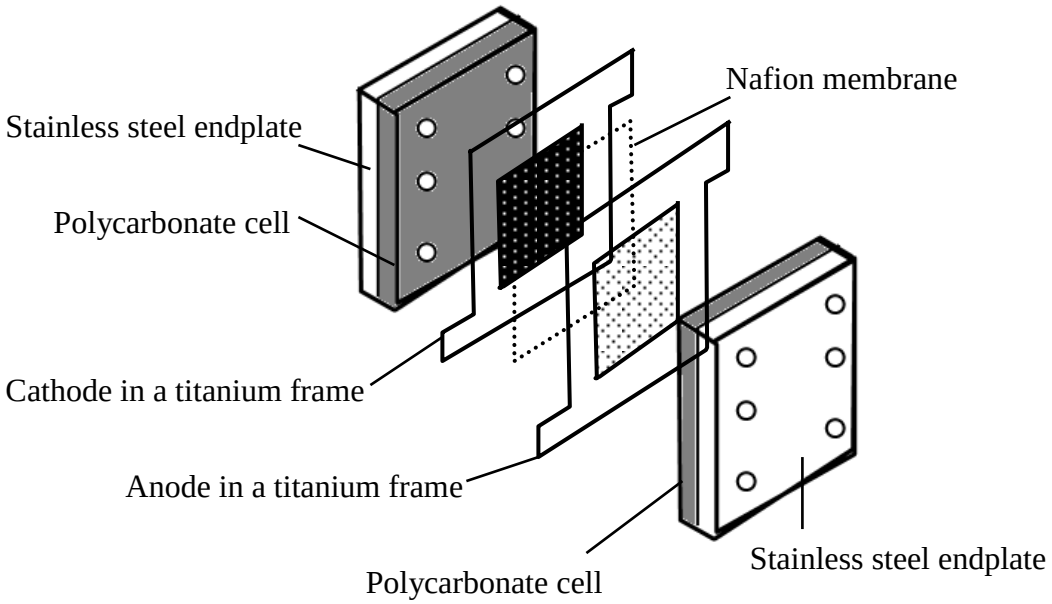

(b)

Figure 2.8 Showing of (a) photograph and (b) schematic of the polycarbonate cell 35.0 cm^2.

2.5 The spectrometer

The spectrometer employed throughout the work reported in this thesis was a UV/VIS 200 nm FF Concave Holograph Spectrometer with Xenon Flash Lamp and an Astranet UV-Vis fibre optic spectrometer utilizing 1.0 cm path length flow cells, see figs. 2.9 (a)-(b).

(a)

(b)

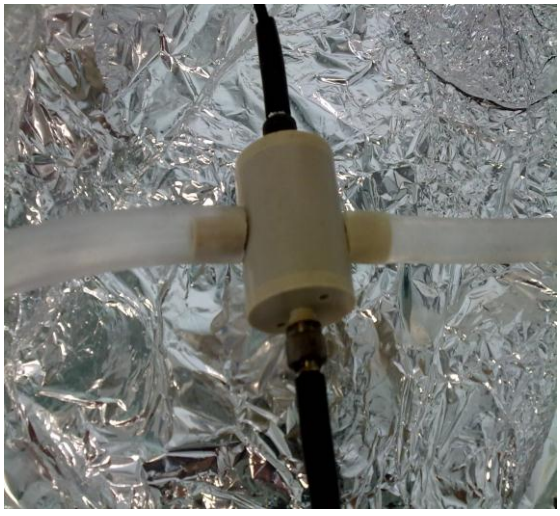

(c)

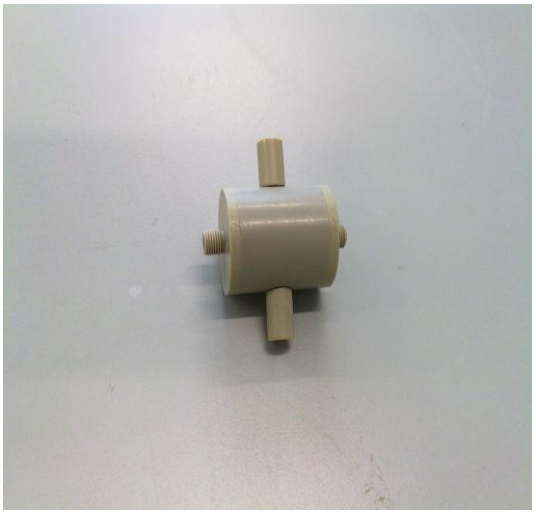

(d)

Figure 2.9 Photographs of (a) UV/VIS 200 nm FF Concave Holograph Spectrometer and Xenon flash lamp, (b) the Astranet spectrometer, (c) and (d) the flow cell.

2.6 Scanning electron microscope (SEM) and Energy Dispersive X-ray analysis (EDX)

Scanning electron microscopy (SEM) micrographs were obtained using a JEOL 5300 LV instrument fitted with Rontec and Si (Li) Energy Dispersive X-ray (EDX) detectors cooled by liquid nitrogen. The SEM (see fig. 2.10) was operated at 25 kV, but the magnification was limited to 5000x due to charging of the sample. All SEM/EDX runs were carried out by the Materials Analytical Unit, Newcastle University [6].

Figure 2.10 Photograph of Scanning electron microscope (SEM) and Energy Dispersive X-ray analysis (EDX) [2].

2.7 X-ray Photoelectron spectrometry (XPS)

X-ray Photoelectron spectra were obtained by Dr. Adrain Boatwright using the Kratos AXIS ULTRA instrument in the Centre for Surface Chemical Analysis in Nottingham University. The XPS spectrometer (see fig. 2.11) employed a monochromated Al K_α source (1486.6 eV) operated at an emission current of 3 mA and 12 kV anode potential. The detector was operated in Fixed Analyser Transmission (FAT) mode, with a pass energy of 80 eV for wide scans and pass energy 20 eV for high resolution scans. The magnetic immersion lens system allows the area of analysis to be defined by apertures, a

'slot' aperture of 300 μm x 700 μm for wide/survey scans and high resolution scans; see fig. 2.11. The takeoff angle for the photoelectron analyser was 90 degrees and acceptance angle of 30 degrees (in magnetic lens mode). Electrons emitted from the top surface of the sample are taken through an electrostatic/magnetic lens system (Hybrid lens) and a Concentric Hemispherical Analyser (CHA). This sorts the electrons by energy; electron detection and counting is then achieved with a triple channel plate and delay line detector (DLD). For non-conducting samples, a charge neutraliser filament above the sample surface gives a flux of low energy electrons providing uniform charge neutralisation. The analysis chamber pressure is typically better than 5 $x10^{-9}$ Torr (actual pressure 1 x 10^{-8} Torr) [7].

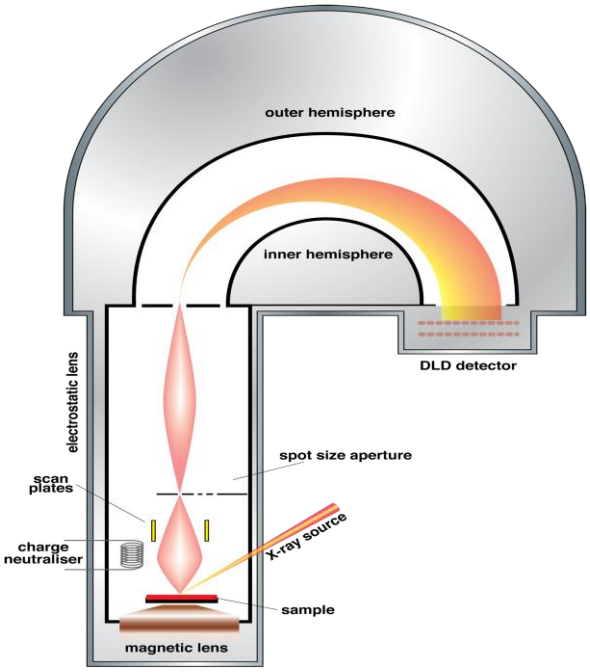

Figure 2.11 Schematic of the electron path through the lenses and detection system on X-ray Photoelectron Spectroscopy (XPS) instrument [7].

For surface analysis, a wide survey scan and high resolution scan was carried out for each sample. The high resolution scans were usually charge corrected to the main C 1s peak = 285 eV and then quantified to compare the amounts of each element present,

using Kratos sensitivity factors. Components are fitted under the peaks to give chemical information. Wide scans were run for 20 minutes and high resolution scans for 10-30 minutes. Step size 1 eV for wide scans, range 0-1400 eV binding energy. Step size 0.1 eV for high resolution scans, with various binding energy ranges depending on the element. Data analysis was carried out using CASAXPS software with Kratos sensitivity factors to determine atomic % values from the peak areas [7].

Samples must be compatible with Ultra High Vacuum (UHV) therefore must not outgas substantially. Samples were inserted into an airlock for transfer into the main UHV chamber. Typically samples pumped down quickly, usually 1/2 hour. Powders or more gassy samples could be pumped overnight in the airlock. XPS is very surface sensitive, detecting information from 5-10 nm, so fingerprints or surface contamination will cover surface information. Therefore it was important not to touch surfaces once prepared or to leave residues from cleaning. Samples were stored in glass jars, or wrapped in household foil and not plastic bags, as these contain very mobile silicone release agents, which can contaminate the surface [7]. A photograph of apparatus of XPS is shown in fig. 2.12.

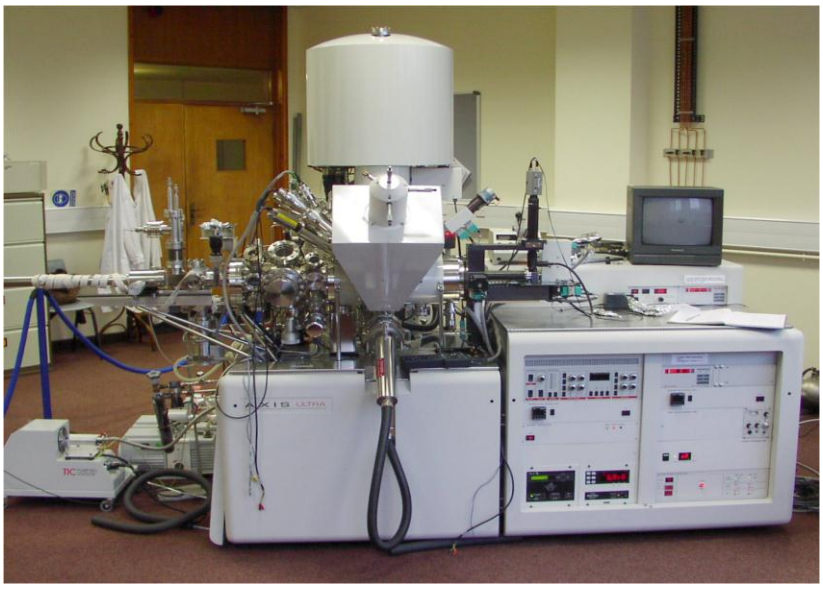

Figure 2.12 Photograph of X-ray Photoelectron spectroscopy (XPS): Kratos AXIS ULTRA XPS [7].

2.7.1 Results

XPS data were obtained on two 0.8 cm x 0.8 cm anodes, AJED26D (500:8:3 Sn:Sb:Ni mole ratio in coating solution) AJED26G and AJED26H (500:8:3:0.1 Sn:Sb:Ni:Au in dipcoating solution), see Chapter 4, tables 4.1-4.3 for details. AJED26D was chosen as representative of the standard composition before use, and AJED26G and AJED26H as representative of the anodes containing Au, the latter also having been employed in a 96 hour electrolysis to probe durability. Figure 2.13 (a) shows a typical XPS spectrum, that of AJED26D and fig. 2.13 (b) shows the Sn 3d region of the spectrum in fig. 2.13 (a). Unfortunately, the technique was insufficiently sensitive to detect the Ni or Au in the anodes. However, by comparison of the energies of the 487.2 eV and 495.5 eV Sn features with the literature values of the Sn $3d_{5/2}$ and $3d_{3/2}$ peak [8], 486.7 eV and 495.1 eV, respectively, it was confirmed that Sn was present as Sn^{IV} oxide.

2.8 Time-of-flight Secondary Ion Mass Spectrometry (ToF-SIMS)

Time of Flight Secondary Ion Mass Spectrometry (ToF-SIMS) measurements were carried out by Dr. David Scurr of the Laboratory of Biophysics and Surface Analysis (LBSA), School of Pharmacy, Nottingham University [9]. The measurements were carried out using a ToF-SIMS version IV (ION-ToF GmbH), see fig. 2.14.

ToF-SIMS uses an ion beam to sputter material (as secondary ions) from the surface of the sample. The secondary ions enter the "flight tube" and their mass determined to two decimal places [10] by measuring the exact time it takes for the ions to reach the detector. The three typical operating modes are: surface spectroscopy (mass spectra), surface imaging (element mapping) and depth profiling [11].

The spatial resolution of the LBSA instrument is better than 100 nm, using gallium ions. Depth profiling is achieved using Ar^+ or Cs^+ ions [9].

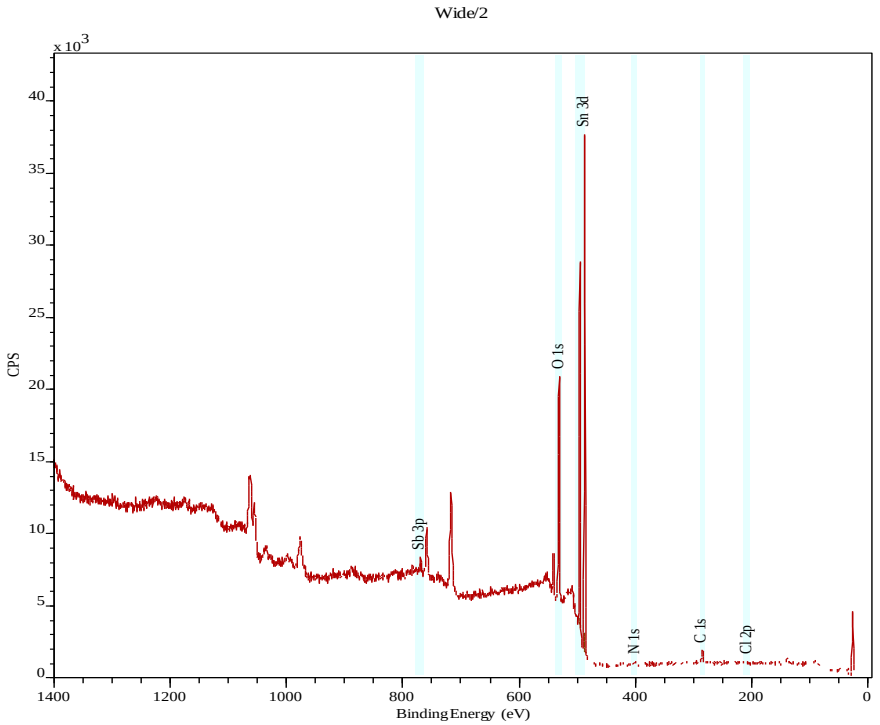

(a)

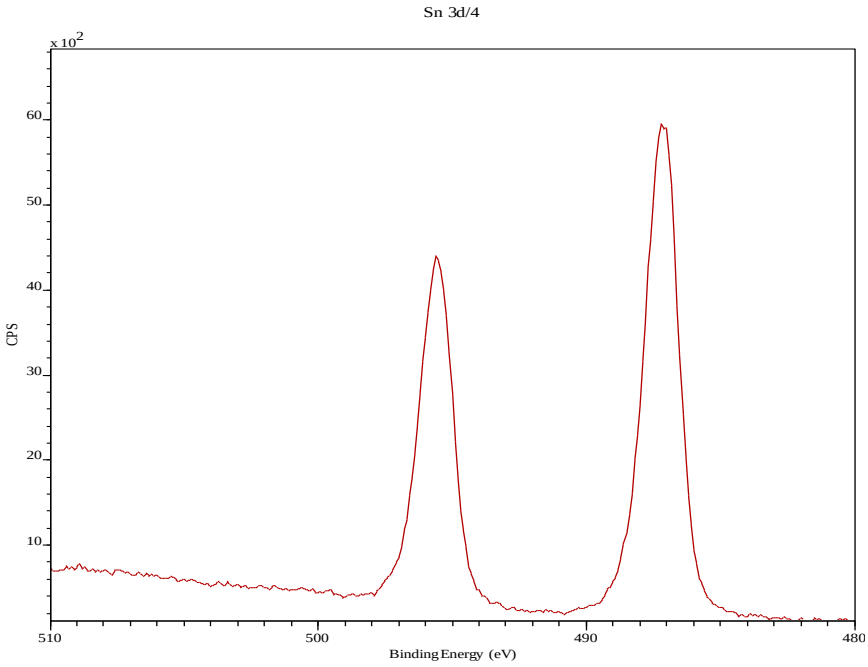

(b)

Figure 2.13 (a) XPS spectrum of anode AJED26D (0.64 cm^2, 500:8:3 Sn:Sb:Ni mole ratio in coating solution); see text for details. (b) Sn 3d region of the spectrum in (a).

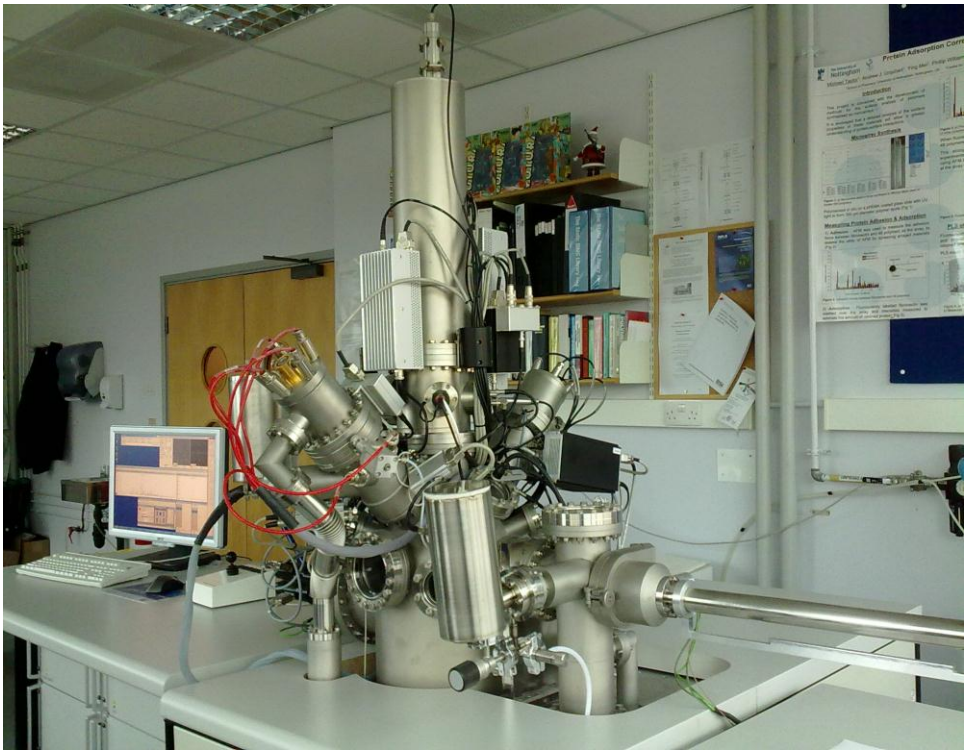

Figure 2.14 A photograph of the Nottingham University ToF-SIMS version IV instrument [9].

2.8.1 Results

ToF-SIMS was able to detect Ni in AJED26G and AJED26H, see fig. 2.15, but not Au; however, Dr. Scurr stated that the intensities of the ToF-SIMS peaks could not be related to the amount of the element present in the sample. Unfortunately, time did not allow an in-depth study, but the data are promising.

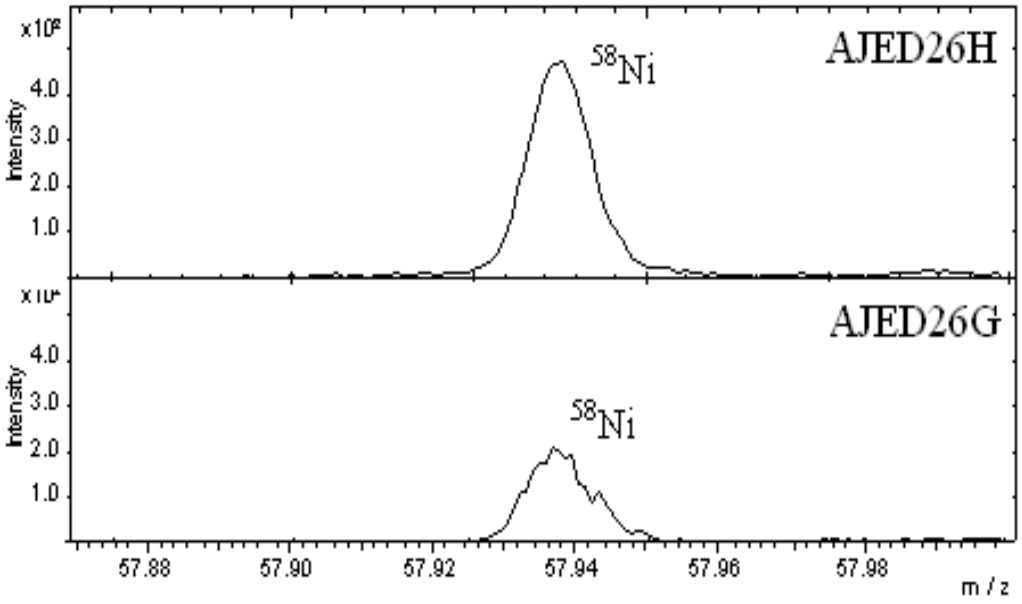

(a)

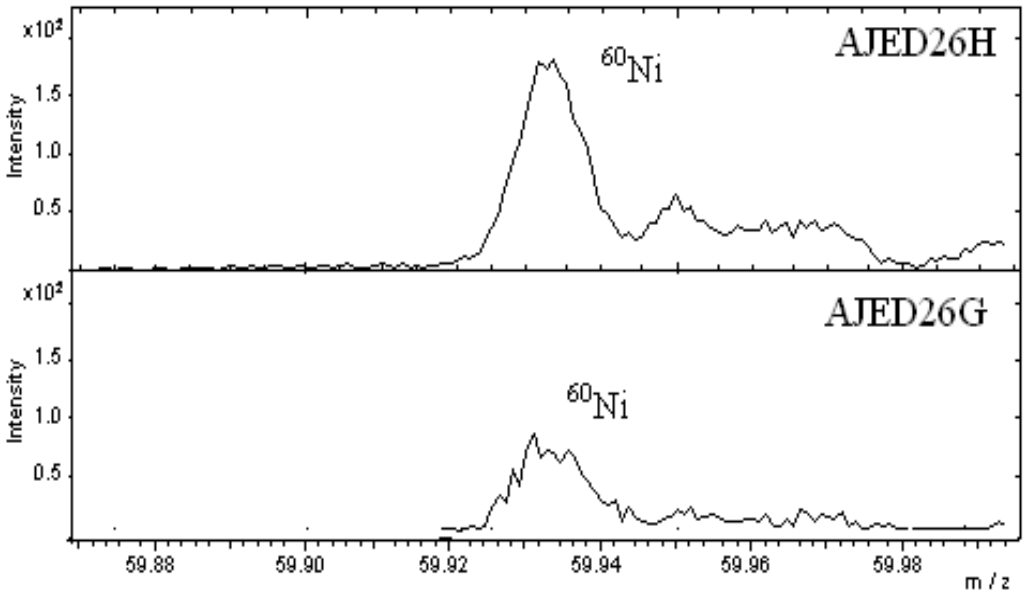

(b)

Figure 2.15 ToF-SIMS spectra of anodes AJED26G and AJED26H showing the (a) ^{58}Ni and (b) ^{60}Ni region.

2.9 Calculation of current efficiency and energy consumption from the flow rate and absorbance of dissolved or gas phase ozone

2.9.1 Current efficiency

The determination of the current efficiency for ozone production by measuring the UV absorbance of the gas phase ozone evolved from the anode is, theoretically at least, relatively straightforward [12][13]. The key is that the ozone must first be diluted with a carrier gas such as air or nitrogen, as the absorbances of pure ozone are linear region of the current efficiency, *i.e.* 5% efficiency would give a gas phase absorbance of about 5 in a 1 cm path length gas cell, 40% efficiency would give an absorbance of 40. If the spectrophotometer was capable of maintaining the linear relationship between absorbance and concentration. This is not possible; the maximum absorbance measurable such that the Beer Lambert Law is obeyed is generally quoted as *ca.* 0.9 see, for example, [14].

Thus, for a total flow rate f cm^3 min^{-1} (anode gas flow + diluent):

$$A = \varepsilon C \ell \tag{2.1}$$

$$C = \frac{A}{\varepsilon \ell} \tag{2.2}$$

Where ε is the extinction coefficient = 3000 dm^3 mol^{-1} cm^{-1}, C the concentration in mol dm^{-3} and ℓ is the path length = 1 cm.

Let steady state have been established (*e.g.* saturation of the anolyte by the O_3+O_2 anode gas); in 1 s, *f/60* ml of gas will have passed the UV detector or *f/6000* dm^3.

The number of moles of ozone in *f*/60000 dm^3, $\eta_{O3,actual}$, is given by:

$$n_{O3,actual} = \frac{Af}{\varepsilon \ell 60000} \tag{2.3}$$

The number of moles of ozone generated in 1 s at a current *I* assuming 100% current efficiency is:

$$\dot{n}_{O3,100\%} = \frac{I}{6F} \tag{2.4}$$

Since ℓ = 1 cm the actual current efficiency is thus:

$$\Phi^{e}_{O3} = 100\left[\frac{\dot{n}_{O3,actual}}{\dot{n}_{O3,100\%}}\right] \tag{2.5}$$

$$\Phi^{e}_{O3} = 100\left[\frac{\left(\frac{Af}{\varepsilon\ell 60000}\right)}{\left(\frac{I}{6F}\right)}\right] \tag{2.6}$$

$$\Phi^{e}_{O3} = \frac{AfF}{100\varepsilon\ell} \tag{2.7}$$

$$\Phi^{e}_{O3} = \frac{96480Af}{300000I} \tag{2.8}$$

$$\Phi^{e}_{O3} = \frac{0.32Af}{I} \tag{2.9}$$

Equation (2.9) also applies to the generation of ozone in solution using the flow cell configuration, with *f* now the anolyte flow rate in $cm^3\ min^{-1}$. Under these conditions, the current efficiency so obtained is an underestimate, as O_3 escaping into the gas phase is neglected.

2.9.2 Energy consumption

The current (I/Amps) = the charge passed (Q/Coulombs) per second. Thus, the moles of ozone generated per second n is given by:

$$n = \frac{\Phi^e I}{6F100} \tag{2.10}$$

where Φ^e is the efficiency in % (*i.e.* 23%) and F is the Faraday, 96480 C mol^{-1}. n is in moles per hour is:

$$n = \frac{3600\Phi^e I}{6F100} \quad moles\ hr^{-1} \tag{2.11}$$

The mass, m, of ozone in kg hr^{-1} is:

$$m = \frac{6\,\Phi^e I48}{F1000} \quad kg\ hr^{-1} \tag{2.12}$$

Excluding all external loads (*e.g.* pumps) the energy consumption of the cell, W (kW):

$$W = \frac{VI}{1000} \tag{2.13}$$

Thus the energy consumption W_{O3} in kW hr kg^{-1} O_3 is given by:

$$W_{O3} = \frac{W}{m} = \frac{\left[\frac{VI}{1000}\right]}{\left[\frac{6\Phi^e_{O3} I48}{F1000}\right]} \tag{2.14}$$

$$W_{O3} = \frac{VIF}{6\Phi^e_{O3} I48} \tag{2.15}$$

$$W_{O3} = \frac{96480V}{228\Phi^{e}_{O3}} \tag{2.16}$$

$$W_{O3} = \frac{335V}{\Phi^{e}_{O3}} \quad kW\ hr\ kg^{-1}\ O_3 \tag{2.17}$$

For example, anode AJED2D gave a dissolved ozone absorbance of 0.46 and current 0.29 A at a flow rate of 100 $cm^3\ min^{-1}$ and cell voltage of 2.7 V in an acid/acid cell From equation (2.9) and (2.17), the current efficiency is *ca.* 50% and the minimum energy consumption is 18 kW hr kg^{-1} O_3, calculated as below:

$$\Phi^{e}_{O3} = \frac{0.32\ (0.46)(100 cm^3\ min^{-1})}{0.29A} = 50\% \tag{2.18}$$

$$W_{O3} = \frac{335(2.7V)}{50\%} = 18\ kW\ hr\ kg^{-1}\ O_3 \tag{2.19}$$

The same calculation on MEA comprising anode HCED22 experiment 1 (7.0 cm x 5.0 cm in Ti frame) in a water/air cell yields a current efficiency of *ca.* 12% and minimum energy consumption of 44 kW hr kg^{-1} O_3 at a cell voltage of 1.6 V:

$$\Phi^{e}_{O3} = \frac{0.32\ (0.45)(60 cm^3\ min^{-1})}{0.70A} = 12\% \tag{2.20}$$

$$W_{O3} = \frac{335(1.6V)}{12\%} = 44\ kW\ hr\ kg^{-1}\ O_3 \tag{2.21}$$

2.10 References

1. Wang, Y. H., S. Cheng, K. Y. Chan and X. Y. Li, "Electrolytic Generation of Ozone on Antimony and Nickel-Doped Tin Oxide Electrodes," *Journal of the Electrochemical Society* 152(11): D197-D200 (2005).
2. Vicent, F., E. Morallón, C. Quijada, J. L. Vázquez and A. Aldaz, "Characterization and Stability of Doped SnO_2 Anodes," *Journal of Applied Electrochemistry* 28: 607-612 (1998).
3. Lozano, B. C., Ch. Comninellis and A. De Battisti, "Service Life of Ti/SnO_2-Sb_2O_5 Anodes," *Journal of Applied Electrochemistry* 27(8): 970-974 (1997).
4. Lozano, B. C., Ch. Comninellis and A. De Battisti, "Physicochemical Properties of SnO_2-Sb_2O_5 films Prepared by the Spray Pyrolysis Technique," *Journal of the Electrochemical Society* 143(1): 203-209 (1996).
5. Cheng, S. A., and K. Y. Chan, "Electrolytic Generation of Ozone on an Antimony-Doped Tin Dioxide Coated Electrode," *Electrochemical and Solid-State Letters* 7(3): D4-D6 (2004).
6. Advanced Chemical and Material Analysis (ACMA), *Scanning Electron Microscope (SEM) and Energy Dispersive X-ray Analysis (EDX).* School of Chemistry and School of Chemical Engineering and Advanced Materials, Newcastle University, Newcastle upon Tyne (2010).
7. Centre for Surface Chemical Analysis, *X-ray Photoelectro Spectrometry (XPS).* School of Chemistry, Nottingham University, Nottingham (2010).
8. Farrell, T., "Surface Oxide on Au, Cu, Sn, Pb, and Some of Their Alloys: an ESCA Study," *Metal Science* 10(3): 87-93(7) (1976).
9. Laboratory of Biophysics and Surface Analysis (LBSA), *Time of Flight-Secondary Ion Mass Spectrometry (ToF-SIMS).* School of Pharmacy, Nottingham University, Nottingham (2010).
10. Mogk, D. W., and E. A. Mathez, "Carbonaceous films in midcrustal rocks from the KTB borehole, Germany, as characterized by Time-of-Flight, Geochemistry, Geophysics, Geosystems (G3)," *American Geophysics Union* (2000).
11. Briggs, D., and M. P. Seah, *Practical Surface Analysis, Ion and Neutral Spectroscopy*. 2nd Edition, Sussex: John Wiley and Sons Ltd., p. 19-25 (1982).

12. Onda, K., T. Ohba, H. Kusunoki, S. Takezawa, D. Sunakawa and T. Araki, "Improving Characteristics of Ozone Water Production With Multilayer Electrodes and Operating Conditions in a Polymer Electrolyte Water Electrolysis Cell," *Journal of the Electrochemical Society* 152(10): D177-D183 (2005).
13. Stucki, S., G. Theis, R. Kötz, H. Devantay and H. J. Christen, "In Situ Production of Ozone in Water Using a Membrel Electrolyzer," *Journal of the Electrochemical Society* 132(2): 367-371 (1985).
14. Harris, D. C., *Quantitative Chemical Analysis*. 4th Edition, New York: W. H. Freeman and Company, p. 132 (1948).
15. Nemes, A., I. Fábián and G. Gordon, "Experimental Aspects of Mechanistic Studies on Aqueous Ozone Decomposition in Alkaline Solution," *Ozone Science and Engineering* 22: 287-304 (2000).

Chapter 3

System development

and the recycle problem

3. System development and the recycle problem

At its heart, this chapter has the measurement of ozone in the cells and systems developed in Newcastle. It is placed before the chapter on the development of the anode synthesis (Chapter 4) as the latter relies upon a good understanding of the electrolysis cells and methods of ozone measurement employed.

3.1 The Molar decadic extinction coefficient

Initially, Chan et al. employed a value of 4800 $dm^3\ mol^{-1}\ cm^{-1}$ for the extinction coefficient of ozone at λ_{max} = 255 nm in the gas phase (see fig. 3.1 (i)) and 3000 $dm^3\ mol^{-1}\ cm^{-1}$ in the liquid phase, λ_{max} = 258 nm, see fig. 3.1 (ii) [1].

In contrast to the extinction coefficient employed by Chan, the majority of papers in the literature quote a value of 3000 ± 125 $mol^{-1}\ dm^3\ cm^{-1}$ for both the gas and aqueous phase extinction coefficients, see for example: [2][3][4][5], with a typical gas phase value of 3024 $dm^3\ mol^{-1}\ cm^{-1}$ at 254 nm and aqueous phase value of 2900 $dm^3\ mol^{-1}\ cm^{-1}$ at 258 nm [6]. Hence, in all the work presented in this thesis, a value of 3000 $dm^3\ mol^{-1}\ cm^{-1}$, as recommended by the International Ozone Association [4], will be employed.

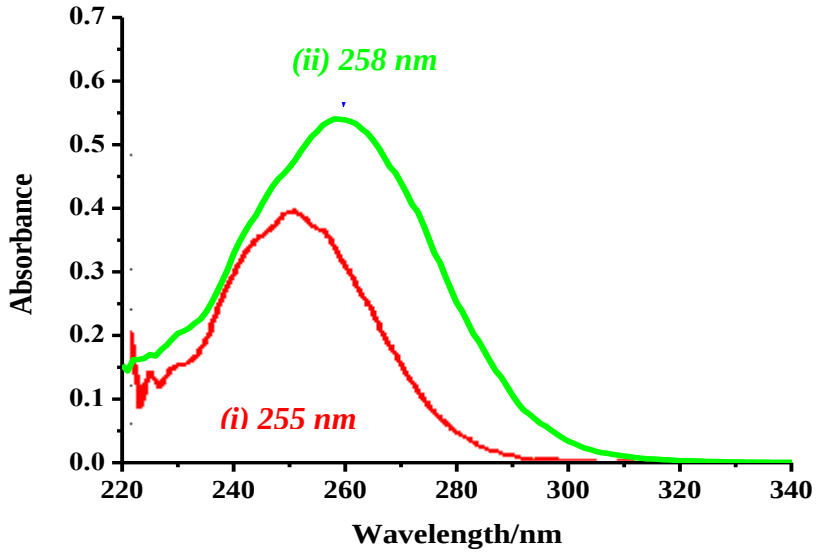

Figure 3.1 UV-Vis spectra of ozone; (i) O_3 in $O_3/O_2/N_2$ stream (ii) O_3 in 0.5 M H_2SO_4.

3.2 Recycle and single pass operation

3.2.1 The initial recycle system

Due to financial constants, the early (*i.e.* prior to my joining the Newcastle group) measurements of ozone generation were carried out using recycle system and measuring the volumes of H_2 and O_2 gas evolved by employing inverted measuring cylinders (typically 100 cm^3). The charge passed during each experiment was monitored as an independent parameter. The equipment is shown in figs. 3.2 (a) and (b). Later, a fibre optic, 1.0 cm path length UV cell (Astranet Systems Ltd) was included immediately after the electrochemical cell to monitor the dissolved ozone concentration.

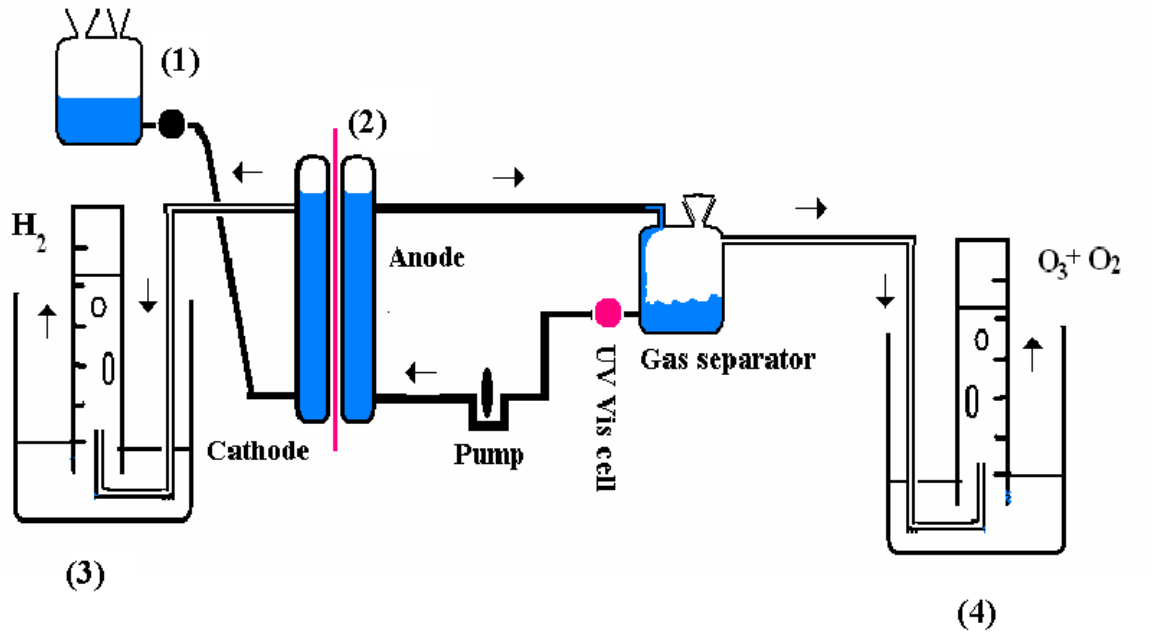

Figure 3.2 (a) Schematic of the electrochemical cell and system used to measure the evolved gases in the initial experiments on electrochemical ozone generation: (1) reservoir for catholyte; (2) electrochemical cell; (3) and (4) gas bubblers and inverted volumetric flasks to collect gases evolved at anode and cathode.

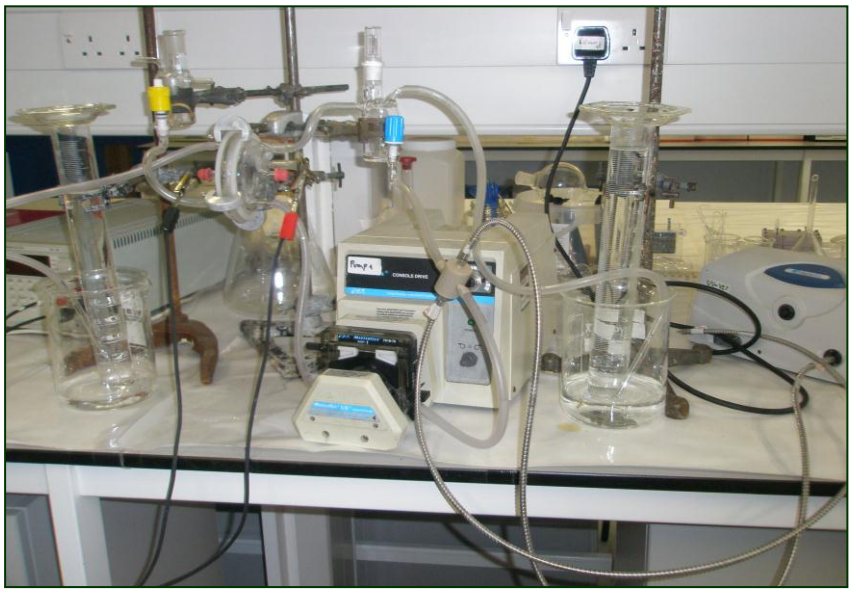

Figure 3.2 (b) Photograph of the system in fig. 3.2 (a).

Once the anolyte was saturated with ozone (monitored using UV-Vis cell) it was assumed that all the ozone produced was in the gas phase and hence its measurement gives the efficiency. Thus:

$$3H_2O \rightarrow O_3 + 6H^+ + 6e^- \qquad (3.1)$$

V_a = evolved anode gas volume, cm^3; V_c = cathode gas volume, cm^3.

$$n_a = \frac{P\,V_a}{RT} = n_{O2} + n_{O3} \qquad (3.2)$$

$$\frac{P\,V_a}{RT} = \Phi^e_{O3}\frac{Q}{6F} + \Phi^e_{O2}\frac{Q}{4F} \qquad (3.3)$$

Where Q is the charge passed.

$$\frac{Q}{2F} = n_{H2} = \frac{P\,V_c}{RT};\; Q = 2F\,\frac{P\,V_c}{RT} \tag{3.4}$$

$$\frac{P\,V_a}{RT} = \Phi^e_{O3}\left\{\frac{2F\left[\frac{P\,V_c}{RT}\right]}{6F}\right\} + \Phi^e_{O2}\left\{\frac{2F\left[\frac{P\,V_c}{RT}\right]}{4F}\right\} \tag{3.5}$$

$$V_a = \Phi^e_{O3}\frac{2\,V_c}{6} + \Phi^e_{O2}\frac{2\,V_c}{4} \tag{3.6}$$

$$V_a = \Phi^e_{O3}\frac{V_c}{3} + \Phi^e_{O2}\frac{V_c}{2} \tag{3.7}$$

$$\frac{V_a}{V_c} = \frac{\Phi^e_{O3}}{3} + \frac{\Phi^e_{O2}}{2} \tag{3.8}$$

$$\Phi^e_{O3} + \Phi^e_{O2} = 1 \tag{3.9}$$

$$\Phi^e_{O2} = \left(1 - \Phi^e_{O3}\right) \tag{3.10}$$

$$\frac{V_a}{V_c} = \frac{\Phi^e_{O3}}{3} + \frac{\left(1 - \Phi^e_{O3}\right)}{2} \tag{3.11}$$

$$\Phi^e_{O3} = 3 - \left[6\,\frac{V_a}{V_c}\right] \tag{3.12}$$

In this way, measurement of the volumes of gas evolved at cathode and anode allowed (in principle) the determination of the anode current efficiency for ozone.

The total number of moles of gas generated at the anode is *(n_{O2} + n_{O3})*, which is:

$$n_{O2} + n_{O3} = \frac{P\,V}{RT} = \frac{V_a}{V_m} \tag{3.13}$$

where V_m = molar volume. Hence, from above: from substitution from equation (3.3).

$$\frac{V_a}{V_m} = \Phi^e_{O3}\frac{Q}{6F} + \Phi^e_{O2}\frac{Q}{4F} \tag{3.14}$$

Remembering that $\Phi^e_{O2} = \left(1 - \Phi^e_{O3}\right)$ and re-arranging gives:

$$\Phi^e/\% = 100\left[\frac{12F}{Q}\right]\left[\frac{Q}{4F} - \frac{V_a}{V_m}\right] \tag{3.15}$$

which provides an additional measure/check of the ozone efficiency.

A typical experiment (carried out by Dr. Henriette Christensen of Clarizon Ltd) using a *ca.* 2.5 cm x 2.5 cm anode (HCED34, mole ratio 500:8:1 Sn:Sb:Ni in the coating solution) prepared with an electrodeposited interlayer (EDIL, see Chapter 4: the electrodeposition method was ED1 and the catalyst coating method CC1 in tables 4.2 and 4.3) is shown in fig. 3.3 (a); the data in the figure were collected after ozone saturation of the anolyte, taken as the dissolved ozone absorbance rising to a constant value.

Generally, the gas volume measurements required *ca.* 20 minutes to settle down, after which the efficiencies calculated from the anolyte gas volume and charge passed on the one hand, and (anode + cathode) gas volumes on the other agreed to within *ca.* 5%, providing that the ratio of the actual to calculated hydrogen gas volumes ($H_{2(obs)}/H_{2(calc)}$, the latter calculated from the charge passed) was 1.00 ± 0.05, which was taken as a first check on the validity of the data.

Given the stability of the $H_{2(obs)}/H_{2(calc)}$ ratio throughout the experiment depicted in fig. 3.3 (a), the large apparent decline in the current efficiency for ozone generation must reflect a "hold-up" in gas evolution at the anode or, more likely, in gas escaping out of the collecting cylinder at the anode. Thus, if worst case scenario is assumed, *i.e.* that all the ozone escapes, then:

$$\Phi^{e}_{True} = 3 - \left[6 \frac{V_a}{V_c} \right] \tag{3.16}$$

Φ_{True}^{e} is the actual current efficiency.

$$V_{a,app} = V_{O2} \tag{3.17}$$

$$V_{O2} = \left(1 - \Phi^{e}_{True}\right) \left(\frac{V_m I}{4F} \right) \tag{3.18}$$

V_m = molar volume, $V_{a,app}$ = apparent anode gas volume and V_{O2} = volume of O_2.

$$V_c = \frac{V_m I}{2F} \tag{3.19}$$

$$\Phi^{e}_{App} = 3 - \left[6 \frac{V_{a,app}}{V_c} \right] = 3 - 6 \left\{ \left[\left(1 - \Phi^{e}_{True}\right) \frac{V_m I}{4F} \right] \left[\frac{V_m I}{2F} \right] \right\} = 3\, \Phi^{e}_{True} \tag{3.20}$$

Φ_{App}^{e} is the apparent current efficiency.

Thus, if any ozone escapes from the collecting cylinder, or dissolves before being collected, the apparent efficiency will be greater than the true efficiency, in the extreme by a factor of 3; hence the determination of current efficiency by this method was very likely to be unreliable.

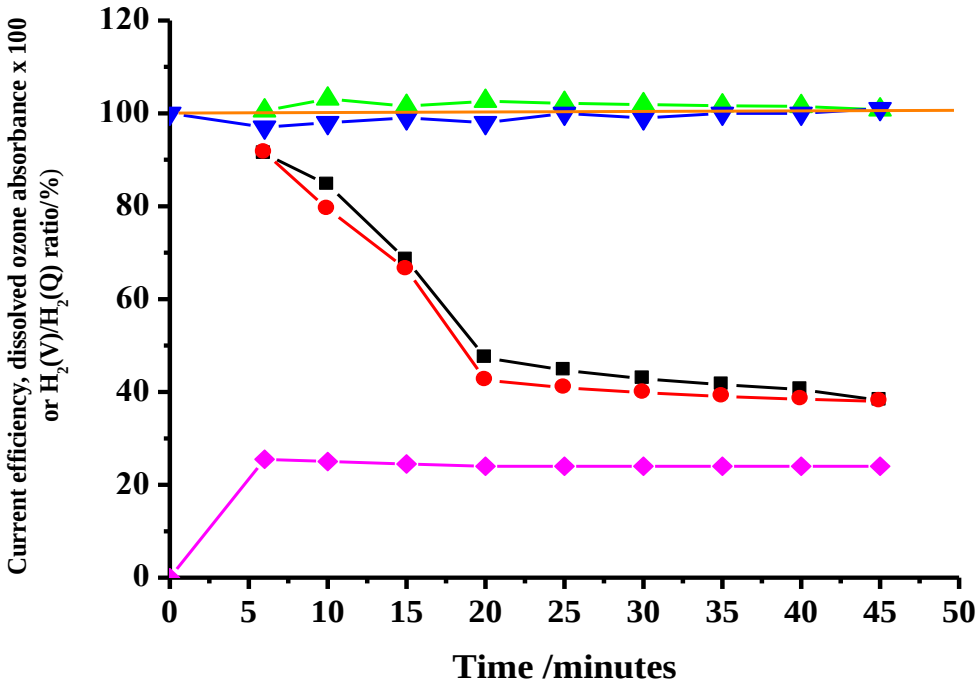

Figure 3.3 (a) Plots of efficiency calculated from anode and cathode gas volume (■); efficiency calculated from anode gas volume and charge (●); ratio of actual H_2 volume to that calculated from the charge (▲); dissolved ozone absorbance x 100 (▼) and current (A) x 100 (◆). The experiment was carried out in the glass cell using a 2.5 cm x 2.5 x cm ozone anode HCED34 and 5.0 cm x 5.0 cm Pt/Ti cathode immersed in 0.5 M H_2SO_4 and separated by a Nafion 117 membrane and at cell voltage 2.7 V.

During the experiment in fig. 3.3 (a), the current remained essentially constant at *ca.* 0.25 A, and the dissolved ozone absorbance at *ca.* 1.0, the latter corresponding to a steady state solution concentration of 3.3 x 10^{-4} M or 16 ppm. Figure 3.3 (b) summarises the behavior of the anode over 14 experiments, each *ca.* 40-45 minutes in duration, in terms of the dissolved ozone absorbance and current at the end of the experiment. Over the time period 3.5 days covered by the figure, the anode seems to retain its activity in that the absorbance in solution oscillates around *ca.* 0.9, perhaps even increasing at the end of the period. The current appear to decrease from *ca.* 0.24 to 0.20 A and then remained almost constant. Bearing in mind that experiment 1 was carried out after 4

days electrolysis in 0.5 M H_2SO_4, the data in fig. 3.3 (b) suggests that the anode was reasonably stable.

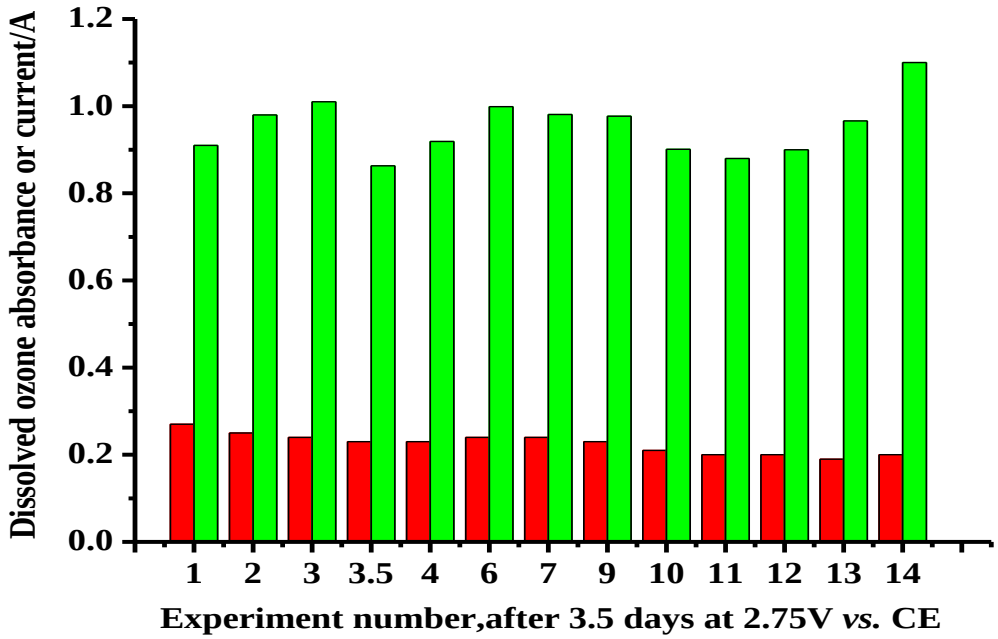

(b)

Figure 3.3 (b) Plot of the current (■) and the dissolved ozone absorbance (■) at the end of each experiment for 14 successive experiments using a 2.5 cm x 2.5 cm ozone anode. Experimental conditions are in fig. 3.3 (a).

It is possible to estimate the current efficiency from the solution concentration of ozone once saturation has occurred. Thus:

Assuming that, in a recycle experiment, once the anolyte is saturated, all the ozone produced escapes into the gas phase.

Henry's Law constant for ozone (H_{O3}) in 0.5 M H_2SO_4 at 21 ºC is 0.22 [8], where:

$$[O_3]_{soln} = 0.22[O_3]_{gas} \qquad (3.21)$$

Hence:

$$[O_3]_g = \frac{[O_3]_s}{0.22} = \frac{A}{0.22\varepsilon\ell} \tag{3.22}$$

ℓ = 1.0 cm, ε = 3000 $dm^3\ mol^{-1}\ cm^{-1}$

$$[O_3]_g = \frac{A}{660M} = 1.5A \text{ mol } m^{-3} = \frac{P_{O3}}{RT} \tag{3.23}$$

$$P_{O3} = 1.5RTA \tag{3.24}$$

$$P_{O2} = 1.01x10^5 - 1.5RTA \tag{3.25}$$

$$\frac{P_{O3}}{P_{O2}} = \frac{1.5RTA}{(1.01x\,10^5 - 1.5RTA)} = \frac{\frac{\Phi^e I}{6F}}{\left[(1-\Phi^e)\frac{I}{4F}\right]} = \frac{2\,\Phi^e}{3\,(1-\Phi^e)} \tag{3.26}$$

Where Φ^e is fractional current efficiency.

Let $P' = \frac{1.5RTA}{(1.01x10^5 - 1.5RTA)}$

$$P' = \frac{2\,\Phi^e}{3\,(1-\Phi^e)} \tag{3.27}$$

$$\Phi^e = \frac{3\,P'}{2+3\,P'} \tag{3.28}$$

This gives Φ^e = 5.4% at 21 ºC.

Assuming that the maximum concentration of O_2 in acid is roughly the same as in water [9] = 1 mM, then n/V = 1.01 x 10^5/RT = 41.3 mol m^{-3} = 0.041 mol dm^{-3} and $[O_2]_{sol}$ = 1 x 10^{-3} = $H_{O2}[O_2]_g$ = H_{O2} x 0.04; H_{O2} = 0.024 *i.e.* 10x less than H_{O3}, in agreement with the literature[10]. The efficiency calculated from Henry's Law was consistently and significantly lower than the *ca.* 40% calculated from the anode/cathode gas volumes and anode volume/charge passed, see fig. 3.3 (a), supporting concerns over the validity of the gas volume approach.

3.2.2 The use of gas phase absorbance measurements

In order to develop an accurate, reliable and consistent analytical method for gas phase measurement, in recycle system, N_2 gas was fed into the gas separator at a constant flow rate to dilute the ozone with a Cole-Palmer WU series N_2 flow meter system. This dilution is necessary as the ozone absorbances expected at high efficiencies are >> 3: thus, in a recycle experiment, once steady state is attained, the flow rate of anode gas (O_3 + O_2) is dV/dt (in cm^3 s^{-1}), this exits the cell, passes through the UV cell, through a glass bubbler and is trapped in a volumetric cylinder. In the absence of any diluent N_2 gas:

Assume a current I and a fractional current efficiency for O_3 (6e) of Φ_{O3}^e. The amount of ozone produced per second, $\frac{dn_{O3}}{dt}$, is:

$$\frac{dn_{O3}}{dt} = \frac{\Phi_{O3}^e I}{6F} \tag{3.29}$$

Similarly, the amount of oxygen per second:

$$\frac{dn_{O2}}{dt} = \frac{\Phi_{O2}^e I}{4F} \tag{3.30}$$

The total number of moles of gas (O_3+O_2) generated per second is:

$$\frac{dn_{gas}}{dt} = \frac{\Phi_{O3} I}{6F} + \frac{\Phi_{O2} I}{4F} \tag{3.31}$$

Given that 1 mole of an ideal gas occupies 24.5 dm^3 at 298 K and 1 atm process, the total volume of gas produced at the anode in $dm^3\ s^{-1}$ is:

$$\frac{dV_{gas}}{dt} = \left\{ \left(1 - \Phi^{e}_{O3}\right) \frac{I}{4F} + \frac{\Phi^{e}_{O3} I}{6F} \right\} 24.5 \tag{3.31}$$

$$\frac{dV_{gas}}{dt} = \left\{ \frac{\left(IF - 6IF\ \Phi^{e}_{O3}\right) + 4IF\ \Phi^{e}_{O3}}{24F} \right\} 24.5 \tag{3.32}$$

$$\frac{dV_{gas}}{dt} = \left\{ \frac{\left(3 - \Phi^{e}_{O3}\right) I}{12F} \right\} 24.5 \tag{3.33}$$

At steady state, let the absorbance at 259 nm be *A*. The concentration of ozone corresponding to this absorbance will be the same when trapped in the cylinder as in the flow from the cell.

Let the ozone be trapped for t seconds. This gives a volume, $V = \left(\frac{dV}{dt}\right) t$.

$$A = \varepsilon C \ell \tag{3.34}$$

$$A = \frac{\varepsilon\ \ell\ \Phi^{e}_{O3}}{V} \tag{3.35}$$

From (3.30):

$$\frac{dn_{O3}}{dt} = \frac{\Phi^{e}_{O3} I}{6F} \tag{3.36}$$

$$n_{O3} = \frac{\Phi^{e}_{O3} It}{6F} \tag{3.37}$$

$$A = \frac{\varepsilon \ell \ \Phi^{e}_{O3} It}{6FV} \tag{3.38}$$

ε = 3000 $dm^3\ mol^{-1}\ cm^{-1}$, ℓ = 1.0 cm:

$$A = \frac{3000 \ell \ \Phi^{e}_{O3} It}{6FV} \tag{3.39}$$

$$A = \frac{500 \ \Phi^{e}_{O3} It}{FV} \tag{3.40}$$

Replacing $V_{gas} = \frac{dV_{gas}}{dt} t$ by (3.33);

$$A = \left\{ \left(\frac{500 \ \Phi^{e}_{O3} It}{F} \right) \left(\frac{1}{\left(3 - \Phi^{e}_{O3}\right) I} \right) \right\} 24.5 \tag{3.41}$$

$$A = \frac{245 \ \Phi^{e}_{O3}}{\left(3 - \Phi^{e}_{O3}\right)} \tag{3.42}$$

From equation (3.42) it can be calculated the gas phase ozone absorbance expected for each current efficiency, and the results are shown below; note there is no dependence on current. At $\Phi^{e} \leq 10\%$, the plot is linear, see fig. 3.4. At any reasonable current efficiency, the gas phase absorbance expected is >> 3, proving that dilution of the anode gas stream is essential.

Figure 3.5 (a) shows plots of gas phase absorbance, dissolved ozone absorbance and current obtained during the 6th experiment using anode AJED2F (see fig. 3.5 (b)) which was carried out in recycle system and using a UV-Vis cell to monitor the gas phase absorbance of ozone, see fig. 3.5 (b). The N_2 flow rate was 10 $cm^3\ min^{-1}$, current 0.24 A and the gas phase absorbance 0.59, giving a current efficiency of 7.8%. The steady-state dissolved ozone absorbance was 0.85; using the Henry's Law method discussed above

(equations (3.21) to (3.28), this equates approximately to an efficiency of 3.3%, assuming P = 1 atm and T = 294 K. As an order-of-magnitude comparison the efficiencies determined *via* the two different approaches agree quite well; at least they strongly suggest that the ozone current efficiency in recycle system was <10%. This proved to be a very significant observation and is dealt with in detail in the next section.

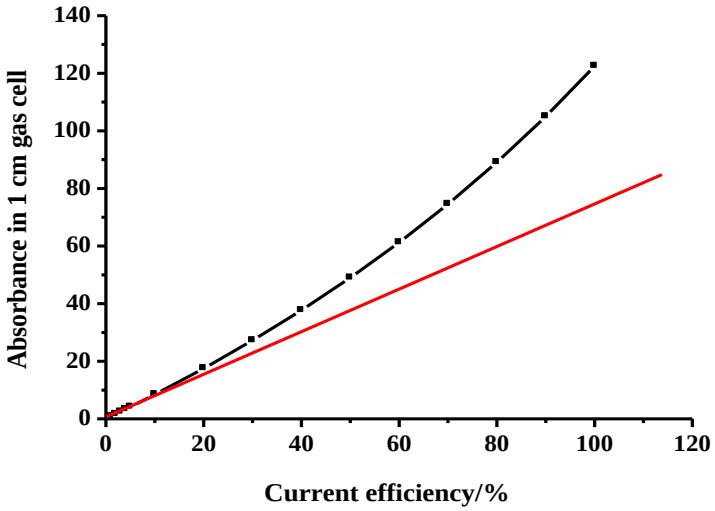

Figure 3.4 Plot of calculated gas phase ozone absorbance vs. current efficiency.

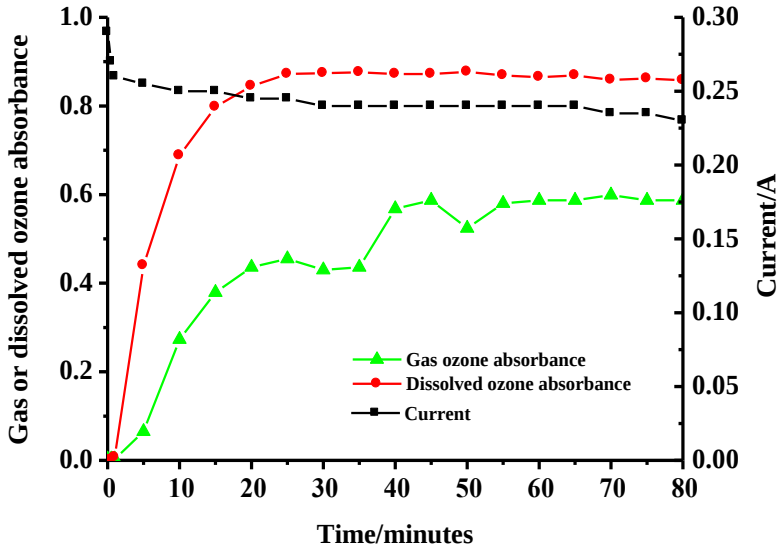

Figure 3.5 (a) Plots of current (■), gas phase (▲) and dissolved (●) ozone absorbance during a recycle experiment using a 2.5 cm x 2.5 cm anode AJED2F at a cell voltage of 2.7 V and an anolyte flow rate of 30 cm^3 min^{-1}, N_2 gas flow rate was 10 cm^3 min^{-1}.

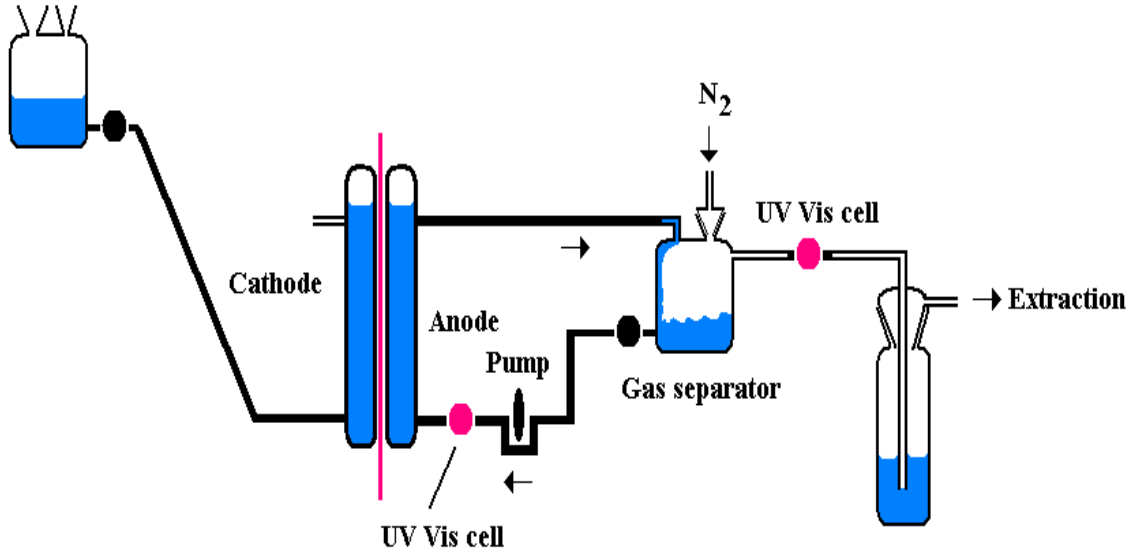

Figure 3.5 (b) Diagram of recycle system from experiment in fig. 3.5 (a).

3.2.3 The anomalously low efficiencies determined in recycle experiments compared to single pass experiments

From equation (3.21), in a recycle experiment, it would be expected;

$$A_s/(A_g \times f) = 0.22 \qquad (3.43)$$

Where A_s = steady state dissolved ozone absorbance, A_g = steady state gas phase ozone absorbance and f = N_2 flow rate in $cm^3\ min^{-1}$, since the path length is constant at 1.0 cm in gas and liquid experiments and there are being assumed $\varepsilon_g = \varepsilon_s = 3000\ dm^3\ mol^{-1}cm^{-1}$.

Figure 3.6 shows data from the first experiment using anode AJED2H; as may be seen from the figure, the ratio of the dissolved to gas phase ozone absorbances was 0.26, in reasonable agreement with the predicted value of 0.22. The subsequent two experiments both gave ratios of 0.21. However, these data appear to be anomalous, as nearly all the other recycle experiments using the anodes AJED2 series gave absorbance ratios of between 0.18 and 0.11, *i.e.* 1.3 a factor of 2.2 x lower than predicted, see table 3.1.

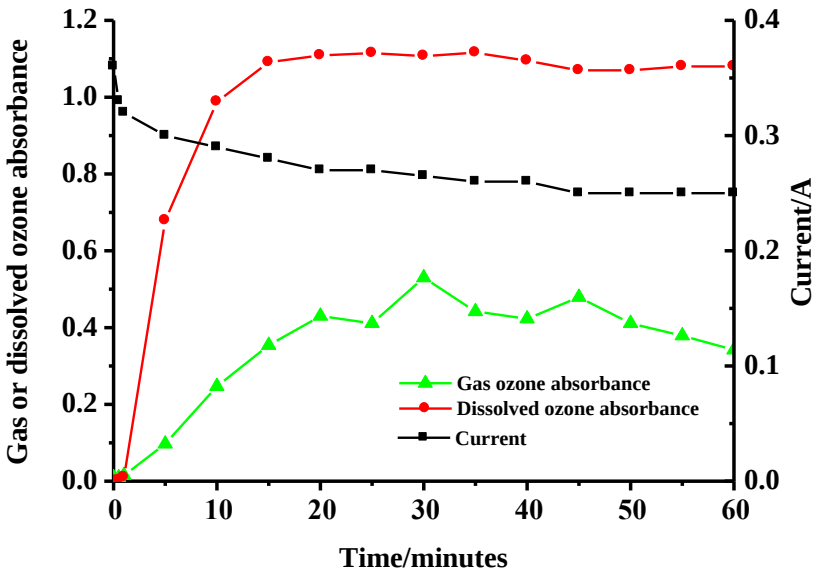

Figure 3.6 Plot of current (■), gas phase (▲) and dissolved (●) ozone absorbance during a recycle experiment using anode AJED2H (6.25 cm^2) in 0.5 M H_2SO_4 at a cell voltage of 2.7 V and an anolyte flow rate of 30 cm^3 min^{-1}, N_2 flow rate was 10 cm^3 min^{-1}.

Anodes	Experiment	$A_s/A_g f$ (cm^{-3} min)
AJED2A	1	0.13
	2	0.15
AJED2B	1	0.12
	2	0.15
AJED2C	1	0.11
	2	0.11
AJED2D	1	0.12
	2	0.14
AJED2E	1	0.17
	2	0.14
AJED2F	5	0.14
	6	0.14
AJED2G	1	0.15
	2	0.14
AJED2H	1	0.26
	2	0.21
	3	0.22

Table 3.1 Ratio of dissolved ozone absorbance to actual gas phase absorbance (i.e. gas absorbance x N_2 flow rate) determined during the recycle experiments employing the anodes AJED2 series.

Figures 3.7 (a) to (c) show the absorbance of ozone in solution and the current during three sequential single pass experiments using the system shown in fig. 3.8. The data in fig. 3.5 (a) and figs. 3.7 (a)-(c) are tabulated in table 3.2. (The first experiment of anode AJED2F was discontinued due to a problem with the system and hence is not included in the table).

As may be seen from the table, the data in figs. 3.7 (a)-(c) correspond to average current efficiencies of between 25-38%. In fact, it was found generally that the current efficiency measured in recycle system was <10% in approximate agreement with calculations based on Henry's Law, yet employing the same anodes in single pass system resulted in current efficiencies > 20% and even as high as *ca.* 50% [11].

Name of anode (System)	**Exp. No.**	**Current /A**	**Anolyte flow rate /cm^3 min^{-1}**	**N_2 flow rate /cm^{3}min^{-1}**	**Gas Abs**	**Dissolved ozone Abs**	**Φ^e_{O3} Gas /%**	**Φ^e_{O3} Dissolved /%**
AJED2F (Single pass)	2	0.27	30	-	-	0.80	-	28.4
		0.27	100	-	-	0.30	-	35.6
		0.27	30	-	-	0.82	-	29.2
	3	0.25	30	-	-	0.69	-	26.5
		0.25	100	-	-	0.30	-	38.4
		0.25	30	-	-	0.69	-	26.5
	4	0.24	30	-	-	0.62	-	24.8
		0.24	100	-	-	0.25	-	33.3
		0.24	30	-	-	0.62	-	24.8
AJED2F (Recycle)	5	0.23	30	10	0.56	0.80	7.8	-
	6	0.24	30	10	0.59	0.85	7.8	

Table 3.2 Summary of the data obtained during 2nd-6th experiments using anode AJED2F.

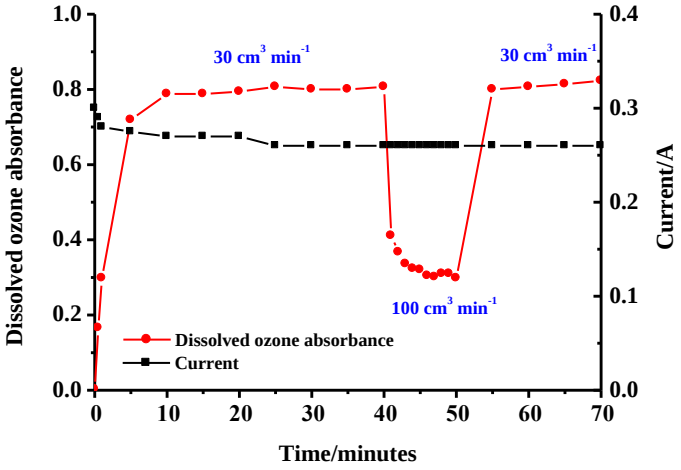

(a) Experiment 2

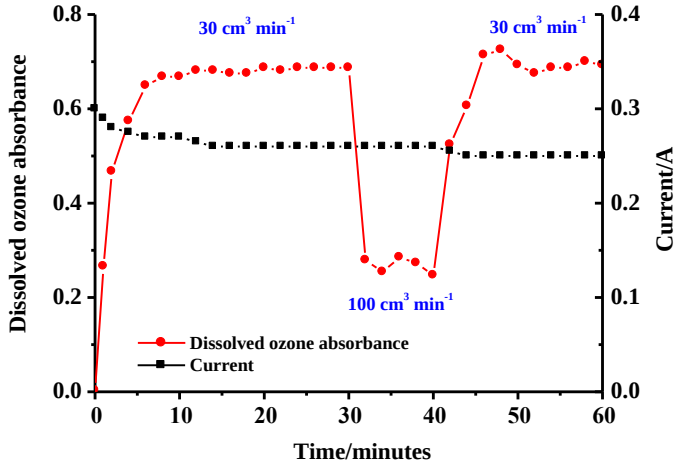

(b) Experiment 3

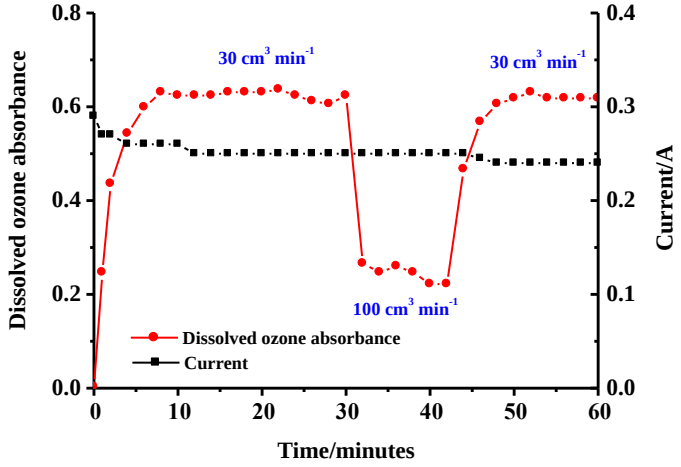

(c) Experiment 4

Figure 3.7 Plots of current (■) and dissolved ozone absorbance (●) during three sequential single pass experiments using anode AJED2F in 0.5 M H_2SO_4 (a) experiment 2, (b) experiment 3, (c) experiment 4 at flow rate of 30, 100 and 30 cm^3 min^{-1}, respectively.

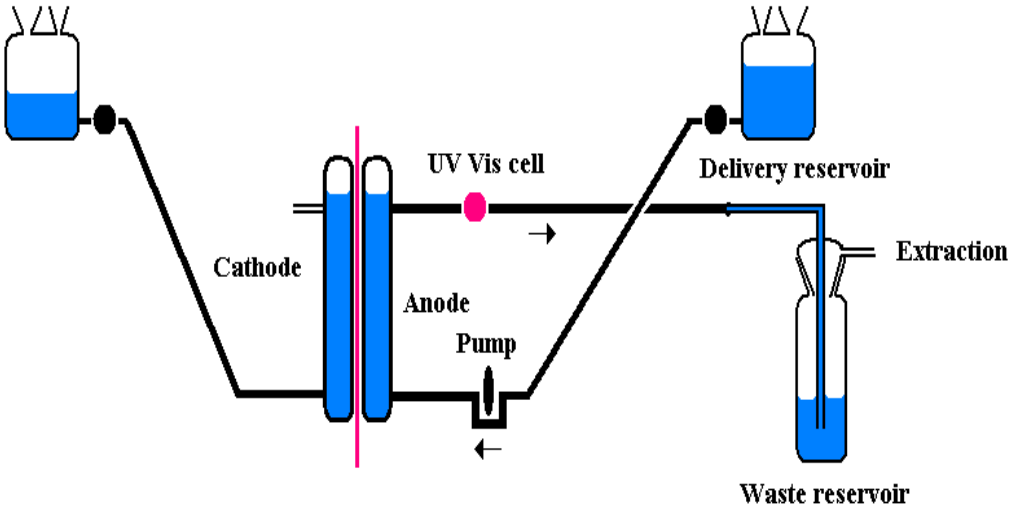

Figure 3.8 Diagram of single pass system.

As an additional confirmation on the gas phase analytical method, the output of an Onnic ES2115A Cold Corona Discharge generator [12] (see fig. 3.9) was monitored using the Astranet fibre optic spectrometer. The flow rate of air through the generator was 1.9 dm^3 min^{-1} and gave a gas phase ozone absorbance of 0.067 corresponding to a measured ozone production rate of 0.12 g hr^{-1}, in agreement with the company rating of 0.1 g hr^{-1} [12].

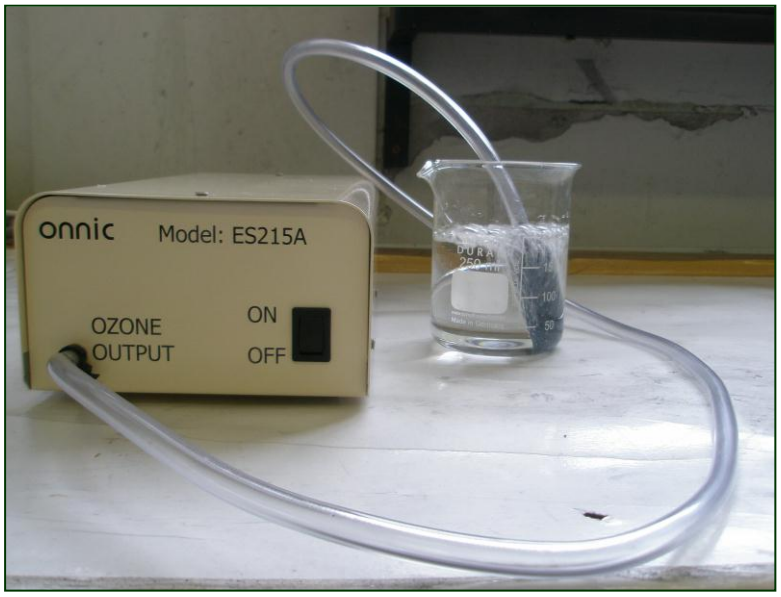

Figure 3.9 Photograph of the Onnic ES215A Cold Corona Discharge generator.

Final confirmation of the validity of the UV-Vis spectroscopic analysis came through the simultaneous determination of the efficiency of ozone generation using the 6.25 cm^2 anode AJED27B (see Chapter 4, tables 4.1-4.3 for details) by UV-Vis spectroscopy and iodometric titration. The latter is the standard method recommended by the International Ozone Association; see [10] for details. These experiments were carried out in collaboration with Dr. Taner Yonar of Uludag University, Turkey and a schematic diagram and photo of the experimental system employed are shown in figs. 3.10 (a) and (b).

The cell was connected for recycling of the anolyte and operated at a flow rate of 30 cm^3 min^{-1} and at a constant current of 0.2 A (cell voltage 2.7-2.8 V) to facilitate the calculations. The gas evolved from the anode was diluted with N_2 gas at a flow rate of 80 or 90 cm^3 min^{-1}. Electrolysis was allowed to take place for 14 minutes before the anode gas was directed through the Dreschel bottles containing the aqueous KI solution, to allow saturation of the anolyte by ozone to take place and a steady state to be established.

Briefly, the iodometric method relies on the oxidation of I^- by O_3 at pH 2.0 [10] according to:

$$O_3 + 2H^+ + 2I^- \rightarrow O_2 + 2H_2O + I_2 \qquad (3.44)$$

Followed by the determination of the amount of iodine so formed by titration with sodium thiosulfate with starch indicator [10]:

$$I_2 + 2S_2O_3^{2-} \rightarrow 2I^- + 2S_4O_6^{2-} \qquad (3.45)$$

Thus 250 cm^3 of 2% wt aqueous KI were placed in two Dreschel bottles placed in series after the UV cell (see fig. 3.10 (b)).

Once ozone monitoring had ceased, the brown solutions were placed separately into an Erlen Meyer flask, 20-30 cm^3 of 2.0 N H_2SO_4 with 2-3 drops of starch solution and titrated with 0.1 N Na_2SO_3.

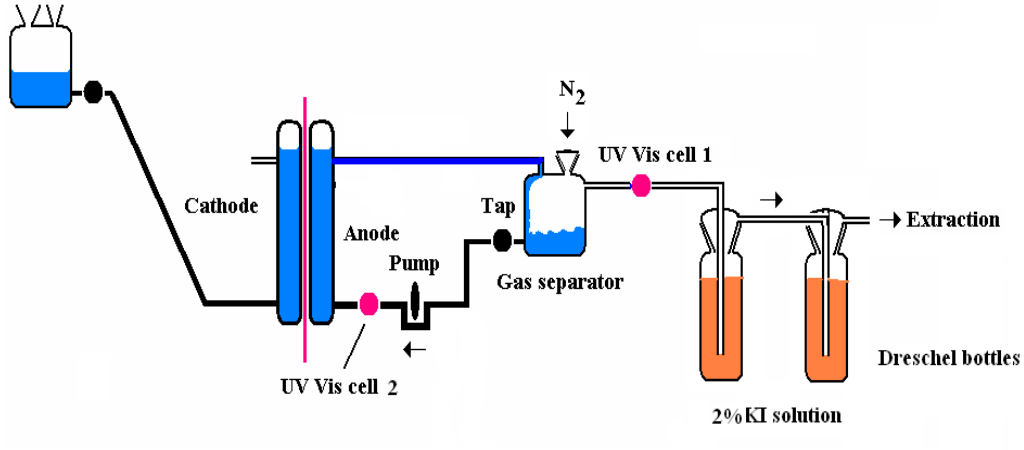

(a)

(b)

Figure 3.10 (a) Schematic representation of the experimental system employed to determine the ozone efficiency of anode AJED27B simultaneously by UV-Vis spectroscopy and iodometry and (b) Photograph of the system.

Two experiments were carried out and data from the first experiment are presented as typical in fig. 3.11. As may be seen from fig. 3.11 the average current efficiency over the period monitored by UV-Vis was 9%, corresponding to an ozone production rate of 90 μg min^{-1} compared to 112 μg min^{-1} determined by iodometry. The analogous data obtained during the second experiment were 119 μg min^{-1} and 128 μg min^{-1}, respectively agreement to within 10% and hence entirely satisfactory.

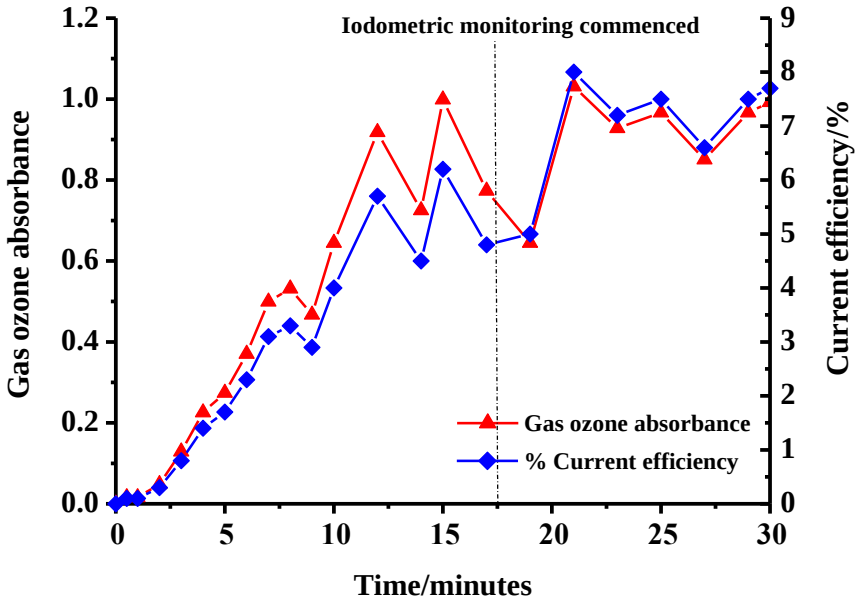

Figure 3.11 Plots of the gas phase ozone absorbance (▲) and current efficiency (♦) determined during the electrolysis of in 0.5 M H_2SO_4 the glass cell using the 6.25 cm^2 anode AJED27B and a Pt/Ti mesh cathode in the glass cell at a constant current of 0.2 A and anolyte flow rate of 30 cm^3 min^{-1}. The anode gas flow was diluted with N_2 at a flow rate of 80 cm^3 min^{-1}.

Further confirmation that calculation of ozone efficiency from measurement of gas phase ozone was a valid approach was provided by studies using a commercial, electrochemical ozone cell imported from China, see fig. 3.12. The cell was based around a membrane electrode assembly (MEA) comprising a paste of PbO_2 powder/Nafion/Pt particles on porous carbon cathode. The electrodes were *ca.* 2.0 cm x 2.0 cm in geometric area, water being pumped pass each electrode; the cathode generated hydrogen (an interesting characteristic given that the unit was aimed at the

domestic market). The experimental equipment employed to test the cell is shown schematically in fig. 3.12 (b).

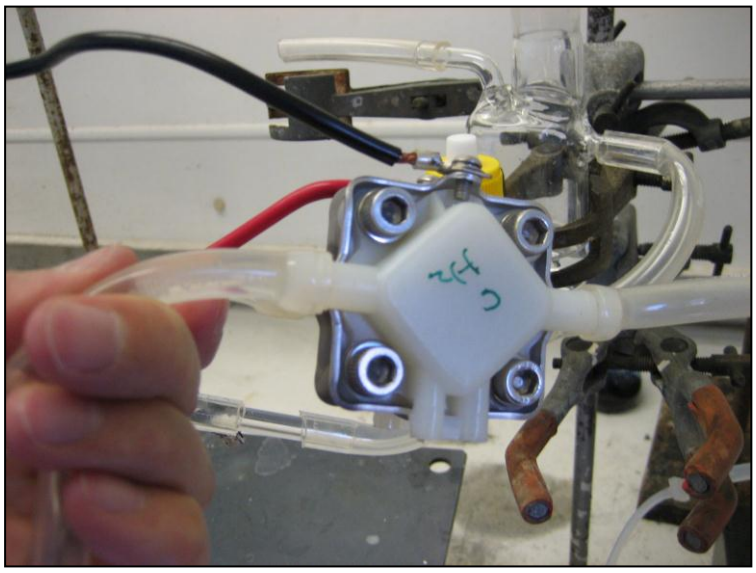

(a)

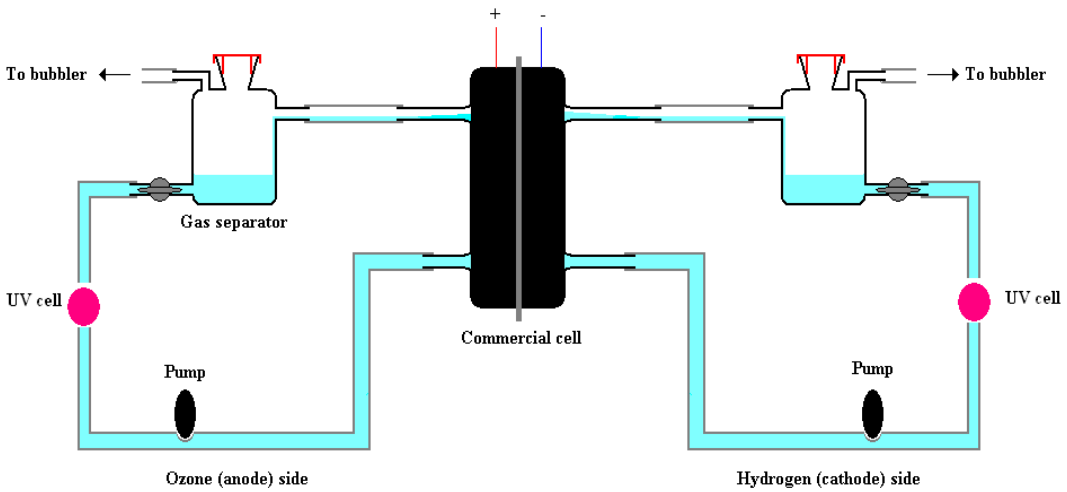

(b)

Figure 3.12 (a) Photograph of the electrochemical ozone cell imported from China and (b) Schematic of experimental equipment using the "Chinese" cell: the UV-Vis flow cell (1.0 cm path length) was inserted either between the gas separator and the pump on the anode side for solution measurements, or immediately after the gas outlet from the gas separator, for gas phase measurements.

Figure 3.13 shows the gas phase ozone absorbance obtained (i) without employing N_2 gas as diluent and (ii) with 12.5 cm^3 min^{-1} N_2. As can be seen from the figure, in the latter experiment, the N_2 was shut off after 2100 seconds. Without N_2 diluent, the ozone absorbance corresponded to a current efficiency of *ca.* 0.5% with the added N_2, the current efficiency was comparable at 0.3%.

When the diluent N_2 was shut off, the ozone absorbance returned to *ca.* its value in (i). The behavior of the absorbance on diluting with N_2 and without added N_2 strongly suggests the absence of saturation or other such spectroscopic effects, whilst the current efficiency of ≤1% was within the specification of the cell. It is worth nothing that, despite the very high currents, the PbO_2 anode gave very poor current efficiency. Thus it appears from the above that operation in recycle system actually does reduce the ozone efficiency.

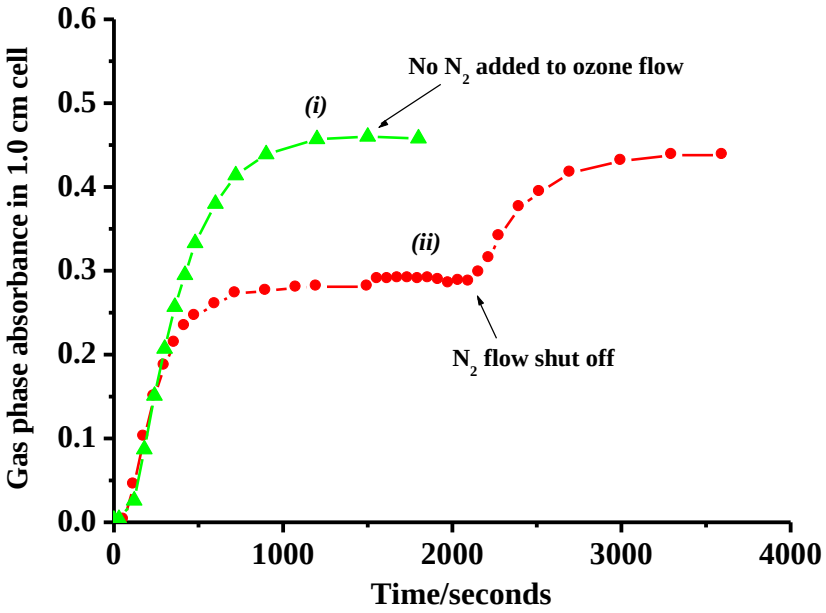

Figure 3.13 The gas phase ozone absorbance measured using the Chinese cell (fig. 3.12 (a)) and the experimental system in fig. 3.12 (b). The anolyte gas flow rate was: (i) 7.0-7.5 cm^3 min^{-1} N_2 (▲) and (ii) 5.5-6 cm^3 min^{-1} + 12.5 cm^3 min^{-1} N_2 (●). Cell voltage 3.0 V, current ca. 2.0 A and at room temperature.

Before proceeding, it should be noted that the increase in current efficiency generally determined as anolyte flow rate is increased, and exemplified by the data in table 3.2 and figs. 3.5 and 3.7 is consistent with the literature [11][13][14][15][16] where more ozone is entrained in the anolyte at higher flow rates giving higher current efficiencies when calculated only for the production of dissolved ozone. Flow rates >30 dm^3 hr^{-1} have been reported as being optimum for maximum ozone efficiency. Cui et al. [16] attributed this to higher flow rates improving mass transfer and dislodging bubbles. However, it is more generally accepted that increased flow rates improve ozone dissolution and hence more ozone is entrained in solution [13][15] relative to that in the gas phase, with the overall efficiency remaining unchanged [13][15][17].

The data in table 3.2 suggest that predicting current efficiency from the dissolved ozone absorbance in recycle experiments is not feasible and, perhaps, it is not correct to assign the same value, or very similar values, to both the gas phase and liquid phase absorption coefficients. Previous work (see discussion of CCD generator above) and the literature [18] strongly suggest that the gas phase extinction coefficient is 3000 dm^3 mol^{-1} cm^{-1}, but the solution value is less certain. Taking an average of the ratios in table 3.1 suggests ε_s = 1977 dm^3 mol^{-1} cm^{-1} which does not seem reasonable, as none of the values quoted in the literature vary by from 3000 ± 10% dm^3 mol^{-1} cm^{-1}. Interestingly, however, if the former value is employed for the dissolved ozone absorbance in fig. 3.5 (a), the current efficiency estimated *via* Henry's Law is 7.8%, matching that calculated from the gas phase absorbance.

The above discussion of recycle operation suggests that introducing ozone at the inlet of the electrochemical cell somehow reduces the current efficiency of ozone generation. In order to test this postulate, the experiment depicted in figs. 3.14 (a)-(c) was carried out. Thus, fig. 3.14 (a) shows plots of dissolved ozone absorbance at the outlet and inlet of the electrochemical cell using the single pass system shown in fig. 3.14 (c). At 40 minutes, ozone-containing 0.5 M H_2SO_4 replaced the ozone-free acid in the supply reservoir, causing ozone to appear at the inlet and a step in ozone absorbance at the outlet, see fig. 3.14 (a). Figure 3.14 (b) shows a plot of current efficiency from the data

in fig. 3.14 (a), calculated from the difference in the ozone absorbances. As may be seen from fig. 3.14 (b), the current efficiency decreased from 22.5% to 20% when the ozone absorbance at the inlet increased from 0 to 0.17.

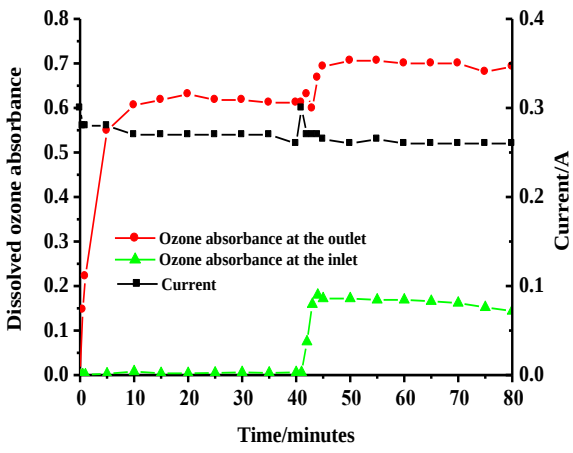

(a)

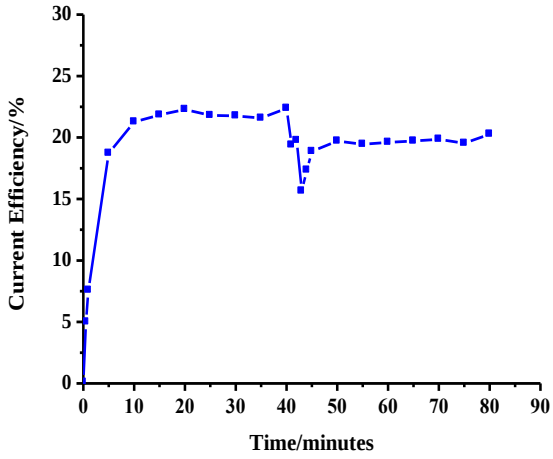

(b)

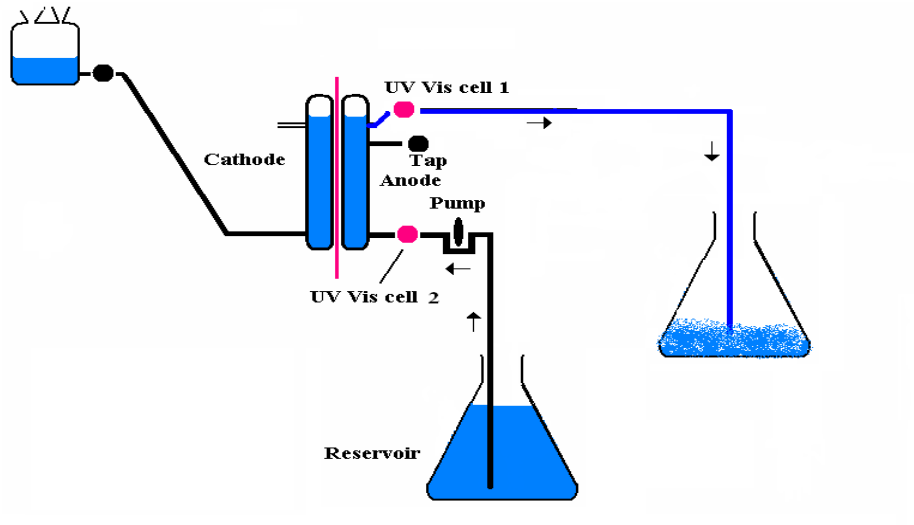

(c)

Figure 3.14 Plots of (a) current (■), dissolved ozone absorbance at the outlet to the electrochemical cell (●) (UV-Vis cell 1 in (c)) and dissolved ozone absorbance at the inlet of the electrochemical cell (▲) (UV-Vis cell 2 in (c)). (b) Plot of current efficiency (■) vs. time calculated from the data in (a), using the difference between the dissolved ozone absorbances at the outlet and inlet of the electrochemical cell. (c) Schematic of the experimental system used in (a) on anode AJED2F.

The data in figs. 3.14 (a) and (b) prompted a more detailed investigation of the effect of ozone concentration at the inlet of the electrochemical cell on the ozone current efficiency using anode AJED2F. A series of experiments were carried out using the experimental equipments shown in figs. 3.15 (a) and (b).

The equipment shown schematically in fig. 3.15 (a) was essentially a recycle system with two gas separators; the separator immediately before the electrochemical cell was a conical flask either with or without anti-bumping granules and either stirred or unstirred. The presence of anti-bumping granules and stirring enhanced the release/decay of dissolved ozone and allowed some control over the ozone concentration in the anolyte (0.5 M H_2SO_4) entering the electrochemical cell.

A series of experiments, experiments 15-21 and 23-30, were carried out over a period covering 3 months. Typical data obtained an anolyte flow rate of 30 cm^3 min^{-1} and cell voltage of 2.7 V are shown in figs 3.16 (a) and (b). Figure 3.16 (a) shows the ozone absorbance at the inlet and after the outlet, and the current, whilst fig. 3.16 (b) shows the corresponding plot of current efficiency. Figure 3.17 (a) shows current efficiency *vs.* experiment number for the various experiments using anode AJED2F; in essence, the x-axis represents the usage of the anode (the experiments varied between 40 and 120 minutes). As may be seen from the figure, there appears to be no clear correlation between the use of the anode and current efficiency. However, a plot of current efficiency *vs*. the solution ozone absorbance at the inlet of the electrochemical cell (see fig. 3.17 (b)) does show a clear (negative) correlation, with the efficiency declining from *ca.* 27-30% in "pure" (*i.e.* no O_3) single pass system to *ca.* 8% in "pure" recycle system, the latter in agreement with the gas phase UV-Vis measurements made in recycle system.

From all the above, it appears to be fairly clear that ozone at the inlet of the electrochemical cell has a negative effect upon ozone evolution at the Ni/Sb-SnO_2 electrocatalyst.

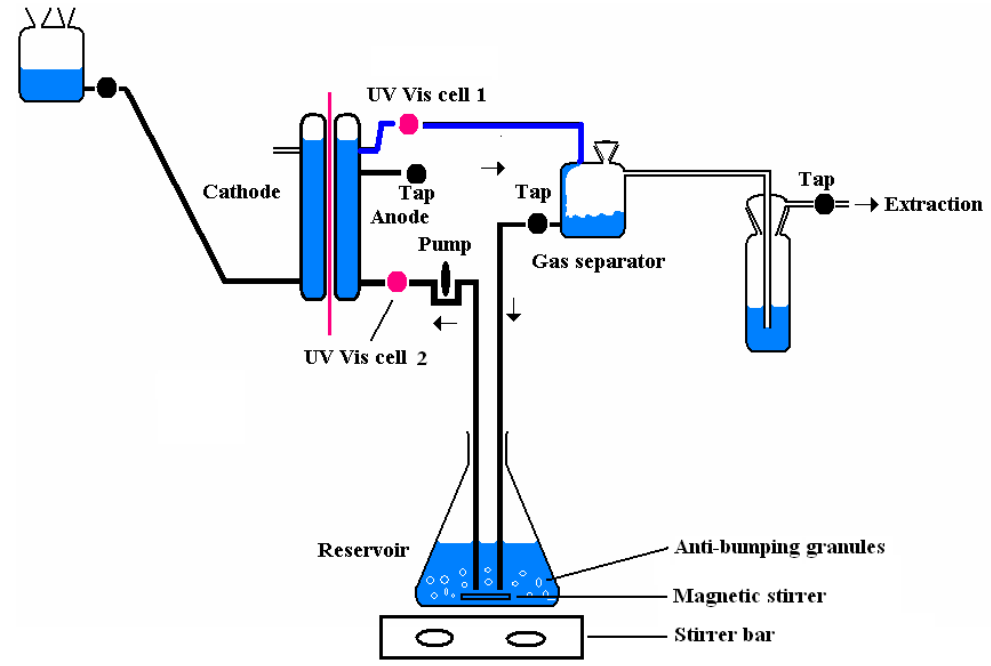

(a)

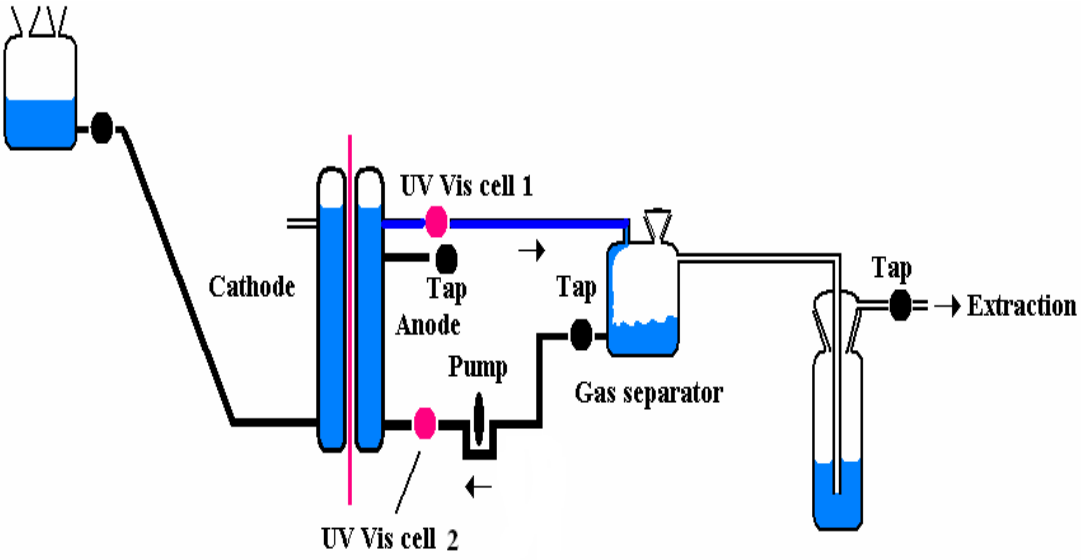

(b)

Figure 3.15 (a) Recycle equipment employing the conventional, small gas separator and a 2000 cm^3 conical flask containing 200 g of anti bumping granules and stirrer bar, stirred using a magnetic stirrer and (b) Conventional recycle equipment.

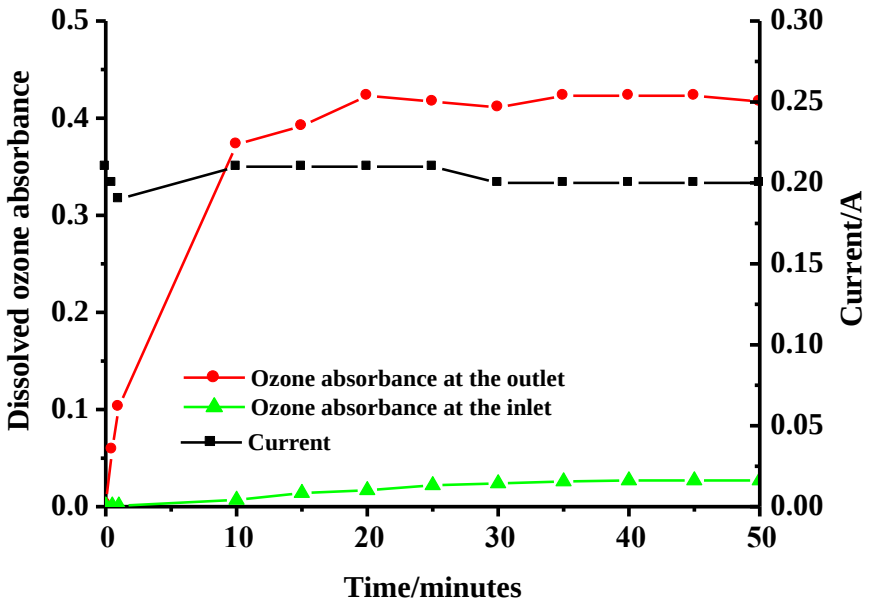

Figure 3.16 (a) Plots of current (■), dissolved ozone absorbance at outlet (●) and at the inlet (▲) of the electrochemical cell vs. electrolysis time obtained using anode AJED2F at a cell voltage of 2.7 V and anolyte flow rate of 30 cm^3 min^{-1} using the experimental equipment in fig. 3.15 (a).

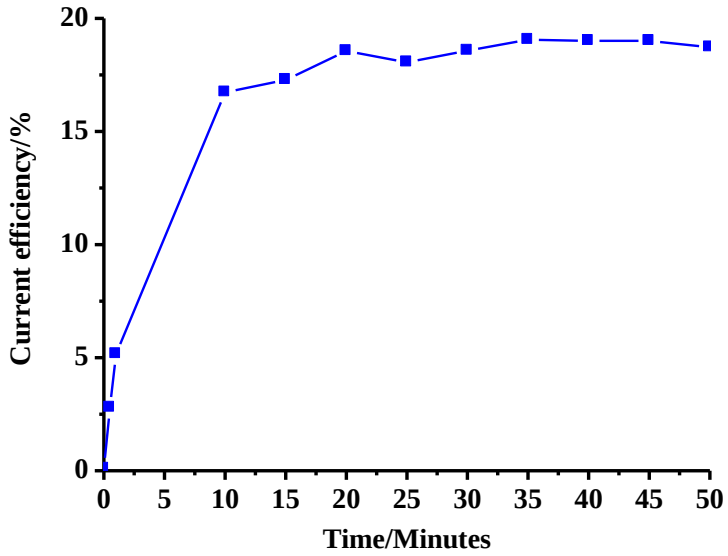

Figure 3.16 (b) Plot of current efficiency vs. time from the data in fig. 3.16 (a), taking the difference between the outlet and inlet dissolved ozone absorbances.

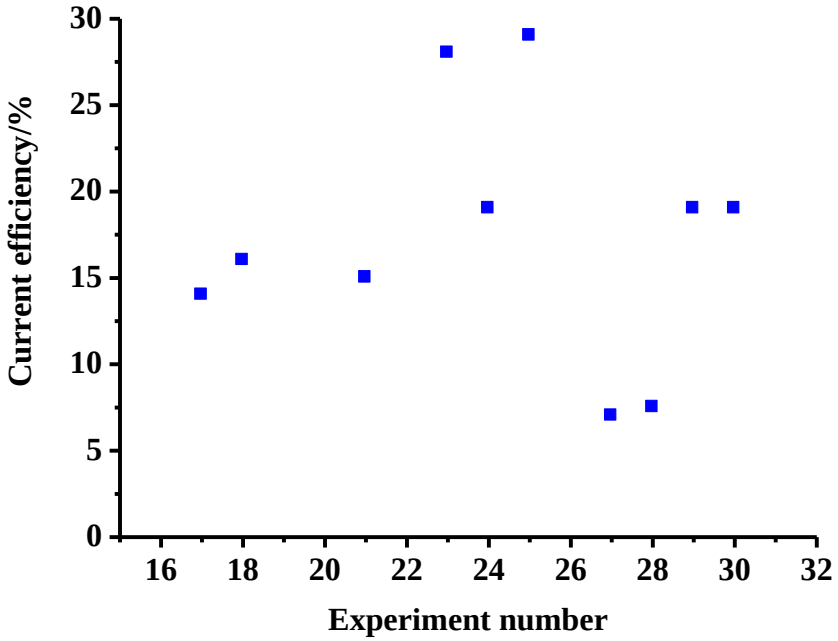

Figure 3.17 (a) Plot of current efficiency vs. experiment number for anode AJED2F using the systems in figs. 3.15 (a) and (b) and the same experimental conditions as in fig 3.16 (a).

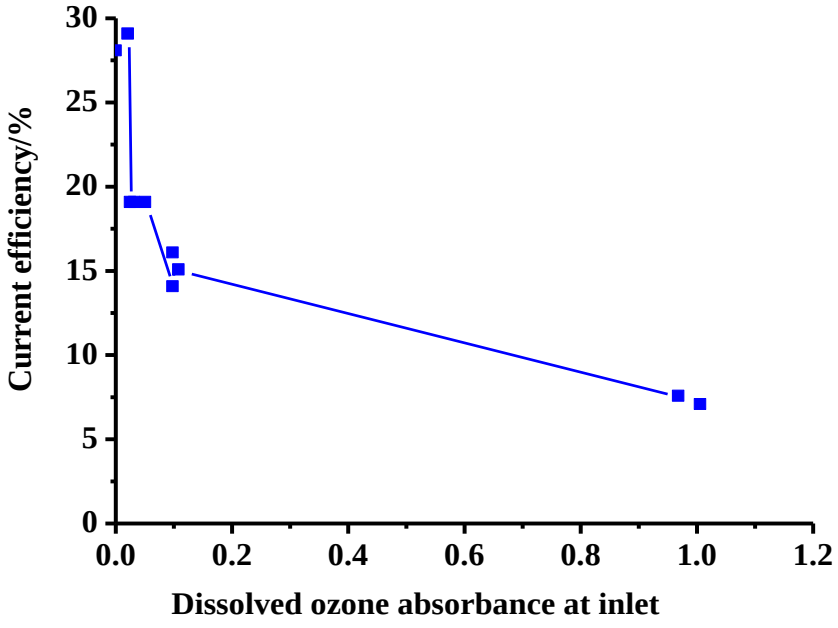

Figure 3.17 (b) Plot of current efficiency vs. ozone absorbance at inlet for the experiments in fig. 3.17 (a).

3.2.4 Possible mechanisms for the inhibition of electrochemical ozone generation by dissolved ozone

In essence, injection of ozonated electrolyte at the inlet at the bottom of the electrochemical cell reduced the ozone concentration in solution by the time the anolyte leaving the cell reached the UV-Vis cell after the outlet of the electrochemical cell. This suggested that either less ozone was generated at the anode surface or the ozone that was generated decays during travel between the anode and UV-Vis cell. It seems unreasonable to postulate that the relatively small concentration of ozone at the inlet of the cell in the experiment in fig. 3.14 (a) above could have any effect relative to the very high ozone concentration next to the anode. It is also worth noting from fig. 3.14 (a) that no change in current was determined when the ozone concentration at the inlet to the electrochemical cell increased from zero. In fact, in general, (i) the currents determined in single pass and recycle experiments were essentially the same and (ii) did not show any change when ozonated H_2SO_4 was injected at the inlet to the electrochemical cell. Hence, the detrimental effect of ozone did not affect the rate of electron transfer across the anode/electrolyte interface; it was either significantly enhanced the decay of ozone, switched active sites for ozone production over to O_2 and/or intercepted active intermediates.

One possible explanation is that it was not ozone that was responsible for the decrease in current efficiency, but a long-lived intermediate from its decay or a co-product that could catalyze further ozone decay. Sehested et al. [18] studied the decay of ozone concentration in pH 2 $HClO_4$ in order to investigate the observation that the decay of ozone at pH 0-4 is much faster than would be predicted on the basis of the generally-accepted mechanism involving initiation by OH [19]. Sehested et al. found that, at 22 ºC and pH 2 in the absence of added H_2O_2, the rate of ozone decay was independent of the surface area of the reaction vessel, with H_2O_2 being formed as the primary product. The amount of H_2O_2 produced decreased as the size of the reaction vessel increased. In contrast, on adding H_2O_2, the decomposition rate depended both upon peroxide concentration and the size of the reaction vessel. The authors interpreted their data in terms of the mechanism depicted in scheme 3.1 with both the initiation reactions (3.46),

(3.47) and (3.51) and termination reactions (3.54)-(3.56) catalysed by the surface of the reaction vessel. The authors postulated that H_2O_2 increased the rate of decay of ozone by reacting to form OH and O_2^-/HO_2 radicals, equation (3.51), that propagate the surface catalyzed, chain decomposition process. The work of Sehested et al. [19] suggests that peroxide, formed in parallel with ozone in the electrochemical cell, would catalyze the decomposition of ozone when operating the cell in recycle mode.

$$O_3 \Leftrightarrow O + O_2 \qquad (3.46)$$

$$O \text{ or } O_3^* + H_2O \rightarrow 2OH \text{ or } H_2O_2 + O_2 \quad \text{(surface reaction)} \qquad (3.47)$$

$$OH + O_3 \rightarrow HO_2 + O_2 \qquad k = 1.1 \times 10^8 \ M^{-1}s^{-1} \qquad (3.48)$$

$$OH_2 + O_3 \rightarrow OH + 2O_2 \qquad k < 10^4 \qquad (3.49)$$

$$OH_2 \Leftrightarrow O_2^- + H^+ \qquad K = 1.59 \times 10^{-5} \text{ M} \qquad (3.50)$$

$$H_2O_2 + O_3 \rightarrow OH + HO_2 + 2O_2 \qquad k = 0.025 \ M^{-1}s^{-1} \qquad (3.51)$$

$$O_2^- + O_3 \rightarrow O_3^- + O_2 \qquad k = 1.5 \times 10^9 \ M^{-1}s^{-1} \qquad (3.52)$$

$$O_3^- + H^+ \rightarrow OH + O_2 \qquad k = 9 \times 10^9 \ M^{-1}s^{-1} \qquad (3.53)$$

$$OH + OH \rightarrow H_2O_2 \qquad k = 6 \times 10^9 \ M^{-1}s^{-1} \qquad (3.54)$$

$$OH + HO_2 \rightarrow H_2O + O_2 \qquad k = 7 \times 10^9 \ M^{-1}s^{-1} \qquad (3.55)$$

$$HO_2 + HO_2 \rightarrow H_2O_2 + O_2 \qquad k = 8 \times 10^5 \ M^{-1}s^{-1} \qquad (3.56)$$

Scheme 3.1 The mechanism of ozone decay postulated by Sehested and co-workers [19].

3.2.5 The possible role of H_2O_2 in ozone decay

As a first step in determining if H_2O_2 is produced during recycling experiments, fig. 3.18 shows UV-Vis spectra of a series of H_2O_2 solutions formed by diluting 35% H_2O_2 with water and H_2SO_4 to give H_2O_2/0.5 M H_2SO_4; the UV-Vis spectra were taken using a 1.0 cm path length cuvette. The spectra of H_2O_2 of concentrations >1 mM are showing false maxima due to light limitations at the detector, and the true band maximum is clearly below 200 nm. The spectra in fig. 3.18 are in broad agreement with the literature [20][21] in that they show a steady increase in absorption as the wavelength is decreased from 350 nm with no maximum at λ > 200 nm.

For comparison with fig. 3.18, spectra collected during one of the experiments depicted in figs. 3.17 (a) and (b) were chosen (experiment 29 using anode AJED2F) and the equipment in fig. 3.15 (a) without anti-bumping granules. As well as collecting spectra, the failure of the stirrer gave the opportunity to detect any possible products from the decay of ozone following a relatively 'rapid' increase in ozone at the inlet of the electrochemical cell.

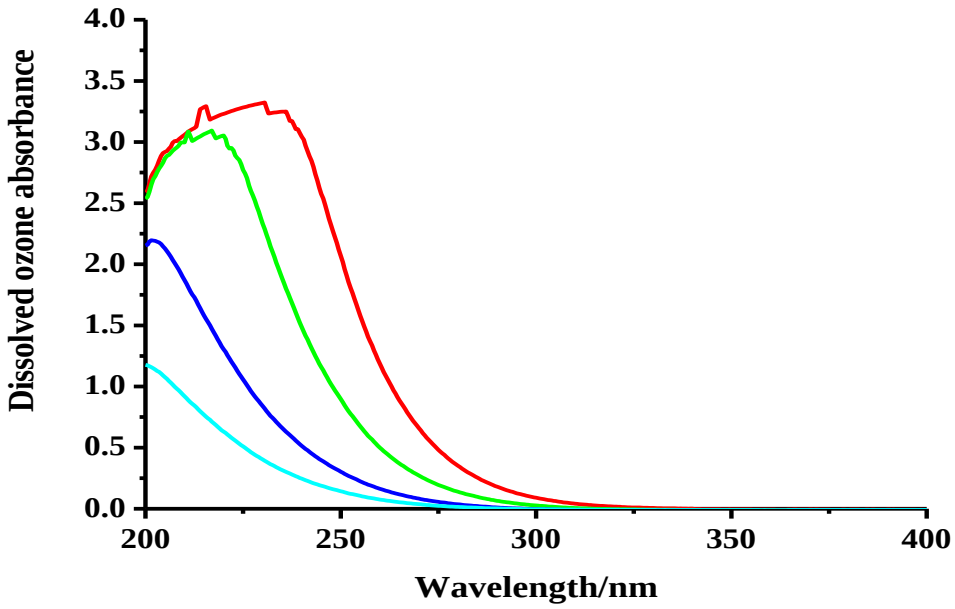

Figure 3.18 The UV-Vis spectrum of H_2O_2 in 0.5 M H_2SO_4 at a concentration of (——) 0.18 M, (——) 0.1 M, (——) 0.01 M and (——) 0.001 M.

Figure 3.19 (a) shows plots of ozone absorbance at the inlet and outlet of the electrochemical cell and the current, and figs. 3.19 (c) and (d) spectra collected at the outlet of the cell, from 70 minutes into the experiment (*i.e.* covering the period before and after the failure of the stirrer). The spectra suggested a non linear dependence of absorbance on concentration, which was unsurprising given the high absorbance involved and the non-linearised nature of the detector of the Astranet. It was not clear from figs. 3.19 (c) and (d) that H_2O_2 was being formed. As may be seen, the spectra did not appear to increase linearity with peroxide concentration at any particular wavelength; this was not unexpected as the Astranet spectrometer showed clear non-linear behaviour at absorbances > 0.7.

In order to probe this further, recycle experiments were carried out with larger anodes (6.0 x 4.0 cm) in a polycarbonate electrochemical cell (see figs. 3.20 (a) and (b)) at a fixed current of 1.3 A (0.2-0.3 A in the experiments employing anodes AJED22 series above). During the first experiment, using the system shown schematically in figs. 3.15 (a) and (b), the dissolved ozone absorbance was measured at the inlet to the electrochemical cell, and the gas phase absorbance also measured.

Figures 3.20 (a) and (b) show plot of (a) gas and dissolved ozone absorbances as a function of time and (b) the corresponding plots of current efficiency (determined from the gas phase ozone absorbance) and cell voltage. Both dissolved and gas phase absorbances showed an initial very rapid rise to high values before declining steadily. Figures 3.21 (a) and (b) show spectra collected at the outlet to the electrochemical cell (a) during the electrolysis and (b) once the cell was switched to open circuit. During the electrolysis, fig. 3.21 (a), the decrease in dissolved ozone was clear; however, the absorbance to the low wavelength side of the ozone peak did not show such a decline. Once the cell is switched to open circuit, fig. 3.21 (b), the ozone declines to zero, but there was a clear, residual absorption, see fig. 3.21 (c), consistent with the presence of H_2O_2. The half life for the decay was between 3 and 4 minutes, strongly suggesting an enhanced decay over that expected for the 1^{st} order process [19]. If the decay of the ozone was being facilitated by the production of H_2O_2 and, as postulated by Sehested et

al. [19], it is catalysed by the surfaces of the reactor, then we would expect to see some effects if the tubes to/from the gas separator were shortened, and the gas separator itself replaced by a smaller unit. To this end, the experiment described below was carried out.

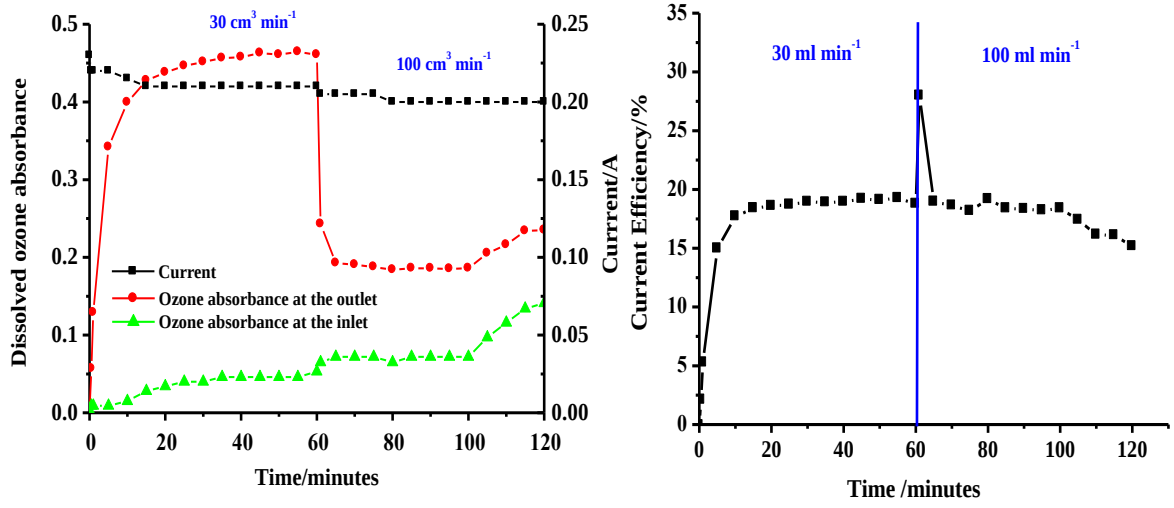

(a) *(b)*

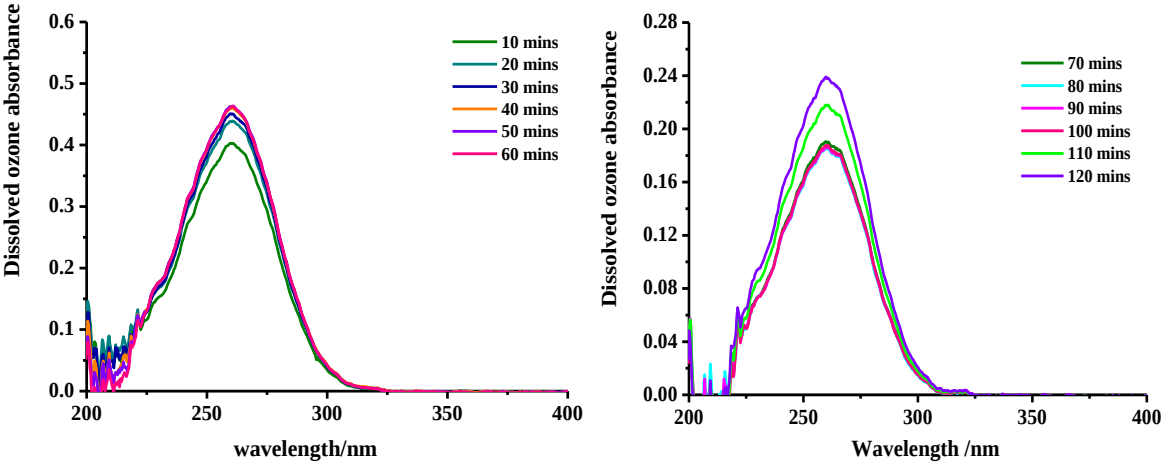

(c) *(d)*

Figure 3.19 (a) Plots of current (■), dissolved ozone absorbance at the outlet to the electrochemical cell (●) and at the inlet of the electrochemical cell (▲), (b) plot of the current efficiency as a function of time, (c) and (d) the UV-Vis spectrum of AJED2F anode experiment 29 at the outlet of the electrochemical cell in 0.5 M H_2SO_4, 2.7 V, flow rate 30 and 100 cm^3 min^{-1} on single pass system.

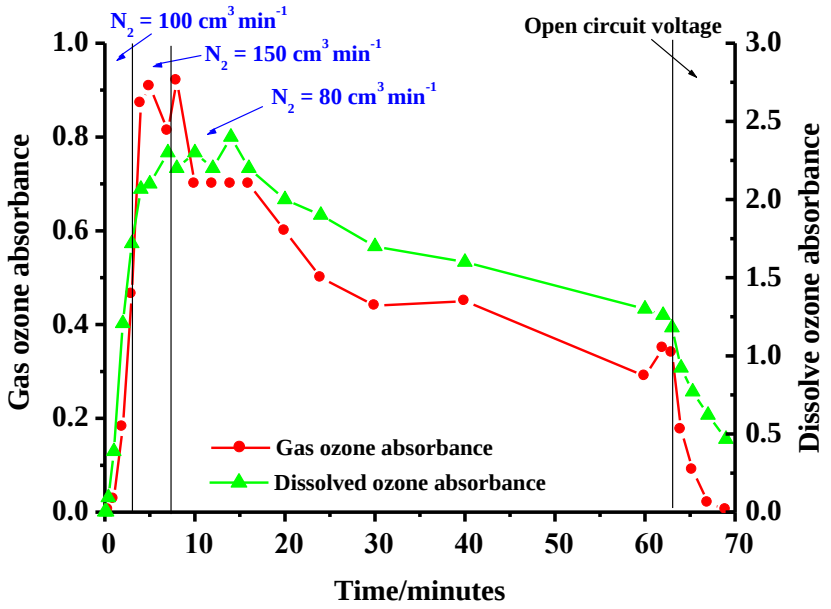

(a)

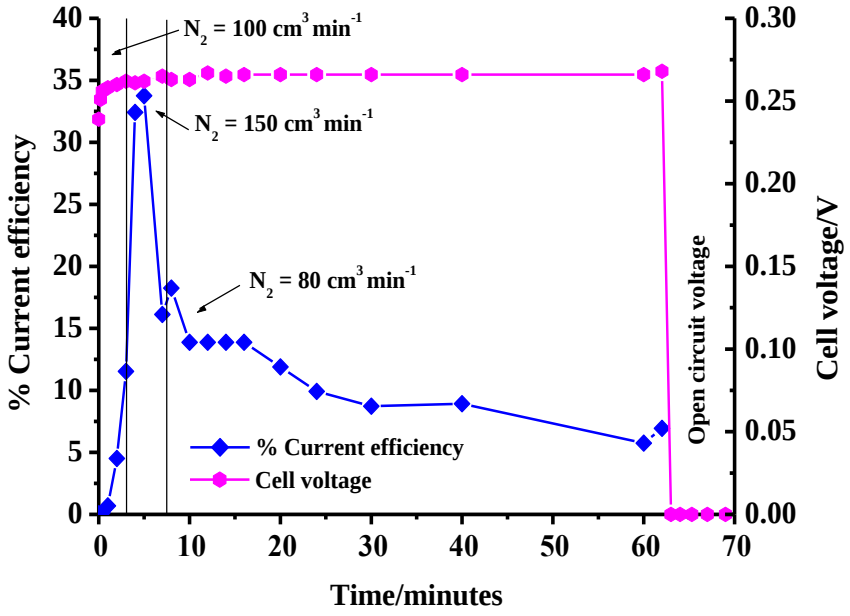

(b)

Figure 3.20 Plots of recycle system using standard glass separator and UV-Vis cell before anode AJED22I experiment 3 in 0.5 M H_2SO_4 at 2.7 V and anolyte flow rate of 30 cm^3 min^{-1}(a) gas (▲) and dissolved ozone absorbance (●) vs. time and (b) % current efficiency (◆) and cell voltage (●) vs. time.

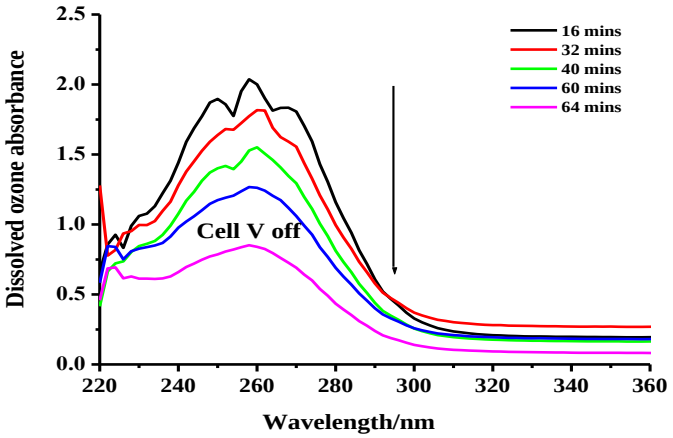

(a)

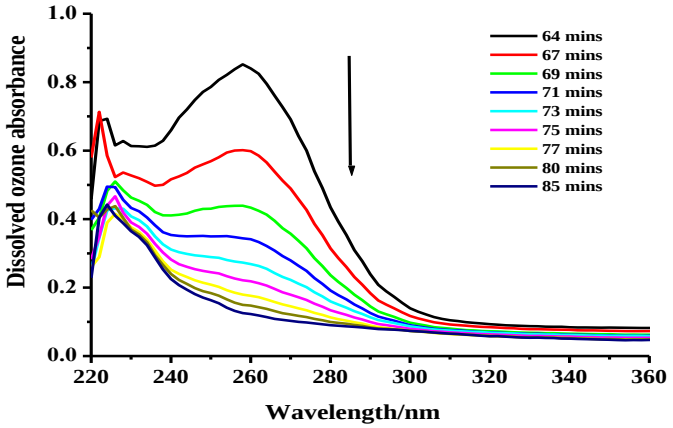

(b)

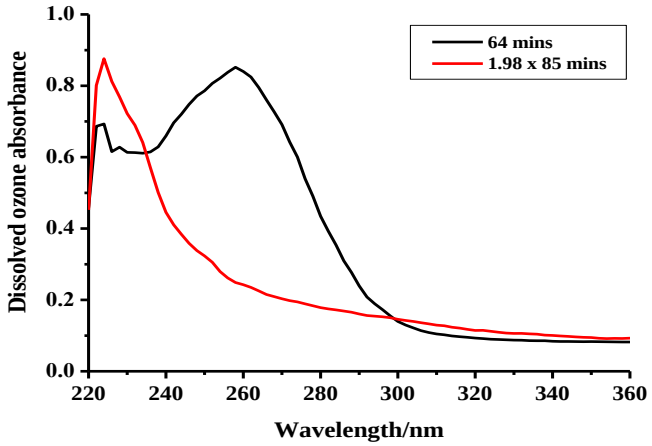

(c)

Figure 3.21 Spectra of dissolved ozone absorbance at the outlet of electrochemical cell (a) during electrochemical, (b) after switched to open circuit and (c) dissolved ozone absorbance consistently declines with H_2O_2 for the experiments in fig. 3.20.

Figure 3.22 (a) shows a diagram of the modified system, and fig. 3.22 (b) a photograph of the same. Figures 3.23 (a) and (b) show the corresponding plots of absorbance and efficiency. Various anolyte and N_2 flow rates were employed during the experiment depicted in figs. 3.22 and 3.23, but this does not detract from the general conclusions that may be drawn. Thus, it is clear from figs. 3.23 (a) and (b) that the dissolved and gas phase ozone absorbances are significantly lower in the former, suggesting that some deterioration in the selectivity of the catalyst has taken place (as both experiments were carried out at 1.3 A), and this is confirmed by fig. 3.23 (b) which shows an efficiency around 5-6%, (*ca.* 4% from Henry's Law calculation using dissolved ozone absorbance).

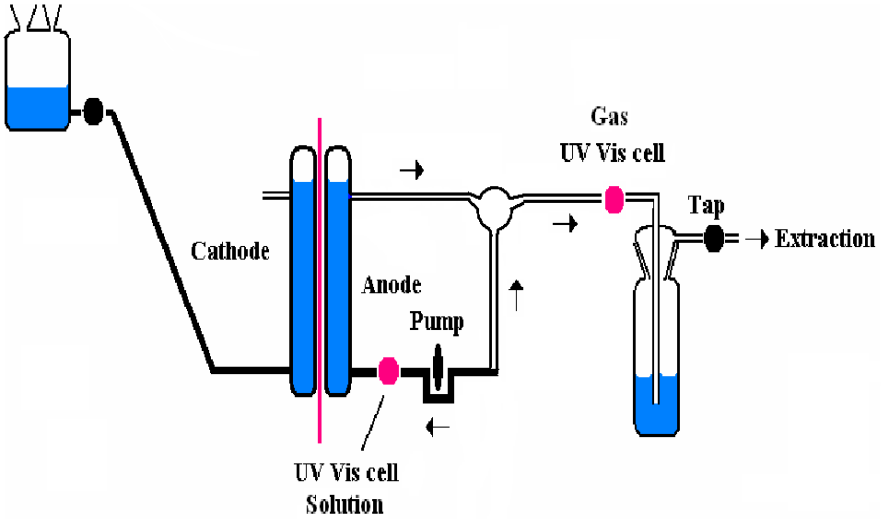

(a)

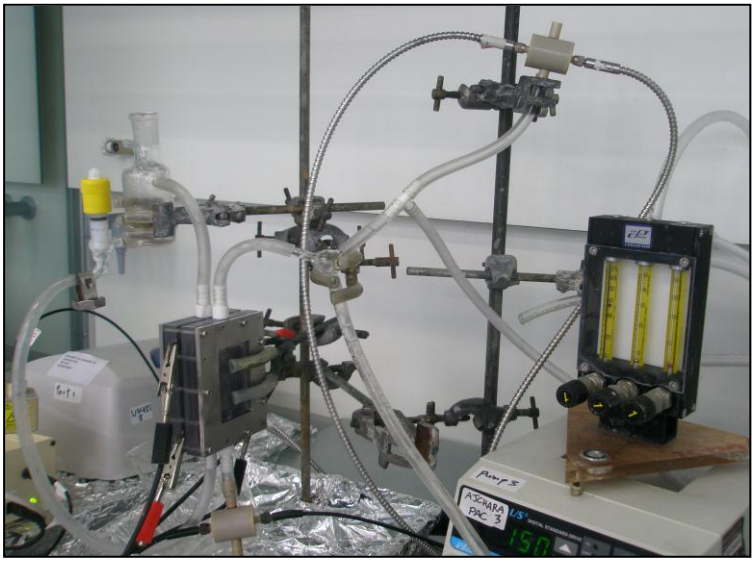

(b)

Figure 3.22 (a) A diagram and (b) a photograph of the modified system.

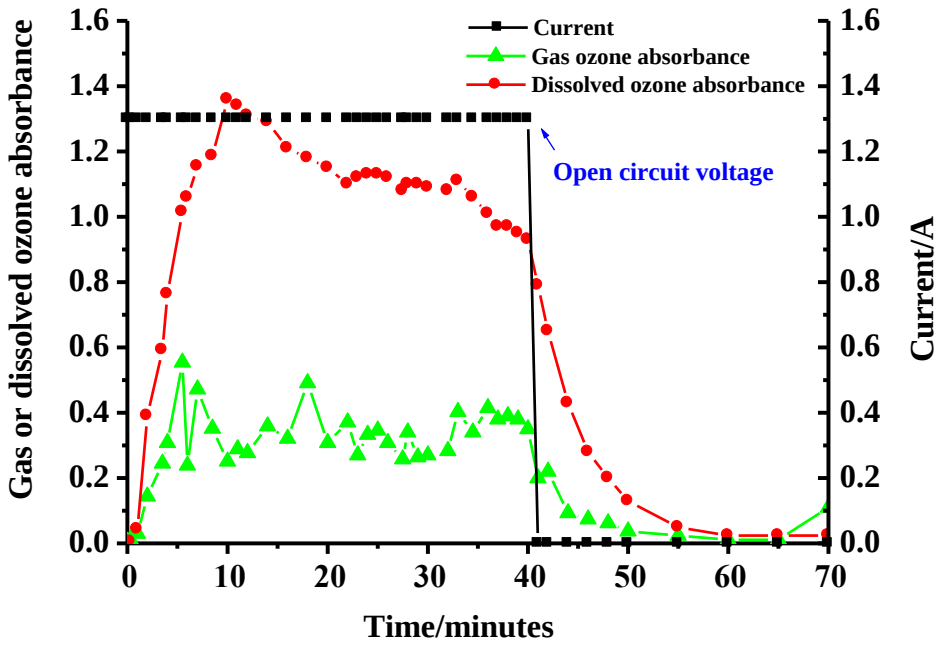

(a)

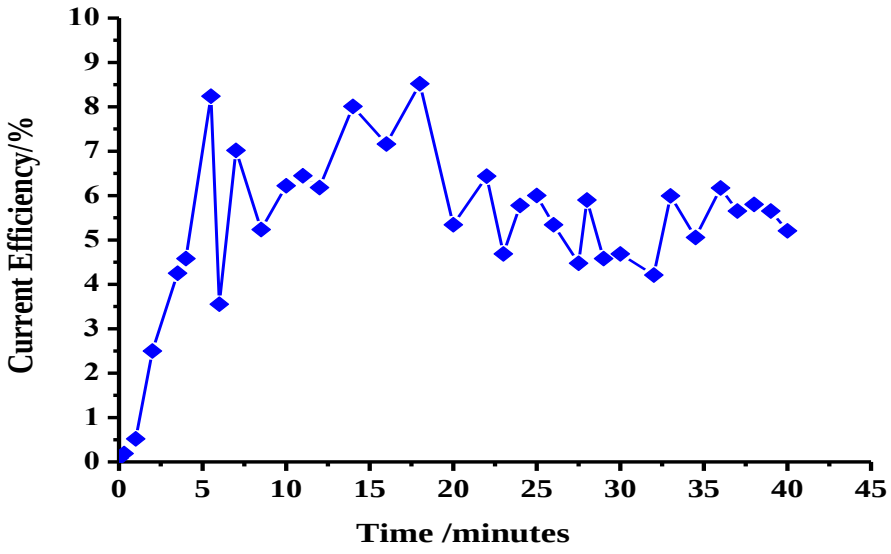

(b)

Figure 3.23 (a) Plot of the current (■), and gas phase (▲) and dissolve (●) ozone absorbance and (b) % current efficiency (♦) of anode AJED22I experiment 7 in 0.5 M H_2SO_4 with small glass separator and external anolyte circuit minimized 2.7 V and anolyte flow rate of 30 and 150 cm^3 $min^{-1}$and N_2 varying flow rate 60-100 cm^3 min^{-1}.

Figure 3.24 (a) shows UV-Vis spectra collected at the outlet of the electrochemical cell from 0 to 40 minutes during the experiment depicted in figs. 3.22 and 3.23, after which the cell was switched to open circuit and the spectra shown in fig. 3.24 (b) collected. The behavior of the O_3 peak intensity is shown in fig. 3.24 (c) along with the absorbance at 230 nm; the former shows an initial rise followed by a slow decay. In contrast, the "H_2O_2 absorbance at 230 nm" to the low wavelength side of the O_3 peak remains almost constant after the initial increase, and does not show the 27% decrease exhibited by the O_3 peak. This is supported by the difference spectrum in fig. 3.24 (d) which shows the spectrum collected at 10 minutes in fig. 3.24 (a) subtracted from that taken at 35 minutes. Whilst the decrease in the O_3 peak is clear, the curve returns to zero in the low wavelength region, suggesting no change in H_2O_2 concentration.

Figure 3.24 (b) shows the spectra collected when the cell was switched to open circuit. Again, a residual absorption due to H_2O_2 may be seen. It is worth nothing that (i) the apparent, steady state H_2O_2 absorbance at 225 nm during electrolysis, see fig. 3.24 (a), of 0.4 is very similar to that seen in fig. 3.21 (a), (ii) the half life for the decay of the O_3 in fig. 3.24 (c) is 3.5 minutes, the same as that determined in the experiment in fig. 3.21 (b). The similarity of the data obtained using two experimental equipments with such different characteristics apart from the common electrochemical cell suggests that ozone decay is taking place in the electrochemical cell rather than in the circuit external to the cell, and may be due to peroxide formation. However, caution is required as the presence of an adsorption to the low wavelength side of the ozone peak is not definitive proof of peroxide formation, particularly as the detector response is poor in this region.

The above data suggest that, in recycle system, the decrease in ozone current efficiency is due to a process, or processes, which take place in the electrochemical cell, rather than in the external tubes and glassware. The reduced current efficiency is calculated with both glass cells and the polycarbonate cell, suggesting the cell material is not responsible. This leaves the electrode and Nafion polymer electrolyte membrane.

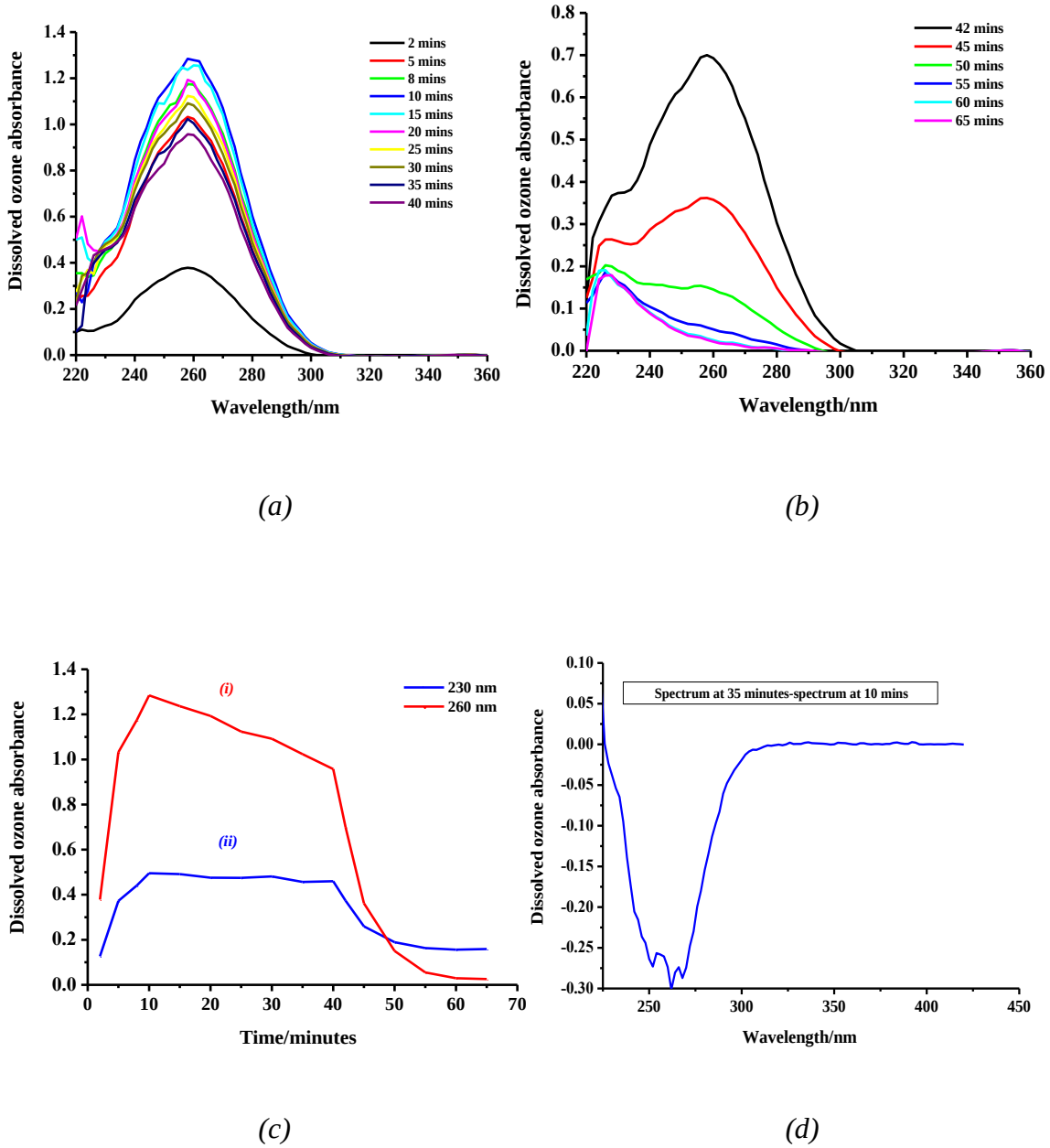

Figure 3.24 UV-Vis spectra collected at the outlet of the electrochemical cell (a) during the experiment and (b) after switched to open circuit at 40 minutes depicted in figs. 3.22 and 3.23. (c) The intensities of the ozone bands at (i) 260 nm and (ii) the "H_2O_2" feature at 230 nm in (a) and (b) plotted as a function of time. (d) The spectrum collected at 10 minutes in fig. 3.24 (a) subtracted from that taken at 35 minutes.

3.2.6 The possible effect of Nafion

In order to assess the possible detrimental effect of Nafion, an experiment was conducted in which a 6.25 cm^2 anode was tested in single pass system as follows. An anode (AJED13D prepared by methods ED1 and CC4, see table 4.1-4.3, 6.25 cm^2, Sn:Sb:Ni; 500:8:1) was tested in single pass system in a glass cell, and the results obtained are shown in figs. 3.25 (a)-(d).

As may be seen from the figures, the anode was very active with a current efficiency for ozone generation of at least 30%. The electrode was then coated with 5% Nafion solution using a paintbrush, dried for 1 hour, and then tested in the glass cell in 0.5 M H_2SO_4 at a cell voltage of 2.7 V and an anolyte flow rate of 30 cm^3 min^{-1}. The electrode was then soaked in isopropanol for 30 minutes and tested again under the same conditions.

Figures 3.26 (a)-(d) show data obtained from a repeat of the single pass experiment in figs. 3.25 (a)-(d) using the Nafion-coated anode. As may be seen from a comparison of the two sets of data, coating the anode with Nafion did not have a detrimental effect on the current (see figs. 3.25 (a) and (b) and figs. 3.26 (a) and (b)), but reduces the current efficiency by *ca.* 30% (see figs. 3.25 and 3.26 (d)). It is difficult to judge from the UV-Vis spectra collected during the two experiments (figs. 3.25 (c) and 3.26 (c)) whether the Nafion coating enhances the production of H_2O_2 due to the noise in fig. 3.26 (c). The anode was immersed in isopropanol for 30 minutes, washed with water and the single pass experiment replaced. This coating/removal procedure was repeated several times and the results so obtained are summarised in figs. 3.27 (a) and (b) and table 3.3.

It is clear from fig. 3.27 (a) that coating with Nafion reduces current efficiency but, from fig. 3.27 (b) and table 3.3, has little effect upon the current, strongly suggesting that Nafion (at least in *direct contact* with the catalyst) 'switches over' to O_2 evolution a high proportion (up to 50%) of the active sites for O_3. Immersion in isopropanol alcohol (IPA) to dissolve the Nafion restores some activity, with longer immersion being more

effective (experiments 11 and 12 *cff.* 8-10). However, there does appear to be an underlying loss of selectivity in the data in fig. 3.27 (a) and table 3.3.

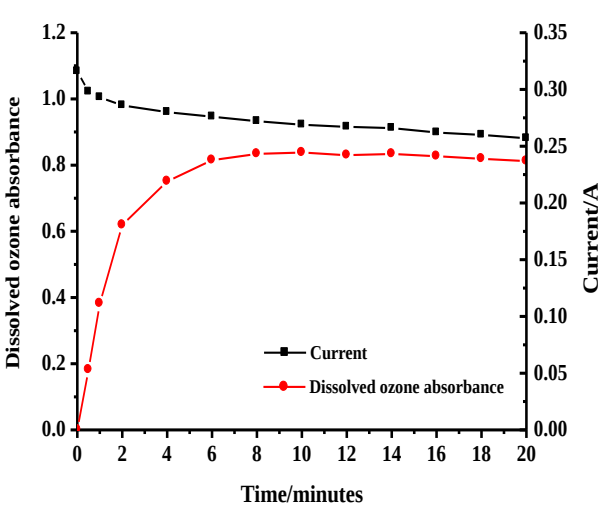

(a)

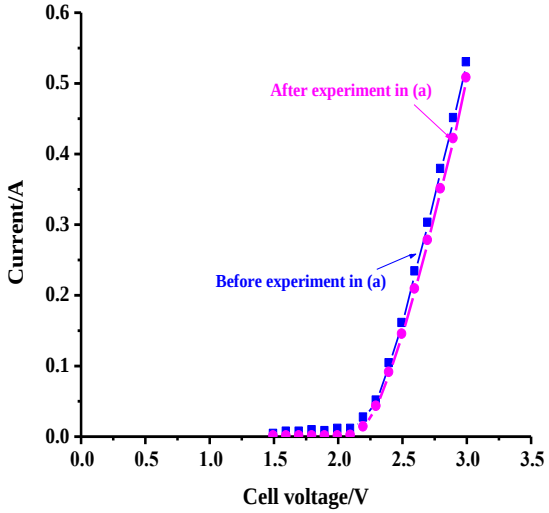

(b)

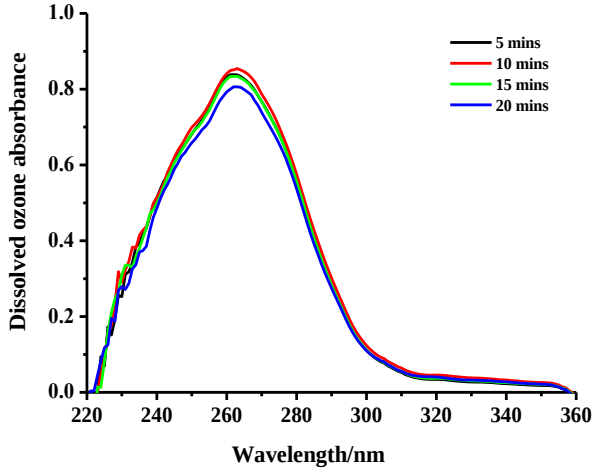

(c)

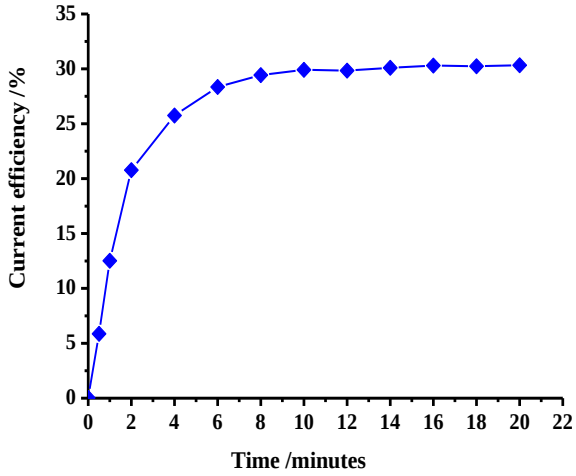

(d)

Figure 3.25 Plots of (a) current (■), dissolved ozone absorbance (●), (b) plot of current before (■) and after (●) experiment on polarization curve, (c) UV-Vis spectra and (d) % current efficiency (♦) of anode AJED13D experiment 3 before coating with 5% Nafion solution and testing in 0.5 M H_2SO_4 at a cell voltage of 2.7 V and an anolyte flow rate of 30 cm^3 min^{-1}.

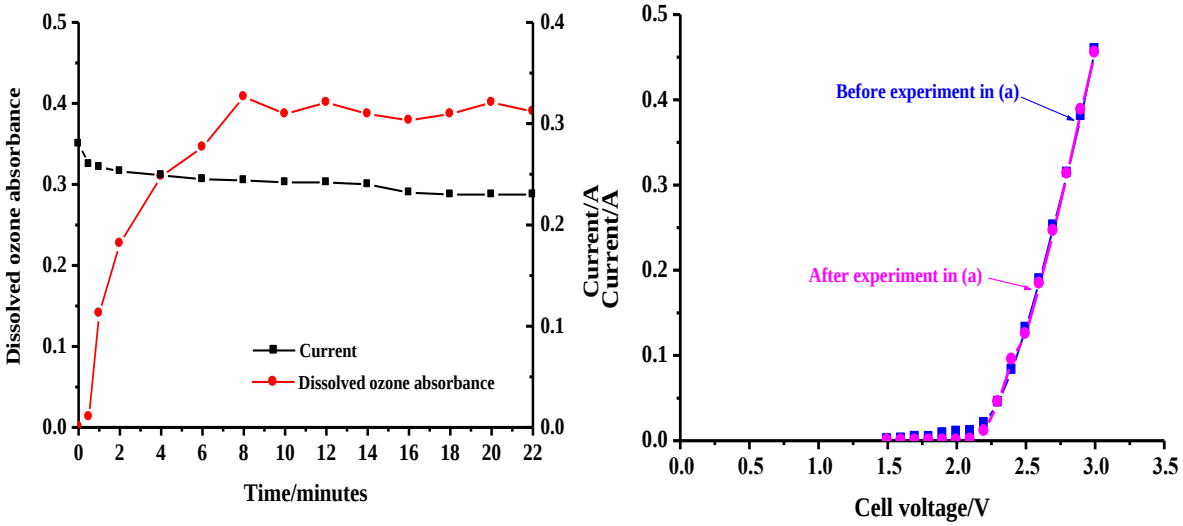

(a) *(b)*

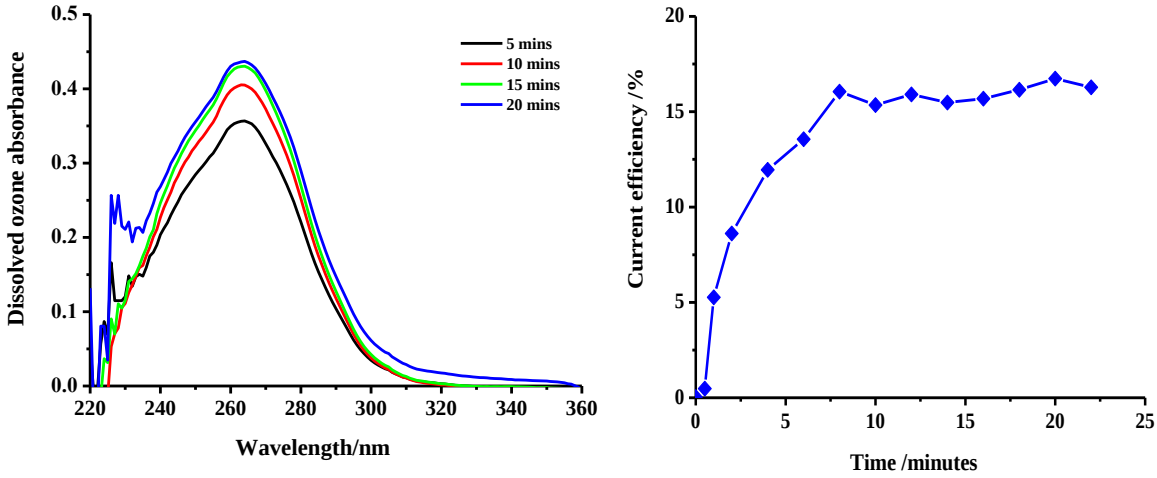

(c) *(d)*

Figure 3.26 Plots of (a) current (■), dissolved ozone absorbance (●), (b) plot of current before (■) and after (●) experiment on polarization curve, (c) UV-Vis spectra and (d) % current efficiency (♦) of anode AJED13D experiment 4 after coating with 5% Nafion solution and testing in 0.5 M H_2SO_4 at a cell voltage of 2.7 V and an anolyte flow rate of 30 cm^3 min^{-1}.

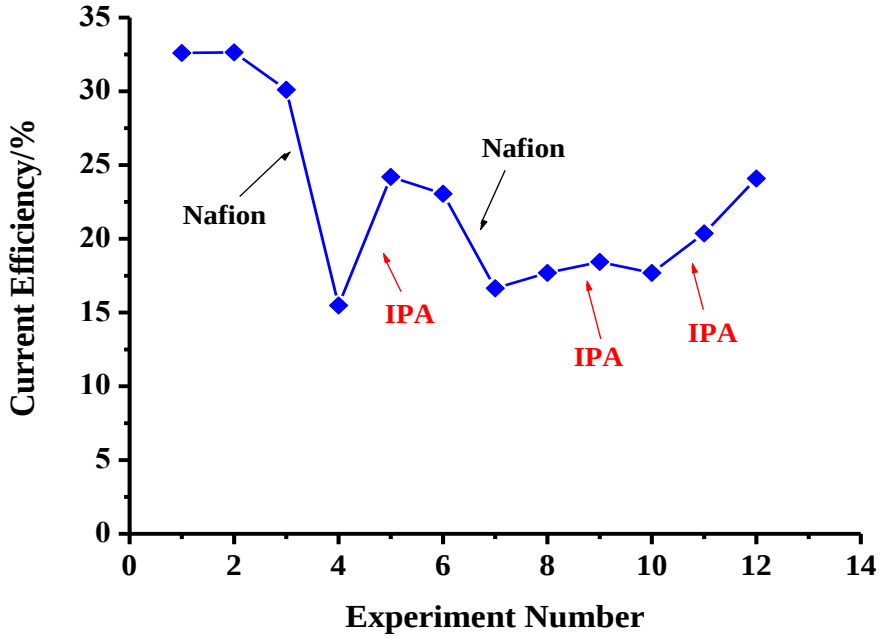

(a)

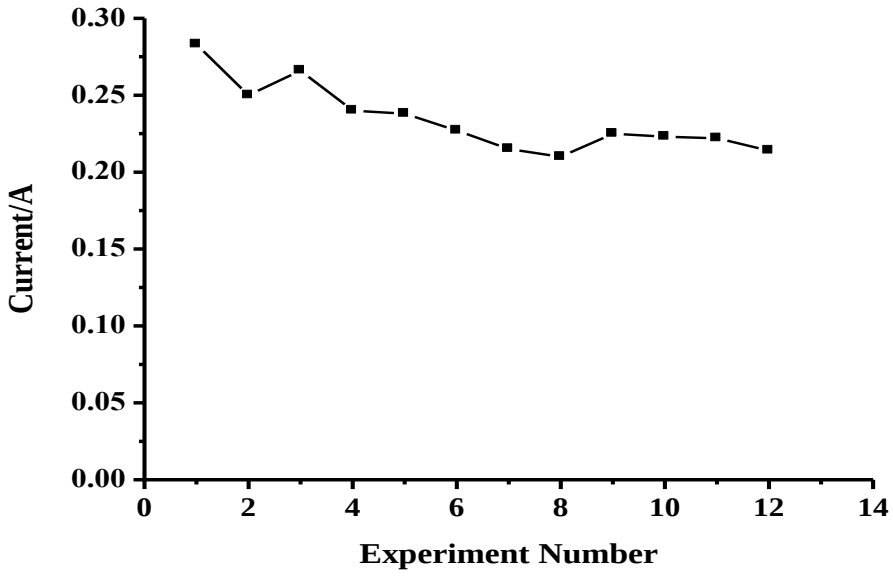

(b)

Figure 3.27 Plot of (a) % current efficiency (♦) and (b) current (■) vs. time determined during the testing of anode AJED13D in 0.5 M H_2SO_4 at a cell voltage of 2.7 V and an anolyte flow rate of 30 cm^3 min^{-1}.

Exp. No.	Current (A)	Absorbance	Φ^{e}_{O3} /%	Voltage (V)	Flow rate (cm^3 min^{-1})	Comment
1	0.283	0.961	32.60	2.7	30	Single pass system
2	0.250	0.850	32.64	2.7	30	Single pass system
3	0.266	0.834	30.10	2.7	30	Before coating with 5% Nafion solution
4	0.240	0.387	15.48	2.7	30	After coating with 5% Nafion solution 1 hour
5	0.238	0.536	24.20	2.7	30	After washing with isopropanol 30 minutes
6	0.227	0.545	23.05	2.7	30	
7	0.215	0.373	16.65	2.7	30	After coating with 5% Nafion solution 1 hour
8	0.210	0.387	17.69	2.7	30	
9	0.225	0.432	18.43	2.7	30	After washing with isopropanol 30 minutes
10	0.223	0.411	17.69	2.7	30	
11	0.222	0.471	20.37	2.7	30	After washing with isopropanol 4 nights
12	0.214	0.537	24.09	2.7	30	

Table 3.3 Summary results of the Nafion experiments using anode AJED13D in the glass cell.

Figure 3.28 (a) and (b) show UV-Vis spectra collected during experiments 11 and 12, which are representative of all the experiments after those depicted in figs. 3.25 and 3.26 above, in that there was showed the shoulder to lower wavelength tentatively attributed to H_2O_2. These data may indicate the participation of Nafion in the production of H_2O_2; but the poor detector response in the region < 240 nm complicates interpretation of the data.

The data above clearly indicate that Nafion in *direct contact* with the anode has a detrimental effect on the selectivity towards ozone evolution. In order to determine whether such direct contact was necessary or whether the presence of Nafion remote from the anode would also have a detrimental effect (*i.e.* in recycle system 'catalysing' the decay of ozone) a series of experiments were carried out using a battery separator. Celgard 2400 is a 25 μm thick microporous monolayer polypropylene membrane [22]. The membrane has excellent resistance to acids and oxidation, with a uniform pore structure (41% porosity 0.043 μm pore size) and high chemical and thermal stability. The membrane finds major application in low temperature, primary lithium batteries and is hydrophobic; hence, prior to use, the membrane was immersed in isopropyl alcohol for 2 hours and then washed thoroughly with Millipore water.

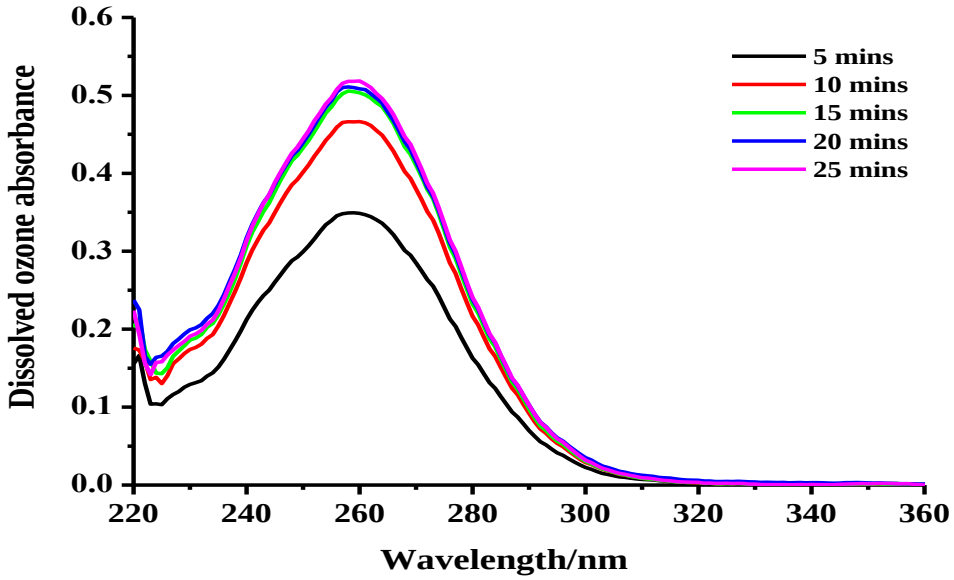

(a)

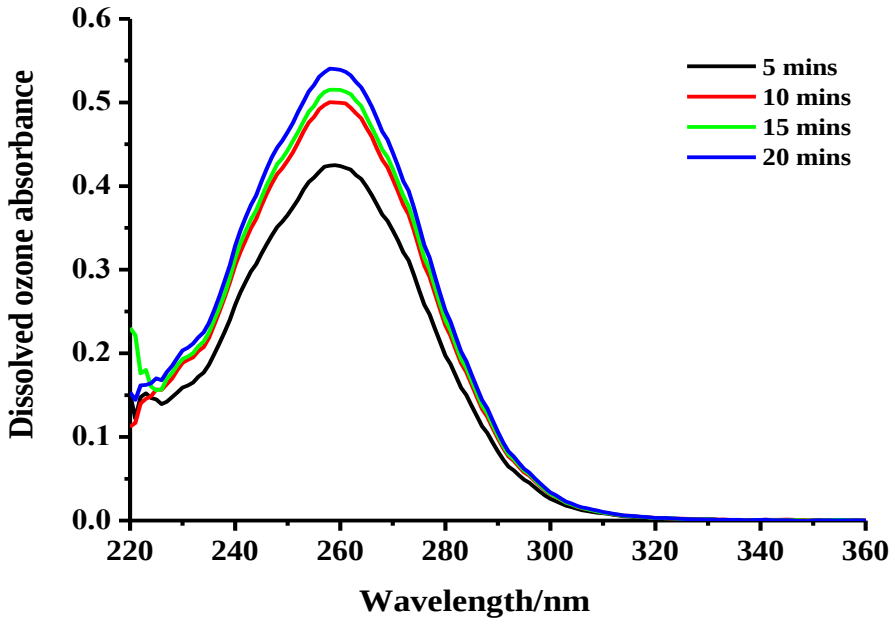

(b)

Figure 3.28 UV-Vis spectra of anode AJED13D in (a) experiment 11 and (b) experiment 12 after washing with isopropanol and testing in 0.5 M H_2SO_4 at a cell voltage of 2.7 V and an anolyte flow rate of 30 cm^3 min^{-1}.

A sample of Celgard 2400 was employed in place of Nafion in the glass cell with anode AJED2H (6.25 cm^2, Sn:Sb:Ni; 500:8:4). Anode AJED2H gave a current of 0.23 A and an efficiency of 23% prior to the experiments discussed below.

Figures 3.29 (a)-(c) show data from the first experiment using the Celgard membrane, carried out in single pass system. The current was *ca.* 0.18 A, *ca.* 20% less than that observed with Nafion, and the current efficiency was also *ca.* 18%, *ca.* 20% lower. However, this performance was very encouraging given the fact that it was the first experiment with the membrane, and suggest that the membrane could be a viable (and cheaper) alternative to Nafion in acid/acid applications.

Figure 3.29 (b) shows the UV-Vis spectra collected during the experiment in fig. 3.29 (a), the spectra showed the shoulder to lower wavelengths due (possibly) to H_2O_2.

Figures 3.30 (a)-(c) show a recycle experiment carried out after the experiment in figs. 3.29 (a)-(c). As has been consistently determined, the current efficiency calculated from the ozone gas absorbance in the experiment using the Celgard membrane was significantly lower (3.5%) than that determined in single pass system (18%, see above). This suggests strongly that Nafion was not responsible for the reduced efficiency in recycle system. This leaves either: (1) the anode participating in ozone decay; (2) the decay being an inherent factor at high solution ozone concentrations or (3) there is a problem with ozone gas measurements using UV-Vis spectroscopy. Option (2) would seem to be ruled out by the work of Stucki et al. [6], using a PEM (water/water) cell and PbO_2 anode, who showed that injecting electrolyte containing up to 25 ppm O_3 (equivalent to an absorbance of 1.6) at the inlet of the anode compartment did not effect current efficiency.

The ratio between the intensity of the 'H_2O_2' shoulder (taken at 225 nm) and the main peak intensity seemed to be reasonably consistent around 40%, irrespective of single pass or recycle modes of operation. Coupled with the very low emission intensity in this

region, the data do not unambiguously support the generation of H_2O_2 or of any species enhancing the decay of ozone.

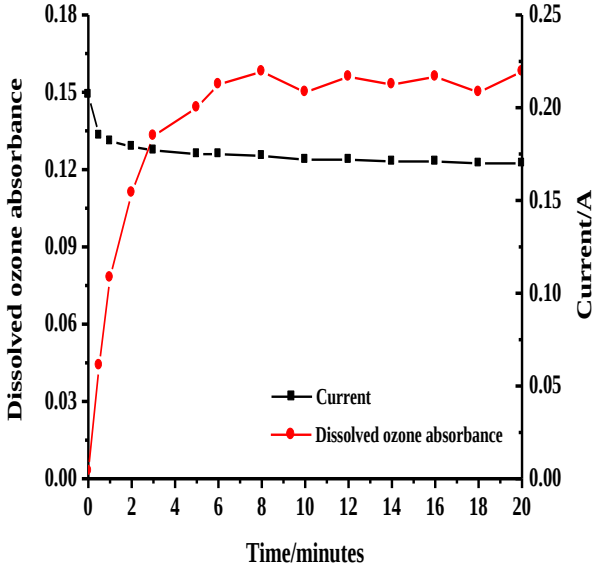

(a)

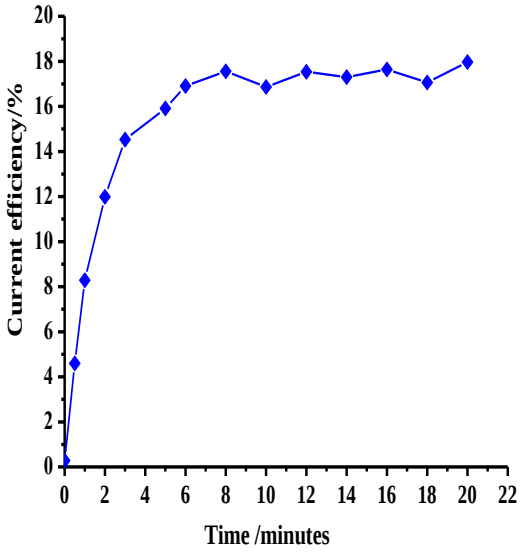

(b)

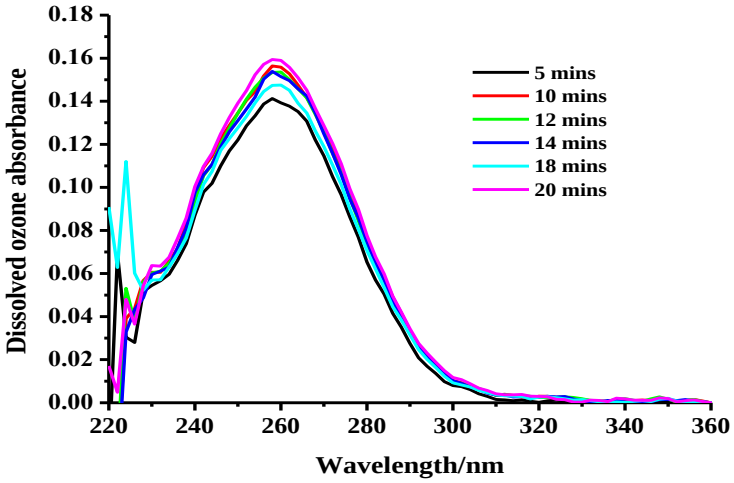

(c)

Figure 3.29 Plots of (a) current (■), dissolved ozone absorbance (●), (b) % current efficiency (◆) and (c) UV-Vis spectra collected during the experiment of anode AJED2H experiment 11 with Celgard membrane in 0.5 M H_2SO_4 at a cell voltage of 2.7 V and anolyte flow rate of 30 cm^3 min^{-1}.

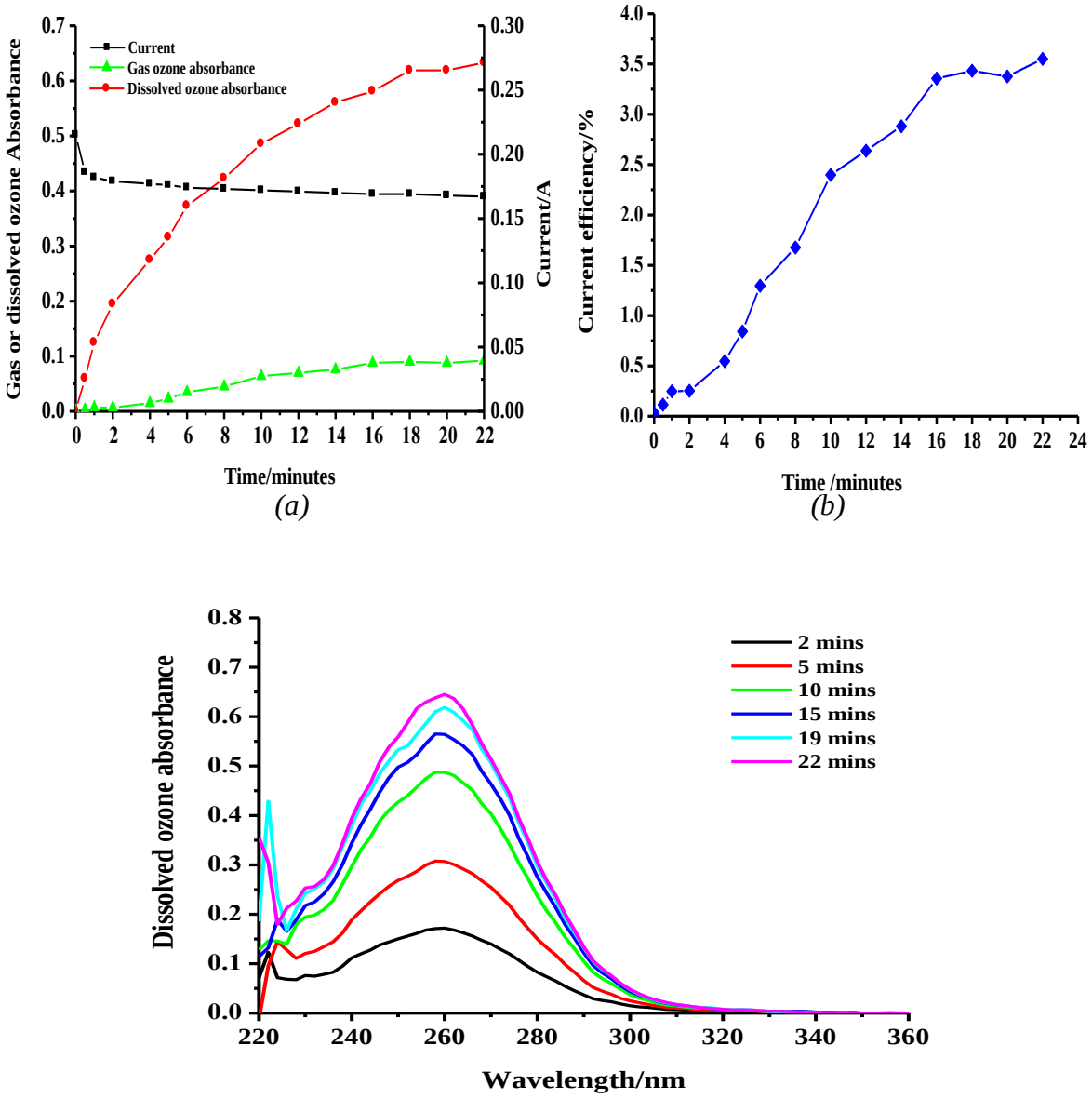

Figure 3.30 Plots of (a) current (■), dissolved (●) and gas (▲) ozone absorbance, (b) current efficiency calculated from the gas phase ozone absorbance (◆) and (c) UV-Vis spectra collected during the experiment of anode AJED2H experiment 16 with Celgard membrane in 0.5 M H_2SO_4 at a cell voltage of 2.7 V and an flow rate of 30 cm^3 min^{-1}.

It should, of course, be noted that Stucki and co-workers employed water at the anode rather than aqueous sulphuric acid; however, there are no reports in the literature to my knowledge of ozone in solution having an adverse effect upon electrochemical ozone generation.

Having eliminated the possible detrimental rôle of Nafion, it was decided to check that the chemical composition of the acid did not affect the efficiency of ozone generation. To this end, single pass and recycle experiments were carried out in 0.1 M $HClO_4$ and 0.05 M H_2SO_4, the data are summarised in table 3.4.

Exp. No.	**Electrolyte**	**Current (A)**	**Φ^e_{O3}/% Single pass**	**Φ^e_{O3}/% Recycle**	**Intensity at 255 nm/ Intensity at 258 nm**
11	0.5M H_2SO_4	0.17	17	-	0.38
12	0.05M H_2SO_4	0.07	15	-	-
13	0.05M H_2SO_4	0.04	-	4.5	0.43
14	0.1M $HClO_4$	0.04	-	5.5	0.39
15	0.1M $HClO_4$	0.04	19	-	0.44
16	0.5M H_2SO_4	0.17	-	3.5	0.39

Table 3.4 Summary of Nafion membrane at various concentrations of acid solution.

The data in the table are presented in the order that the experiments were carried out, so that any underlying decay in anode activity and/or selectivity that may be taking place was clear; judging by the current and current efficiencies determined, this was not a problem over the timescale represented by the data in the table. From the table, it is clear that the efficiencies measured in recycle system are consistently and markedly lower than those measured in single pass system, irrespective of the nature of the electrolyte employed. Taken in conjunction with the fact that this was determined generally when using Nafion as the membrane, these data suggested strongly that the difference in ozone efficiency measured between single pass and recycle systems under acid/acid operation is due to the anode in same way.

3.2.7 A consideration of the ozone evolution mechanism

In order to explain why the presence of ozone in the anode compartment of an electrochemical cell may inhibit ozone evolution at Ni/Sb-SnO_2 anodes, it is necessary to have a mechanism. To this end, the theories of Electrochemical Ozone Production (EOP to distinguish it from the electrochemical Oxygen Evolution Reaction, OER) in the literature are all based on the same four steps (see, for example, [23][24][25] and references therein) irrespective of the chemical nature of the anode:

$$H_2O \rightarrow (OH^{\cdot})_{ads} + H^+ + e^- \quad (3.57)$$

$$(OH^{\cdot})_{ads} \rightarrow (O^{\cdot})_{ads} + H^+ + e^- \quad (3.58)$$

$$2(O^{\cdot})_{ads} \rightarrow (O_2)_{ads} \quad (3.59)$$

$$(O_2)_{ads} \rightarrow O_2 \quad (3.60)$$

$$(O^{\cdot})_{ads} + (O_2)_{ads} \rightarrow (O_3)_{ads} \rightarrow O_3 \quad (3.61)$$

$$(O_3)_{ads} \rightarrow O_3 \quad (3.62)$$

Scheme 3.2 The mechanism of electrochemical ozone evolution commonly reported in the literature [23][24][25].

More sophisticated mechanisms have the $(O^{\cdot})_{ads}$ and $(O_2)_{ads}$ species diffusing to sites specifically active for O_2 and O_3 evolution (see, for example, [24]).

It is generally accepted that the first step, (3.57), is rate determining. It was generally determined in all the relevant experiments reported in this thesis that the presence of ozone in the anolyte had no effect upon the current, including experiments using the standard recycle equipment shown in fig. 3.15 (b) where the ozone concentration could be $>3.3x10^{-4}$ M.

Thus, if the mechanism broadly represented by scheme 3.2 is accepted, it is the subsequent fate of the $(O^{\cdot})_{ads}$ formed in the rate determining step that is the real issue of relevance to the work reported in this chapter, as this has no effect upon the current, but will affect the ratio of O_3 to O_2, as this will depend critically on what species are adsorbed on the surface, and where they are adsorbed, given the stringent requirement that $(O^{\cdot})_{ads}$ and $(O_2)_{ads}$ must be adjacent for ozone formation.

The last step in scheme 3.2 (3.62), should more correctly be represented as an equilibrium (as should (3.60)):

$$(O_3)_{ads} \leftrightarrow O_3 \tag{3.63}$$

In which case, high concentrations of ozone in the electrolyte may be expected to inhibit the release of free O_3 due to Le Chatalier's principle; but this alone does not explain the lack of any effect upon the current and, by implication, the switching off of O_3 active sites and switching on of O_2 active sites.

Under conditions of high concentrations of O_3 we may expect reactions such as (3.63) and (3.64) to occur:

$$(O^{\cdot})_{ads} + (O_3)_{ads} \rightarrow 2(O_2)_{ads} \rightarrow 2O_2 \tag{3.64}$$

$$(O^{\cdot})_{ads} + O_3 \rightarrow 2(O_2)_{ads} \rightarrow 2O_2 \tag{3.65}$$

Which would clearly result in an apparent switchover from O_3 to O_2, with no change in current, as would the displacement of $(O_2)_{ads}$ by O_3:

$$(O_2)_{ads} + O_3 \rightarrow (O_3)_{ads} + O_2 \tag{3.66}$$

3.3 The anode potential

The two-electrode cells employed during the work reported in this thesis precluded the application of a reference electrode, and hence typical anode potentials were not measured. However, it was decided to determine the anode potential under typical operating conditions to allow comparison with the standard reduction potentials of couples likely to be present in the electrolyte or generated therefrom.

It is possible to estimate the anode potential, as follows.

The cell voltage V_{cell} comprises several components (see fig. 3.31):

$$|V_{cell}| = \phi_a - \phi_c = \delta\phi_a + jR_{elec}' + jR_{Nafion}' + |\delta\phi_c| \qquad (3.67)$$

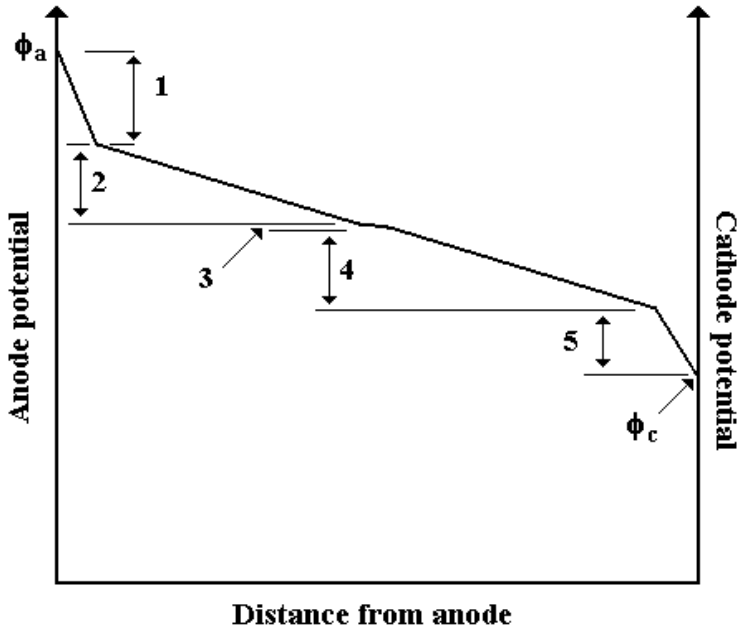

Figure 3.31 The potential drops across an electrochemical cell. (1) $\delta\phi_a$ and (5) $\delta\phi_c$ the Inner Galvani Potential differences across the anode and cathode/electrolyte interfaces [26], (2) and (4) the IR drop across the electrolyte (total resistance = R_{elec}'), and (3) the IR drop across the Nafion (resistance = R_{elec}').

Where ϕ_a and ϕ_c are the Inner Galvani potentials [26], at the anode and cathode, (using ϕ to avoid confusion with the electrode potentials at zero current, see below), $\delta\phi_a$ is the Inner Galvani potential difference across the double layer at the anode and $\delta\phi_c$ that at the cathode.

When no current flows:

$$\delta\phi_a = \phi_a - \phi_0 \text{ and } \delta\phi_c = \phi_c - \phi_0 \tag{3.68}$$

ϕ_0 is the Inner Galvani potential of the electrolyte. When current is flowing, the Inner Galvani potential of the electrolyte near the anode will not be equal to that near the cathode; the difference will simply be the Ohmic drop across the cell. j is the current density passing through both electrodes (A cm^{-2}), R_{elec}' and R_{Nafion}' are the resistance of the acid electrolyte and the resistance of Nafion, respectively, in Ω cm^{-2}. Hence:

$$\delta\phi_a = |V_{cell}| - jR'_{elec} - R'_{Nafion} - |\delta\phi_c| \tag{3.69}$$

As the counter electrode reaction is the generation of hydrogen at Pt, it can be assumed that $\delta\phi_c \approx |\eta_c|$ the overpotential at the hydrogen-evolving cathode (a correction of 0.018 V should be made to allow for the pH difference between the standard solution pH of 0 and that of the 0.5 M H_2SO_4 of 0.3, but this correction will cancel out overall). $\delta\phi_c$ can be determined by a consideration of the Butler-Volmer equation and the limiting current density, $j_{L,Cath}$:

$$j = \frac{j_0\left(e^{\left(\beta_A \eta f\right)} - e^{\left(-\beta_c \eta f\right)}\right)}{1 + \left[\left(\frac{j_0 e^{\left(\beta_A \eta f\right)}}{j_{L,An}}\right) - \left(\frac{j_0 e^{\left(-\beta_c \eta f\right)}}{j_{L,Cath}}\right)\right]} \tag{3.70}$$

The derivation of equation (3.70) and the subsequent calculation of $\delta\phi_a$ are detailed in the Appendix.

Using reasonable values of the various experimental parameters gives a value of 2.3 V for $\delta\phi_a$ at a typical current density (38.0 mA cm^{-2}) observed at a cell voltage of 2.7 V. Such a value is clearly sufficient to oxidize water to oxygen, but insufficient to produce OH radicals (E° = 2.38 V *vs.* SHE [27]. Hydrogen peroxide could also be produced (E° = 1.76 V *vs.* SHE [28]; however, as was stated above, it is not clear that this is has been observed in the experiments reported in this thesis. Peroxydisulfate (E° = 2.08V *vs.* SHE [29]) has also been postulated as a possible product at high current densities in sulphuric acid (see, for example, [23][30]) but its formation has been discounted [13][31][32][33], and the experiments described in this thesis were all carried out at significantly lower current densities (<40 mA cm^{-2}) than those routinely employed in experiments where $S_2O_8^{2-}$ is a postulated product.

For ozone evolution, $\delta\phi_a$ may be expressed as[26]:

$$\delta\phi_a = (E_a^{o\prime} - E_c^{o\prime}) + |\eta_a| \qquad (3.71)$$

where $E_a^{o\prime}$ and $E_c^{o\prime}$ are the anodic and cathodic potentials observed at zero current, corrected for the pH of 0.3. $E_a^{o\prime}$-$E_c^{o\prime}$ = 1.51 V; hence, under these conditions, the anodic overpotential for ozone $|\eta_a|$ = 0.79 V.

3.4 The effect of the gas separator

Fujishima's paper on Boron doped diamond (BDD) anodes generating ozone in single pass system [34][35] states that bubbles in the solution can lead to an overestimate of ozone efficiency (presumably due to scattering of light and hence apparent enhancement of the ozone peak intensity). To assess this, the experimental equipment shown below, fig. 3.32, was employed, with a glass gas separator immediately after the UV-Vis cell at the electrochemical cell outlet and a second UV-Vis cell after the separator. The separator had a volume of *ca.* 55.0 cm^3.

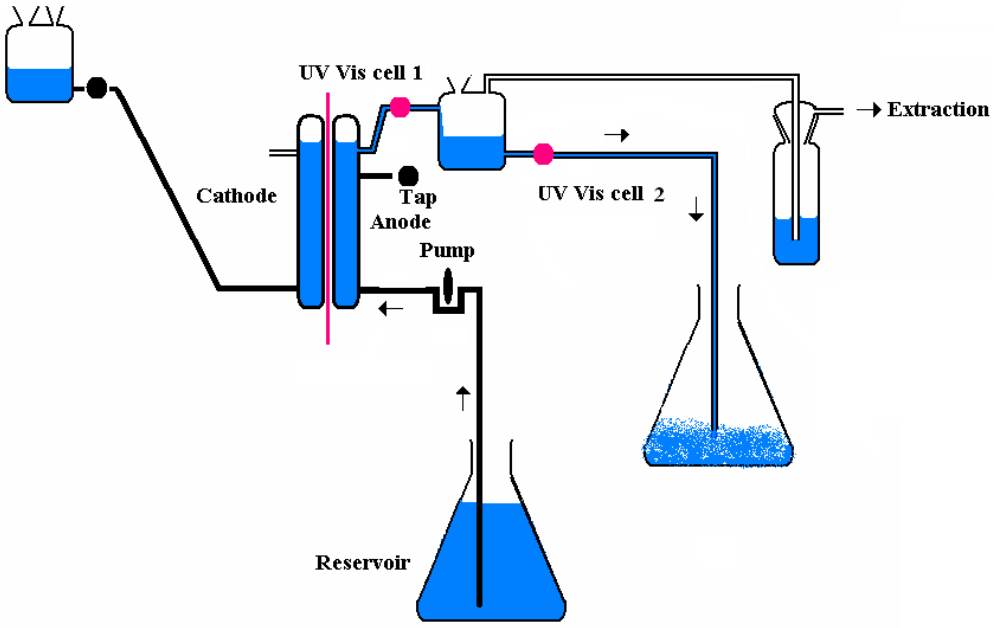

Figure 3.32 The experimental arrangement employed to assess the effect of the gas separator.

Plots of the current and dissolved ozone absorbances before and after the gas separator are shown in fig. 3.33 (a), and the corresponding current efficiencies in fig. 3.33 (b).

From fig. 3.33 (b) it can be seen that ozone gas was released from the separator amounting to a drop of *ca.* 20-25% in current efficiency, irrespective of flow rate (*i.e.* from 12 or 15% before gas separator at 30 cm^3 min^{-1} to 15 or 18% after the gas separator at flow rate 100 cm^3 min^{-1}). However, it was not clear whether this was due to bubbles enhancing the apparent ozone absorbance, or the real loss of ozone from solution to gas phase. In any case, in most measurements reported in this thesis, a separator was employed.

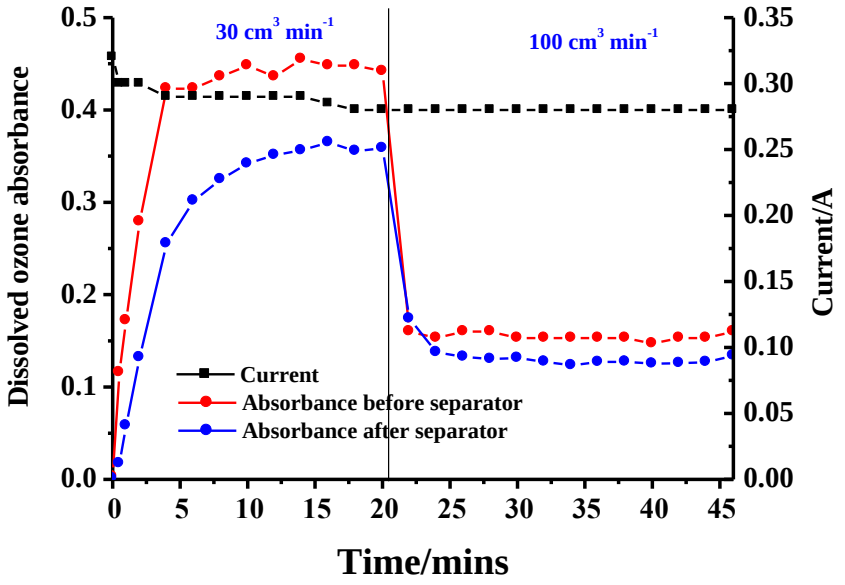

Figure 3.33 (a) Plot of current (■), dissolved ozone absorbance before the gas separator (cell 1) (●) and after the gas separator (cell 2) (●) in 0.5 M H_2SO_4 at anolyte flow rates 30 and 100 cm^3 min^{-1}, cell voltage 2.7 V of anode AJED2D (6.25 cm^2, 500:8:2).

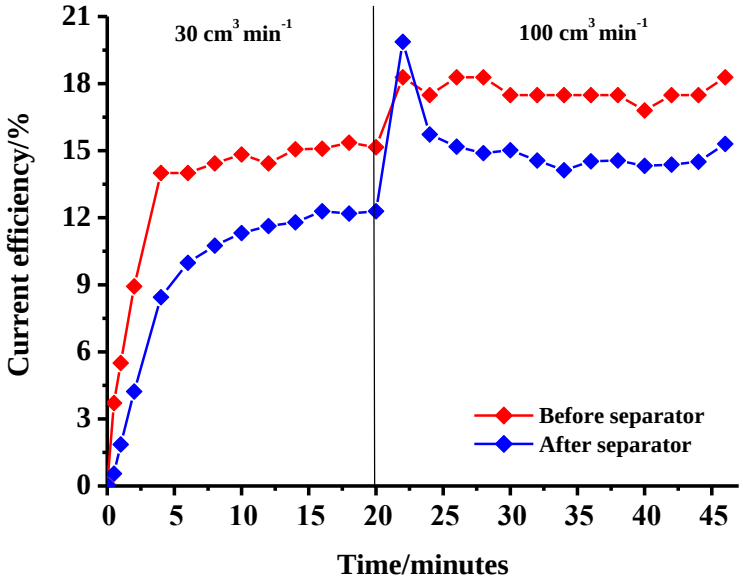

Figure 3.33 (b) Plots of the ozone current efficiencies from the experiments in figs. 3.32 and 3.33 (a); taken from the dissolved ozone absorbances before (♦) and after (♦) the gas separator.

3.5 Conclusions

The most appropriate extinction coefficient for the UV absorption band of ozone is 3000 $dm^3 mol^{-1} cm^{-1}$ for both gas phase ozone and dissolved ozone in aqueous solution.

The electrochemical generation of ozone in single pass and recycle systems were investigated, the latter aimed at generating high concentrations of gas phase ozone once the anolyte was saturated with ozone. In general, the current efficiency determined with recycle system was significantly less than that determined using single pass operation due to the displacement of key adsorbed intermediates by O_3. The possible rôle of the cell material on ozone production was rejected, although the presence of Nafion in direct contact with Ni/Sb-SnO_2 anodes was found to cause a switch in active sites from O_3 to O_2 evolution. Thus, the catalyst formulation was not suitable for the production of high concentrations of ozone in the gas phase by operation in recycle system.

Celgard 2400 is a promising alternative to Nafion in acid/acid cells for electrochemical ozone generation.

In single pass system, current efficiencies up to 50% have been obtained in acid electrolyte (calculated only from the ozone in solution), with efficiency increasing with anolyte flow rate due to more efficient entrainment of ozone.

3.6 References

1. Wang, Y. H., S. Cheng, K. Y. Chan and X. Y. Li, "Electrolytic Generation of Ozone on Antimony and Nickel-Doped Tin Oxide Electrodes," *Journal of the Electrochemical Society* 152(11): D197-D200 (2005).
2. Kilpatrick, M. L., C. C. Herrick and M. Kilpatrick, "The Decomposition of Ozone in Aqueous Solution," *Journal of the American Chemical Society* 78(9): 1784-1789 (1956).
3. Hoigné, J., and H. Bader, "The Role of Hydroxyl Radical Reactions in Ozonation Processes in Aqueous Solution," *Water Research* 10(5): 377-386 (1976).
4. Nemes, A., I. Fábián and G. Gordon, "Experimental Aspects of Mechanistic Studies on Aqueous Ozone Decomposition in Alkaline Solution," *Ozone Science and Engineering* 22: 287-304 (2000).
5. DeMore, W. B., and M. Patapoff, "Comparison of Ozone Determinations by Ultraviolet Photometry and Gas-Phase Titration," *Environmental Science and Technology* 10(9): 897-899 (1976).
6. Stucki, S., G. Theis, R. Kötz, H. Devantay and H. J. Christen, "In Situ Production of Ozone in Water Using a Membrel Electrolyzer," *Journal of the Electrochemical Society* 132(2): 367-371 (1985).
7. Summary Report, *WEV34ED PEM cell Summary*. October (2010).
8. Levanov, A. V., I. V. Kuskov, E. E. Antipenko and V. V. Lunin, "The Solubility of Ozone in Aqueous Solutions of Sulfuric, Phosphoric, and Perchloric Acids," *Russian Journal of Physical Chemistry A* 82(7): 1126-1131 (2008).
9. Seidel, A., *Kirk-Othmer Encyclopaedia of Chemical Technology*. 5th Editions, Vol. 17, New Jersey: John Wiley and Sons Inc., p. 768-822 (2006).
10. Rakness, K., G. Gordon, B. Langlais, W. Masschelein, N. Matsumoto, Y. Richard, C. M. Robson and I. Somiya, "Guideline for Measurement of Ozone Concentration in the Process Gas From and Ozone Generator," *Ozone Science and Engineering* 18: 209-229 (1996).
11. Christensen, P. A., W. F. Lin, H. Christensen, A. Imkum, J. M. Jin, G. Li and C.M. Dyson, "Room Temperature, Electrochemical Generation of Ozone with

50% Current Efficiency in 0.5 M Sulfuric Acid at Cell Voltages < 3V," *Ozone Science and Engineering* 31(4): 287-293 (2009).

12. 1st figure "summary of Ajchara's data from 11 April 2008-9 May 2008".
13. Stucki, S., H. Baumann, H. J. Christen and R. Kötz, "Performance of a Pressurized Electrochemical Ozone Generator," *Journal of Applied Electrochemistry* 17(4): 773-778 (1987).
14. Onda, K., T. Ohba, H. Kusunoki, S. Takezawa, D. Sunakawa and T. Araki, "Improving Characteristics of Ozone Water Production With Multilayer Electrodes and Operating Conditions in a Polymer Electrolyte Water Electrolysis Cell," *Journal of the Electrochemical Society* 152(10): D177-D183 (2005).
15. Kraft, A., M. Stadelmann, M. Wünsche and M. Blaschke, "Electrochemical Ozone Production Using Diamond Anodes and a Solid Polymer Electrolyte," *Electrochemistry Communication* 8: 883-886 (2006).
16. Cui, Y. H, Y. H. Wang, B. Wang, H. H. Zhou, K. Y. Chan and X. Y. Li, "Electrochemical Generation of Ozone in a Membrane Electrode Assembly Cell with Convective Flow," *Journal of The Electrochemical Society* 156(4): E75-E80 (2009).
17. Tatapudi, P., and J. M. Fenton, "Synthesis of Ozone in a Proton Exchange Membrane Electrochemical Reactor," *Journal of the Electrochemical Society* 140(12): 3527-3530 (1993).
18. Sehested, K., H. Corfitzen, J. Holcman and E. J. Hart, "On the Mechanism of the Decomposition of Acidic O_3 Solutions, Thermally or H_2O_2-Initiaed," *The Journal of Physical Chemistry A* 102(16): 2667-2672 (1998).
19. Sehested, K., H. Corfitzen, J. Holcman, C. H. Fischer and E. J. Hart, "The Primary Reaction in the Decomposition of Ozone in Acidic Aqueous Solutions," *Environmental Science and Technology* 25(9): 1589-1596 (1991).
20. Holt, R. B., C. K. McLane and O. Oldenberg, "Ultraviolet Adsorption Spectrum of Hydrogen Peroxide," *The Journal of Physical Chemistry* 16(3): 225-229 (1948).
21. Phibbs, M. K., and P. A. Giguère, "Hydrogen Peroxide and Its Analogues," *Canadian Journal of Chemistry* 29(6): 490-493 (1951).

22. Retrieved on 13th July 2009. www.celgrad.com/pdf/product datasheets/2400_Data_Sheet_2009_05_20033.pdf.
23. Michaud, P. A., M. Panizza, L. Ouattara, T. Diaco, G. Foti and Ch. Comninellis. "Electrochemical Oxidation of Water on Synthetic Boron-Doped Diamond Thin Film Anodes," *Journal of Applied Electrochemistry* 33: 151-154 (2003).
24. Franco, D. V., L. M. D. Silva, W. F. Jardim and J. F. C. Boodts, "Influence of the Electrolyte Composition on the Kinetics of the Oxygen Evolution Reaction and ozone Production processes," *Journal of the Brazilian Chemical Society* 17(4): 746-757 (2006).
25. Kim, J. and G. V. Korshin, "Examination of *in situ* Generation of Hydroxyl Radicals and Ozone in a Flow-through Electrochemical Reactor," *Ozone: Science and Engineering* 30: 113-119 (2008).
26. Hamman, C. H., A. Hamnett and W. Vielstich, *Electrochemistry*, 2nd Edition, Weinheim: Wiley-VCH Verlag GmbH and Co. KGaA, p.77-81 (2007).
27. Bard, A. J., R. Parsons and J. Jordan, *Standard Potentials in Aqueous Solution*. New York and Basel: International Union of Pure and Applied Chemistry, p. 63 (1985).
28. Bard, A. J., R. Parsons and J. Jordan, *Standard Potentials in Aqueous Solution*. New York and Basel: International Union of Pure and Applied Chemistry, p. 57 (1985).
29. Bard, A. J., R. Parsons and J. Jordan, *Standard Potentials in Aqueous Solution*. New York and Basel: International Union of Pure and Applied Chemistry, p. 107 (1985).
30. Seader, J. D. and C. W. Tobias, "Ozone by Electrolysis of Sulfuric Acid," *Industrial and Engineering Chemistry* 44(9): 2207-2211 (1952).
31. Da Silva, L. M., L. A. D. Faria and J. F. C. Boodts, "Green Processes for Environmental Application. Electrochemical Ozone Production" *Pure Applied Chemistry* 73(12): 1871-1884 (2001).
32. Da Silva, L. M., M. H. P. Santana and J. F. C. Boodts, "Electrochemistry and Green Chemical Processes: Electrochemical Ozone Production," *Quimica Nova* 26(6): 880-888 (2003).

33. Thanos, J. C. G., H. P. Fritz and D. Wabner, *Journal of Applied Electrochemistry* 14: 389 (1984).
34. Arihara, K., C. Terashima and A. Fujishima, "Electrochemical Production of High-Concentration Ozone-Water Using Freestanding Perforated Diamond Electrodes," *Journal of the Electrochemical Society* 154(4): E71-E75 (2007).
35. Arihara, K., C. Terashima and A. Fujishima, "Application of Freestanding Perforated Diamond Electrodes for Efficient Ozone-Water Production," *Electrochemical and Solid-State Letters* 9(8): D17-D20 (2006).

Chapter 4

The evolution of the anode synthesis

4. The evolution of the anode synthesis

Undoped SnO_2 should be an insulator, and hence its resistivity of *ca*. 7.25 x 10^{-3} Ω cm is taken as evidence for a defect structure incorporating *e.g*. O vacancies or adventitious donors [1]. SnO_2 anodes are usually doped with Sb to improve the conductivity of the electrodes (resistivities *ca*. 10^{-5}-10^{-4} Ω cm [1][2]), with the Sb (as Sb^V) replacing Sn^{IV} due to their similar ionic radii [2]; at higher dopant levels, however, Sb^{III} centres are incorporated [3][4] which act as trap sites for the e^- generated by Sb^V causing a rise in resistivity [2].

As was stated in Chapter 1, the project was inspired by the work of K. Y. Chan in Hong Kong University, and this will be described first.

4.1 The work of K. Y. Chan

Chan employed titanium substrates in the form of meshes and foils due to the good corrosion resistance and reasonable cost of titanium [5][6]. In the first paper [5], Chan incorrectly reported that Sb-doped SnO_2 was active for electrochemical ozone generation. However, it was reported in a latter paper that the activity of the original Sb-doped SnO_2 electrodes was, in fact, due to trace nickel contamination [6] probably from a nickel-plated spatula [7]. Hence, the details of the anode synthesis will be taken predominantly from the second paper. However, it should be noted that Foller and Tobias [8] reported ozone evolution from an Sb-doped SnO_2 anode in 5 M H_2SO_4 at 0 ºC with a short-lived current efficiency of *ca.* 4%. The authors also reported that the SnO_2 coating completely dissolved within a short (unspecified) time.

Chan employed 0.8 cm x 0.8 cm x 0.05 cm Ti foil spot-welded with a 1.0 mm diameter Ti wire. The foil was etched in 10% boiling oxalic acid solution for 1 hour, and then rinsed with deionized water and dried. The foil was dipcoated from a mixture of $SbCl_3$, $SnCl_4.5H_2O$ and $NiCl_2.6H_2O$ in ethanol, dried at 100 ºC for 10 minutes and then calcined at 520 ºC for 10 minutes. After the eighth coating, the electrode was dried and then calcined at 520 ºC for 1 hour [5][6].

During the early stages of the collaboration between Hong Kong and Newcastle, the synthesis procedure changed quickly in two important respects: the Ti foil was replaced by mesh (to facilitate application in Membrane Electrode Assembly (MEA) based water-air cells [9]) and with the introduction of an Electro Deposited Inter Layer (EDIL) to protect the Ti substrate [10][11]. A summary of the general procedure for synthesising the ozone anodes is given in fig. 4.1 and 4.2. The mechanism by which Ni/Sb-SnO_2 anodes produce ozone has not been investigated to date [5][6].

4.2 Summary of catalyst development

The most significant changes in the synthesis procedure have been in the electrodeposition and catalyst coating steps; these are summarised in table 4.1 and given in more detail in tables 4.2 and 4.3. The anodes are numbered sequentially in series, those involving electrodeposition having electrodeposition before the number. Individual electrodes within a series are identified by letters: A, B, C or a, b, c etc.

The various steps in the synthesis procedure are discussed in more detail in the section below.

A very large number of experiments were carried out during the period of my research project (described in over 80 detailed weekly reports); space does not thus allow an exhaustive discussion of all the data concerning the catalyst development. Hence, this section commences with a commentary on the development of the synthetic procedure summarised in tables 4.1-4.3. Subsequent sections then highlight key aspects of the various steps in the synthesis.

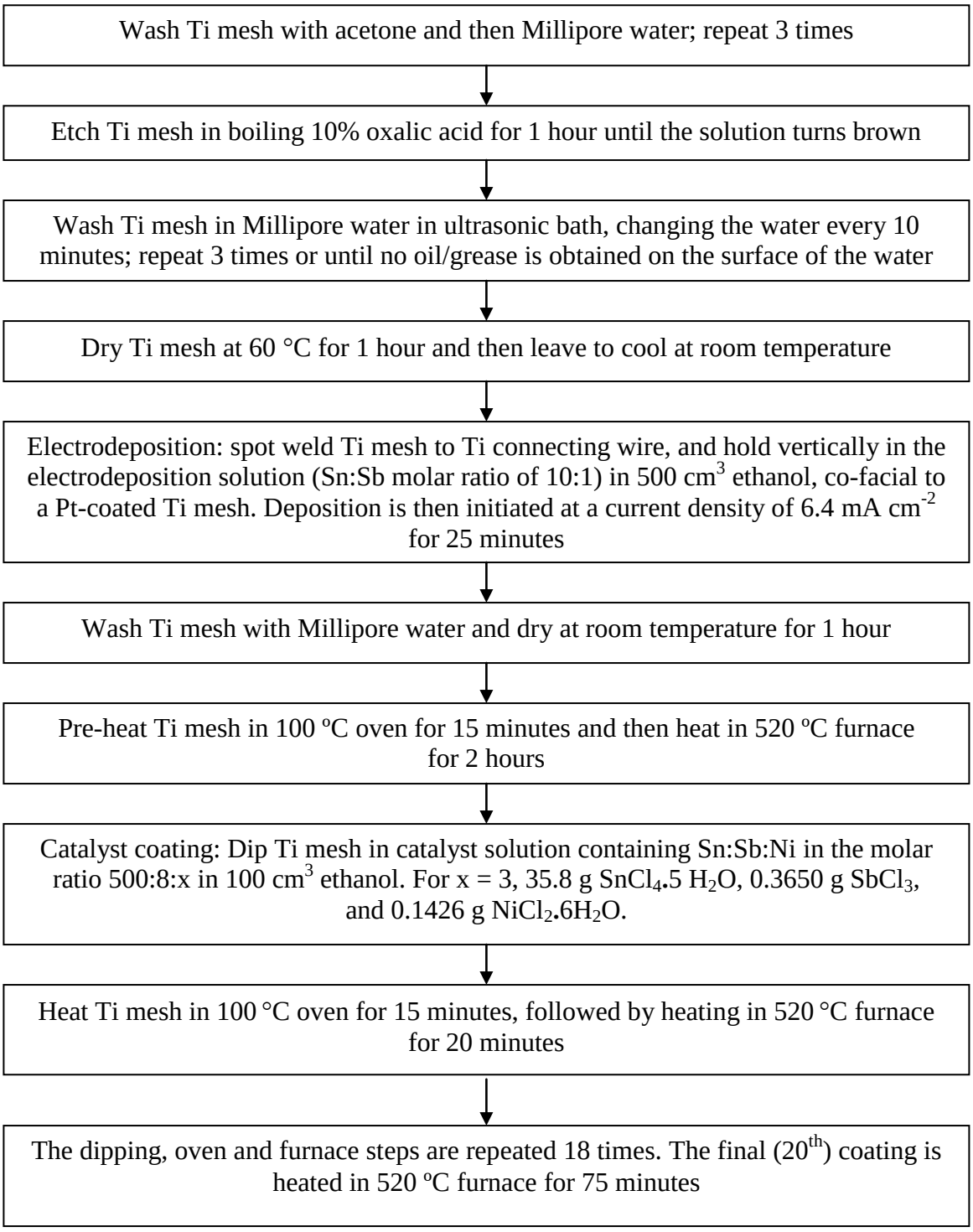

Figure 4.1 Summary of the basic steps in the ozone anode synthesis procedure.

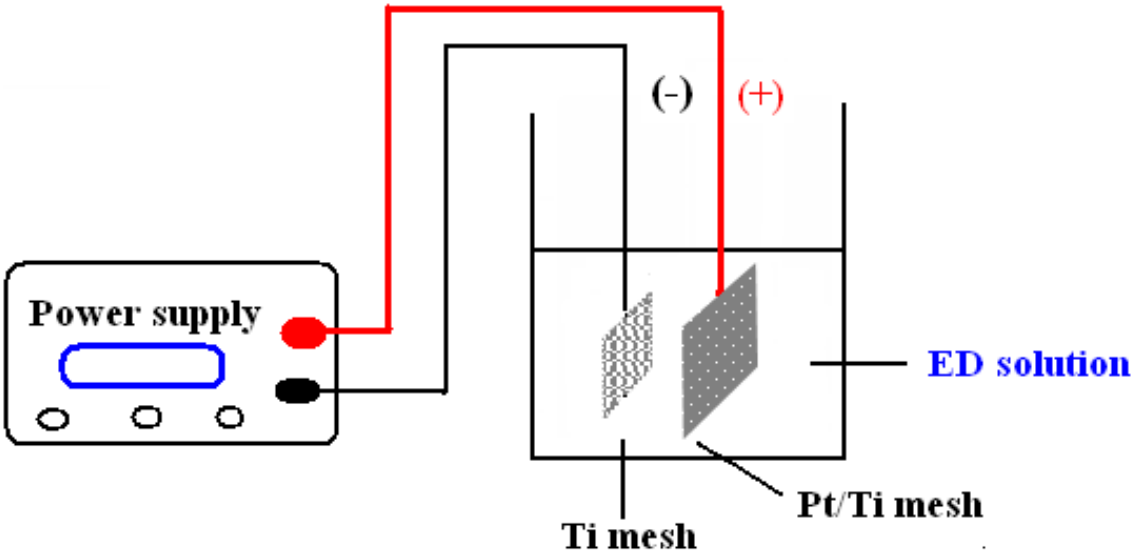

(a)

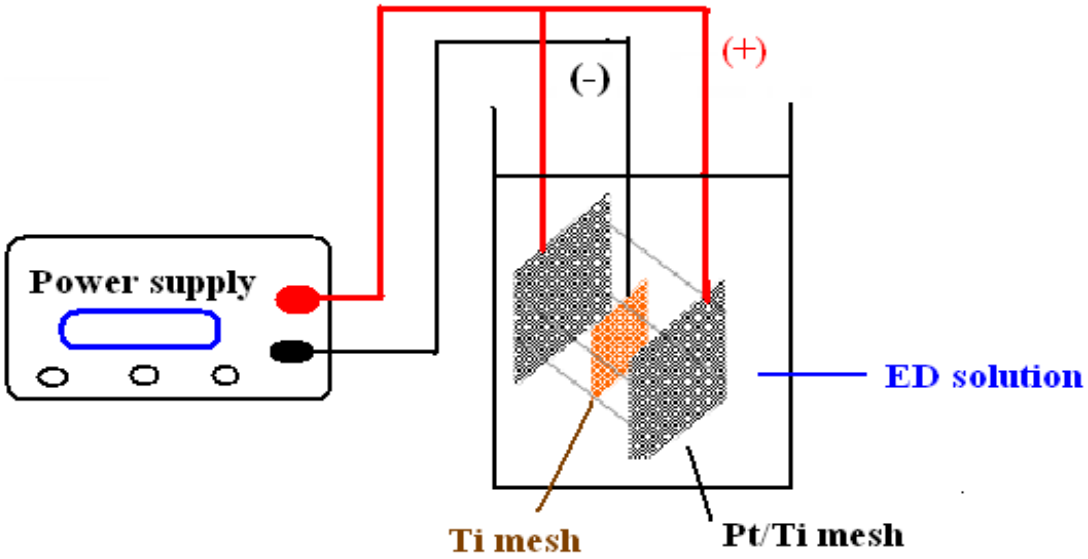

(b)

Figure 4.2 (a) Cell configuration 1 and (b) Cell configuration 2 employed in the electrodeposition step.

Anode series	Size /cm^2	ED method and configuration (see table 4.2)	Post-heating	Catalyst solution, Sn:Sb:Ni:Au ([HCl]/vv)	Catalyst coating method (see table 4.1)	Coats	Pyrolysis
AJED1	6.25	NED	-	500:8:1 [3%]	CC1	20	100 °C (15 mins) and 520 °C (20 mins)
		1 and 1	100 °C (15 mins) and 520 °C (2 hrs)				
AJED2	6.25	1 and 1	100 °C (15 mins) and 520 °C (2 hrs)	500:8:1 [3%] 500:8:2 [3%] 500:8:3 [3%] 500:8:4 [3%]	CC1	20	100 °C (15 mins) and 520 °C (20 mins)
AJED3	6.25	1 and 1	100 °C (15 mins) and 520 °C (2 hrs)	500:8:0.2, 2.5, 5.0, 10.0 [3%]	CC1	20	100 °C (15 mins) and 520 °C (20 mins)
AJED4	6.25	2 and 1	100 °C (15 mins) and 520 °C (2 hrs)	500:8:2 [3%] 500:8:3 [3%] 500:8:4 [3%]	CC2	20	100 °C (15 mins) and 520 °C (20 mins)
AJED5	6.25	3 and 1	100 °C (15 mins) and 520 °C (2 hrs)	500:8:2, 3, 4 [3%]	CC3	20	100 °C (15 mins) and 520 °C (20 mins)
AJED6	4.00	NED	-	500:8:3 [3%]	CC3	20	100 °C (15 mins) and 520 °C (20 mins)
AJED7	4.00	NED	-	500:8:3 [3%]	CC3	20	100 °C (15 mins) and 520 °C (20 mins)
AJED8	4.00	NED	-	500:8:3 [3%]	CC3	20	100 °C (15 mins) and 520 °C (20 mins)
AJED9	6.25	1 and 1	100 °C (15 mins) and 520 °C (2 hrs)	500:8:1 [5%] 500:8:1	CC4	20	100 °C (15 mins) and 520 °C (20 mins)
AJED10	6.25	NED	-	500:8:1 [5%]	CC4	20	100 °C (15 mins) and 520 °C (20 mins)
		1 and 1	100 °C (15 mins) and 520 °C (2 hrs)				
AJED11	6.25	1 and 1	100 °C (15 mins) and 520 °C (2 hrs)	500:8:3 [5%]	CC4	20	100 °C (15 mins) and 520 °C (20 mins)

Anode series	Size /cm^2	ED method and configuration (see table 4.2)	Post-heating	Catalyst solution, Sn:Sb:Ni:Au ([HCl]/vv)	Catalyst coating method (see table 4.1)	Coats	Pyrolysis
AJED12	6.25	1 and 1	100 °C (15 mins) and (1)480 °C (20 mins) (2)480 °C (40 mins) (3)520 °C (20 mins) (4)520 °C (40 mins)	500:8:1 [5%]	CC4	20	100 °C (15 mins) and (1)480 °C (20 mins) (2)480 °C (40 mins) (3)520 °C (20 mins) (4)520 °C (40 mins)
AJED13	6.25	1 and 1	100 °C (15 mins) and 520 °C (2 hrs)	500:8:1 [5%]	CC4	(1) 10 (2) 20	100 °C (15 mins) and (1) 460 °C (10 mins) (2) 460 °C (20 mins) (3) 520 °C (10 mins) (4) 520 °C (20 mins)
AJED14	35.00	NED	-	500:8:3 [5%] 500:8:3:3 [5%]	CC5	7	100 °C (15 mins) and ramp temp 460 °C at dwell every 20 mins (2 hrs)
AJED15	35.00	NED 4 and 1	100 °C (15 mins) and 520 °C (2 hrs)	500:8:1:1.5 [7.5%] 500:8:1:3 [7.5%] 500:8:3:1.5 [7.5%] 500:8:3:3 [7.5%]	CC6	20	100 °C (15 mins) and 520 °C (20 mins)
AJED16	35.00	4 and 1	100 °C (15 mins) and 520 °C (2 hrs)	500:8:1 [7.5%]	CC6-CC8	20	100 °C (15 mins) and 520 °C (20 mins)
AJED17	35.00	NED 4 and 1	100 °C (15 mins) and 520 °C (2 hrs)	-	-	-	-
AJED18	42.00	5 and 1	100 °C (5 mins) and 390 °C (1 hour)	500:8:1	CC9	14	100 °C (5 mins) and (1) 390 °C (10 mins) (2) 460 °C (10 mins) (3) 520 °C (10 mins)
AJED19	6.25	7-10 and 1+2	100 °C (15 mins) and 520 °C (2 hrs)	500:8:3 [3%]	CC10	20	100 °C (15 mins) and 520 °C (20 mins)

Anode series	Size /cm^2	ED method and configuration (see table 4.2)	Post-heating	Catalyst solution, Sn:Sb:Ni:Au ([HCl]/vv)	Catalyst coating method (see table 4.1)	Coats	Pyrolysis
AJED20	35.0	6 and 1	100 °C (5 mins) and 390 °C (1 hour)	500:8:3:1.5 [7.5%]	CC11	20	100 °C (5 mins) and 460 °C (10 mins)
AJED21	6.25	7 and 1, 11-13 and 2	(1) 100 °C (15 mins) and 520 °C (2 hrs) (2) 100 °C (5 mins) and 390 °C (1 hour)	-	NCC	-	-
AJED22	6.25	12 and 2	100 °C (5 mins) and 390 °C (1 hour)	500:8:3 [3%]	CC12	15, 20	100 °C (5 mins) and 460 °C (10 mins)
AJED23	0.64	14-15 and 2	100 °C (5 mins) a nd 390 °C (1 hour)	-	NCC	-	-
AJED24	6.25	7 and 1, 12, 16 and 2	100 °C (5 mins) and 390 °C (1 hour)	-	NCC	-	-
AJED25	6.25	17-20 and 1	100 °C (15 mins) and 520 °C (2 hrs)	-	NCC	-	-
AJED25E	6.25	20 and 1	100 °C (15 mins) and 520 °C (2 hrs)	500:8:3	CC12	20	100 °C (5 mins) and 460 °C (10 mins)
AJED26	0.64	NED	-	500:8:0 500:8:3 500:8:3:0.1	CC12	20	100 °C (5 mins) and 460 °C (10 mins)
		14 and 2	100 °C (5 mins) and 390 °C (1 hour)				
AJED27	6.25	20 and 1	100 °C (15 mins) and 520 °C (2 hrs)	500:8:3 500:8:3:0.1 500:8:3:0.3 500:8:3:1.5	CC12	20	100 °C (5 mins) and 460 °C (10 mins)
	0.64	21 and 1					

NED = No electrodeposition step

Table 4.1 Summary of the evolution of the overall anode synthesis procedure.

ED Method	Composition of ED solution	Descriptions	Anodes AJED Series
ED1	0.5 M Sn : 0.05 M Sb (10:1), HCl 5 cm^3 in 500 cm^3 ethanol	Ti mesh is connected with connecting wire, co-facial to a 6.0 x 4.0 cm Pt-coated Ti mesh. Deposition is fixed at a current density 6.4 mA cm^{-2} (0.040A/6.25cm^2) for 25 minutes. Wash Ti mesh with DI water and dry at room temperature 1 hour. Pre-heat Ti mesh in 100 ºC oven for 15 minutes and then heat in 520 ºC furnace for 2 hours.	1, 2, 3, 9, 10, 11, 13, 12 (480 °C, also)
ED2	0.5 M Sn : 0.05 M Sb (10:1), HCl 5 cm^3 in 500 cm^3 ethanol	Ti mesh is connected with connecting wire, co-facial to a 6.0 x 4.0 cm Pt-coated Ti mesh. Deposition is fixed at current density of 6.4 mA cm^{-2} (0.040A/6.25cm^2) for 24 minutes by 12 minutes for side A and turn on 12 minutes for side B. Wash Ti mesh with DI water and dry at room temperature 1 hour. Pre-heat Ti mesh in 100 ºC oven for 15 minutes and then heat in 520 ºC furnace for 2 hours.	4
ED3	0.5 M Sn : 0.05 M Sb (10:1), HCl 5 cm^3 in 500 cm^3 ethanol	Ti mesh is connected with connecting wire, co-facial to a 6.0 x 4.0 cm Pt-coated Ti mesh. Deposition is fixed at current density of 6.4 mA cm^{-2} (0.040A/6.25cm^2) for 48 minutes by 24 minutes for side A for 2 times and turn on 24 minutes for side B for 2 times. Wash Ti mesh with DI water and dry at room temperature 1 hour. Pre-heat Ti mesh in 100 ºC oven for 15 minutes and then heat in 520 ºC furnace for 2 hours.	5
ED4	0.5 M Sn : 0.05 M Sb (10:1), HCl 7.5 cm^3 in 500 cm^3 ethanol	Ti mesh is connected with connecting wire, co-facial to a 6.0 x 4.0 cm Pt-coated Ti mesh. Deposition is fixed at current density of 6.4 mA cm^{-2} (0.224A/35.0cm^2) for 25 minutes by 12.5 minutes for side A and turn on 12.5 minutes for side B. Wash Ti mesh with DI water and dry at room temperature 1 hour. Pre-heat Ti mesh in 100 ºC oven for 15 minutes and then heat in 520 ºC furnace for 2 hours.	15, 16, 17
ED5	1.25 M Sn : 0.05 M Sb (25:1), no HCl in 500 cm^3 ethanol	Ti mesh is connected with connecting wire, co-facial to a 6.0 x 4.0 cm Pt-coated Ti mesh. Deposition is fixed at current density of 4.8 mA cm^{-2} (0.202/42.0cm^2) for 1 minute, followed by current density at 2.4 mA cm^{-2} (0.101/42.0cm^2) for 20 minutes. Wash Ti mesh with DI water and dry at room temperature 1 hour. Pre-heat Ti mesh in 100 ºC oven 5 minutes and then heat in 390 ºC furnace 1 hours.	18
ED6	1.25 M Sn : 0.05 M Sb (25:1), HCl 10 cm^3in 1000 cm^3 ethanol	Ti mesh is connected with connecting wire, co-facial to a 6.0 x 4.0 cm Pt-coated Ti mesh. Deposition is fixed at current density of 3.5 mA cm^{-2} (0.147/35.0 cm^2) for 1 minutes followed by current density at 17.2 mA cm^{-2} (0.073A/35.0 cm^2) for 20 minutes. Wash Ti mesh with DI water and dry at room temperature 1 hour. Pre-heat Ti mesh in 100 ºC oven 5 minutes and then heat in 390 ºC furnace 1 hours.	20

ED Method	Composition of ED solution	Descriptions	Anodes AJED Series
ED7	0.5 M Sn : 0.05 M Sb(10:1), HCl 5 cm^3 in 500 cm^3 ethanol	Ti mesh is connected with connecting wire, co-facial to a 6.0 x 6.0 cm Pt-coated Ti mesh. Deposition is fixed at a current density 40 mA cm^{-2} (0.250A/6.25cm^2) for 25 minutes. Wash Ti mesh with DI water and dry at room temperature 1 hour. Pre-heat Ti mesh in 100 ºC oven for 15 minutes and then heat in 520 ºC furnace for 2 hours.	19A-I, 21A and 21B, 24A and B (100 °C 5 mins and 390 °C 10 mins)
ED8	0.5 M Sn : 0.1 M Sb (10:2), HCl 5 cm^3 in 500 cm^3 ethanol	Ti mesh is connected with connecting wire, co-facial to a 6.0 x 6.0 cm Pt-coated Ti mesh. Deposition is fixed at a current density 40 mA cm^{-2} (0.250A/6.25cm^2) for 25 minutes. Wash Ti mesh with DI water and dry at room temperature 1 hour. Pre-heat Ti mesh in 100 ºC oven for 15 minutes and then heat in 520 ºC furnace for 2 hours.	19a-m, 19M and N (0.64 cm^2)
ED9	0.5 M Sn : 0.1 M Sb (10:2), HCl 5 cm^3 in 500 cm^3 ethanol	Ti mesh is connected with connecting wire, co-facial to a 6.0 x 6.0 cm Pt-coated Ti mesh. Deposition is fixed at current density of 2.5 mA cm^{-2} (0.016A/6.25cm^2) for 1 minute followed by current density at 1.25 mA cm^{-2} (0.008A/6.25 cm^2) for 20 minutes. Wash Ti mesh with DI water and dry at room temperature 1 hour. Pre-heat Ti mesh in 100 ºC oven for 15 minutes and then heat in 520 ºC furnace for 2 hours.	19J-L
ED10	0.5 M Sn : 0.1 M Sb (10:2), HCl 5 cm^3 in 500 cm^3 ethanol	Ti mesh is connected with double anode cell assembly (two 5.0 x 5.0 cm Pt-coated Ti meshes). Deposition is fixed at current density of 20 mA cm^{-2} (0.125A/6.25cm^2) for 25 minutes. Wash Ti mesh with DI water and dry at room temperature 1 hour. Pre-heat Ti mesh in 100 ºC oven for 15 minutes and then heat in 520 ºC furnace for 2 hours.	19i-l
ED11	0.5 M Sn : 0.1 M Sb (10:2), HCl 5 cm^3 in 500 cm^3 ethanol	Ti mesh is connected with double anode cell assembly (two 5.0 x 5.0 cm Pt-coated Ti meshes). Deposition is fixed at current density of 2.5 mA cm^{-2} (0.016A/6.25cm^2) for 1 minute followed by current density at 1.25 mA cm^{-2} (0.008A/6.25 cm^2) for 20 minutes. Wash Ti mesh with DI water and dry at room temperature 1 hour. Pre-heat Ti mesh in 100 ºC oven for 15 minutes and then heat in 520 ºC furnace for 2 hours.	21C and D
ED12	0.5 M Sn : 0.1 M Sb (10:2), HCl 10 cm^3 in 1000 cm^3 ethanol	Ti mesh is connected with double anode cell assembly (two 5.0 x 5.0 cm Pt-coated Ti meshes). Deposition is fixed at current density of 2.5 mA cm^{-2} (0.016A/6.25cm^2) for 1 minute followed by current density at 1.25 mA cm^{-2} (0.008A/6.25 cm^2) for 20 minutes*. Wash Ti mesh with DI water and dry at room temperature 1 hour. Pre-heat Ti mesh in 100 ºC oven 5 minutes and then heat in 390 ºC furnace 1 hours.	22, 21E-J (*5, 10, 15 minutes, also), 24C-H (*5, 10, 15 minutes, also)

ED Method	Composition of ED solution	Descriptions	Anodes AJED Series
ED13	No Sn : 0.1 M Sb (0:2), HCl 5 cm^3 in 500 cm^3 ethanol	Ti mesh is connected with double anode cell assembly (two 5.0 x 5.0 cm Pt-coated Ti meshes). Deposition is fixed at current density of 2.5 mA cm^{-2} (0.016A/6.25cm^2) for 1 minute followed by current density at 1.25 mA cm^{-2} (0.008A/6.25 cm^2) for 20 minutes* in electrodeposition solution of 500 cm^3 Sn:Sb;0:2 (HCl 5 cm^3). Wash Ti mesh with DI water and dry at room temperature 1 hour. Pre-heat Ti mesh in 100 ºC oven 5 minutes and then heat in 390 ºC furnace 1 hours.	21K-R (*5, 10, 15 minutes, also)
ED14	0.5 M Sn : 0.1 M Sb (10:2), HCl 10 cm^3 in 1000 cm^3 ethanol	Ti mesh is connected with double anode cell assembly (two 3.0 x 3.0 cm Pt-coated Ti meshes). Deposition is fixed at a current density 5.0 mA cm^{-2} (0.003A/0.64 cm^2) for 1 minute followed by current density at 2.5 mA cm^{-2} (0.002A/0.64cm^2) for 20 minutes*. Wash Ti mesh with DI water and dry at room temperature 1 hour. Pre-heat Ti mesh in 100 ºC oven for 5 minutes and then heat in 390 ºC furnace for 1 hours.	23A-G (*5, 10, 15 minutes, also), 26
ED15	No Sn : 0.1 M Sb (0:2), HCl 10 cm^3 in 1000 cm^3 ethanol	Ti mesh is connected with double anode cell assembly (two 3.0 x 3.0 cm Pt-coated Ti meshes). Deposition is fixed at a current density 5.0 mA cm^{-2} (0.003A/0.64 cm^2) for 1 minute followed by current density at 2.5 mA cm^{-2} (0.002A/0.64cm^2) for 20 minutes*. Wash Ti mesh with DI water and dry at room temperature 1 hour. Pre-heat Ti mesh in 100 ºC oven for 5 minutes and then heat in 390 ºC furnace for 1 hours.	23H-N (*5, 10, 15 minutes, also)
ED16	0.5 M Sn : 0.1 M Sb (10:2), HCl 10 cm^3 in 1000 cm^3 ethanol	Ti mesh is connected with double anode cell assembly (two 5.0 x 5.0 cm Pt-coated Ti meshes). Deposition is fixed at current density of 2.5 mA cm^{-2} (0.016A/6.25cm^2) for 20 minutes. Wash Ti mesh with DI water and dry at room temperature 1 hour. Pre-heat Ti mesh in 100 ºC oven 5 minutes and then heat in 390 ºC furnace 1 hours.	24I
ED17	0.5 M Sn : 0.05 M Sb (10:1), HCl 10 cm^3 in 1000 cm^3 ethanol	Ti mesh is connected with connecting wire, co-facial to a 2.5 x 2.5 cm Pt-coated Ti mesh. Deposition is fixed at a current density 6.4 mA cm^{-2} (0.040A/6.25cm^2) for 25 minutes. Wash Ti mesh with DI water and dry at room temperature 1 hour. Pre-heat Ti mesh in 100 ºC oven for 15 minutes and then heat in 520 ºC furnace for 2 hours.	25A
ED18	No Sn : 0.1 M Sb (0:2), HCl 10 cm^3 in 1000 cm^3 ethanol	Ti mesh is connected with connecting wire, co-facial to a 2.5 x 2.5 cm Pt-coated Ti mesh. Deposition is fixed at a current density 6.4 mA cm^{-2} (0.040A/6.25cm^2) for 25 minutes. Wash Ti mesh with DI water and dry at room temperature 1 hour. Pre-heat Ti mesh in 100 ºC oven for 15 minutes and then heat in 520 ºC for 2 hrs.	25B

ED Method	Composition of ED solution	Descriptions	Anodes AJED Series
ED19	0.5 M Sn : 0.1 M Sb (10:2), HCl 10 cm^3 in 1000 cm^3 ethanol	Ti mesh is connected with connecting wire, co-facial to a 6.0 x 6.0 cm Pt-coated Ti mesh. Deposition is fixed at a current density 6.4 mA cm^{-2} (0.040A/6.25cm^2) for 25 minutes. Wash Ti mesh with DI water and dry at room temperature 1 hour. Pre-heat Ti mesh in 100 ºC oven for 15 minutes and then heat in 520 ºC furnace for 2 hours.	25C
ED20	0.5 M Sn : 0.1 M Sb (10:2), HCl 10 cm^3 in 1000 cm^3 ethanol	Ti mesh is connected with connecting wire, co-facial to a 2.5 x 2.5 cm Pt-coated Ti mesh. Deposition is fixed at a current density 6.4 mA cm^{-2} (0.040A/6.25cm^2) for 25 minutes*. Wash Ti mesh with DI water and dry at room temperature 1 hour. Pre-heat Ti mesh in 100 ºC oven for 15 minutes and then heat in 520 ºC furnace for 2 hours.	25D-H (*5, 10, 15, 25 minutes, also), 27A-L
ED21	0.5 M Sn : 0.1 M Sb (10:2), HCl 10 cm^3 in 1000 cm^3 ethanol	Ti mesh is connected with connecting wire, co-facial to a 1.0 x 1.0 cm Pt-coated Ti mesh. Deposition is fixed at a current density 6.4 mA cm^{-2} (0.006A/1.0cm^2) for 25 minutes in electrodeposition solution of 1000 cm^3 Sn:Sb;10:2 (HCl 10 cm^3). Wash Ti mesh with DI water and dry at room temperature 1 hour. Pre-heat Ti mesh in 100 ºC oven for 15 minutes and then heat in 520 ºC furnace for 2 hours.	27M-P
NED	-	No electrodeposition	1, 6, 7, 8, 14 (35 cm^2)

Table 4.2 The evolution of the electrodeposition step in the anode synthesis.

Catalyst Coating Method	Composition of catalyst solution, Sn:Sb:Ni:Au, [[HCl]/vv] in 100cm^3 ethanol (series)*	Descriptions	Anodes AJED series*
CC1	500:8:1:0 [3%] (1), (2) and (3) 500:8:2:0 [3%] (2) 500:8:3:0 [3%] (2) 500:8:4:0 [3%] (2)	Ti mesh is dipped into the coating solution for 1 minute and stirred 1 minute before withdrawing. Wait for all bubbles to pop by holding to dry around 1 minute. Heat Ti mesh in 100 °C oven for 15 minutes, follow by heating in 520 °C furnace for 20 minutes. The dipping, oven and furnace steps were repeated 18 times. The final (20th) coating is heated in 520 ºC furnace for 75 minutes.	1, 2, 3
CC2	500:8:2:0 [3%], 500:8:3:0 [3%], 500:8:4:0 [3%],	Ti mesh is coated with coating solution by a small wood paintbrush both sides for many dips. Wait for all bubbles to pop by holding to dry around 1 minute. Heat Ti mesh in 100 °C oven for 15 minutes, follow by heating in 520 °C furnace for 20 minutes. The dipping, oven and furnace steps were repeated 18 times. The final (20th) coating is heated in 520 ºC furnace for 75 minutes.	4
CC3	500:8:2:0 [3%] (5) 500:8:3:0 [3%] (6), (7) and (8)	Ti mesh is coated with coating solution by a small wood paintbrush; three strokes per side. One 'dip' into the coating solution per side. Wait for all bubbles to pop by holding to dry around 1 minute. Heat Ti mesh in 100 °C oven for 15 minutes, follow by heating in 520 °C furnace for 20 minutes. The dipping, oven and furnace steps are repeated 18 times. The final (20th) coating is heated in 520 ºC furnace for 75 minutes.	5, 6, 7, 8
CC4	500:8:1:0 (9) 500:8:1:0 [5%] (9), (10), (11), (12E-F) and (13)	Ti mesh is dipped into the coating solution for 40 seconds and stirred 1 minute before withdrawing. Wait for all bubbles to pop by holding to dry around 1 minute. Heat Ti mesh in 100 °C oven for 15 minutes, follow by heating in 520 °C furnace for 20 minutes. The dipping, oven and furnace steps are repeated 18 times. The final (20th) coating is heated in 520 ºC furnace for 75 minutes.	9, 10, 11, 12E-F, 13
CC5	500:8:3:0 [5%], 500:8:3:3 [5%]	Ti mesh is dipped into the coating solution for 40 seconds without stirring or shaking. Wait for all bubbles to pop by holding to dry around 1 minute. Heat Ti mesh in 100 °C oven for 15 minutes, follow by heating in 520 °C furnace 20 minutes. The dipping, oven and furnace steps are repeated 6 times. The final (7th) coating is set ramp temperature in 460 °C furnace at rate 8 °C/minute and dwell time every 20 minutes until 2 hours.	14

Catalyst Coating Method	Composition of catalyst solution, Sn:Sb:Ni:Au, [[HCl]/vv] in 100 cm^3 ethanol (series)*	Descriptions	Anodes AJED series*
CC6	500:8:1:1.5 [7.5%] (15) and (17) 500:8:1:3 [7.5%] (15) 500:8:3:1.5 [7.5%] (15) 500:8:3:3 [7.5%] (15) 500:8:1:0 [7.5%] (16)	Ti mesh is dipped into the coating solution for 40 seconds and withdraw at an angle, hold with mesh at an angle to allow excess solution to flow back over mesh. Wait for all bubbles to pop by pegging out to dry on line for 2-3 minutes. Heat Ti mesh in 100 °C oven for 15 minutes, follow by heating in 520 °C furnace 20 minutes. The dipping, oven and furnace steps are repeated 18 times. The final (20^{th}) coating is heated in 520 ºC furnace for 75 minutes.	15, 16, 17
CC7	500:8:1:0 [7.5%]	Ti mesh is dipped into the coating solution for 40 seconds and withdraw at an angle, hold with mesh at an angle to allow excess solution to flow back over mesh. Wait for all bubbles to pop by hair dryer to dry for 2-3 minutes. Heat Ti mesh in 100 ^{0}C oven for 15 minutes, follow by heating in 520 ^{0}C furnace 20 minutes. The dipping, oven and furnace steps are repeated 18 times. The final (20^{th}) coating is heated in 520 ºC furnace for 75 minutes.	16
CC8	500:8:1:0 [7.5%]	Ti mesh is dipped into the coating solution for 40 seconds and withdraw at an angle, hold with mesh at an angle to allow excess solution to flow back over mesh. Wait for all bubbles to pop by blowing by mouth to dry for 2-3 minutes. Heat Ti mesh in 100 °C oven for 15 minutes, follow by heating in 520 °C furnace 20 minutes. The dipping, oven and furnace steps are repeated 18 times. The final (20^{th}) coating is heated in 520 ºC furnace for 75 minutes.	16
CC9	500:8:1:0	Ti mesh is dipped into the coating solution for 40 seconds and withdraw at an angle, hold with mesh at an angle to allow excess solution to flow back over mesh. Wait for all bubbles to pop by pegging out to dry on line for 2-3 minutes. Heat Ti mesh in 100 °C oven for 5 minutes, follow by heating in 460 °C furnace for 10 minutes. The dipping, oven and furnace steps are repeated 12 times. The final (14^{th}) coating is heated in 390, 460 and 520 ºC for 1 hour.	18
CC10	500:8:3:0 [3%]	Ti mesh is dipped into the coating solution for 40 seconds and withdraw at an angle, hold with mesh at an angle to allow excess solution to flow back over mesh. Wait for all bubbles to pop by holding around 2-3 minute. Heat Ti mesh in 100 °C oven for 15 minutes, follow by heating in 520 ^{0}C furnace for 20 minutes. The dipping, oven and furnace steps are repeated 18 times. The final (20^{th}) coating is heated in 520 ºC furnace for 75 minutes.	19

Catalyst Coating Method	Composition of catalyst solution, Sn:Sb:Ni:Au, [[HCl]/vv] in 100 cm^3 ethanol (series)*	Descriptions	Anodes AJED series*
CC11	500:8:3:1.5 [7.5%]	Ti mesh is dipped into the coating solution for 40 seconds and withdraw at an angle, hold with mesh at an angle to allow excess solution to flow back over mesh. Wait for all bubbles to pop by holding around 2-3 minutes. Heat Ti mesh in 100 °C oven for 5 minutes, follow by heating in 460 °C furnace for 10 minutes. The dipping, oven and furnace steps are repeated 18 times. The final (20^{th}) coating is heated in 460 ºC furnace for 1 hour.	20
CC12	500:8:3:0 [3%] (22) 500:8:3:0 (25E) 500:8:0:0 (26), (27) 500:8:3:0 (26), (27) 500:8:3:0.1 (26), (27) 500:8:3:0.3 (26), (27) 500:8:3:1.5 (27)	Ti mesh is dipped into the coating solution for 40 seconds and withdraw at an angle, hold with mesh at an angle to allow excess solution to flow back over mesh. Wait for all bubbles to pop by blowing my mouth to dry for 2-3 minutes. Heat Ti mesh in 100 °C oven for 5 minutes, follow by heating in 460 °C furnace for 10 minutes. The dipping, oven and furnace steps are repeated 18 times. The final (20^{th}) coating is heated in 460 ºC furnace for 1 hour.	22, 25E, 26, 27
CC13	500:8:1:0 [5%]	Ti mesh is dipped into the coating solution for 40 seconds and stirred 1 minute before withdrawing. Wait for all bubbles to pop by holding to dry around 1 minute. Heat Ti mesh in 100 °C oven for 15 minutes, follow by heating in 480 °C furnace for (i) 20 and (ii) 40 minutes. The dipping, oven and furnace steps are repeated 18 times. The final (20^{th}) coating is heated in 480 ºC furnace for 75 minutes.	12A-B (i), 12C-D (ii)
CC14	500:8:1:0 [5%]	Ti mesh is dipped into the coating solution for 40 seconds and stirred 1 minute before withdrawing. Wait for all bubbles to pop by holding to dry around 1 minute. Heat Ti mesh in 100 °C oven for 15 minutes, follow by heating in 520 °C furnace for 40 minutes. The dipping, oven and furnace steps are repeated 18 times. The final (20^{th}) coating is heated in 520 ºC furnace for 75 minutes.	12G-H
NCC	-	No catalyst coating	21, 23, 24, 25

Table 4.3 The evolution of the catalyst coating step in the anode synthesis.

Anodes AJED1A-D and AJNED1A-D (*i.e.* with and without electrodeposition layer) were tested using the recycle system; one (anode AJNED1B) was tested using single pass system but showed low current efficiency, 9% at 30 cm^3 min^{-1}. During these tests it was realised that the efficiencies calculated in single system were significantly higher than those in recycle, hence single pass system was routinely employed to assess the activity and selectivity of the anodes from this point on. Anodes AJED2A-H were made in order to investigate the effect of Ni content, and were generally active, 20-40%, with some being tested many times (*e.g.* anodes AJED2F, more than 40 times, giving efficiencies between 25 and 40% at an anolyte flow rate of 100 cm^3 min^{-1}). Anodes AJED3A-E were intended to investigate further the effect of Ni content, as a complement to the 2 series, but all gave low current efficiencies despite currents being reasonable *i.e.* 0.3-0.4 A. Anodes AJED4A-C were an attempt to get a reproducible synthesis, differing from previous syntheses as follows:

- Immersing in acetone to clean meshes replaced by wiping with a tissue soaked in acetone.
- Immersing in water to wash off acetone replaced by immersion and sonication for 5 minutes.
- Coating by immersion replaced by brushing.
- Compressed air was also pumped through furnace during pyrolysis.

These anodes gave low currents, 0.03-0.1 A with efficiencies 15-42%, and were not tested extensively.

Anodes AJED4D-F arose from work by another member of the group who suggested flowing air through the furnace during the pyrolysis of the catalyst coating could be beneficial. Other parameters that were changed were:

- 2.5 cm x 2.5 cm Pt/Ti counter electrode replaced 6.0 cm x 4.0 cm electrode in electrodeposition.

- The electrodeposition is carried out in four segments of 12 minutes, turning the Ti mesh each time, instead of a single 25 minute experiment with no turning.

These anodes gave currents of 0.1-0.2 A and efficiencies of 20-33%, which were not a significant improvement in performance, and flowing air was not employed further. Anodes AJED4G-I were an attempt to backtrack, *i.e.* keeping the 4-segment electrodeposition but returning to the original 6.0 cm x 4.0 cm Pt/Ti counter electrode. Anodes AJED4G-I gave irreproducible currents between 0.2-0.3 A and efficiencies between 12 and 23%. Hence, anode AJED4J was dip-coated and gave more a reproducible activity and selectivity, of 0.20-0.23 A and *ca.* 16% (*i.e.* but low) current efficiency.

Anodes AJED5A and B explored the use of painting the catalyst coating rather than dip-coating. The currents were quite high, 0.37-0.44 A, but efficiencies consistently low, 9-13%.

Anodes AJED6-8 series were made to fit a commercial electrochemical ozone cell imported from China; this aspect of the project was not fruitful in terms of the results it produced, and will not be discussed further.

Anodes AJED9A-H were made to assess the effect of the presence or absence of added HCl in the electrodeposition and catalyst solutions, see section 4.4.2. Anodes AJED10A-H assessed the effect of the electrodeposited interlayer.

Anodes AJED11A-D explored the reproducibility of the Ni content, all being made with the 'optimum' Ni content of 500:8:3 in the coating solution. The results were disappointing in terms of efficiency, 20-29% on experiment 1 decreasing to 16-22% on experiment 2, but consistent in terms of the interlayer and catalyst loadings, 1.0 mg cm^{-2} and 5.2 mg cm^{-2}. Anodes AJED12A-H and anodes AJED13A-H investigated the effect of pyrolysis time and furnace temperature, respectively, see section 4.5.3.

Anodes AJED14 series were made to investigate the effect of ramping of the furnace temperature during pyrolysis of the catalyst coating. This was based on work by Dr. Henriette Christensen which resulted in two remarkably active and selective anodes; unfortunately, these results could not be reproduced and will not be discussed further.

Anodes AJED15-17 series were made in order to: (i) explore the scale up of the anode synthesis (Anodes AJED15-17 series, the electrodes were 5.0 cm x 7.0 cm to fit the Ti frames employed in the polycarbonate cells, see section 2.4 and fig. 2.4); (ii) to investigate the effect of gold (Anodes AJED15 and 17 series, see section 5.2) and (iii) to investigate the effect of the drying step prior to pyrolysis (Anode AJED16 series, see section 4.5.2).

The anodes AJED18 series were made according to ED5/CC9 to explore the effect of pyrolysis (furnace) temperature, based on a literature by Chan et al. [11]. However, the work added little to the study using the anodes AJED12 and 13 series, and will not be discussed further.

The anodes AJED19 series were an attempt to replicate the activity and durability of the anodes AJED2 series.

The anodes AJED20 series were prepared on 5.0 cm x 7.0 cm substrates using the (then) optimum preparation, that of the highly active anodes HCED15 series made by Dr. Henriette Christensen.

The anodes AJED21-25 series were prepared in an attempt to explore in detail and improve the electrodeposition step in the synthesis, *e.g.* looking at the effect of electrodeposition time, the size of the counter electrode, number of electrodes, rôle of Sn in the electrodeposition solution, etc.

The anodes AJED26 series were prepared on 0.8 cm x 0.8 cm Ti mesh substrates to allow fundamental investigations and elemental analysis by Time of Fight Secondary Ion Mass Spectrometry, ToF-SIMS, and to study the effect of Au.

The final, anodes AJED27 series were made according to the optimum procedure identified in the work on the anodes AJED21-25 series.

In the work described in the sections below the anodes were 2.5 cm x 2.5 cm unless stated otherwise.

4.3 The etching process

Etching of the Ti mesh substrate is routinely performed to remove oxide which would otherwise inhibit the subsequent coating processes and provide an electronically insulating layer [3][12][14]. Lipp and Pletcher highlighted the importance of the pre-treatment of the Ti substrate with respect to the stability of SnO_2 electrodes, (see [12] and references therein). After investigating a variety of treatment processes, these authors concluded that sandblasting was the most effective. However, due to cost implications and the relatively thin nature of the Ti mesh employed in Newcastle, this approach could not be employed, and etching in oxalic acid was used. A study of the effect of etching time was undertaken (in collaboration with Mrs. Amanda Graham of Clarizon Ltd), and the results so obtained are shown below.

Figure 4.3 (a) shows an SEM micrograph of an unetched mesh and figs. 4.3 (b)-(d) micrographs of meshes etched boiling in 10 wt% oxalic acid for various times from 15-120 minutes. The increasing erosion of the Ti surface with etching time is clearly seen in the figures, and is confirmed by fig. 4.4 which shows a plot of mass loss against etching time. Etching for 120 minutes caused significant loss of mass and structural integrity, whilst etching for 60 minutes (see fig.4.3 (c)) resulted in large domains being etched. Hence, it was decided to etch for 30 minutes.

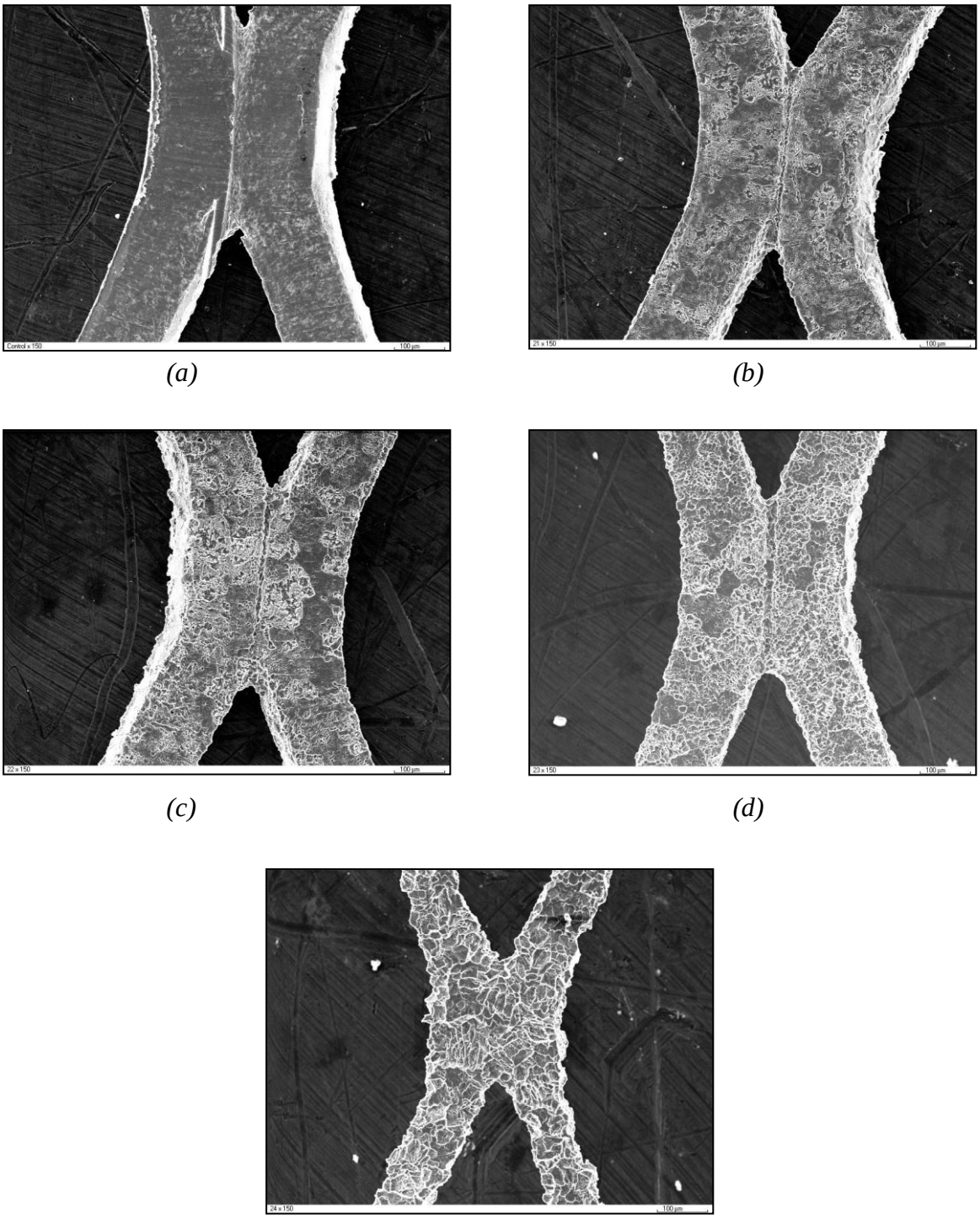

(a) *(b)*

(c) *(d)*

(e)

Figure 4.3 Micrograph of titanium mesh (a) without etching and after etching in boiling 10% oxalic acid for (b) 15 minutes (c) 30 minutes (d) 60 minutes and (e) 120 minutes.

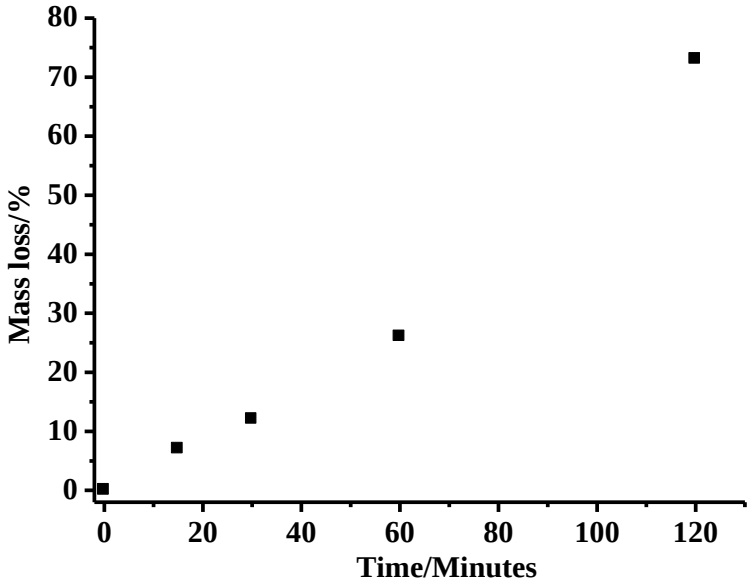

Figure 4.4 Plot of % mass loss vs. etching time for the meshes in figs. 4.3 (a)-(e). The initial masses of the meshes were between 770 mg and 803 mg.

4.4 The electrodeposited interlayer

The use of an Electro Deposited Inter Layer (EDIL) came from previous work on the lifetime of the ozone anodes prepared according to the method developed by Prof Chan. Initially, Chan did not employ any form of interlayer to protect the Ti substrate from the extremely corrosive electrolytes employed, *e.g*. H_2SO_4, H_3PO_4 [5] and $HClO_4$ [5][6], all containing high concentrations of ozone.

To gain an understanding of the possible failure mechanisms of the Ni/Sb-SnO_2 electrodes the most promising starting point is the literature on Sb-SnO_2/Ti anodes, see for example: [3][15][17]. Sb-SnO_2 anodes are an example of dimensionally stable anodes (DSAs) employed in the direct oxidation of organics due to their high oxygen overpotential in, for example, wastewater treatment [19]. Apart from the incorrect report by Chan [5] and the brief comment in the paper by Foller and Tobias [8] Sb-SnO_2 anodes are not considered to be active for ozone generation. The "service life" of Sb-SnO_2/Ti anodes is typically defined as the time taken for the anode potential to rise to

5.0 V *vs.* the reference electrodes (*e.g.* $Hg/Hg_2SO_4.K_2SO_4$ in H_2SO_4 electrolyte). Service lives of less than an hour have been reported [20]. This limited durability has been attributed to the oxidation of the Ti substrate to TiO_2 and consequent spalling of the catalyst layer [13][19]. Montilla and co-workers [13] found that the service life could be increased by utilizing thick catalyst layers (20 coats each applied *via* a brush and followed by pyrolysis at 400 °C for 19 cycles and a final step at 600 °C, 1.8 mg cm^{-2}). This was postulated by the authors to be due to the complete covering of the Ti substrate and hence prevention of anolyte ingress. Chan and co-workers employed 8 dip-coats as this gave the optimum efficiency and EDX showed only a weak Ti peak, suggesting the Ti substrate was fully covered [12].

From the start of the project, thick Ni/Sb-SnO_2 films (20 coats) were employed, a decision later supported by observations linking high catalyst mass to increased activity (see below). However, previous work by the PAC group and by Montilla et al. [13] suggests that thick catalyst coatings alone are not sufficient to guarantee durable anodes.

Based on the hypothesis of 'protecting' the Ti substrate from oxidation, Correa-Lozano et al. [3] found that depositing an IrO_2 interlayer, by thermal decomposition, increased the service life of Sb-SnO_2 electrodes by *ca.* 2 orders of magnitude. The authors postulated that the corrosion of the Sb-SnO_2 was due to stress induced by the oxidation of the non-stoichiometric SnO_{2-x} exposed to the electrolyte and hence its detachment (spallation). This exposed the underlying non- stoichiometric coating leading to progressive, layer-by-layer disintegration. The IrO_2 interlayer benefitted "…the service life of the SnO_2-based anode due to its high anodic stability and its isomorphous structure with TiO_2 and SnO_2" [3]; a somewhat vague justification.

More recent theories postulated that the use of an interlayer prevents the oxidation of the Ti substrate during the pyrolysis of the Sb-SnO_2 coating and/or during electrolysis should the Ti be adventitiously exposed to electrolyte due to, for example, cracks in the coating. Thus, Chen and Nigro [21] employed a sputtered, nanoscale gold film between the Ti substrate and Sb-SnO_2 layer. On the basis of SEM and electrochemical

investigations, the authors postulated that the 12-fold increase in electrode life was due to protection of the Ti substrate by the Au interlayer from oxidation. As was stated above, such oxidation leads to an insulating layer between the Ti substrate and the Sb-SnO_2 layer [11][21][22], and/or stress-related spallation.

The choice of interlayer material is critical as it must adhere to both catalyst and Ti substrate, and be electronically conductive and non-porous. It would also be an advantage (if inhomogeneous catalyst layers are deposited) for it to have a high oxygen overpotential. In order to address these requirements, the Hong Kong group started using an EDIL prepared by electrodeposition from a solution of $SnCl_4.5H_2O$ + Sb_2Cl_3 + HCl in ethanol based on the work by Li et al. [24].

4.4.1 The electrodeposition cell

The initial work in Newcastle stemmed largely directly from the ongoing research in Hong Kong University and/or extensive collaboration between the research groups in the two Universities. The initial entries in tables 4.2 and 4.3 reflect this, representing methodology imported from Hong Kong prior to our research and subsequent improvement/amendment of the synthetic approach.

Early studies on the electrodeposition cell configuration (1 or 2 in figs. 4.2 (a) and (b)) were carried out in collaboration with Ms. Amanda Graham, of Clarizon Ltd. Two sets of two electrodes each were prepared (without catalyst coating), two using electrodeposition cell configuration 1 and two employing configuration 2. Electrodes AGED13 and AGED14 were prepared *via* ED3, whilst electrodes AGED16 and AGED17 employed ED3 but using configuration 2 without any turning of the Ti mesh (employed in ED3/CC1 to try and ensure an even coating but using the same deposition time and current [23]). In both configurations, the separation of the electrodes was *ca.* 1.0 cm.

Electrodes AGED13 and AGED16 were not heated in the furnace at 520 ºC following the drying step at 100 ºC whilst electrodes AGED14 and AGED17 were heated in the

furnace. The mass changes determined during the electrodeposition process are summarised in table 4.4, from which it appeared that configuration 1 resulted in *ca.* 16% loss, whilst heating in the furnace at 520 ºC resulted in a mass loss of *ca.* 5-6%.

The voltages across the cells were *ca.* 2.8 V rising to 3.4 V by the end of each of the four stages of electrolysis using configuration 1, and *ca.* 3.2-3.4 V during the electrodeposition employing the second configuration.

Figures 4.6 (a)-(d) show SEM images of electrodes AGED13, AGED14, AGED16 and AGED17. Taking electrodes AGED13 and AGED14 first, it can be seen that the coverage of the Ti mesh substrate by the EDIL is inhomogeneous, with a large fraction of the Ti surface uncoated. Comparison of fig 4.6 (b) with the SEM image of an EDIL-coated Ti mesh prepared in an identical manner to electrode AGED14, see fig. 4.5, shows a significantly different morphology after heating in the furnace which results in globular particles of the EDIL, suggesting that the ED process using the first cell configuration is somewhat irreproducible; hence the use of configuration 2 in later experiments.

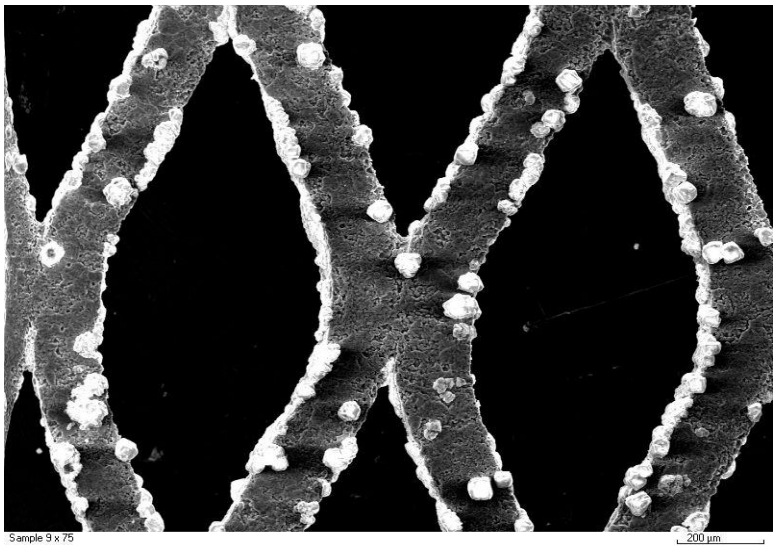

Figure 4.5 SEM image (x75; bar = 200 µm) electrode AGED9 following electrodeposition, drying at 100 ℃ and heating in furnace to 520 ℃ for 2 hours; identical preparation to electrode AGED14.

		Mass or mass change /mg							
Electrodes AGED	**Electro-deposition configuration**	**Post cleaning (a)**	**Post electro-depostion (b)**	**Gain (b-a)**	**Post heating at 100 °C 15 minutes (c)**	**Loss (c-b)**	**Post pyrolysis at 520 °C (d)**	**Loss (d-c)**	**Nett change (d or c -a)**
13	1	296.7	329.6	32.9	329.2	0.4	n/a	n/a	32.5
14	1	291.2	322.7	31.5	322.3	0.4	303.1	19.2	11.9
16	2	283.8	309.9	26.1	309.7	0.2	n/a	n/a	25.9
17	2	278.2	306.3	28.1	306.2	0.1	290.3	15.9	12.1

Table 4.4 Mass changes derived during the formation of the EDILs on 6.25 cm^2 Ti mesh electrodes; AGED13, AGED14, AGED16 and AGED17.

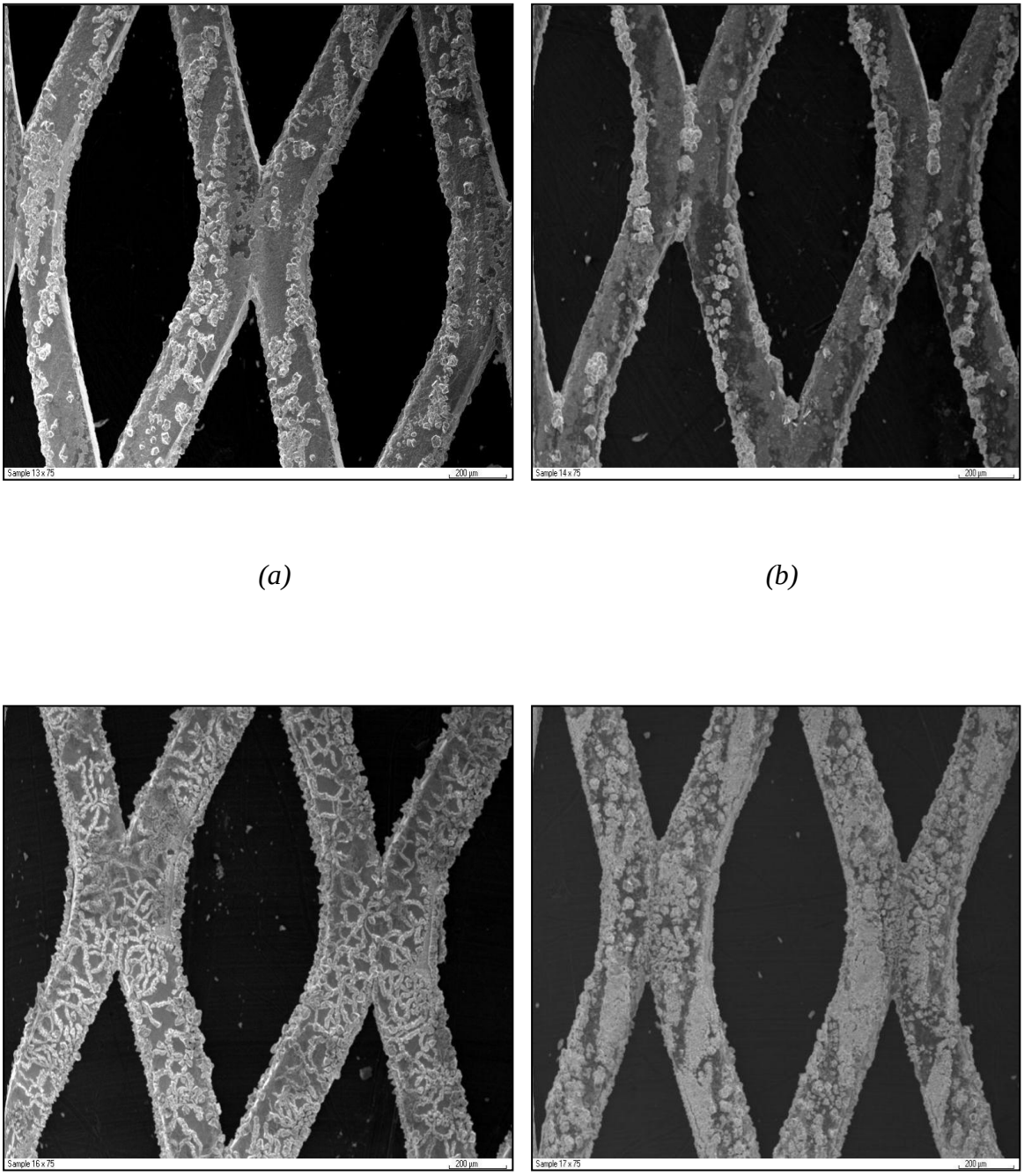

(a) *(b)*

(c) *(d)*

Figure 4.6 SEM images (x75; bar = 200 µm) of electrodes (a) AGED13, (b) AGED14, (c) AGED16 and (d) AGED17.

4.4.2 The effect of HCl

The Hong Kong group did not add HCl to the electrodeposition or catalyst coating solutions [5][6] despite this being done in the paper by Li et al. that inspired the use of the Sn/Sb EDIL [24]. However, it was noticed in Newcastle that coating and electrodepostition solutions often become cloudy, most likely due to the reaction of $SbCl_3$ and/or $SnCl_4$ with adventitious water [25]:

$$SnCl_4 + H_2O \leftrightarrow SnCl_3(OH) + HCl \quad (4.1)$$

$$SnCl_3OH + 3H_2O \leftrightarrow Sn(OH)_4 \downarrow + 3HCl \quad (4.2)$$

$$SbCl_3 + H_2O \leftrightarrow SbOCl \downarrow + 2HCl \quad (4.3)$$

Hence it was decided to investigate whether the addition of HCl, to force the equilibria in equations (4.1)-(4.3) to the left, had any effect upon the electrodeposted interlayer and/or the catalyst coating.

Electrodeposition method ED1 was employed (see table 4.2), *i.e.* differing only in the addition of 5 cm^3 HCl. Similarly, catalyst coating method CC4 was employed. The mass of EDIL and mass of catalyst deposited in four syntheses without HCl in electrodeposition and catalyst solutions (anodes AJED9A-D), and with HCl added to both solutions (anodes AJED9E-H) are shown in fig. 4.7. The corresponding plots of current and ozone efficiency are shown in figs. 4.8 (a) and (b), respectively.

From fig. 4.7 it can be seen that the addition of HCl has no discernible effect on the mass of the EDIL. In contrast, it clearly reduces the mass of catalyst deposited by *ca.* 22%, but has no effect upon the current or current efficiency; the latter was 30.9 ± 2.4% (anodes AJED9A-D) and 30.7 ± 3.1% (anodes AJED9E-H). Thus it was decided to employ HCl in the electrodeposition and catalyst solutions to ensure the equilibria in (4.1) and (4.3) were forced over to $SbCl_3$ and $SnCl_4$.

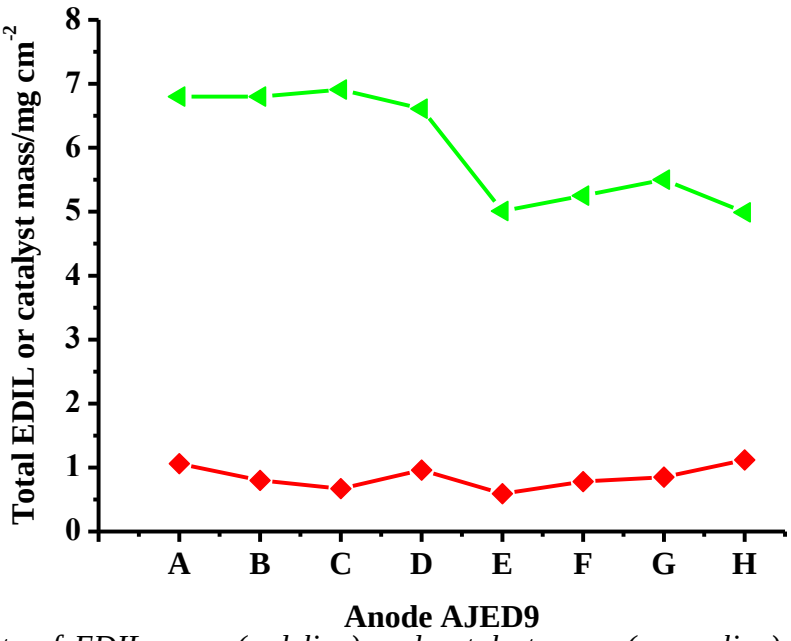

Figure 4.7 Plots of EDIL mass (red line) and catalyst mass (green line), for anodes AJED9A-H; anodes AJED9A-D were made without adding HCl to electrodeposition and catalyst coating solutions, anodes AJED9E-H with HCl added to both (see text for details).

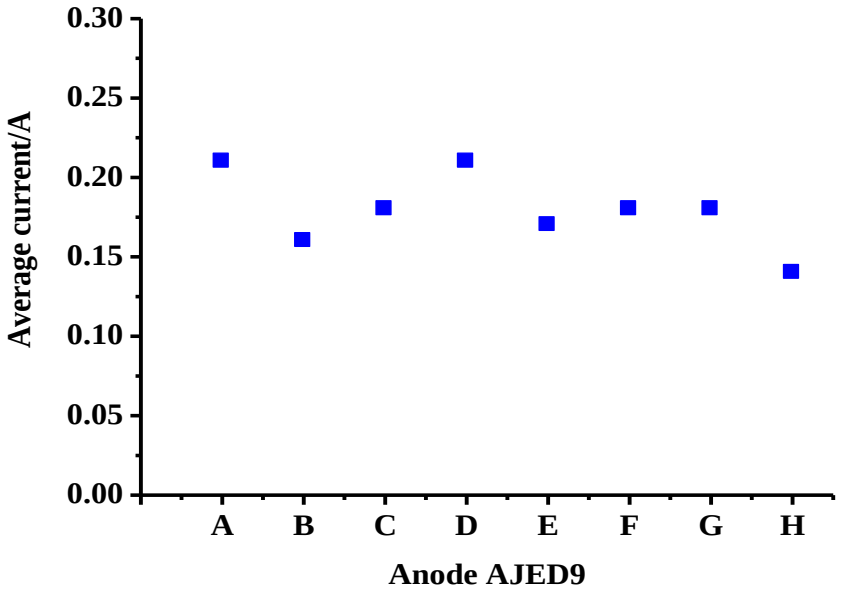

Figure 4.8 (a) The average current measured during electrolysis of 0.5 M H_2SO_4 in the glass cell using anodes AJED9A-H (6.25 cm^2) at 2.7 V and 30 cm^3 min^{-1} anolyte flow rate.

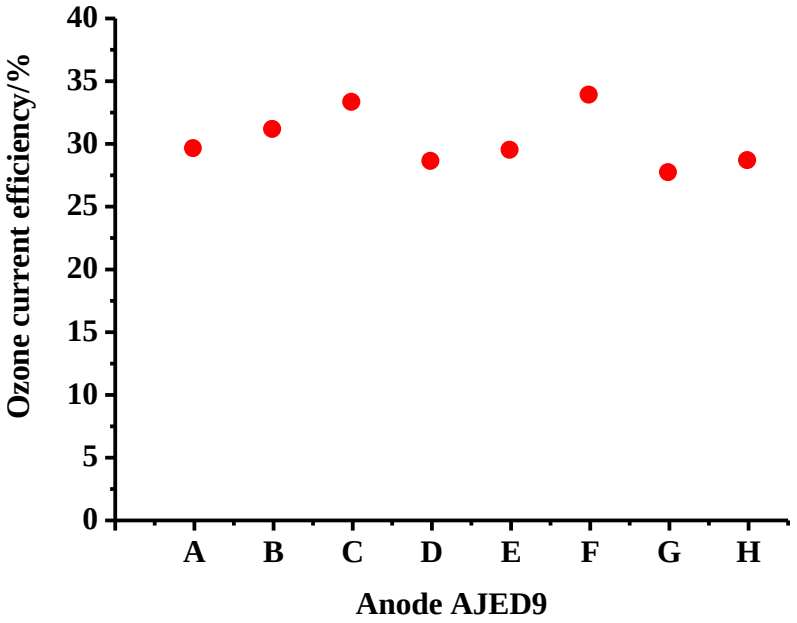

Figure 4.8 (b) The ozone current efficiencies calculated during the experiments depicted in fig. 4.8 (a).

4.4.3 The effect of Sn in the electrodeposition solution

As was stated above, K. Y. Chan's group did not employ an EDIL in their initial work, but research in Newcastle suggested that protecting the Ti substrate enhanced the durability of the anodes. Chan et al. [11] then employed an electrodepostion solution consisting of 43.75 g $SnCl_4{\cdot}5H_2O$ and 1.395 g $SbCl_3$ in 500 cm^3 ethanol, *e.g.* 0.25 M Sn^{IV}: 0.012 M Sb^{III}. The Newcastle group employed 87.5 g $SnCl_4{\cdot}5H_2O$ and 5.7 g $SbCl_3$ in 500 cm^3 ethanol (with added HCl), *i.e.* 0.5 M Sn^{IV}: 0.05 M Sb^{III}.

To investigate the possible effect of the Sn:Sb ratio in the electrodepostion solution, two series of anodes were prepared: anodes AJED19A-H by electrodeposition method ED7 and anodes AJED19a-h by electrodeposition method ED8 (*i.e.* differing only in the ratio of Sn:Sb in the electrodepostion solution). Both sets of electrodes were then coated with catalyst (500:8:3 Sn:Sb:Ni in catalyst coating solution) using catalyst coating method CC10.

The variation in the mass of the EDIL across the anode series is shown in fig. 4.9.

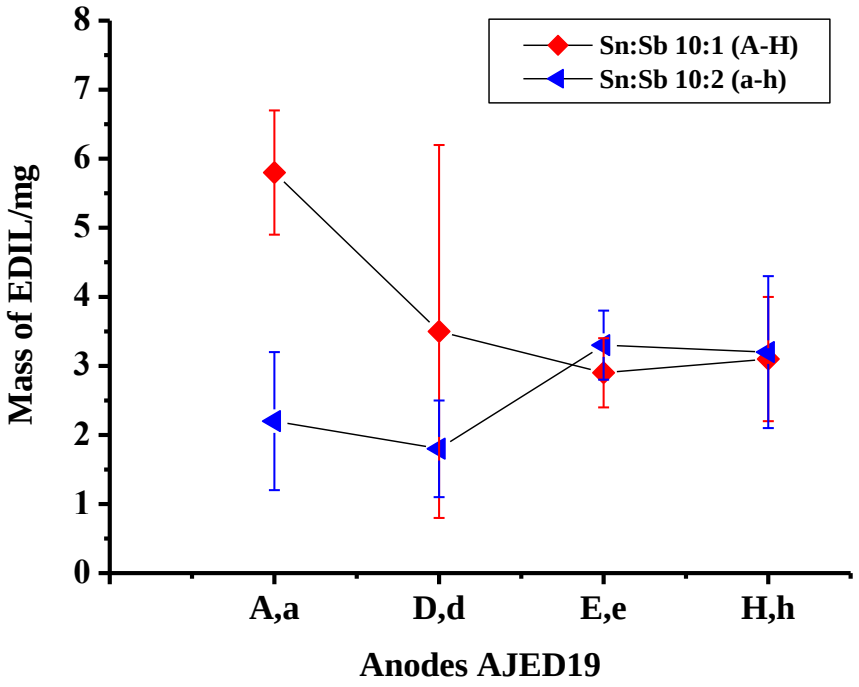

Figure 4.9 Plots of the mass of the EDILs of the anodes AJED19 series, showing the effect of the ratio of Sn:Sb in the electrodeposition solution.

Figure 4.10 shows the variation in the mass of catalyst deposited with the number of dip-coatings of anodes from the two series. Two electrodes from each series were selected for a particular number of coats.

From fig. 4.10 it may be seen that there is little or no variation (for a particular number of dip-coats) between the two sets of electrodes suggesting varying the Sn:Sb in the electrodeposition solution has no effect upon the subsequent catalyst coating process. As may be expected, the mass of catalyst deposited increased with the number of dip-coating. Note the reproducibility within and between series.

Figure 4.11 shows the variation in current of the electrodes in fig. 4.10, taken after 20 minutes during the electrolysis of 0.5 M H_2SO_4 at a cell voltage of 2.7 V in the glass cell and fig. 4.12 the corresponding plots of current efficiency. From fig. 4.11, it can be seen that the current appears to vary in a rather random way for the electrodes fabricated from the 10:1 Sn:Sb solution. In contrast, the electrodes made using the 10:2 electrodeposition

solution showed a relatively clear increase in current with the number of dip-coats. The random variation in the data obtained with anodes AJED19A-H most likely simply reflects the random variation in the EDIL mass across the series, see fig. 4.9.

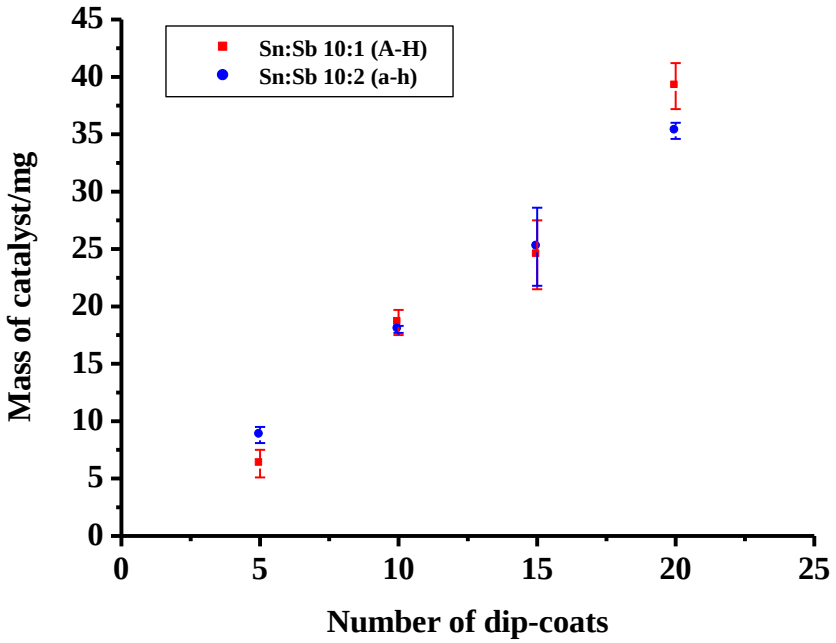

Figure 4.10 The variation in the mass of catalyst deposited vs. the number of dip-coats for the anodes AJED19 series.

Both sets of anodes show (approximately) the same behaviour with respect to the efficiency of ozone generation, see fig. 4.12, increasing from *ca.* 15% to *ca.* 25-30% with increasing catalyst thickness. In terms of the aims of this part of the research programme, it was clear that the 10:1 Sn:Sb electrodepostion solution seemed to give a wider variation in EDIL mass than the 10:2 solution, and also a wider variation in the current and ozone current efficiency; hence it was decided to use the 10:2 molar ratio in the electrodeposition solution.

One interesting observation from the data discussed above is that it appears from fig. 4.12 that increasing the thickness of the catalyst layer increased the efficiency with respect to ozone; *i.e.* the density of surface active sites for ozone increased with catalyst

layer thickness. This was also found by Mr. Khalid Zakaria during his studies on small (0.64 cm^2) Ni/Sb-SnO_2 anodes [26], and was attributed by him to surface enrichment by Ni.

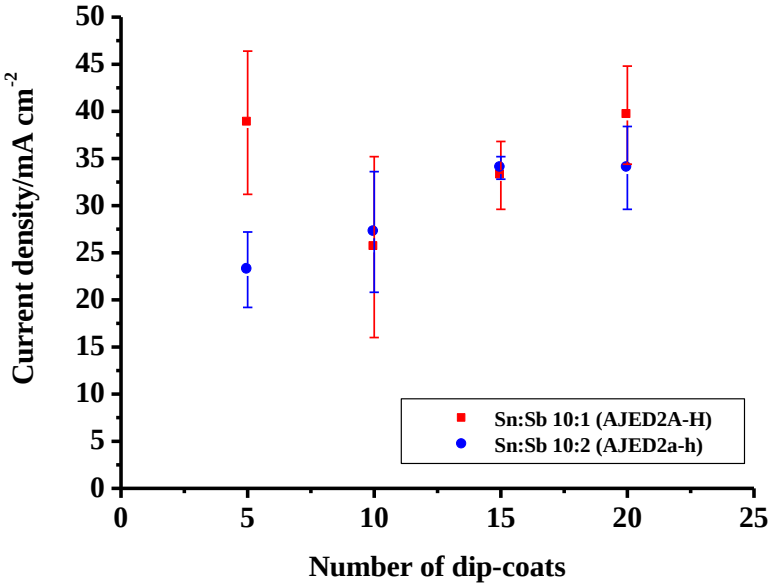

Figure 4.11 The current measured after 20 minutes during the electrolysis of 0.5 M H_2SO_4 at a cell voltage of 2.7 V in the glass cell for the anodes in fig. 4.10.

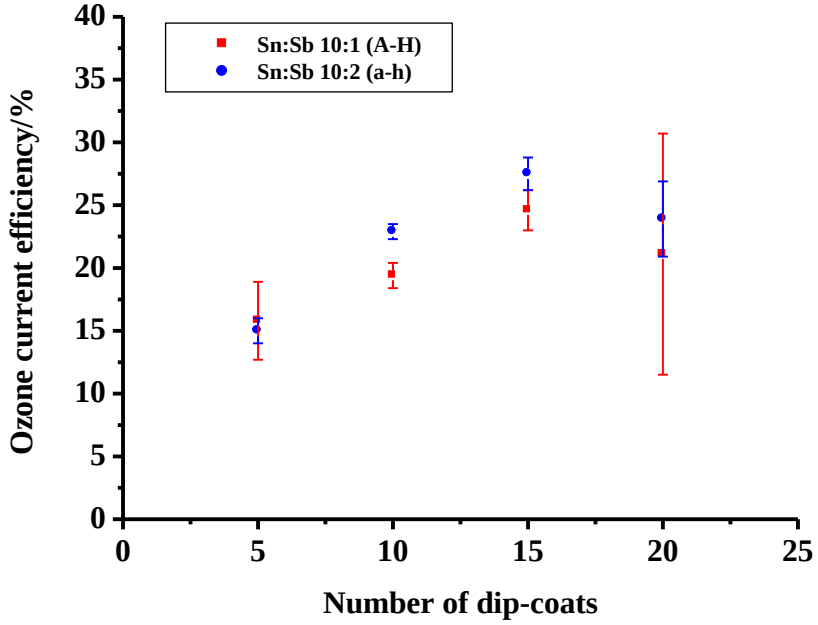

Figure 4.12 Plots of ozone current efficiency vs. the number of dip-coats for the anodes in figs. 4.9-4.11.

It was decided to explore the effect of the composition of the electrodeposition solution further by investigating the effect of electrodeposition time in the presence and absence of $SnCl_4$. A set of anodes, AJED21A-R were made using electrodeposition methods ED7, ED11, ED13 without a catalyst coating, fig. 4.13 shows plots of EDIL mass *vs.* electrodeposition time from solutions with and without $SnCl_4$, and fig. 4.14 shows the corresponding variation in cell voltage during the electrodeposition process.

From fig. 4.13 it can be seen that the EDIL mass increases with electrodeposition time from both solutions; however, the solution containing $SnCl_4$ gives a more linear variation and a large increase overall, than the solution without $SnCl_4$.

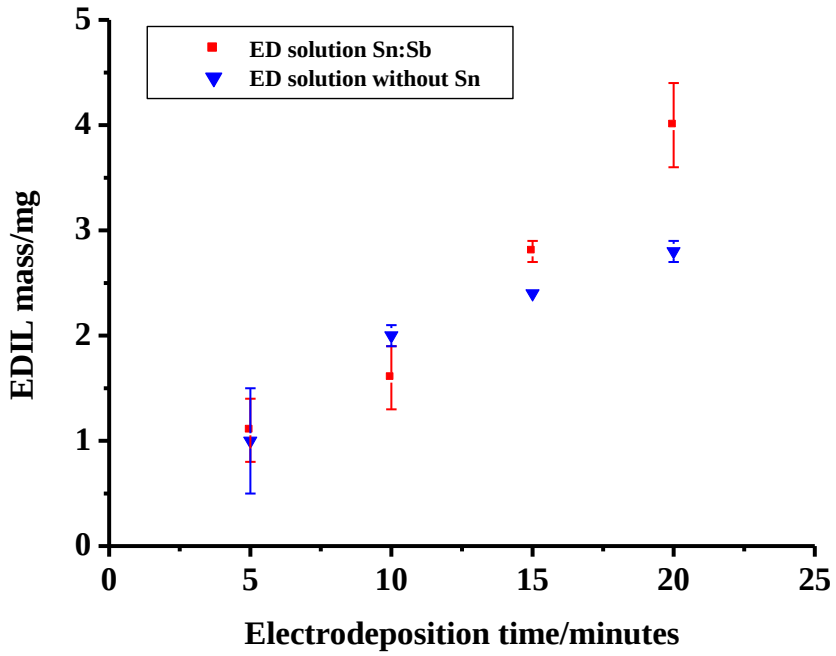

Figure 4.13 Plots of the variation in EDIL mass as a result of varying the electrodeposition time. The 6.25 cm^2 Ti mesh substrates were electrodeposited from 0.1 M $SbCl_3$ in ethanol with (■) or without (▼) 0.5 M $SnCl_4$ using electrodeposition methods ED11-ED13 and cell configuration 2.

There was remarkably little variation in the cell voltage during electrodeposition from either solution, see fig. 4.14. Remarkably, the solution without added $SnCl_4$ gives a *lower* cell voltage, and narrower range of voltages, than the solution with the tin.

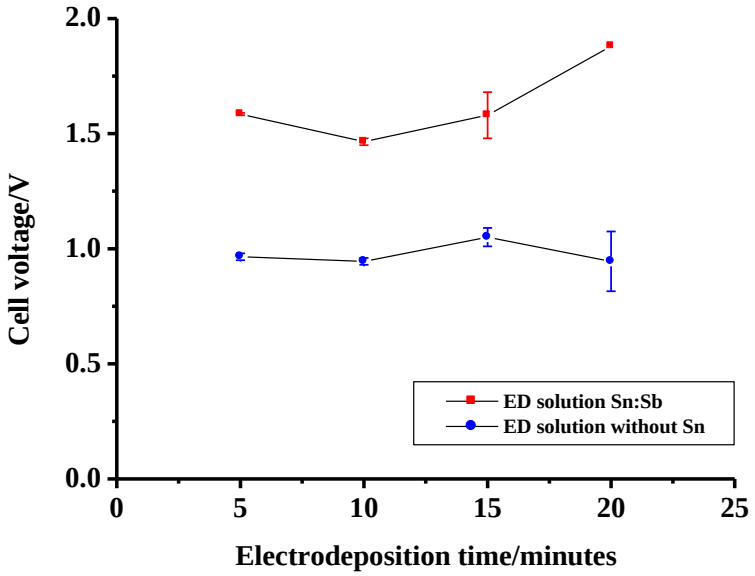

Figure 4.14 Plot of the variation in cell voltage during the experiments depicted in fig. 4.13.

It is clear from figs. 4.13 and 4.14 that omitting Sn from the electrodepostion solution has an effect, but it is not clear whether this is positive or negative with respect to the basic aim of using an EDIL. Further insight into the rôle of Sn in the electrodeposition solution came from the EDX spectra on electrodes AGED13, AGED14, AGED16 and AGED17 (discussed in section 4.4.1 above) see figs. 4.15 (a)-(d). For comparison, an EDX spectrum of a coated electrode, AJED19H, is shown in fig. 4.15 (e). A comparison of figs. 4.15 (a)-(d) with fig. 4.15 (e) shows that the AGED electrodes do not contain any Sn. This was observed generally for all EDILs. The EDX features in figs. 4.15 (a)-(d), due to Sb_2O_5 [2], are summarized in table 4.5.

In order to investigate the above results further, cyclic voltammograms were measured using a 1 cm^2 Ti mesh working electrode immersed in ethanolic 0.05 M $SbCl_3$ + 0.5 M

$SnCl_4.5H_2O$, see figs. 4.16 (a)-(c), using a Ag/AgCl reference electrode and Pt foil counter electrode.

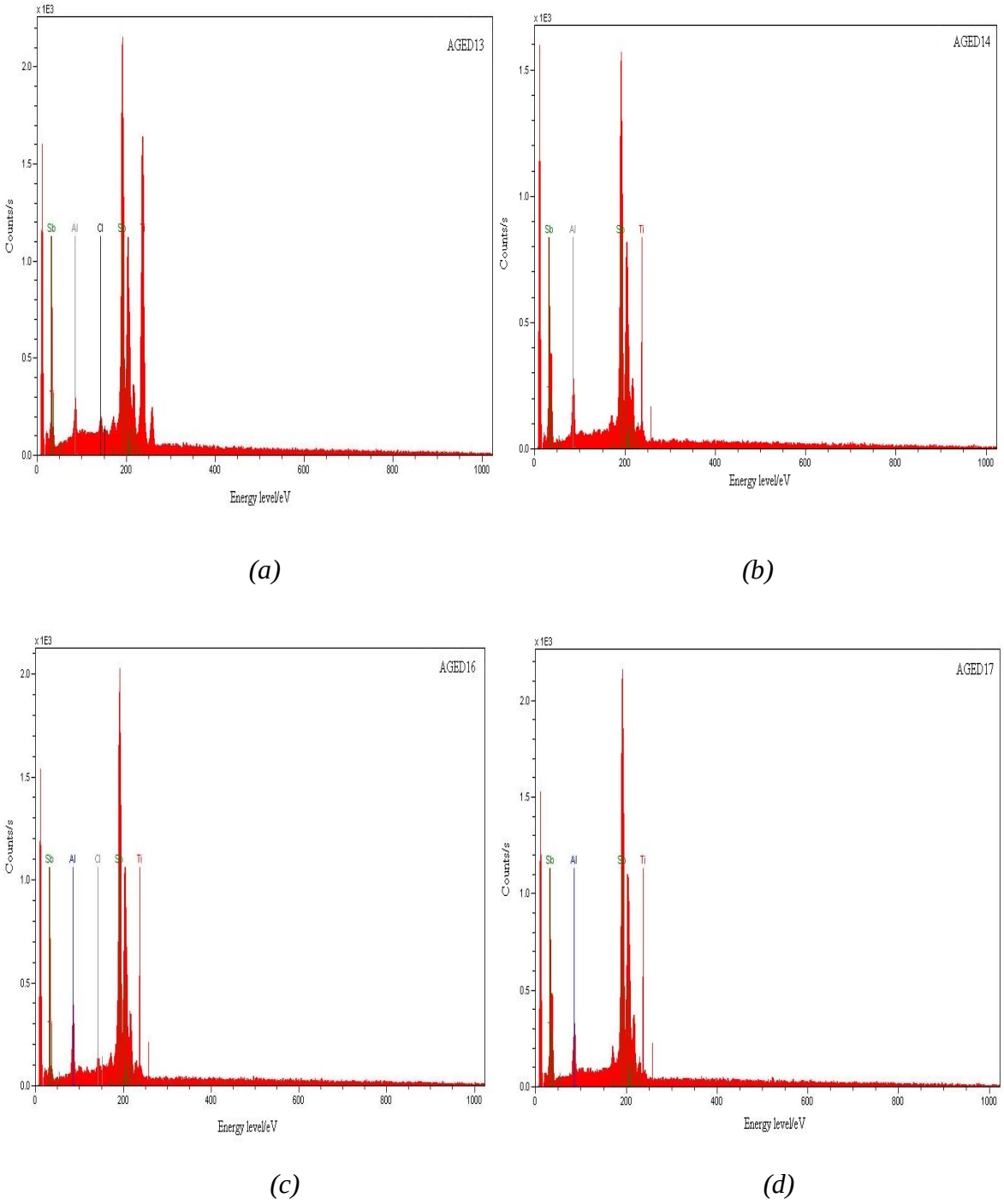

Figure 4.15 EDX spectra of the electrodes (a) AGED13, (b) AGED14, (c) AGED16 and (d) AGED17.

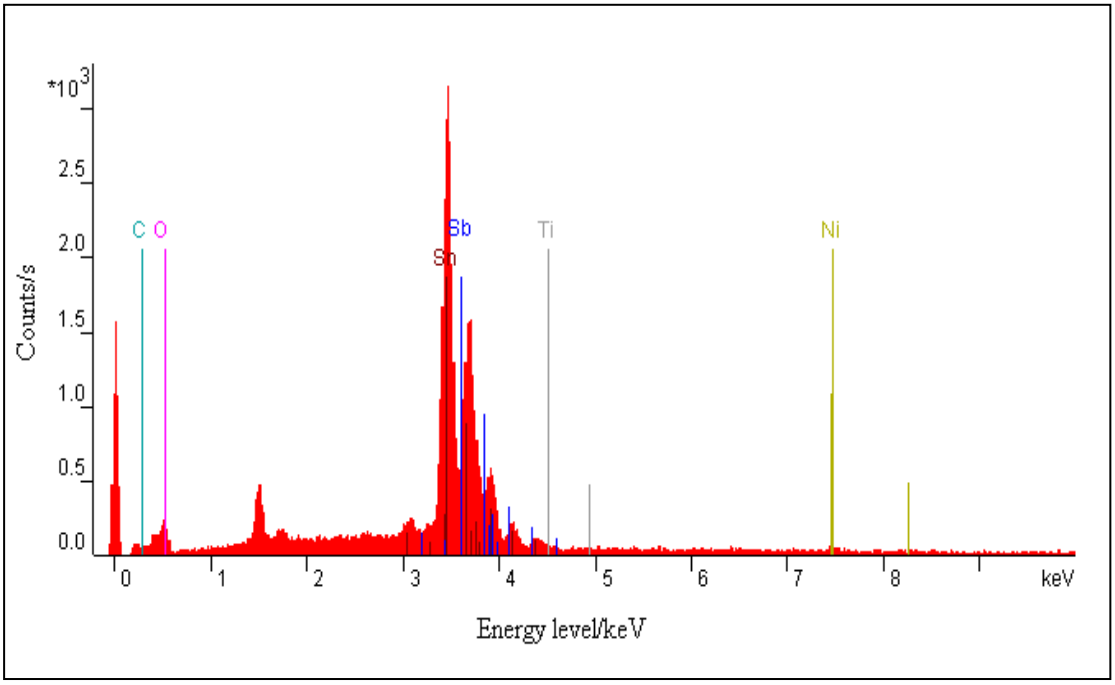

Figure 4.15 (e) EDX spectra of anode AJED19H is shown in for comparison.

Peak/eV	Relative intensity
3.62	1.00
3.88	0.39
4.11	1.12
4.37	0.07

Table 4.5 EDX features due to the Sb-containing EDIL.

The marked similarities between figs. 4.16 (a) and (c) support the preferential deposition of Sb from the $SbCl_3$ + $SnCl_4$ solution.

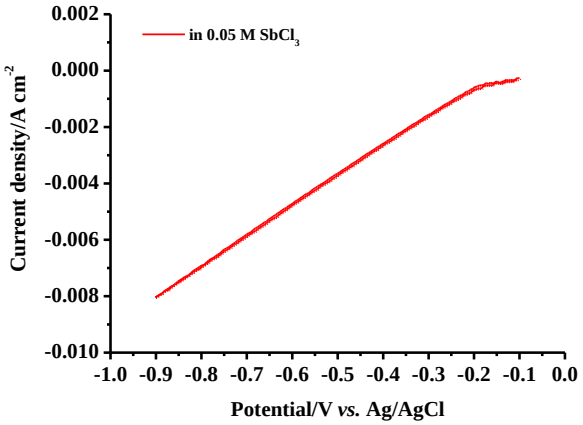

(a)

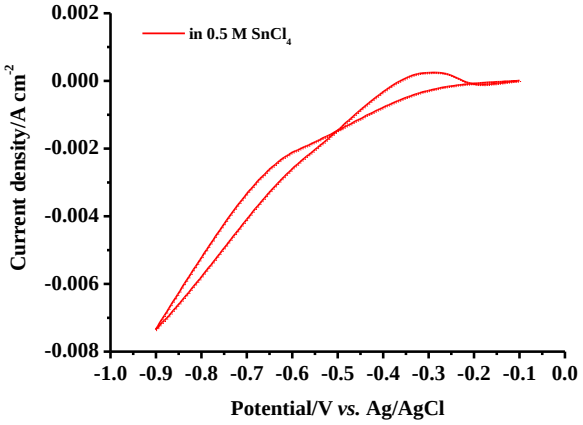

(b)

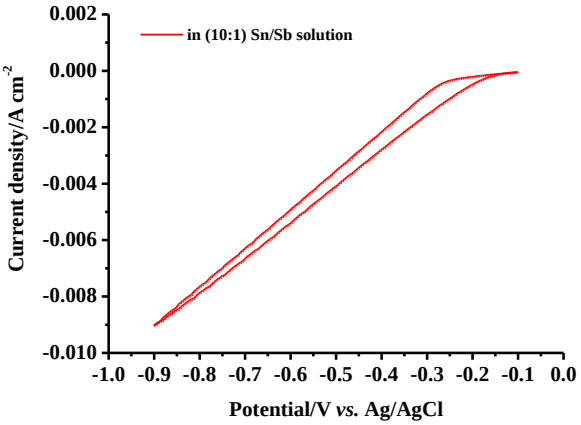

(c)

Figure 4.16 Cyclic voltammograms (100 mV s^{-1}) of 1 cm^2 Ti mesh electrodes immersed in (a) 0.05 M $SbCl_3$, (b) 0.5 M $SnCl_4$ and (c) 0.05 M $SbCl_3$ + 0.5 M $SnCl_4$ in ethanol, Pt/Ti mesh counter electrode, Ag/AgCl reference electrode.

The SEM image of electrode AGED9, fig. 4.6, suggested that the EDIL can melt under certain circumstances, and, if the molten layer does not 'wet' the underlying Ti (perhaps due to a thin layer of oxide having reformed) form globules. In order to investigate the thermogravimetric behaviour of the EDIL on heating, electrodeposition of an EDIL was carried out in an identical manner to electrode AGED13, without subsequent furnace treatment at 520 ºC. In collaboration with Dr. Ashleigh Fletcher of the School of Chemical Engineering and Advanced Materials, a 2.0 cm^2 section of electrode AGED18 was placed in the sample holder of a Stanton Redcroft ST780 thermogravimetric analyzer and heated in air (flow rate 50 cm^3 min^{-1}) from room temperature to 400 ºC at 25 ºC per minute, see fig. 4.17, then 10 °C per minute to 500 ºC.

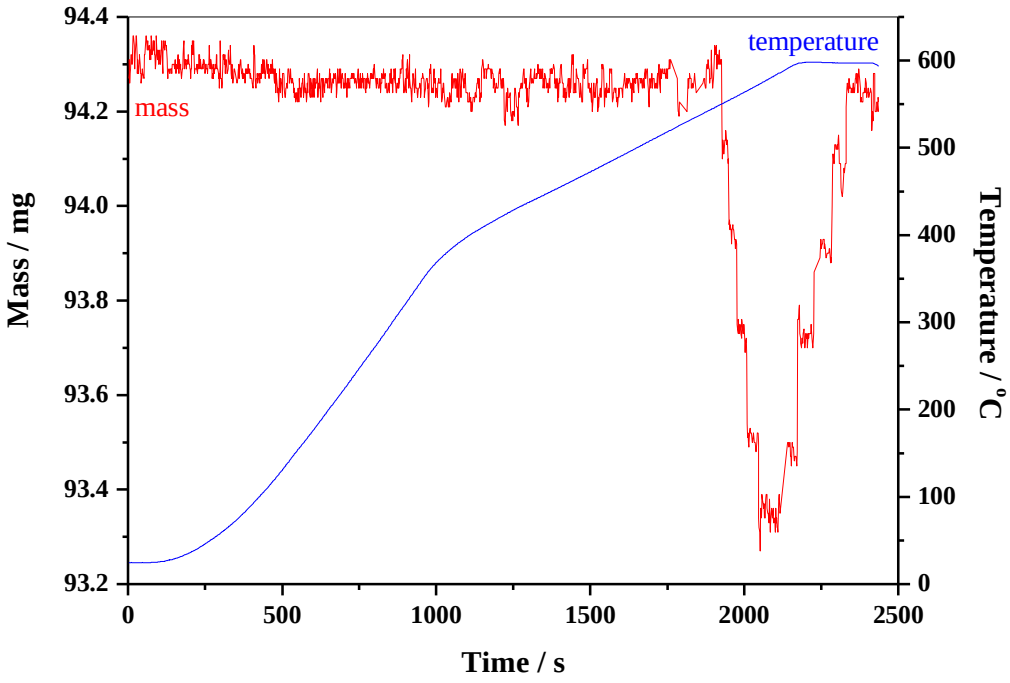

Figure 4.17 The variation in the mass of a 2.0 cm^2 section of EDIL coated Ti mesh electrode (electrode AGED18, red line) with temperature (blue line).

Figure 4.17 suggests that the electrodeposited, Sb-containing layer is stable (in terms of mass) up to *ca.* 550 °C. Ding et al. [20] postulated that during the electrodeposition Sn from Sn^{2+}/H_2SO_4 followed by Sb^{3+}/citric acid, the metallic elements were deposited on

the Ti plate electrodes. Metallic Sb does not melt until 631-656 ºC and oxidizes very little at temperatures up to 250 ºC, igniting at temperatures around its melting point to form Sb_2O_3 as a white smoke [27][28]. Thus it may be that the antimony is formed as the relatively stable metal. However, Bryngelsson and co-workers [29] found that the chemical and physical nature of Sb electrodeposited onto Ni foil from aqueous potassium antimony tartrate trihydrate depended strongly on pH. Using SEM, TEM, Raman, XRD and XPS the authors showed that electrodeposition in the presence of acid resulted in metallic Sb particles with a thin coating of Sb_2O_3 on their surface. However, if the pH was allowed to rise near the electrode (local pH swing) a mixture of Sb_2O_3 and metallic Sb was deposited. Antimony(III) oxide exits in two forms: orthorhombic Calentinite (o-Sb_2O_3) and cubic Senarmontite (c-Sb_2O_3) [28], with c-Sb_2O_3 converting to o-Sb_2O_3 at *ca.* 556 ºC. Interestingly, [25][28], o-Sb_2O_3 oxidizes in oxygen to Sb_2O_4 at 400 ºC, whilst the cubic form sublimes and oxidizes at 460 ºC. The oxidation of o-Sb_2O_3 results in a weight gain of *ca.* 1 wt%, whilst c-Sb_2O_3 undergoes a loss of *ca.* 20 wt% ([28] and references therein).

Given the data and discussion above, and that Ghosh and Kappana [30] found the physical characteristics of electrodeposited Sb to be strongly dependent upon the electrodeposition solution, the irreproducibility in terms of the amount and morphology of the EDIL electrodeposited under identical conditions is not surprising.

4.5 The Catalyst

4.5.1 The effect of Ni

The AJED2 series of anodes were made with nickel content in the precursor solutions ranging from 0 wt% to 0.4 wt% (500:8:0 to 500:8:4 Sn:Sb:Ni) in the catalyst coating solution, using ED1 and CC1. Figure 4.18 shows the current efficiencies at 2.7 V measured using the glass cell.

In contrast to the results obtained by Wang et al. [10], who found the optimum precursor ratio to be 500:8:1, it was found that the optimum Ni content corresponded to a ratio of

between 500:8:2 and 500:8:4 in the precursor mixture; hence 500:8:3 was chosen generally as the catalyst composition employed in the work reported in this thesis.

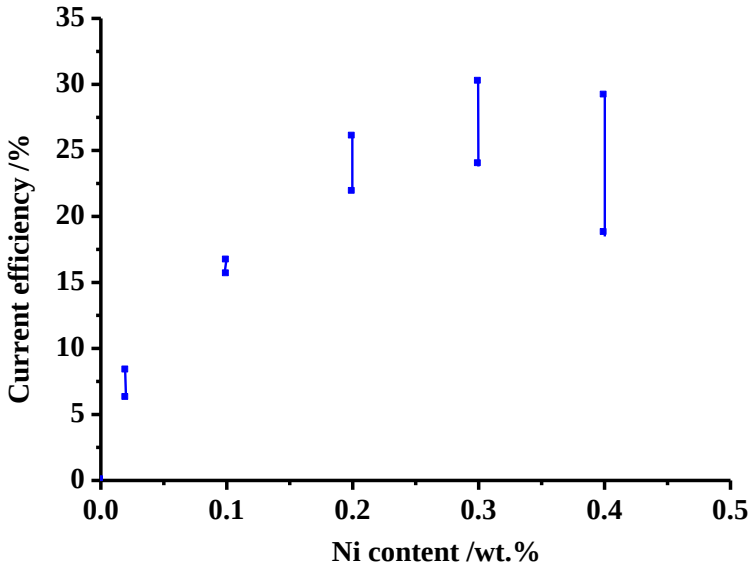

Figure 4.18 Plots of the current efficiencies for ozone measured in single pass system of the anodes AJED2 series (6.25 cm^2) as a function of nickel content in the precursor solution. Glass cell, anolyte (0.5 M H_2SO_4) flow 30 cm^3 min^{-1}, cell voltage 2.7 V. Each point was the average of two experiments.

4.5.2 The effect of drying method after dip-coating

This study was prompted by the work of Dr. Henriette Christensen, who made a highly active and selective series of anodes (anodes HCED15, see Chapter 6), and postulated that a significant contributor to the performance of the anodes was the method of drying after dip-coating and prior to pyrolysis. In order to investigate this further, 6 pairs of anodes were prepared, the details of which are summarised in table 4.6. The anodes were prepared using methods ED1 and broadly CC1. The EDIL-coated Ti mesh substrates (40.0 or 42.0 cm^2 initially) were dip-coated 5 times (instead of the usual 20 times), weighed after each dip-coating, and tested in the polycarbonate cell (see section 2.4). Anodes AJED16A-H were prepared by electrodeposition on 5.0 cm x 8.0 cm substrates. Contact to the meshes was *via* two wires spot-welded down the short edges, see fig 4.19. Anodes AJED16A-D were stood upright in a beaker to dry after dip-coating; anodes

AJED16A and AJED16B allowed to dry in air whilst anode AJED16C and AJED16D were heated gently with a hair drier see; fig. 4.19 and table 4.6.

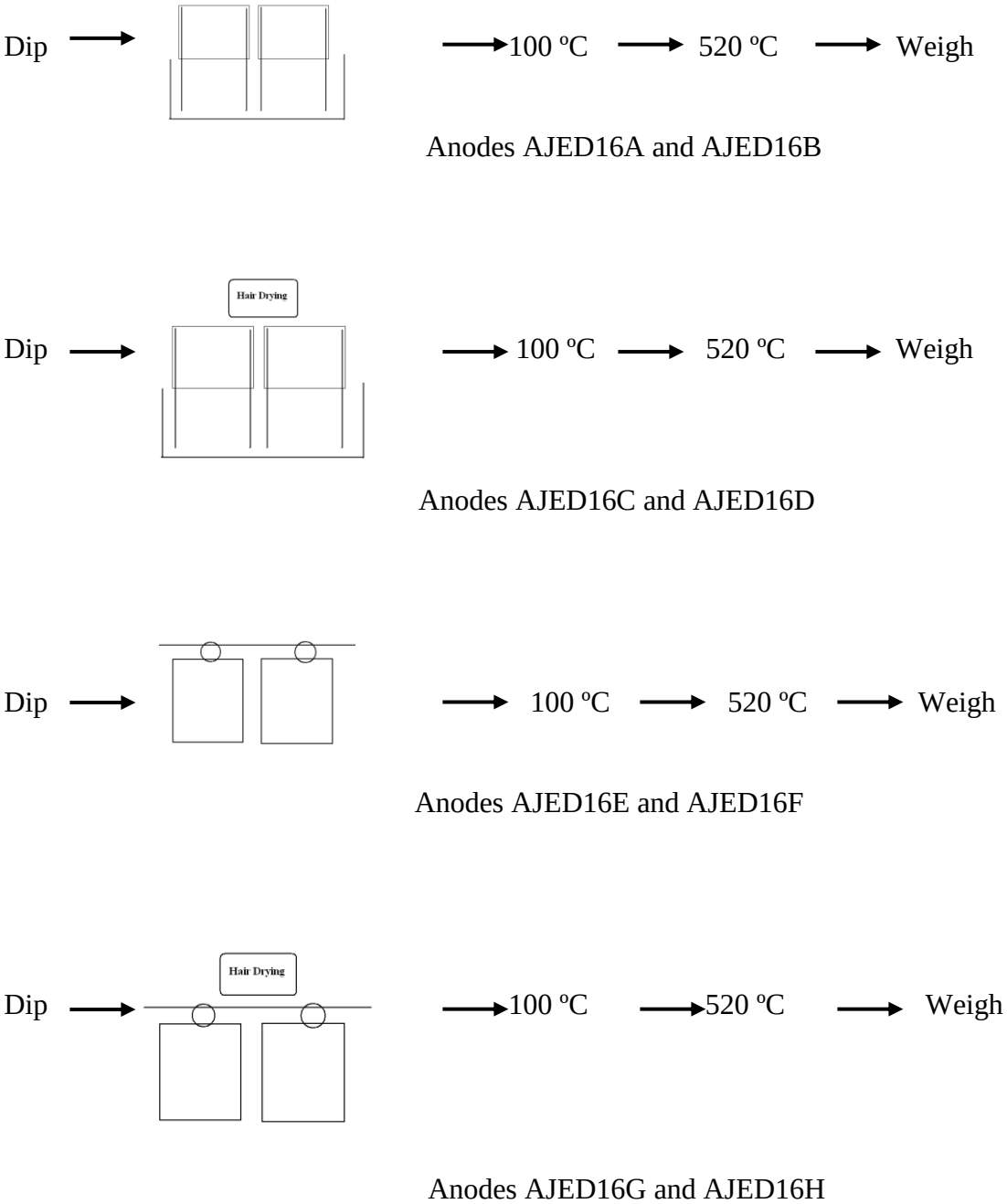

Figure 4.19 Schematic of the arrangement of the wire contacts and the method of drying employed for the anodes AJED16 series.

Anodes AJED16	**Area of mesh during electrodeposition /cm^2**	**Area of mesh during catalyst coating/cm^2**	**Area of mesh during testing/cm^2 facing Nafion membrane**	**Drying procedure after dip-coating**	**Connective wires**
A	40.0	40.0	35.0	Stood, mesh uppermost in beaker.	8.0 cm x 5.0 cm, two wires running down 5 cm sides.
B	40.0	40.0	35.0		
C	40.0	40.0	35.0	Stood, mesh uppermost in beaker and dried with hair drier.	
D	40.0	40.0	35.0		
E	40.0	350	35.0	Wires clipped off. Pegged on line	
F	40.0	35.0	35.0		
G	40.0	35.0	35.0	Wires clipped off. Pegged on line and dried with hair drier.	
H	40.0	35.0	35.0		

Table 4.6 The characteristics of the anodes AJED16 series of anodes and the methodologies employed to dry the anodes after each dip-coat with catalyst solution prior to pyrolysis.

The strategy underlying the synthesis of the anodes AJED16 series was as follows. Pairs A/B and C/D compared the effect of air drying in a beaker, mesh uppermost, to drying with a hair drier. Pairs E/F and G/H compare air drying with drying using a hair drier when the electrodes have the wires removed and the meshes pegged out on a "washing line". Clearly, comparing A/B with E/F and C/D with G/H explores the differences between drying the catalyst coating by standing upright in a beaker to drying on the "washing line".

Unfortunately, as may be seen from fig. 4.20, the strategy was undermined from the start by the irreproducibility of the electrodeposition step (which was common to all the anodes AJED16A-H); thus, all these anodes should have *ca.* the same EDIL loading, which was clearly not the case. The EDIL loading varied from 0.25 mg cm^{-2} to 0.8 mg cm^{-2}. However, the variation in EDIL provided an opportunity to investigate its effect upon the catalyst coating and hence its possible effect upon current and ozone current efficiency, as may be seen below.

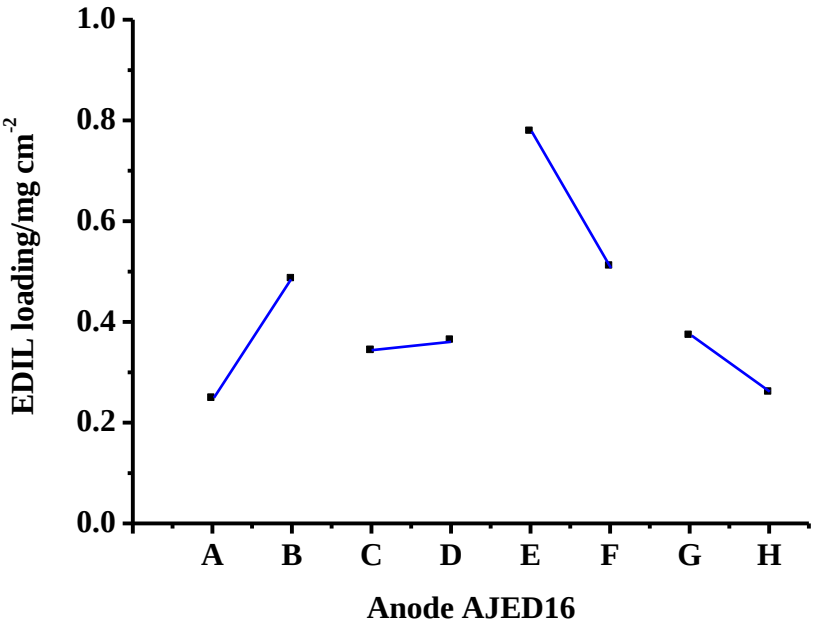

Figure 4.20 The EDIL loading determined during the experiments depicted in fig. 4.19.

Figure 4.21 shows a plot of the catalyst loading after the 1st dip-coating for the anodes AJED16 series. At first sight, there appeared to be a broad trend as the catalyst loading decreased as the EDIL loading increased. If the two subgroups of anodes are now labelled on the plot, see fig. 4.22, then clear patterns emerge. Thus, there is indeed a reproducible inverse relationship between EDIL and catalyst loadings, and this seems to dominate any differences due the variation in drying method; *i.e.* anodes with similar EDIL loadings take up similar loadings of catalyst. In terms of the total catalyst loading after 5 dip-coats see, fig. 4.23, there may have been a maximum in catalyst uptake

around an EDIL loading of *ca.* 0.35 to 0.40 mg cm^{-2}, and there was certainly still an overall downward trend at higher loadings.

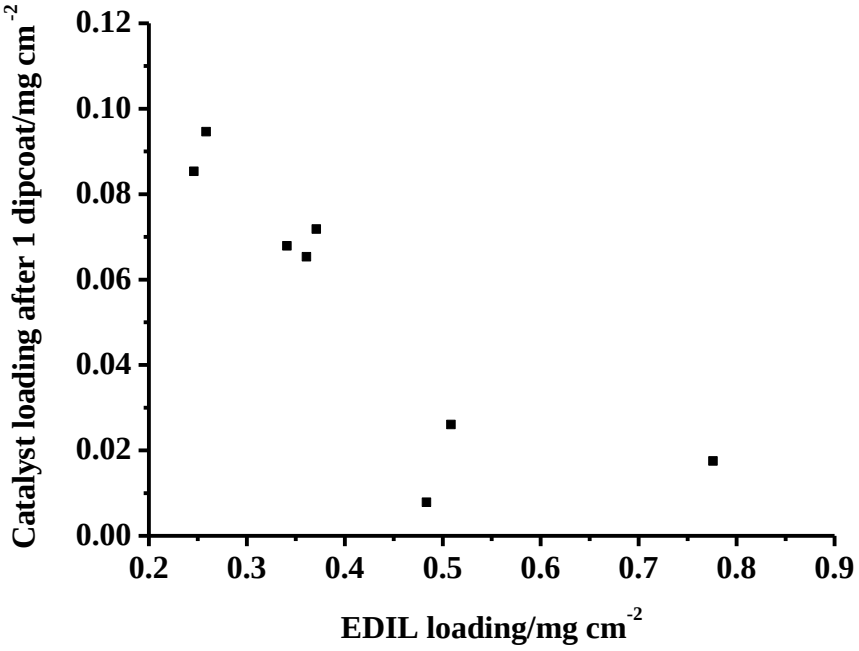

Figure 4.21 Plot of the catalyst loading after the 1st dip-coating vs. EDIL loading for the anodes AJED16 series.

Figures 4.22 and 4.23 suggested that the EDIL is a significant factor in determining the catalyst loading even up to 5 dip-coats. Data obtained by Dr. Henriette Christensen supports the latter observation: thus, fig. 4.24 (a) shows an analogous plot to that in fig. 4.23 using her anodes HCED16 series (7.0 cm x 6.0 cm, ED1 and CC1, 500:8:3:1.5). The electrodes were all prepared using the same electrodeposition and dip-coating methods. Again, the variability in EDIL loading allowed a comparison between the latter and catalyst uptake, and a clear, inverse relationship can be seen in fig. 4.24 (a). The anodes in series HCED16 were dip-coated until a loading of *ca.* 100 mg was attained, which required 19 dip-coats. Figure 4.24 (b) shows that there EDIL loading still influences the catalyst uptake, showing again an inverse relationship.

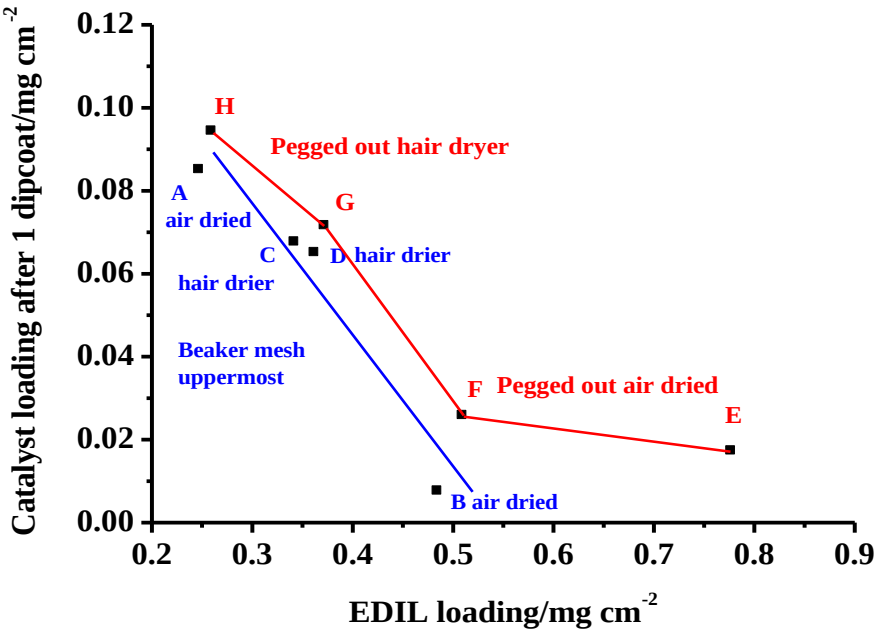

Figure 4.22 The variation in the catalyst loading after 1 dip-coat vs. the EDIL loading on anodes AJED16 series. See label for details.

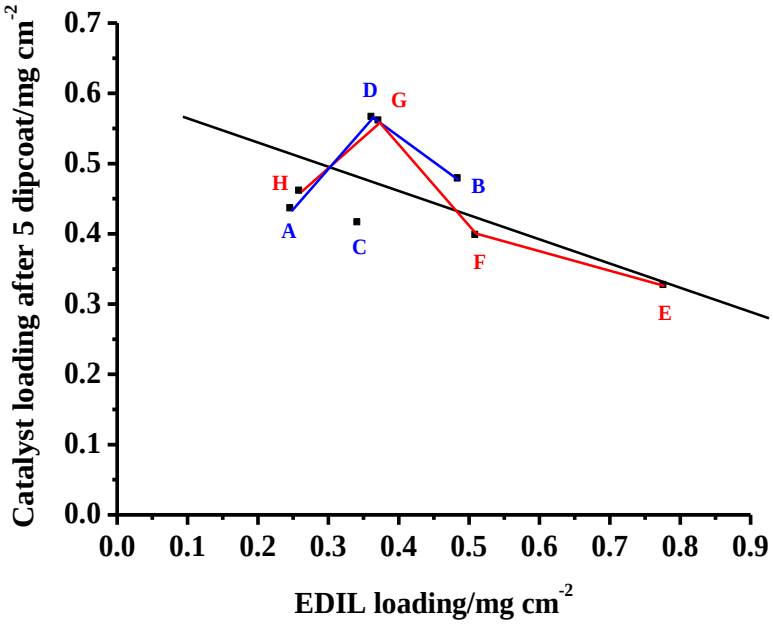

Figure 4.23 The variation in the catalyst loading after 5 dip-coat vs. the EDIL loading on anodes AJED16 series.

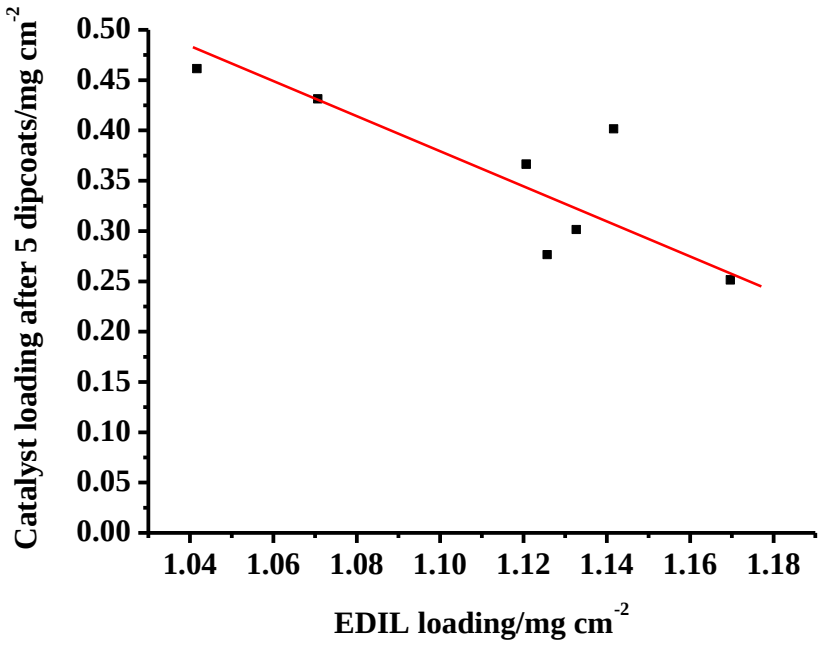

Figure 4.24 (a) The effect of EDIL loading on the catalyst loading after 5 dip-coats vs. the EDIL loading on the anodes HCED16 series.

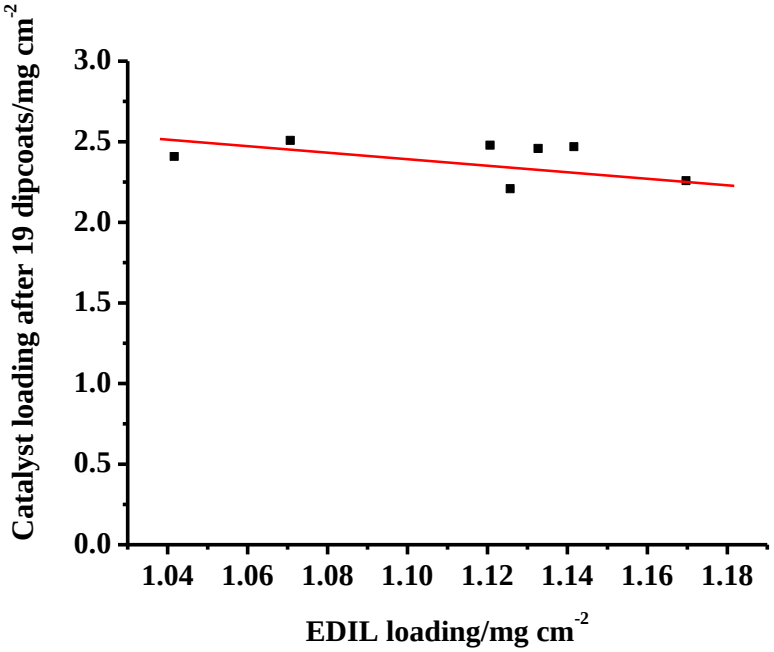

Figure 4.24 (b) The variation in the catalyst loading after 19 dip-coats vs. the EDIL loading on the anodes HCED16 series.

Taking the comparisons further, fig. 4.25 shows a plot of EDIL loading *vs.* the current density measured after 20 minutes electrolysis at 2.7 V in the polycarbonate cell for the anodes AJED16 series. At first sight, whilst anodes AJED16E-H showed a smooth trend, anodes AJED16A-D appeared to show a clear maximum. However, it is clear from the work discussed in previous sections that the current density increases with catalyst loading. In addition, intuitively, it would be expected that the catalyst coating should dominate the electrochemical response of the anodes (rather than the EDIL) once complete coverage of the Ti substrate was attained and at a certain thickness. Thus, fig. 4.26 shows a plot of current density *vs.* catalyst loading for the electrodes in fig. 4.25. The expected increase in current density with catalyst loading was apparent.

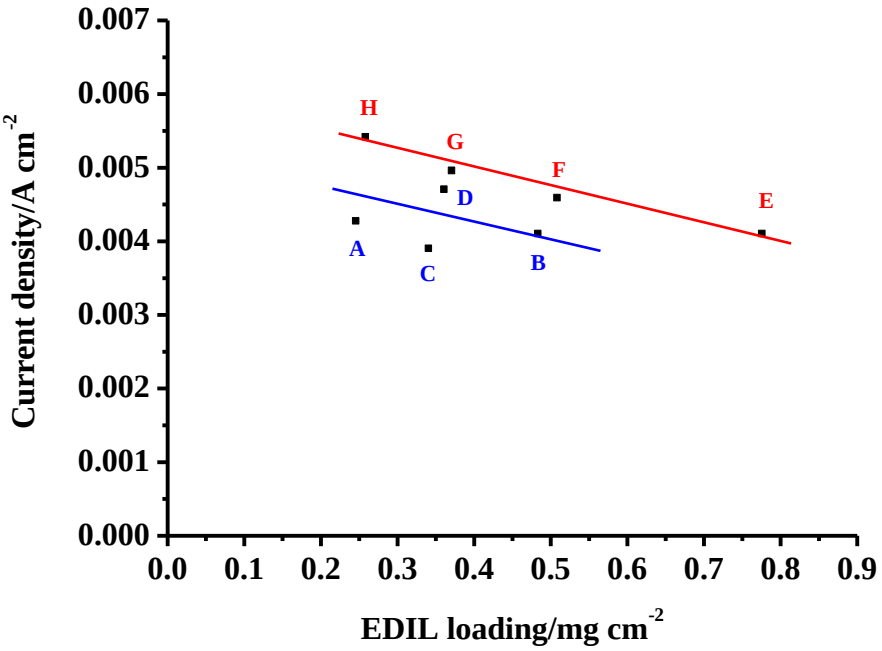

Figure 4.25 Plot of the current density vs. EDIL loading on anodes AJED16 series measured after 20 minutes electrolysis at 2.7 V in the polycarbonate cell.

Finally, fig. 4.27 shows a typical SEM micrograph of the anodes AJED16 series taken from the lower edge of the anode defined as it stood in the beaker, or was pegged on the line, to dry and fig. 4.27 an EDX spectrum from the same region (see red cross in fig. 4.27 (a)). The Sn, Sb and Ti features can be seen clearly in fig. 4.27 (b).

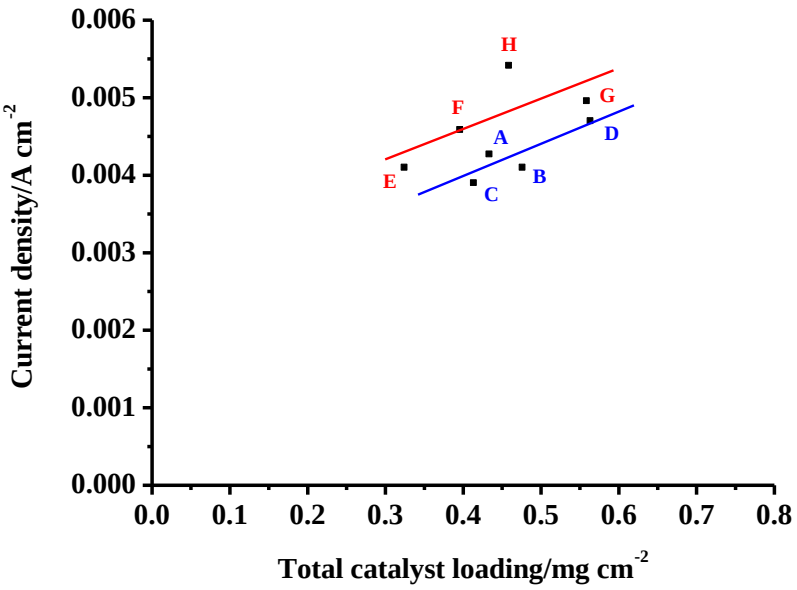

Figure 4.26 Plot of current density vs. catalyst loading for the anodes AJED16 series in fig. 4.25.

Finally, fig. 4.27 shows a typical SEM micrograph of the anodes AJED16 series taken from the lower edge of the anode defined as it stood in the beaker, or was pegged on the line, to dry and fig. 4.27 an EDX spectrum from the same region (see red cross in fig. 4.27 (a)). The Sn, Sb and Ti features can be seen clearly in fig. 4.27 (b).

Figure 4.27 is a SEM micrograph (x5000) (a) and an EDX spectrum (b) of anode AJED16A both taken from the lower edge of the anode. The red cross in (a) marks the region where the EDX spectrum was taken. Figure 4.28 (a) and (b) show plots of (a) the 4.5 keV Ti feature and (b) the 3.45 keV Sn band from the middle and bottom edges of the anodes AJED16 series.

Broadly speaking, the meshes left in a beaker to dry after each dip-coat showed more catalyst coating (and hence less Ti) at the bottom edge of the anode than at the middle, as would be expected from gravity exerting an effect. Heating with a hairdryer did not appear to have a clear effect. In contrast, the reverse appeared to be true for the anodes pegged out to dry on the line.

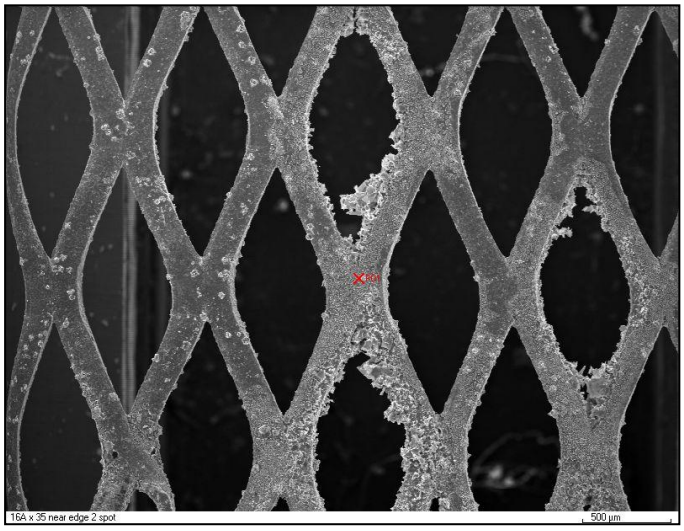

(a)

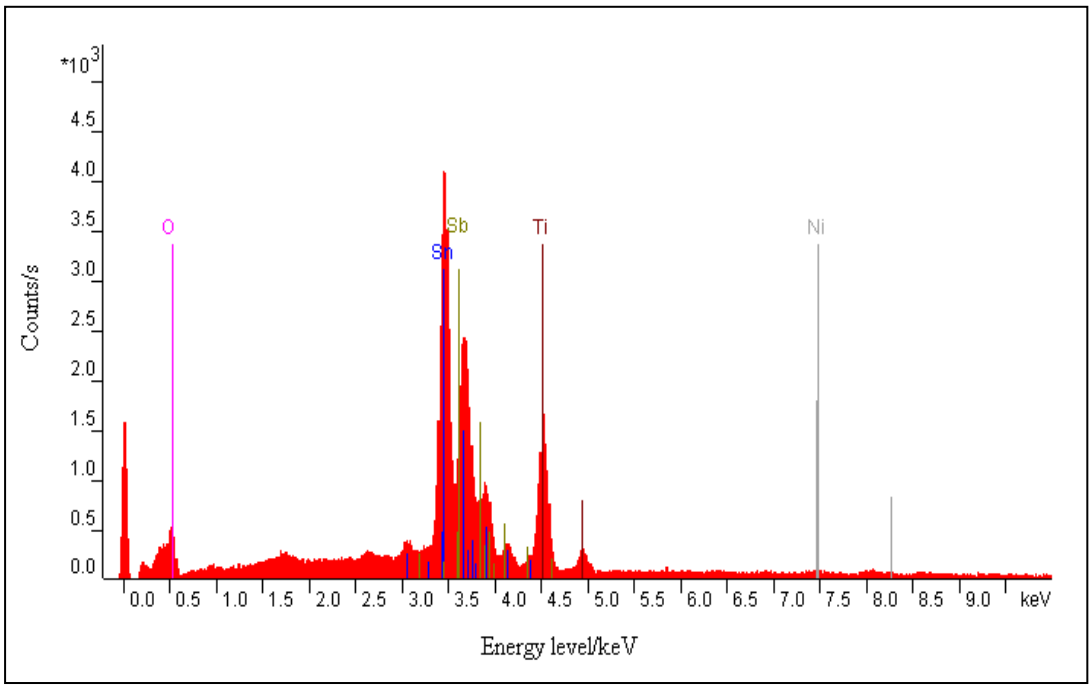

(b)

Figure 4.27 (a) SEM micrograph (x5000) and (b) EDX spectrum of anode AJED16A both taken from the lower edge of the anode.

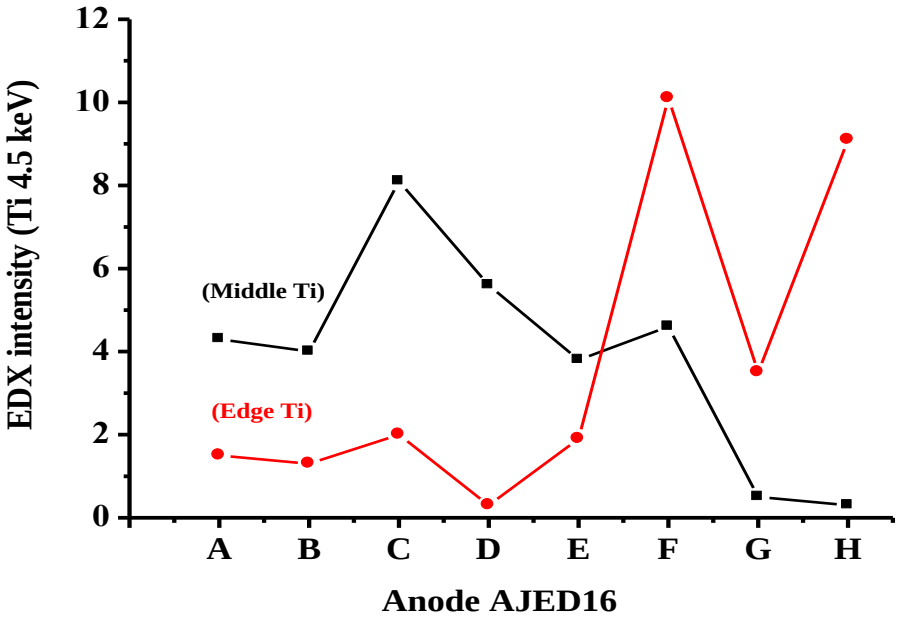

(a)

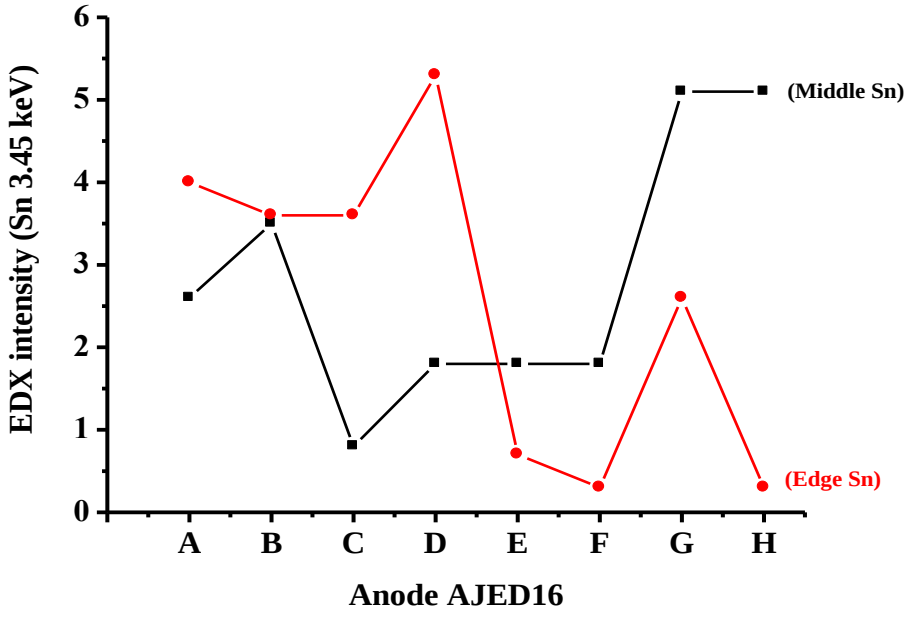

(b)

Figure 4.28 Plot of (a) the 4.5 keV Ti feature and (b) the 3.45 keV Sn band from the middle and edges of the anodes AJED16 series.

4.5.3 The effect of furnace temperature

In order to explore the effect of the pyrolysis temperature, two anode series (2.5 cm x 2.5 cm) were fabricated. The anodes AJED12 series were made to explore the effect of furnace temperature and pyrolysis time, and the anodes AJED13 series to investigate, in addition to temperature and time, the catalyst coating thickness. The characteristics of the two anode series are summarised in tables 4.7 and 4.8.

Anode AJED12	**Area /cm^2**	**Furnace temperature/^{o}C**	**Pyrolysis time/minutes**
A	6.25	480	20
B	6.25	480	20
C	6.25	480	40
D	6.25	480	40
E	6.25	520	20
F	6.25	520	20
G	6.25	520	40
H	6.25	520	40

Table 4.7 Details of the pyrolysis conditions employed in the synthesis of the anodes AJED12 series. All the anodes employed ED1, electrodeposition configuration 1 and CC4, the latter modified according to the table.

Figure 4.29 (a) and (b) show plots of the mass change *vs.* the number of dip-coats of the anodes AJED12 series. The mass changes at dip-coats = 0 is the mass of the EDIL immediately prior to the start of the catalyst coating process. As may be seen from the figure, the electrodeposition step is somewhat irreproducible, giving a range of EDIL masses. In particular anodes AJED12C and AJED12D had significantly higher EDIL masses, and this gave (at least in the case of anode AJED12C) lower catalyst loading. Otherwise, the catalyst uptake following each group of 5 dip-coats was remarkably similar; see figs. 4.29 (a) and (b), following a "saw tooth" pattern. The reason why this should be the case remains unclear.

AJED13 anode	Area /cm^2	Number of dip-coats	Furnace temperature/^{o}C	Pyrolysis time/minutes
A	6.25	10	460	10
B	6.25	10	460	10
C	6.25	20	460	20
D	6.25	20	460	20
E	6.25	20	520	10
F	6.25	20	520	10
G	6.25	10	520	20
H	6.25	10	520	20

Table 4.8 Details of the pyrolysis conditions employed in the synthesis of the anodes AJED13 series. All the anodes employed ED1, electrodeposition configuration 1 and CC4, the latter modified according to the table.

In terms of the final catalyst mass, fig. 4.30 shows the total mass changes for the anodes AJED12 series. From the plot it appears that varying the furnace temperature between 480 ºC and 520 ºC did not have a significant effect upon the total mass of catalyst deposited, but the higher temperature does (apparently) give a more reproducible uptake.

In order to probe the effect of furnace temperature further, the activity and selectivity of the anodes AJED12 series were determined by electrolysis in the glass cell at a voltage of 2.7 V, and typical data are shown in fig. 4.31.

In general, during electrolysis, the anodes AJED12 series showed reasonably stable ozone absorbances and current, with current efficiencies between *ca.* 25 and 35% (measured on the basis of the dissolved zone absorbance alone and hence neglecting any gas phase ozone); fig. 4.32 shows plots of current and current efficiency of the anodes AJED12 series. Each point was the average of two separate experiments.

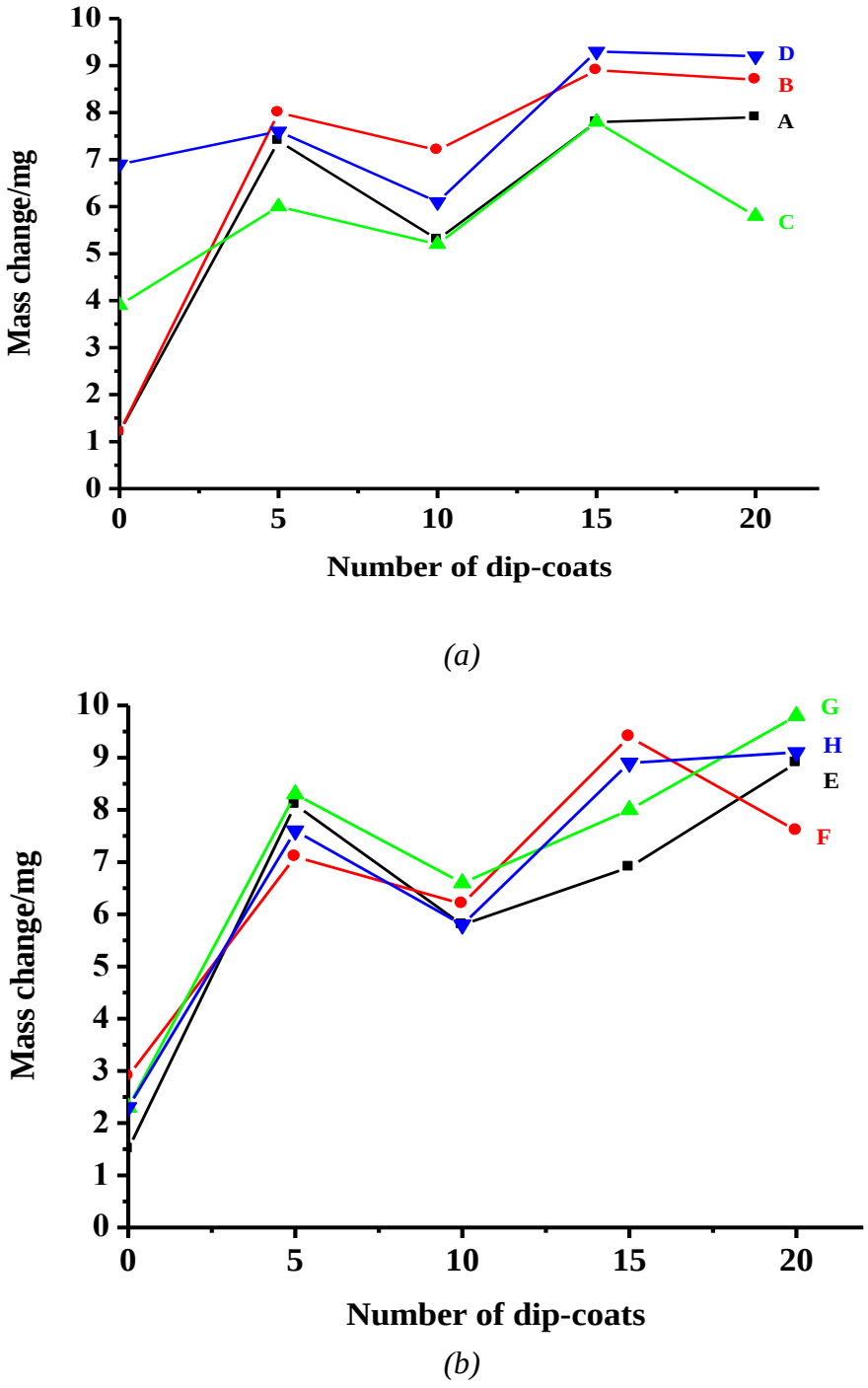

Figure 4.29 Plots of the uptake of catalyst (mg) vs. the number of dip-coats on 2.5 cm x 2.5 cm anodes AJED12 series by (a) anodes AJED12A-D were pyrolysed at 480 ºC; anodes AJED12A-B for 20 minutes, anodes AJED12C-D for 40 minutes and (b) anode AJED12E-H were pyrolysed at 520 ºC; anodes AJED12E-F for 20 minutes, anodes AJED12G-H for 40 minutes.

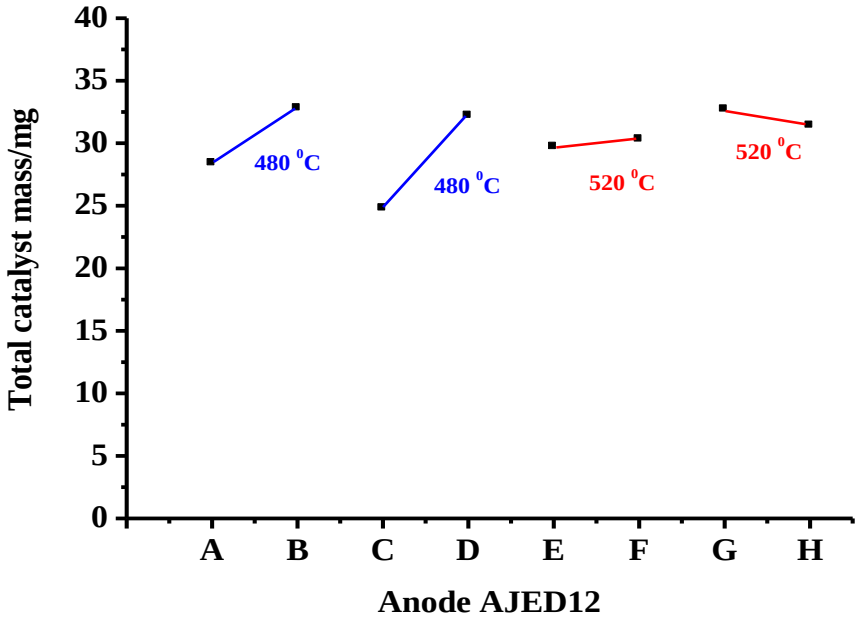

Figure 4.30 The total catalyst uptake (in mg) of the anodes AJED12 series.

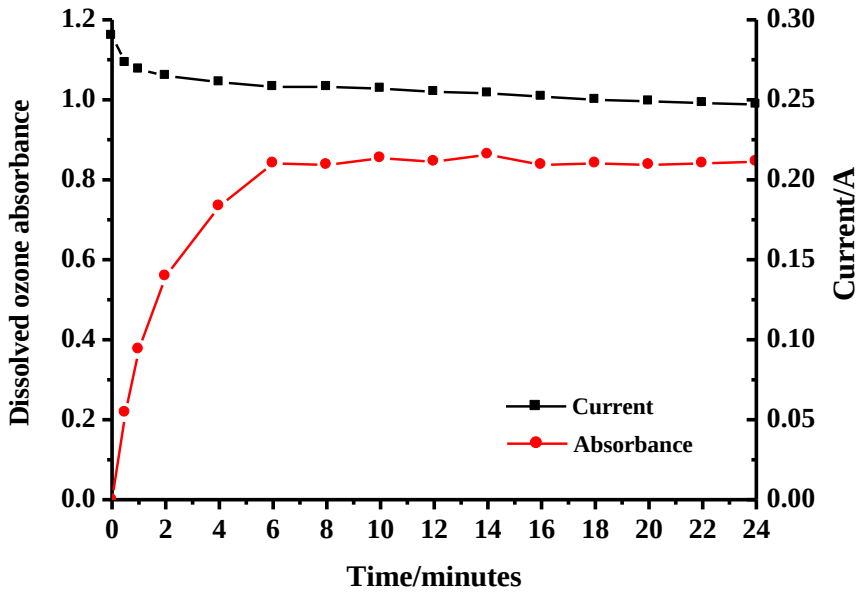

Figure 4.31 Plots of current (■) and dissolved ozone absorbance (●) during the electrolysis of 0.5 M H_2SO_4 using anode AJED12H at a cell voltage of 2.7 V and flow rate of 30 cm^3 min^{-1} in the glass cell.

From fig. 4.32, there does not appear to be any clear relationship between the furnace temperature/pyrolysis time and the current or current efficiency. The AJED13 series of anodes also did not show any clear relationships between the catalyst pyrolysis temperature, time and current or current efficiency. The anodes gave currents between 0.22 and 0.28 A and efficiencies between 20 and 33%.

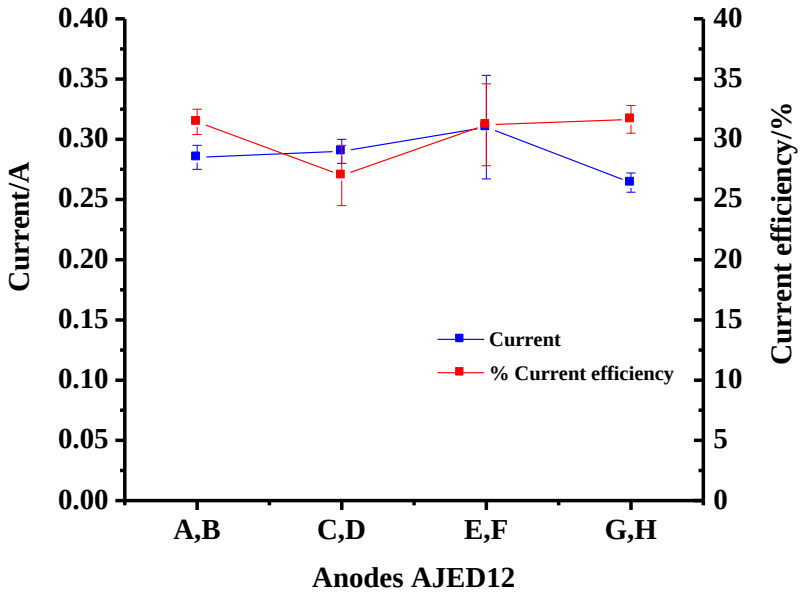

Figure 4.32 Plots of current (■) and ozone current efficiency (■) for the anodes AJED12 series measured as per the experiment depicted in fig. 4.31. Each point was the average of two separate experiments.

4.5.4 EDIL revisited

Section 4.4 and 4.5.3 strongly suggested that the EDIL was a significant influence on the update of catalytic activity of the coating. Hence it was decided to investigate this in more detail. To this end, 24 (2.5 cm x 2.5 cm) anodes were fabricated (anodes AJED19A-L and AJED19a-l) by varying the electrodeposition conditions and (to assess the 'penetration depth' of any potential effect of the EDIL) varying the thickness of the catalyst coating. The synthesis conditions of the various anodes are summarised in table 4.9. All anodes were of nominal composition 500:8:3 and were prepared by CC10. Pyrolysis after electrodeposition was at 520 ºC for 20 minutes.

The catalyst coating method employed was CC10, 2.5 cm x 2.5 cm Ti mesh substrates, 500:8:3 Sn:Sb:Ni in catalyst coating solution.

Anode AJED19	Electrodeposition method	Eectrodeposition cell configuration	Composition of electrodeposition solution, Sn:Sb	Number of dip-coats
A	ED7	1	10:1	20
B	ED7	1	10:1	20
C	ED7	1	10:1	20
D	ED7	1	10:1	20
E	ED7	1	10:1	20
F	ED7	1	10:1	20
G	ED7	1	10:1	20
H	ED7	1	10:1	20
a	ED8	1	10:2	20
b	ED8	1	10:2	20
c	ED8	1	10:2	20
d	ED8	1	10:2	20
e	ED8	1	10:2	20
f	ED8	1	10:2	20
g	ED8	1	10:2	20
h	ED8	1	10:2	20

Table 4.9 The conditions varied during the synthesis of the AJED19 series of anodes.

As usual, a wide range of EDIL loadings were observed, and table 4.10 summarises these.

The anodes were tested for activity in the glass cell by electrolysing 0.5 M H_2SO_4 at a cell voltage of 2.7 V and anolyte flow rate of 30 cm^3 min^{-1}, and the data so obtained are presented in figs. 4.33 (a)-(l) and figs. 4.34 (a)-(d). The data are grouped into narrow ranges of EDIL mass.

Anodes AJED19	Electrodeposition method	Eectrodeposition cell configuration	Composition of electrodeposition solution, Sn:Sb	EDIL mass /mg
A-I	ED7	1	10:1	0.7-6.7
a-h, m	ED8	1	10:2	1.1-4.3
J-L	ED9	1	10:2	0.9-1.8
i-l	ED10	2	10:2	1.4-1.9

Table 4.10 Summary of the range of EDIL masses of the AJED19 series of anodes.

Figures 4.33 (a)-(f) show the variation in the average current measured during electrolysis in the glass cell *vs.* catalyst loading for EDIL masses of 1.05 ± 0.35, 1.75 ± 0.15, 2.35 ± 0.15, 3.25 ± 0.25, 4.05 ± 0.25 and 5.85 ± 0.85 mg cm^{-2}, respectively. The data in fig. 4.33 (a) are fairly scattered, perhaps reflecting the inhomogeneous nature of the EDIL at such coverage. Otherwise, from 1.75 ± 0.15 to 3.25 ± 0.25 mg cm^{-2} the current showed a general increase with catalyst loading. However, at an EDIL mass of 4.05 ± 0.25 mg cm^{-2} (*i.e.* 4.65 ± 0.04 mg cm^{-2}), the current shows a decrease with increased catalyst loading, which is more pronounced in fig. 4.33 (f). It is also worth noting that the catalyst uptake was significantly lower on the meshes with the highest EDIL mass than on the meshes with lower EDIL loadings, in broad agreement with previous results. Figures 4.34 (a)-(f) show the corresponding plots of current efficiency *vs.* catalyst loading. If the point at the highest catalyst loading in fig. 4.34 (h) is disregarded, and if the lack of data at loadings <5 $mgcm^{-2}$ in fig. 4.34 (e) is taken into account, then figs. 4.34 (a)-(f) appear to show a general increase in ozone current efficiency with catalyst loading, as was also observed in section 4.4.3

Figure 4.35 (a) to (d) show the variation in current and current efficiency *vs.* EDIL mass with *ca.* constant catalyst loading (3.15 ± 0.15 mg cm^{-2} and 5.8 ± 0.1 mg cm^{-2}). There do not appear to be any clear trends in the figures; apart from an apparent decrease in current with increasing EDIL mass, consistent with the resistive nature of antimony oxides [25]..

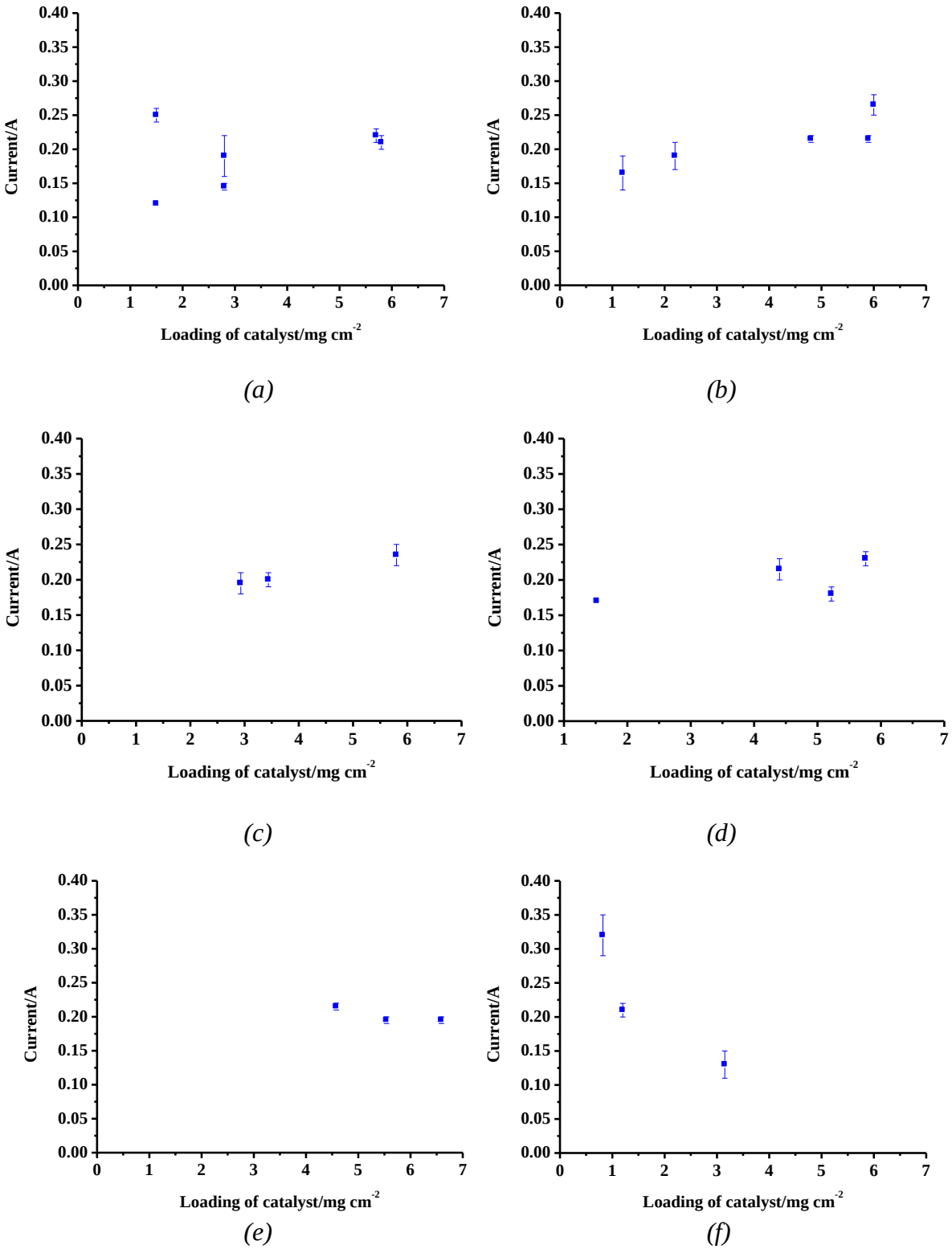

Figure 4.33 Plots of the variation in current vs. catalyst mass of the anodes AJED19 series with ca. constant EDIL loading of (a) 1.05 ± 0.35, (b) 1.75 ± 0.15, (c) 2.35 ± 0.15, (d) 3.25 ± 0.25, (e) 4.05 ± 0.25 and (f) 5.85 ± 0.85 mg cm^{-2}.

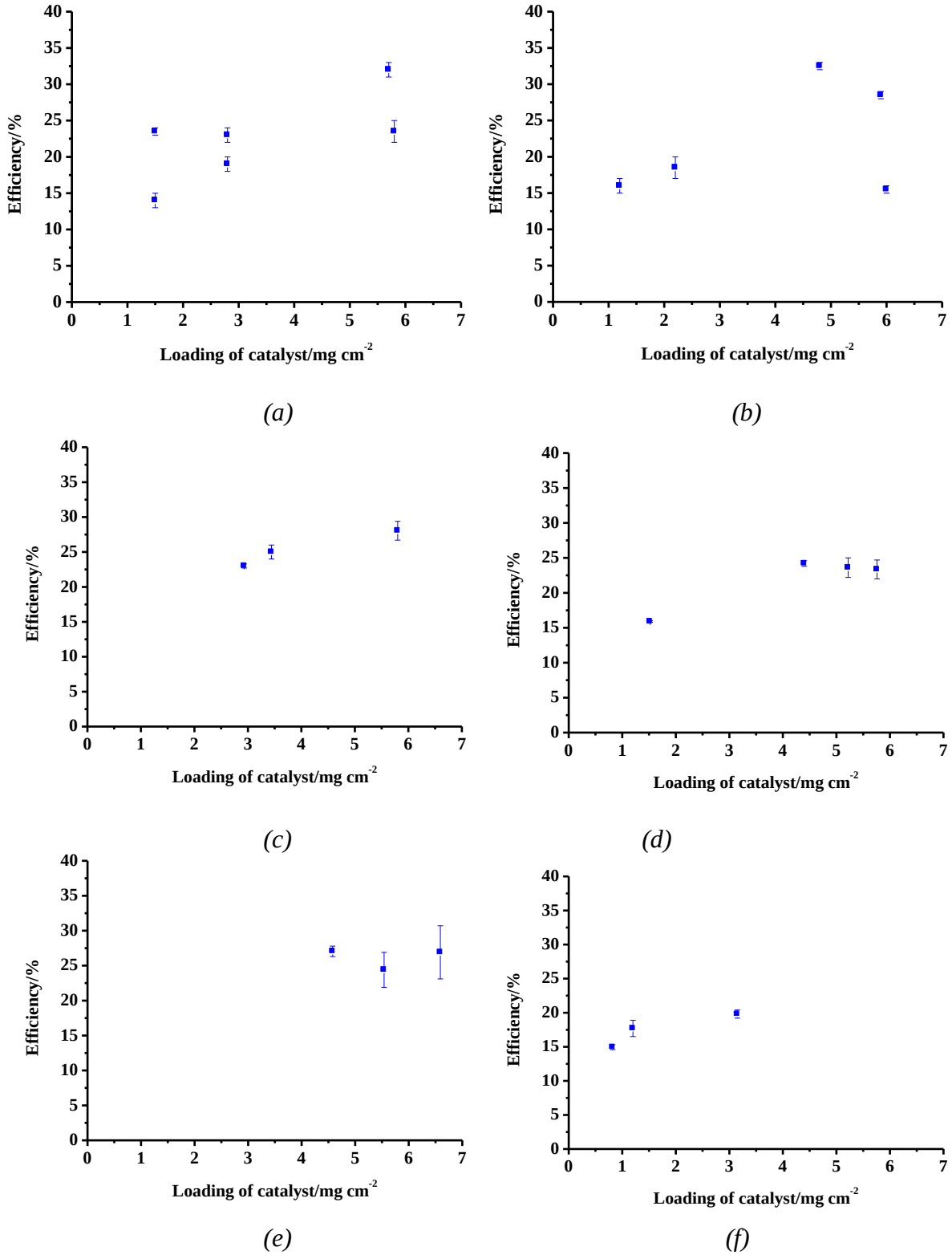

Figure 4.34 Plots of the variation in current efficiency vs. catalyst mass of the anodes AJED19 series with ca. constant EDIL loading of (a) 1.05 ± 0.35, (b) 1.75 ± 0.15, (c) 2.35 ± 0.15, (d) 3.25 ± 0.25, (e) 4.05 ± 0.25 and (f) 5.85 ± 0.85 mg cm^{-2}.

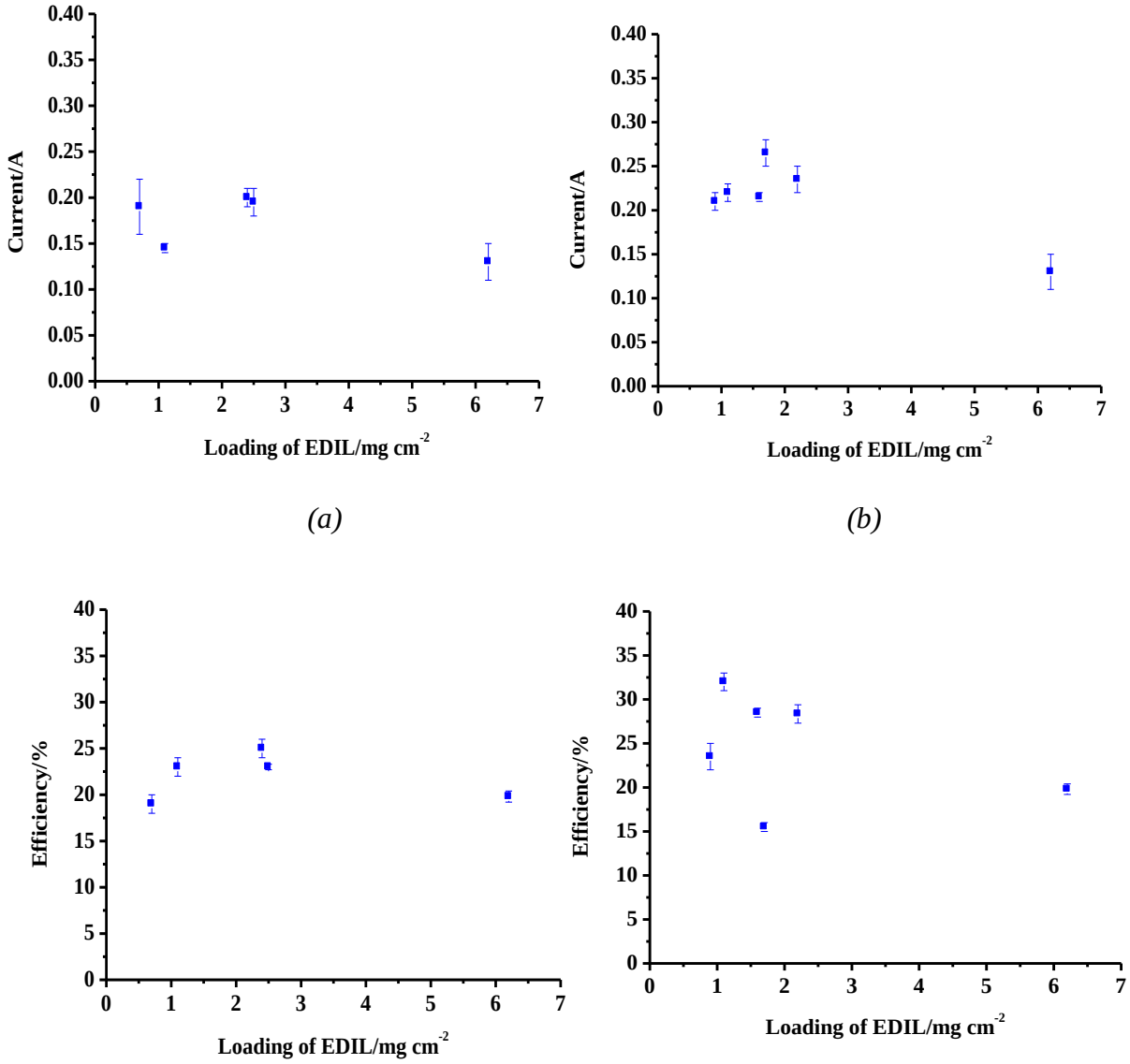

Figure 4.35 (a) and (b) Plots of the variation in current vs. EDIL mass and (c) and (d) Plots of the variation in current efficiency vs. EDIL mass of the anodes AJED19 series with ca. constant catalyst loading of 3.15 ± 0.15 mg cm^{-2} ((a) and (b)) and 5.8 ± 0.1 mg cm^{-2}((c) and (d)).

From table 4.10 it can be seen that ED10 using cell configuration 2 and 10:2 Sn:Sb gave the narrowest distribution of EDIL masses, in agreement with the results in section 4.4.3.

4.6 Conclusions

The electrodeposition of the EDIL is a major source of irreproducibility in the anode synthesis. In the paper by Li et al. which was the inspiration for the Hong Kong group seeking to electrodeposit a Sn + Sb interlayer, no characterisation of the EDIL was carried out. It has shown that Sn does not deposit, only Sb, and that the Sb does not generally form a homogeneous layer upon the Ti mesh substrate, nor does it deposit reproducibly in terms of mass per unit area. My work did not show any advantage in terms of durability of employing the Sb EDIL, and its use has been abandoned in favour of alternative protective coatings.

The irreproducibility of the mass and morphology of the Sb EDIL rendered the search for structure/activity correlations very challenging, as it is clear from the work in this chapter that the EDIL has a significant effect upon catalyst uptake, even up to 20 dip-coats, with catalyst loading generally decreasing as EDIL mass increases. However, the large number of experiments carried out allowed data across the anode series investigated to be grouped according to *ca.* constant EDIL and constant catalyst loading and hence some correlations made. Thus, at EDIL loading ≤ 4 mg cm^{-2} the loading of catalyst generally increased with the number of dip-coats, and current (measured at cell voltage of 2.7 V) also increases with loading, suggesting a porous/3D anode structure. Surprisingly, the ozone current efficiency also increased (*i.e.* the ratio of O_3 to O_2 evolving sites increases), suggesting (perhaps) an enrichment of Ni at the electrode surface. At EDIL > 4 mg cm^{-2} the situation is less clear-cut. At constant catalyst mass, current and current efficiency decrease with EDIL mass. The former could simply be due to the resistance of antimony oxides; however, the latter is less straightforward to explain.

There appeared to be no difference in terms of catalyst uptake, current or current efficiency between anodes pyrolysed at 480 ºC and 520 ºC, irrespective of whether they were pyrolysed for 20 or 40 minutes. In general, it was routinely possible to make anodes having ozone current efficiencies between 25 and 35% at current densities of 30-

50 mA per (geometric) cm^2 of mesh at a cell voltage of 2.7 V in the glass cell. The optimum ratio of Sn:Sb:Ni in the catalyst solution is 500:8:3.

4.7 References

1. Shanthi, S., C. Subramanian and P. Ramasamy, "Growth and Characterization of Antimony Doped Tin Oxide Thin Film," *Journal of Crystal Growth* 197:858-864 (1999).
2. Rajpure, K. Y., M. N. Kusumade, M. N. N. Spallart and C. H. Bhosale, "Effect of Sb Doping on Properties of Conductive Spray Deposited SnO_2 Thin Films," *Materials Chemistry and Physics* 64: 184-188 (2000).
3. Lozano, B. C., Ch. Comninellis and A. De Battisti, "Service Life of Ti/SnO_2-Sb_2O_5 Anodes," *Journal of Applied Electrochemistry* 27(8):970-974 (1997).
4. Lozano, B. C., Ch. Comninellis and A. De Battisti, "Physicochemical Properties of SnO_2-Sb_2O_5 films Prepared by the Spray Pyrolysis Technique," *Journal of The Electrochemical Society* 143(1): 203-209 (1996).
5. Cheng, S. A., and K. Y. Chan, "Electrolytic Generation of Ozone on an Antimony-Doped Tin Dioxide Coated Electrode," *Electrochemical and Solid-State Letters* 7(3): D4-D6 (2004).
6. Wang, Y. H., S. Cheng, K. Y. Chan and X. Y. Li, "Electrolytic Generation of Ozone on Antimony and Nickel-Doped Tin Oxide Electrodes," *Journal of the Electrochemical Society* 152(11): D197-D200 (2005).
7. Chan, K. Y., and P. A. Christensen, *Personal Communication* (2005).
8. Foller, P. C., and C. W. Tobias, "The Anodic Evolution of Ozone," *Journal of the Electrochemical Society* 129(3): 506-515 (1982).
9. Wang, Y. H., S. Cheng and K. Y. Chan, "Synthesis of Ozone from Air *via* a Polymer-Electrolyte-Membrane Cell with a Doped Tin Oxide Anode," *Green Chemistry* 8: 568-572 (2006).
10. Christensen, P. A., W. F. Lin, H. Christensen, A. Imkum, J. M. Jin, G. Li and C.M. Dyson, "Room Temperature, Electrochemical Generation of Ozone with 50% Current Efficiency in 0.5 M Sulfuric Acid at Cell Voltages < 3V," *Ozone: Science and Engineering* 31(4): 287-293 (2009).

11. Cui, Y. H, Y. H. Wang, B. Wang, H. H. Zhou, K. Y. Chan and X. Y. Li, "Electrochemical Generation of Ozone in a Membrane Electrode Assembly Cell with Convective Flow," *Journal of the Electrochemical Society* 156(4): E75-E80 (2009).
12. Lipp, L., and D. Pletcher, "The Preparation and Characterization of Tin Dioxide Coated Titanium Electrodes," *Electrochemica Acta* 42(7): 1091-1099 (1997).
13. Montilla, F., E. Morallón, A. De Battisti and J. L. Vázquez, "Preparation and Characterization of Antimony-Doped Tin Dioxide Electrodes. Part 1. Electrochemical Characterization," *Journal of Physical Chemistry B* 108(16): 5036-5043 (2004).
14. Montilla F., E. Morallón, A. De Battisti, S. Barison, S. Daolio and J. L. Vázquez, "Preparation and Characterization of Antimony-Doped Tin Dioxide Electrodes. Part 3. XPS and SIMS Characterization", *Journal of Physical Chemistry B* 108(41): 15976-15981 (2004).
15. Feng, Y., Y. Cui, B. Logan and Z. Liu, "Performance of Gd-doped Ti-based Sb-SnO_2 Anodes for Electrochemical Destruction of Phenol," *Chemosphere* 70: 1629-1636 (2008).
16. Kotz, R., S. Stucki and B. Carcer, "Electrochemical Waste Treatment Using High Overvoltage Anodes. Part I: Physical and Electrochemical Properties of SnO_2 Anodes," *Journal of Applied Electrochemistry* 21: 14-20 (1991).
17. Watts, R. J., M. S. Wyeth, D. D. Finn and A. L. Teel, "Optimization of Ti/SnO_2-Sb_2O_5 Anode Preparation for Electrochemical Oxidation of Organic Contaminants in Water and Wastewater," *Journal of Applied Electrochemistry* 38: 31-37 (2008).
18. Vicent, F., E. Morallón, C. Quijada, J. L. Vázquez and A. Aldaz, "Characterization and Stability of Doped SnO_2 Anodes," *Journal of Applied Electrochemistry* 28: 607-612 (1998).
19. Adams, B., M. Tian and A. Chen, "Design and Electrochemical Study of SnO_2-Based Mixed Oxide Electrodes," *Electrochemica Acta* 54: 1491-1498 (2009).
20. Ding, H. Y., Y. J. Feng and J. F. Liu, "Preparation and Properties of Ti/SnO_2-Sb_2O_5 Electrodes by Electrodeposition," *Materials Letters* 61: 4920-4923 (2007).

21. Chen, A., and S. Nigro, "Influence of a Nanoscale Gold Thin Layer on Ti/SnO_2-Sb_2O_5 Electrodes," *The Journal of Physical Chemistry B* 107: 13341-13348 (2003).
22. Martelli, G. N., R. Ornelas and G. Faita, "Deactivation Mechanisms of Oxygen Evolving Anodes at High Current Densities," *Electrochemica Acta* 39(11): 1551-1558 (1994).
23. Plieth, W., *Electrochemistry for Materials Science.* 1st Edition, Oxford: Elsevier, (2008).
24. Li, X. Y., Y. H. Cui, Y. J. Feng, Z. M. Xie and J. D. Gu, "Reaction Pathways and Mechanisms of the Electrochemical Degradation of Phenol on Different Electrodes," *Water Research* 39: 1972-1981 (2005).
25. Sherwood, T. F., *Inorganic and Theoretical Chemistry*. 6th Edition, London: William Heinemann Ltd., p. 465 and p. 572 (1942).
26. Christensen, P. A., K. Zakaria and T. P. Curtis, "Structure and Activity of Ni and Sb-Doped SnO_2 Ozone Anodes," *Ozone Science and Engineering* December (2010).
27. Wang, C. Y., *Antimony: Its history, Chemistry, Mineralogy, Geology, Metallurgy, Uses, Preparations, Analysis, Production and Valuation*. 2nd Edition, London: Charles Griffin and Co. Ltd, p 12 (1919).
28. Centers, P. W., "Sublimation-Controlled Oxidation of Antimony Trioxide," *Journal of Solid State Chemistry* 72: 303-308 (1988).
29. Bryngelsson, H., J. Eskhult, L. Nyholm, M. Herranen, O. Alm and K. Edström, "Electrodeposited Sb and Sb/Sb_2O_3 Nanoparticle Coatings as Anode Materials for Li-Ion Batteries," *Chemistry of Materials* 19: 1170-1180 (2007).
30. Ghosh, J. C, and A. N. Kappana, "Electrodeposition of Antimony," *The Journal of Physical Chemistry* 28: 149-160 (1924).

Chapter 5 Anode Durability

5. Anode Durability

5.1 Introduction

It was clear from the studies on the Ni/Sb-SnO_2 anodes (Chapter 4) that, whilst some remained active (in terms of current and current efficiency) over many months of intermittent use before failing (*e.g.* the anodes AJED2 series, see Chapter 4), other anodes lost activity in days or even hours. The deactivation of Ni/Sb-SnO_2 electrodes could be due to, in broad terms, to one or all of three processes:

(1) Physical loss of catalyst due to (i) spallation (stress cracking from formation of TiO_2 under the coating [1]) and/or (ii) corrosion (etching away of the surface as observed by Foller and Tobias [2]);

(2) Formation of a resistive layer due to (i) complete oxidation of the ($Sb^V \rightarrow Sb^{IV} + e^-$) near the catalyst surface to ($Sb^V + Sb^{IV}$) and/or (ii) oxidation of the Ti substrate to TiO_2 or

(3) Loss of active sites through (i) dissolution of Ni or (ii) passivation.

It was hoped that the combination of thick catalyst coatings and the use of an EDIL would address failure mechanisms 1 (i) and 2 (ii). The dissolution of Ni *via* 1 (ii) and 3 (i) could be a very real problem as metallic Ni would be expected to be unstable under strongly oxidising conditions in acidic solution [3] and Foller and Tobias [2] reported that thin Sb-SnO_2 anodes dissolved during operation. However, as well as the Newcastle group, the Hong Kong group also determined Ni/Sb-SnO_2 anodes that survived many weeks or months of (intermittent) operation in aqueous acid electrolyte. Furthermore, the Hong Kong group conducted experiments in which the electrolyte was analyzed by GCMS following electrolysis without appreciable concentrations of Ni^{2+} being detected [4]. In addition, Professor Geoff Kelsall of Imperial College in London produced the phase (Pourbaix) diagram in fig. 5.1 [5] based on thermodynamic calculations using the potentials for the various Ni redox couples in [3][6][7]; (note: reference [3] gives the Ni^{III} species as $Ni(OH)_3$; this is more likely to be NiOOH [8]).

As can be seen from fig. 5.1, at pH 0.3 (the typical pH of the experiments reported in this thesis) and at a cell voltage of 2.7 V *vs.* the counter electrode (which evolves H_2), Ni would be expected to be in the form of the stable Ni^{III} species.

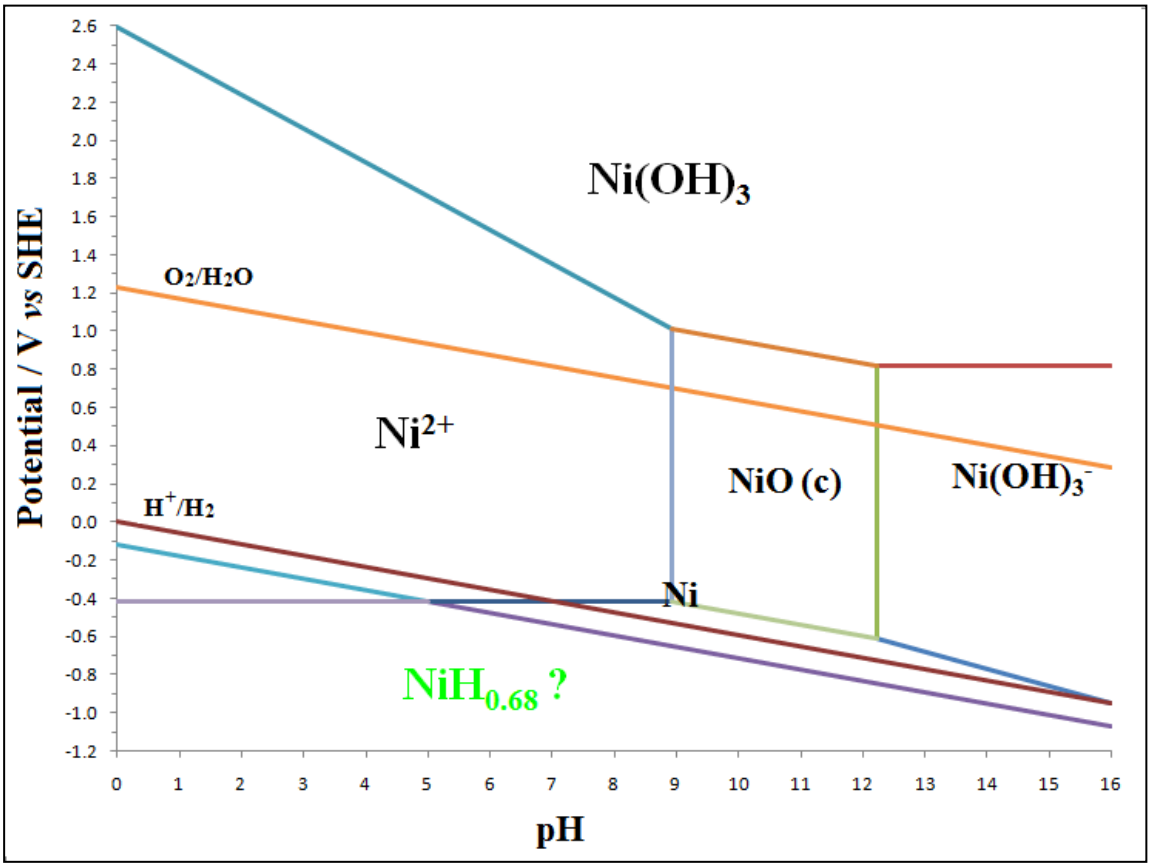

Figure 5.1 Pourbaix diagram for Ni, calculated by Prof. G. Kelsall. See text for details [5].

Section 5.2 deals with spallation and physical loss of catalyst section 5.3 with passivation.

5.2 Physical loss of catalyst and reactivation

In order to explore the durability of the Ni/Sb-SnO_2 anodes, three 2.5 cm x 2.5 cm electrodes were subjected to a series of experiments involving electrolysis and heating in the furnace for 30 minutes (reactivation) interspersed with SEM and EDX measurements

and the measurement of ozone activity in the glass cell, see fig. 3.8. The reactivation steps were included on the advice of Prof. Chan who found that heating at 460 ºC for 30 minutes in air could restore all or some of the ozone activity of deactivated electrodes.

The electrodes chosen for the durability experiments were anodes AJED4F, AJED9F and AJED12E which were made according to electrodeposition and catalyst coating methods ED2/CC2, ED1/CC4 and ED1/CC4 (see table 4.2 and 4.3), respectively. The experimental protocols employed using anodes AJED4F and AJED9F are detailed in tables 5.1 and 5.2. The protocol employed with anode AJED12E was essentially the same as that in table 5.1.

Experiment No.	Experiment	AJED4F
Experiments 1 and 2	O_3 measurement	3/11/08
SEM 1	SEM/EDX	3/11/08
F 1	Reactivation in furnace at 460 ºC for 30 minutes	3/11/08
SEM2	SEM/EDX	5/11/08
Experiments 3 and 4	O_3 measurement	6/11/08
E 1	Electrolyse in 0.5 M H_2SO_4 for 8 hours	7/11/08
Experiments 5 and 6	O_3 measurement	10/11/08
SEM 3	SEM/EDX	13/11/08
F 2	Reactivation in furnace at 460 ºC for 30 minutes	14/11/08
Experiments 7 and 8	O_3 measurement	14/11/08
F 3	Reactivation in furnace at 460 ºC for 30 minutes	17/11/08
Experiments 9 and 10	O_3 measurement	18/11/08
SEM 4	SEM/EDX	19/11/08
E 2	Electrolyse in 0.5 M H_2SO_4 for 8 hours	19/11/08
Experiments11 and 12	O_3 measurement	21/11/08
SEM 5	SEM/EDX	2/12/08

Table 5.1 The experimental protocol employed using anode AJED4F. Experiment = ozone measurement, E = electrolysis (in 0.5 M H_2SO_4 at cell voltage 2.7 V), F = furnace and SEM = analysis.

Experiment No.	Activity	AJED9F
Experiment 1	O_3 measurement	3/11/08
SEM 1	SEM/EDX	3/11/08
F 1	Reactivation in furnace at 460 ºC for 30 minutes	3/11/08
SEM 2	SEM/EDX	5/11/08
Experiments 2 and 3	O_3 measurement	6/11/08
E 1	Electrolyse in 0.5 M H_2SO_4 for 8 hours	10/11/08
Experiment 4	O_3 measurement	11/11/08
SEM 3	SEM/EDX	13/11/08
F 2	Reactivation in furnace at 460 ºC for 30 minutes	14/11/08
Experiments 5 and 6	O_3 measurement	14/11/08
F 3	Re-heat in 460 ºC for 30 minutes	17/11/08
Experiments 7 and 8	O_3 measurement	18/11/08
SEM 4	SEM/EDX	19/11/08
E 2	Electrolyse in 0.5 M H_2SO_4 for 8 hours	19/11/08
Experiments 9 and 10	O_3 measurement	21/11/08
SEM 5	SEM/EDX	2/12/08

Table 5.2 The experimental protocol employed using anode AJED9F. Experiment = ozone measurement, E = electrolysis (in 0.5 M H_2SO_4 at cell voltage 2.7 V), F = furnace and SEM = analysis.

Figure 5.2 (a) and (b) show plots of (a) current and (b) current efficiency *vs.* experiment number for anodes AJED4F and AJED9F, obtained using the glass cell at a cell voltage of 2.7 V.

Taking anode AJED4F first, the current determined at 2.7 V increased from experiment 1 to experiment 2 and then shows a small decline over the next two experiments, apparently unaffected by the furnace treatment (see fig. 5.2 (a)). The current decreased significantly after the first electrolysis, suggesting deactivation, recovers somewhat after the second and third furnace treatments before decreasing significantly again following the second electrolysis. Overall, fig. 5.2 (a) suggests that the activity of anode AJED4F

is decreased with use from experiment to experiment; some fraction of the activity was restored during furnace treatment, but a decreasing fraction with each re-activation. Electrolysis accelerated the decline in activity. The first reactivation had no effect perhaps because the anode was still wholly active.

The variation in the ozone current efficiency essentially supports the observations above, a key difference being the behavior of the anode over the first four experiments. In complete contrast to the current, the current efficiency decreased significantly over the first two runs before being restored by the first reactivation step. This suggests that the ozone active sites switch to O_2 (rather than switching off or being lost) and that this process is reversed by the furnace treatment. Such behavior is consistent with the loss of Ni, perhaps *via* dissolution, and replenishing of the surface by diffusion of Ni from the bulk. The first electrolysis causes a large drop in efficiency as well as current which were essentially irreversible, suggesting physical loss of active sites for both O_2 and O_3 by erosion or spallation.

Anode AJED9F shows somewhat different behavior to anode AJED4F, see figs. 5.2 (a) and (b) on red line. Following the first furnace treatment, the current decreased by *ca.* 30% but the current efficiency increased by *ca.* 15%. The current then steadily increased over experiments 2-5, unaffected by the first electrolysis and (apparently) the second reactivation. In contrast, the current efficiency decreased by 44% after electrolysis, recovering to *ca.* 90% of the efficiency determined during experiment 3 prior to the first electrolysis step. This suggests that the decline in efficiency is again due to the switching of active sites from O_3 to O_2 (rather that physical loss of catalyst) and that this can be reversed by furnace treatment. Both current and current efficiency decreased between experiments 5 and 6, with the decrease in current exacerbated by the third furnace treatment, which (in contrast) restored the current efficiency to *ca.* 36%, suggesting physical loss of catalyst but a switching of active sites to O_3 of the remaining catalyst. The second electrolysis restored some current, but results in a significant (*ca.* 50%) decline in efficiency.

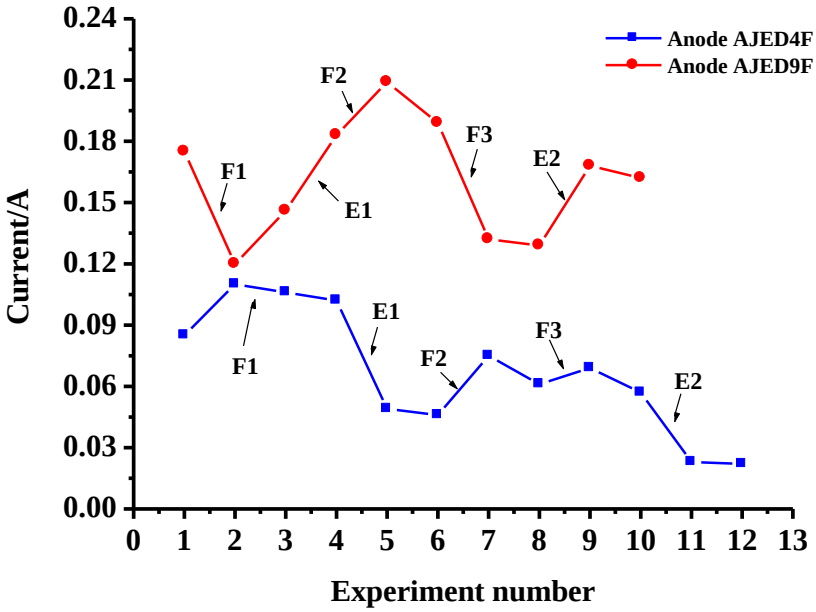

(a)

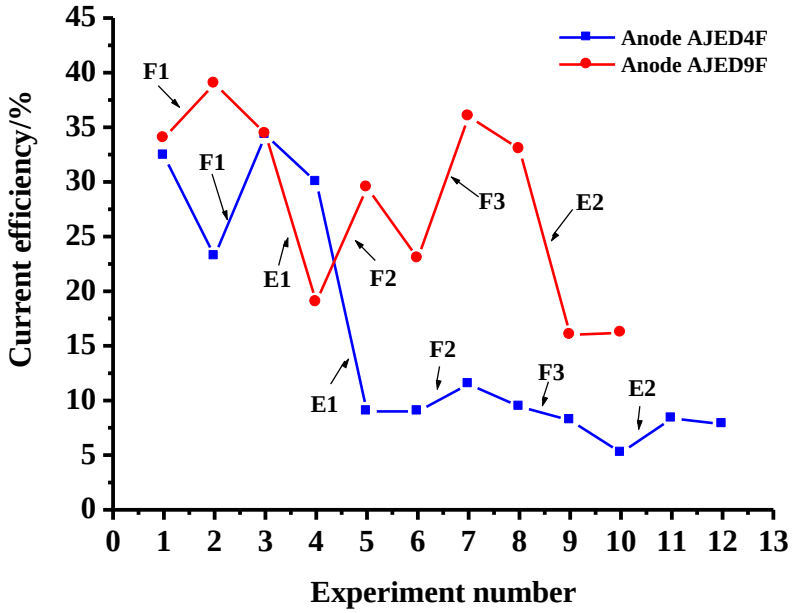

(b)

Figure 5.2 Plot of (a) current and (b) current efficiency vs. experiment number for anode AJED4F (■, blue line) and anode AJED9F (●, red line). The anodes (2.5 cm x 2.5 cm) were tested in single pass system using the glass cell in 0.5 M H_2SO_4 at a cell voltage of 2.7 V and anolyte flow rate of 30 cm^3 min^{-1}. The E (electrolysis) and F (furnace, i.e. reactivation) labels correspond to the entries in table 5.1 and 5.2.

In order to gain more insights into the processes taking place during the experiments depicted in figs. 5.2 (a) and (b), SEM and EDX measurements were taken at regular intervals, and the SEM images are presented in figs. 5.3 and 5.4. The SEM images were taken of the same area of each electrode.

It can be seen from figs. 5.3 (a) and (b) that there was very little difference between the electrode before and after activation. However, following the first electrolysis (fig. 5.3 (c)), the catalyst structure clearly visible at the intersection of the strands in figs. 5.3 (a) and (b) has disappeared, and there appears to be significant loss of catalyst coating from the strands (compare the two right-hand strands in figs. 5.3 (b) and (c)). The catalyst appears to have been removed as a whole layer, rather than as fragments spalling off. That catalyst remains on the Ti mesh may be deduced from a comparison of figs. 5.3 (c) and (d), the former taken after the second and third reactivation following experiment 8, where dark spots indicate further *localized* loss of catalyst (or possibly attack on the Ti substrate). The physical loss of catalyst from anode AJED4F is supported by the catalyst mass loss of 80% determined between the start and end of the experiments depicted in figs. 5.2 and 5.3 and by the SEM data, see fig. 5.4. The latter figure shows plots of the intensities of the 3.48 keV Sn and 4.52 keV Ti EDX peaks of anodes AJED4F and AJED9F obtained from the EDX spectra collected at the specified points during the durability experiments. Figure 5.5 shows the ratio of the intensities of the 3.48 keV (Sn+Sb) peaks and the 3.93 keV (Sb) peak, and figure 5.6 shows a typical EDX spectrum.

From fig. 5.4 it can be seen that, for both anodes, there was a slow decrease in the intensity of the EDX Sn feature, which accelerated after the second electrolysis. In the case of anode AJED4F, this was accompanied by a significant increase in the intensity of the Ti feature as the substrate is exposed by removal of the catalyst layer. Figure 5.5 shows that the ratio of the 3.48 keV feature (Sn + Sb) to the 3.93 keV feature (predominantly Sb) does not change for either anode during the durability studies, suggesting that the relative composition of the anodes in terms of the major constituents does not change. Anode AJED9F loses less of the catalyst coating than anode AJED4F,

26%, during the durability experiments and this seems to be reflected in the lower intensity of the Ti feature in fig. 5.4.

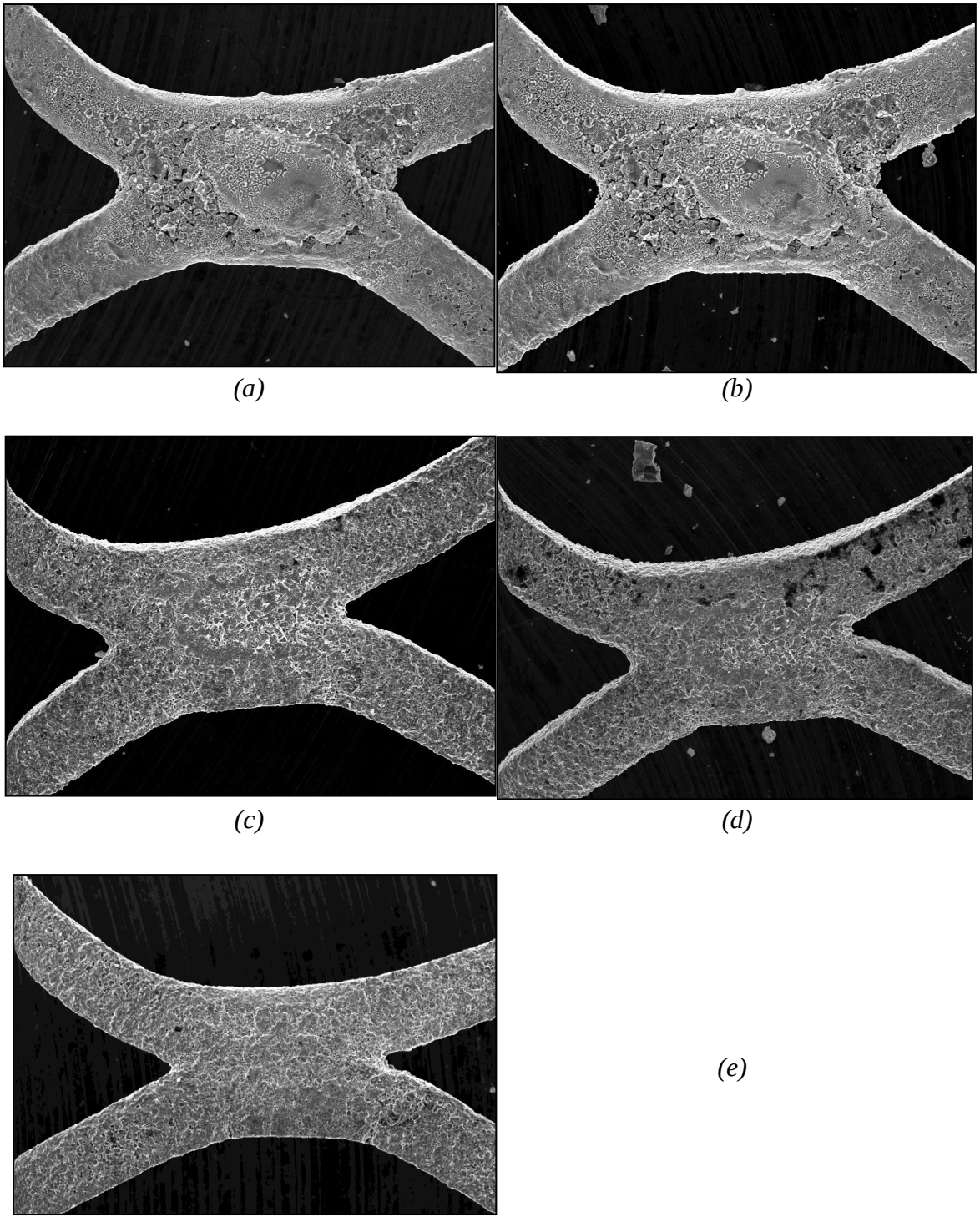

(a) *(b)*

(c) *(d)*

(e)

Figure 5.3 SEM images (x150) of anode AJED4F taken (a) before experiment 1; (b) after the first reactivation (F1); (c) after experiment 6; (d) after experiment 10 and (e) at the end of the durability experiment.

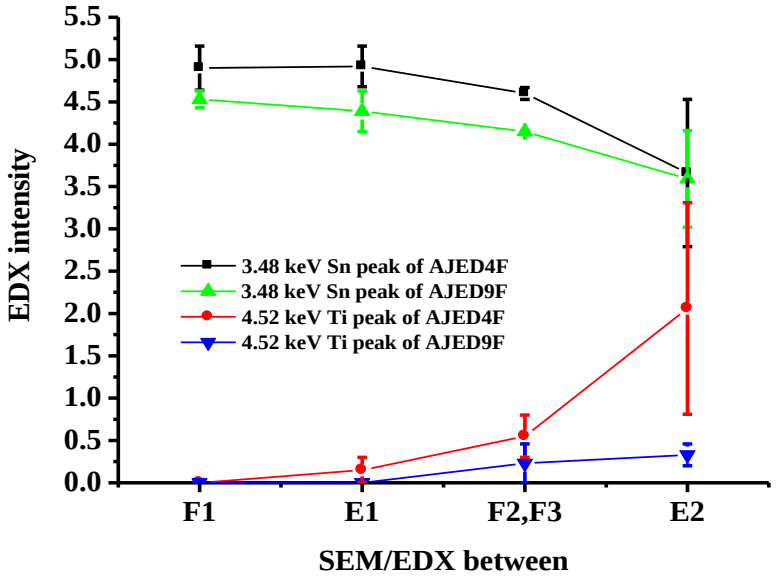

Figure 5.4 Plots of EDX intensity of the 3.48 keV Sn peak of anodes AJED4F (■), AJED9F (▲) and the 4.52 keV Ti peak of anodes AJED4F (●), AJED9F (▼) in the EDX spectra obtained at various times during the experiments in fig. 5.2. The labels correspond to the entries in table 5.1 and 5.2, the E (electrolysis) and F (furnace, i.e. reactivation).

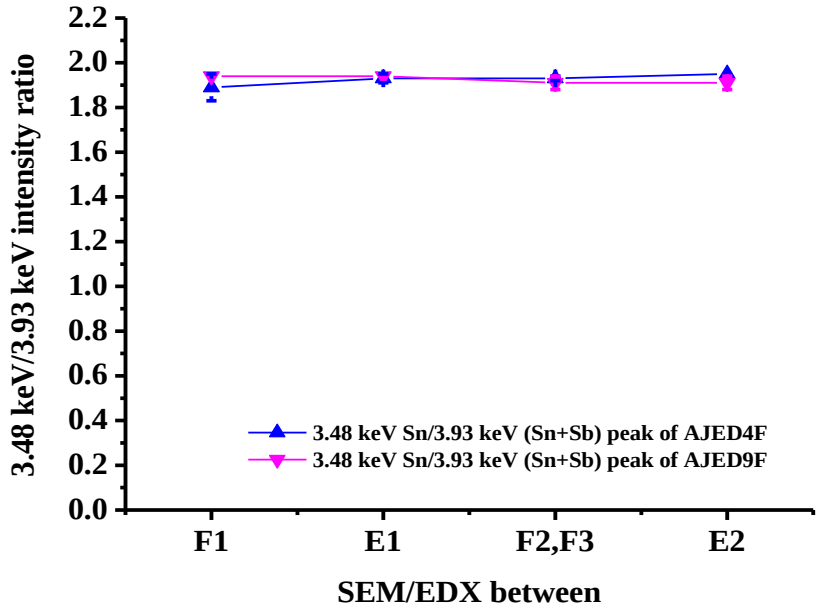

Figure 5.5 Plots of the ratio of the intensity of the 3.48 keV Sn peak to that of the 3.93 keV (Sn + Sb) peak in the EDX spectra of anodes AJED4F (▲) and AJED9F (▼) in fig. 5.4.

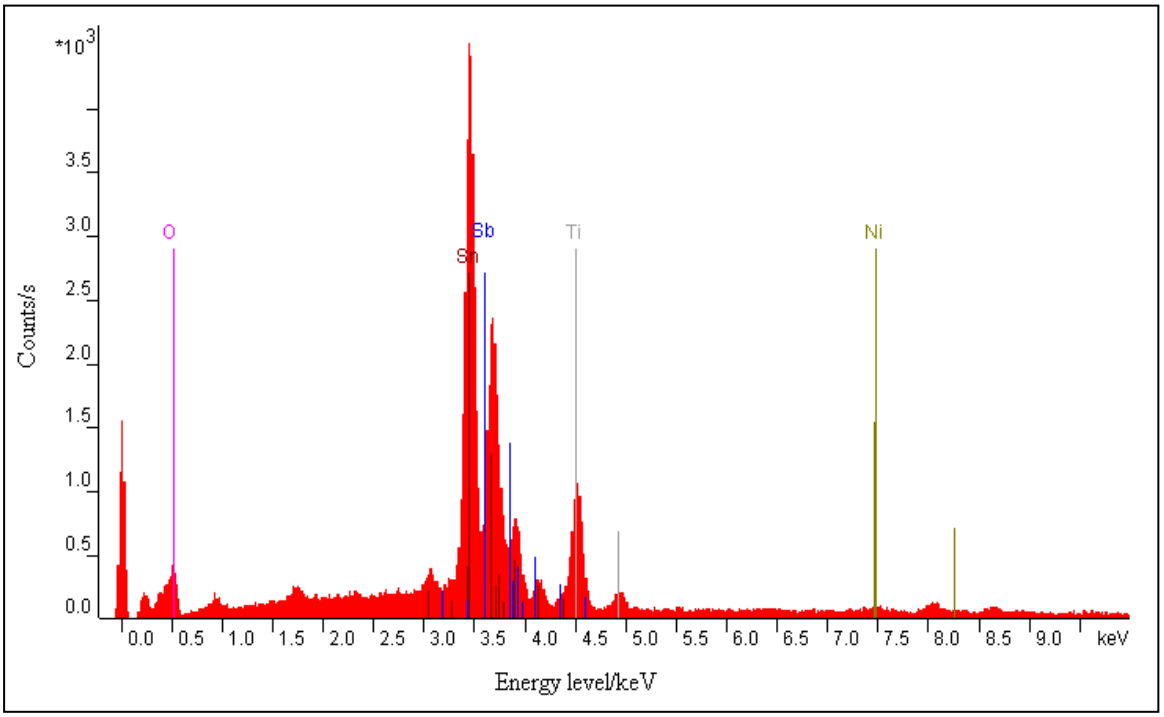

Figure 5.6 Typical EDX spectrum of an area of anode AJED4F taken after the third furnace reactivation carried out after experiment 8.

Figure 5.7 shows the SEM images taken of the same region of anode AJED9F during the durability experiment. As may be seen from the figure, in this region at least, the degradation of the catalyst coating was somewhat different to that of anode AJED4F. Before the experiment commenced, fig. 5.7 (a), it was clear that there were pits/defects in the catalyst coating. After the first activation, there appeared to be very little difference between the images apart from some loss of catalyst from the lower left-hand strand in fig. 5.7 (b). This could simply be due to poor adhesion. However, after the first electrolysis, fig. 5.7 (c), it was clear that large areas of catalyst had spalled off. Those damaged areas on the lower left and top right strands seemed to have their origins in the damaged/incomplete areas of coating visible in fig. 5.7 (a). The losses from the lower right and upper left strands did not seem to originate from such defects; however, the catalyst had clearly fallen away in 'lumps' rather than been eroded layer-by-layer. Following the third reactivation and testing, fig. 5.7 (d), more of the coating seemed to have spalled away from the strands, with no additional damage obvious in the SEM taken at the end of the durability experiment.

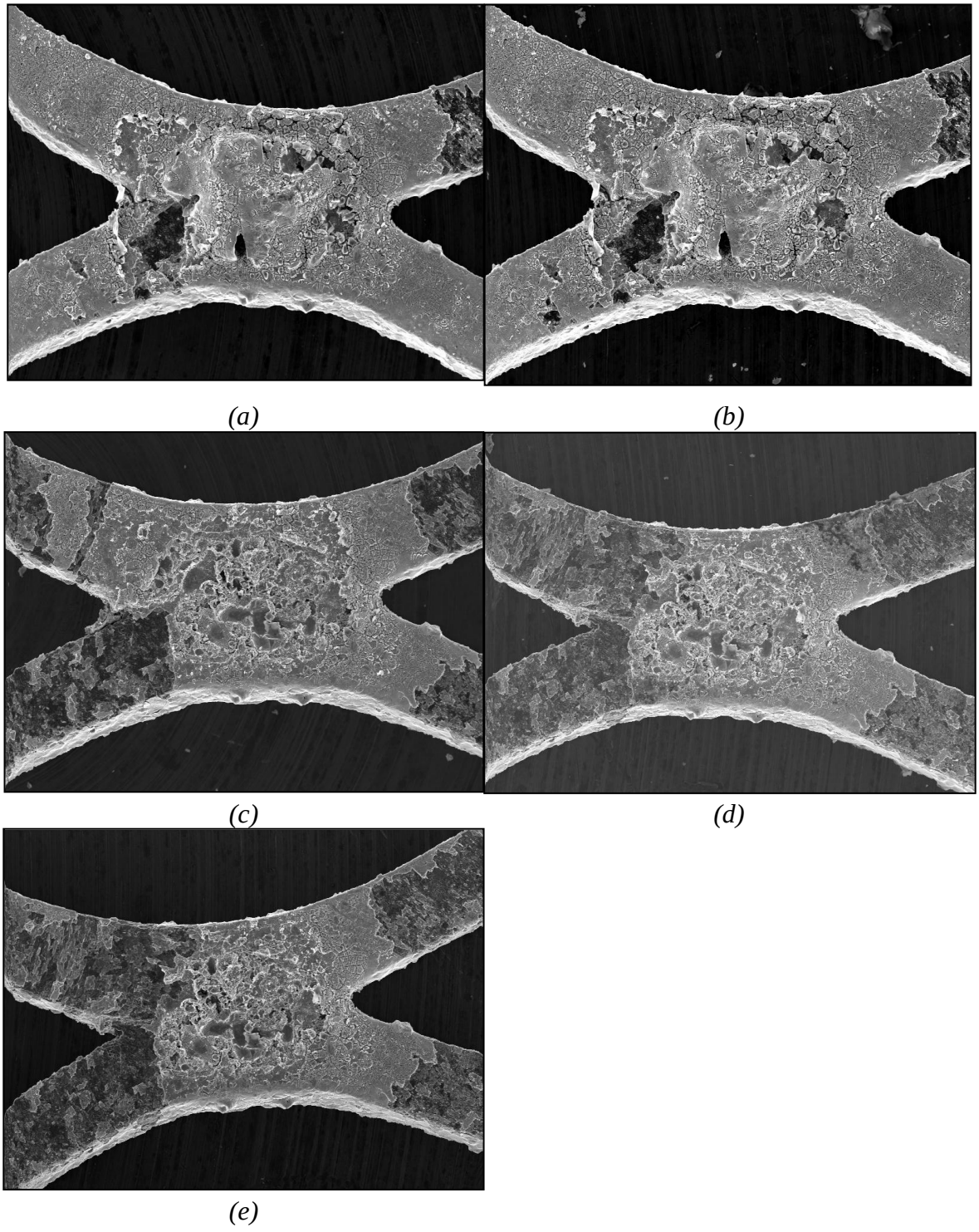

Figure 5.7 SEM images (x150) of anode AJED9F taken (a) before experiment 1 in fig. 5.2 (a); (b) after the first reactivation (F1); (c) after experiment 4; (d) after experiment 8 and (e) at the end of the durability experiment.

Anode AJED12E has elements of the behavior of both anodes AJED4F and AJED9F. The current, see fig. 5.8 (a), behaved as was determined for anode AJED4F in fig. 5.2 (a); *i.e.* overall, a steady decline.

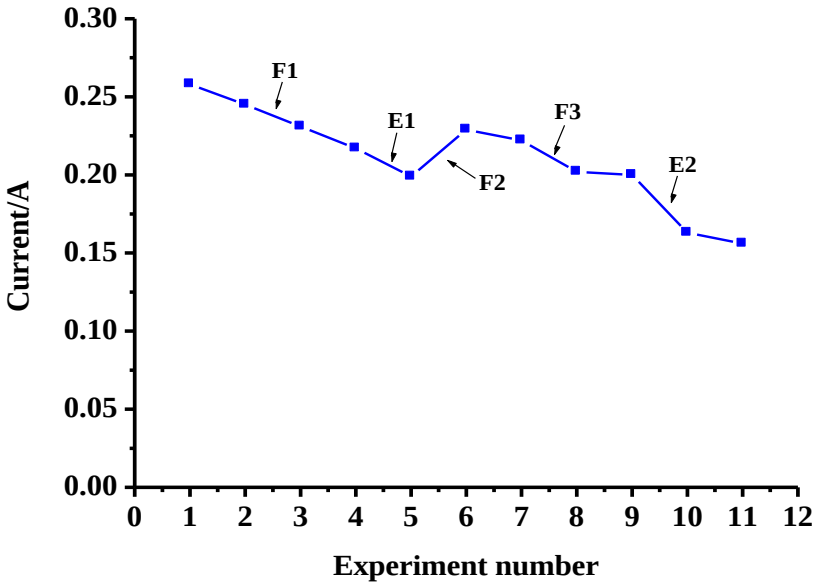

(a)

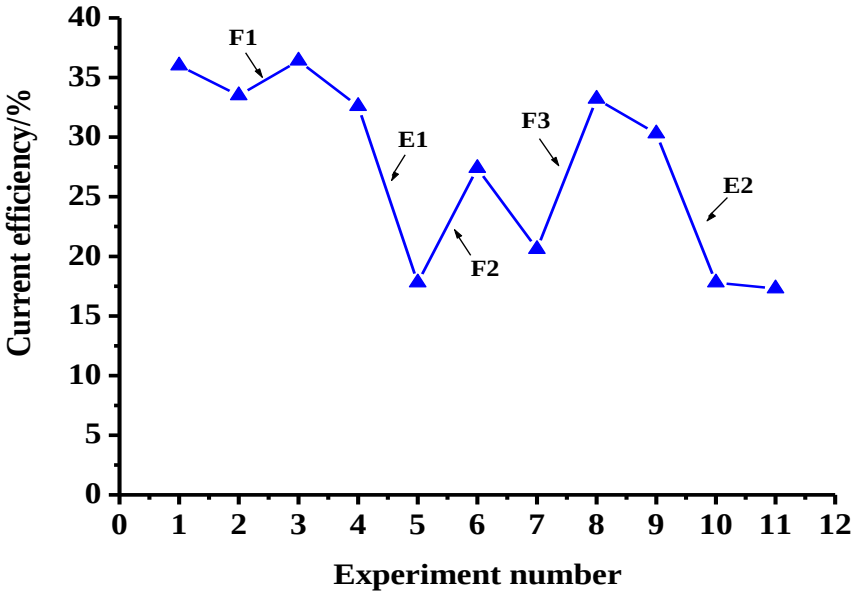

(b)

Figure 5.8 Plots of (a) the current (■) and (b) current efficiency (▲) during an analogous experiment to those in figs. 5.2 (a) and (b) using anode AJED12E.

However, electrolysis did not result in any significant decline in current, nor did the reactivations give any improvement (although F2 did appear to result in a small increase). In contrast, the efficiency showed the large, discontinuous variation observed using anode AJED9F. All the reactivations resulted in increased efficiency and both electrolyses in large decreases. As was the case with anode AJED9F, the first furnace treatment causes a small increase, whilst F2 and F3 result in significant recovery of efficiency. The analogous plots to those in figs. 5.5 showed identical behavior, except no Ti features were determined in the EDX spectra.

Figures 5.9 (a)-(e) show the SEM images collected during the durability experiment on anode AJED12E. The behavior of anode AJED12E seemed to resemble that of anode AJED4F. There is no obvious cracking/spalling away of the catalyst from the Ti substrate; however, the catalyst structure between the two top strands (visible in figs. 5.9 (a) and (b)) disappeared following the first electrolysis, as have the surrounding 'flakes' of coating. No significant changes may then be discerned until the image taken at the end of the experiment where a dark spot due to localized loss may be seen. The total catalyst loss during the durability experiment was *ca.* 13%, comparable to that determined with anode AJED4F rather than anode AJED9F.

5.3 Passivation/corrosion and the addition of Au

In searching for strategies to improve the durability of the Ni/Sb-SnO_2 anodes, Prof. Christensen was severely restricted by the novelty of the electrochemical system. The most logical starting point was studies on methods to enhance the durability of Sb-SnO_2 anodes. Thus, it was believed that the resistance to corrosion of such electrodes could be improved if metal oxides (such as PtO) were added [9].

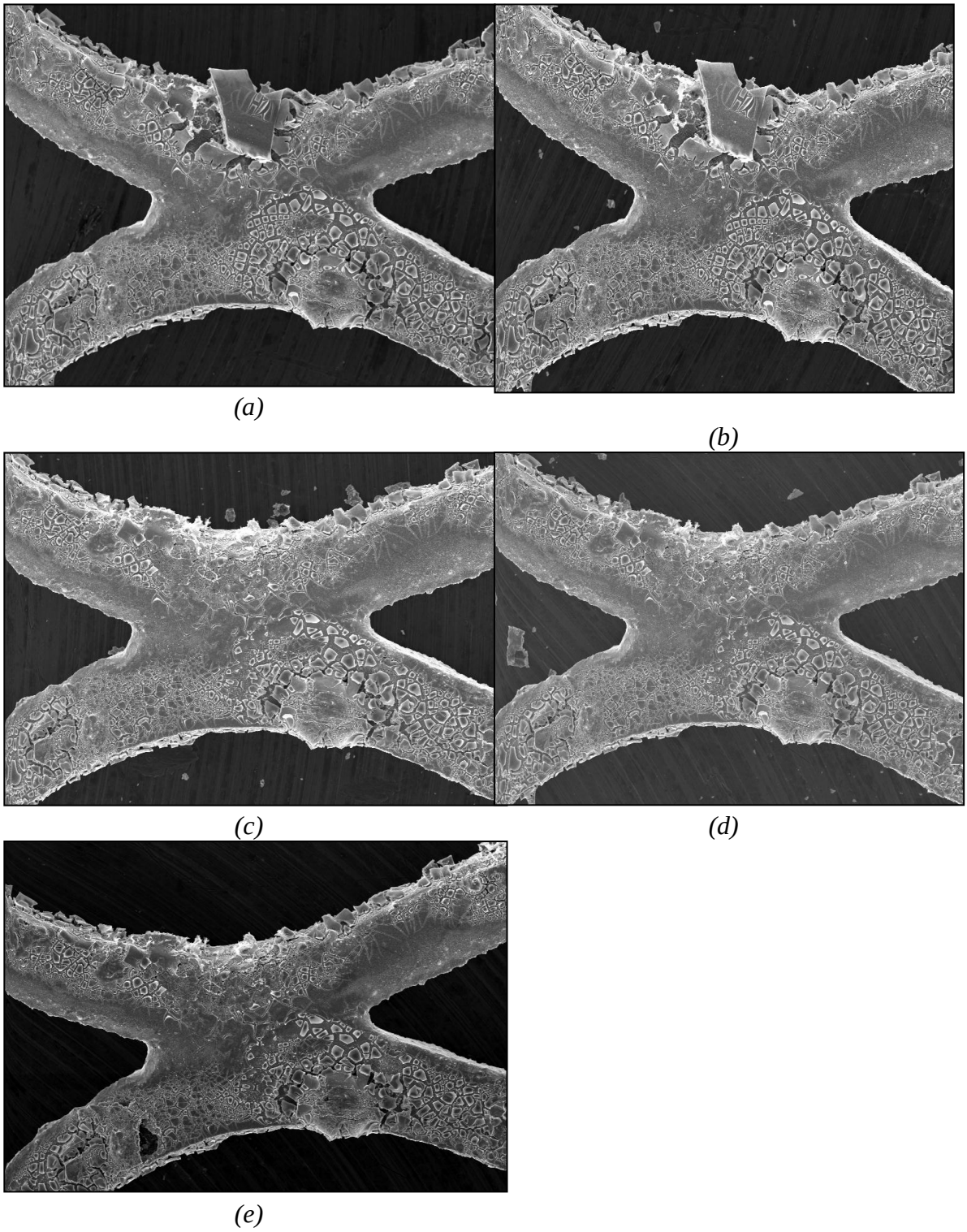

(a)

(b)

(c)

(d)

(e)

Figure 5.9 SEM images (x150) of anode AJED12E taken (a) before experiment 1 in fig. 5.8 (a); (b) after the first reactivation (F1); (c) after experiment 5; (d) after experiment 9 and (e) at the end of the durability experiment.

Vicent, Morallon and co-workers [10] investigated the stability of Sb-SnO_2 and Pt-doped Sb-SnO_2 anodes with the aim of developing stable electrodes for the direct oxidation of organic molecules. Oxygen evolution was employed to probe activity and stability. The authors found that the deactivation of the anode (determined as a sudden, large increase in anode potential) could be delayed significantly by doping with Pt. Thus, doping with Pt (0.42-2% H_2PtCl_6 in coating solution), whilst reducing the oxygen overvoltage by *ca.* 0.5 V, improved the lifetime of the anodes from a few hours up to 760 hours, see figs. 5.10 and 5.11. The authors did not consider the possible role of Pt or PtO in preventing corrosion of the Sb-SnO_2 and hence increasing the lifetime of the anodes; instead, the authors cited a theory reported by Kotz et al. [11] in 1991 that electrode deactivation was due to hydration of the SnO_2 surface, and hence passivation.

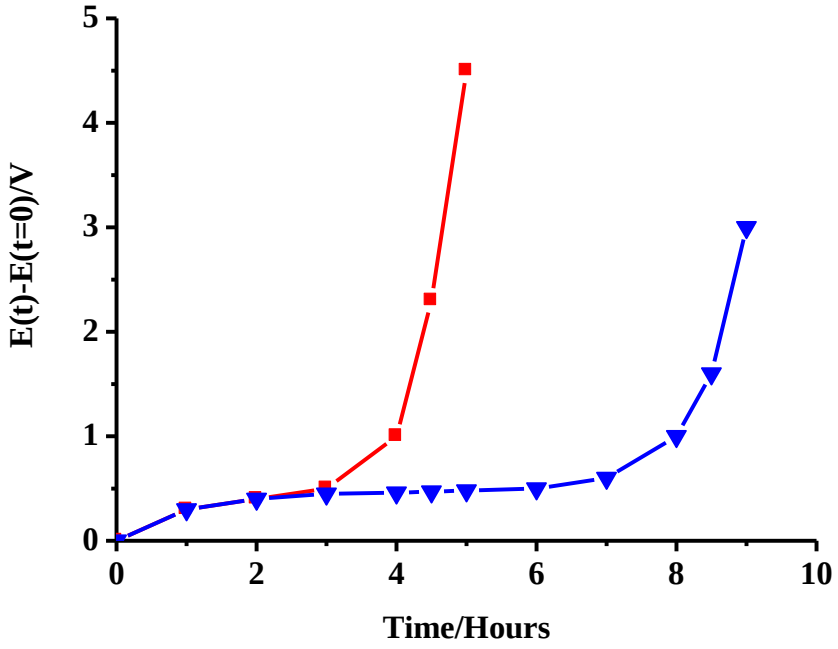

Figure 5.10 The difference between the anode potential at any time t and the anode potential at the start of the experiment, E(t) –E(t=0), against electrolysis time in 0.5 M H_2SO_4 for SnO_2 electrodes doped with antimony with: five spray-pyrolysis sequences (■), nine spray-pyrolysis sequences (▼). Current density (j) = 10 mA cm^{-2}. Taken from [10].

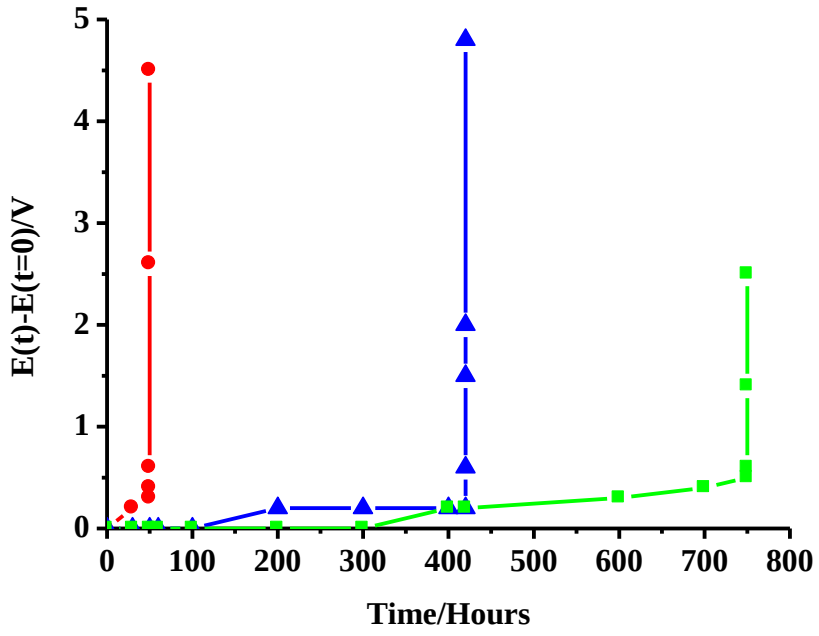

Figure 5.11 The difference between the anode potential at any time t and the anode potential at the start of the experiment, E(t) –E(t=0), against electrolysis time for SnO_2 electrodes doped with antimony and platinum with: five spray-pyrolysis sequences (●) from a 10% $SnCl_4$ + 1% $SbCl_3$ + 0.42% H_2PtCl_6 in ethanol + HCl solution in 0.5 M H_2SO_4, fifteen spray-pyrolysis sequences (▲) from a 10% $SnCl_4$ + 1% $SbCl_3$ + 2.1% H_2PtCl_6 in ethanol + HCl solution in 0.5 M H_2SO_4 and fifteen spray-pyrolysis sequences (■) from a 10% $SnCl_4$ + 1% $SbCl_3$ + 2.1% H_2PtCl_6 in ethanol + HCl solution in 0.5 M K_2SO_4. Current density (j) = 40 mA cm^{-2}. Taken from [10].

In 2004, in a series of papers [12][13][14], Morallon developed the passivation model through a detailed investigation of the failure of Sb-SnO_2 anodes undoped and doped with Pt, using electrochemical techniques [12], XRD and EXAFS [13] and XPS and SIMS [14]. The authors found that addition of Pt up to an optimum concentration of 3 atom% increased the service life of Sb-SnO_2 anodes by up to 2 orders of magnitude.

Both Montilla et al. [12] and Correa-Lozano and co-workers [1] derived that thicker anodes exhibited a 'typical' cracked mud morphology and that this changed on adding Pt to a more compact structure. However, the roughness factor R_f increased on adding Pt by a factor of *ca.* 2.

Montilla and co-workers [12] found that both unused and deactivated Sb-SnO_2 anodes showed capacitive behaviour, whilst the latter clearly showed a higher potential onset for oxygen evolution than the former in cyclic voltammetry experiments; the R_f values of new anodes were slightly lower than those of the deactivated electrodes. In contrast, Pt/Sb-SnO_2 anodes showed capacitive behaviour when new, but the deactivated electrodes exhibited non linear current density *vs.* scan rate plots, suggesting poor capacitive charge transfer between the Ti substrate and the catalyst coating (due to oxidation of the Ti), and a different deactivation route for the Pt-containing electrodes compared to the Pt-free.

In XPS, the O 1s transition overlies the Sb $3d_{5/2}$ peak in XPS spectra; however, the ratio of the latter and the Sb $3d_{5/2}$ feature is well known (1.44 [14]) and hence the Sb and O feature can be deconvoluted. The O 1s feature can be resolved into two contributions: a peak at 531.0 eV which may be attributed to metallic oxide (M-O) and a peak at 532.4 eV attributed to M-OH or hydrated surface species ([14] and references therein). On deactivation of Sb-SnO_2, the ratio of the intensity of the latter peak to the former increased from 0.71 to 1.24; the Sb-SnO_2 anode doped with 3 atom% Pt showed a decrease in the same ratio on deactivation: from 0.67 to 0.51.

The XPS data, taken together with the results of the electrochemical experiments, were taken by Montilla as strong evidence for the deactivation of Sb-SnO_2 *via* the formation of a passivating OH-containing layer at the SnO_2/electrolyte interface. Pt was postulated as preventing this, and hence significantly extending the service life; with added Pt, deactivation was postulated as occurring through long term attack on the Ti substrate and the formation of a passivating layer at the Ti/catalyst interface, possibly TiO_2.

Although Montilla et al. have focussed on the passivation theory, they also obtained XRD data showing marked effects on deactivation, and a significant impact of the addition of Pt on these effects which may point to alternative mechanisms for deactivation. Thus, SnO_2 cassiterite exhibits a rutile type structure. Sb forms a solid solution with Sn, resulting in a decrease in the unit cell volume on doping [13]. The

authors found that Sb-SnO_2 doped with 3 atom% Pt had a larger crystallite size than in the absence of Pt, 59 Å *cff.* 45 Å, whilst the unit cell volume in the presence of Pt was 69.00 Å compared to 70.22 Å. On deactivation, the unit cell volume of Sb-SnO_2 decreased by 2% whilst the crystallite size decreased by 36%; in contrast, the Pt-doped anodes showed little change in these parameters, suggesting that the Pt prevents the structural changes associated with the deactivation of the Sb-SnO_2.

Professor Christensen postulated that Montilla's 'surface disruption' strategy, whether preventing passivation or structural change, was worth pursuing. Reasoning, that Pt would increase the current efficiency of O_2 evolution to an unreasonable extent if included in the catalyst coating, he suggested the use of Au and Pb as possible dopants [15] and part of my project was to investigate the use of Au.

5.3.1 Initial studies using Au

The initial work on gold-containing Ni/Sb-SnO_2 anodes ('PC series') was carried out immediately before my arrival in Newcastle. A ratio of 500:8:1:1.5 was chosen for the mole ratio of Sn:Sb:Ni:Au in the dip-coating solution ($AuCl_3$ was employed as the source of Au). The electrodeposition and catalyst coating methods employed were closest to ED1 and CC4, respectively. 6.25 cm^2 Ti mesh substrates were employed.

The initial studies were carried out before the routine use of the glass cell, and the electrochemical cell and system employed is shown in figs. 5.12 (a) and (b).

The data was promising, as may be seen from figs. 5.13 (a) to (d). Figures 5.13 (a) and (b) show plots of the ozone solution absorbance *vs.* time for anode PC6 and figs. 5.13 (c) and (d) for anode PC8, respectively, both prepared on 2.5 cm x 2.5 cm Ti mesh substrates. The plots were obtained in the large glass cell after the specified, continuous, periods of electrolysis cell depicted in figs. 5.12 (a) and (b). After each electrolysis, the anolyte and catholyte were replaced and the experiments in the figures carried out typical currents were *ca.* 0.2 A. Figures 5.13 (b) and (d) show plots of (dissolved ozone absorbance/current) for the experiments in figs. 5.13 (a) and (c).

As may be seen, there appears to be a steady activation of the anodes; both anodes show very little ozone activity when freshly prepared, but activate steadily with electrolysis time.

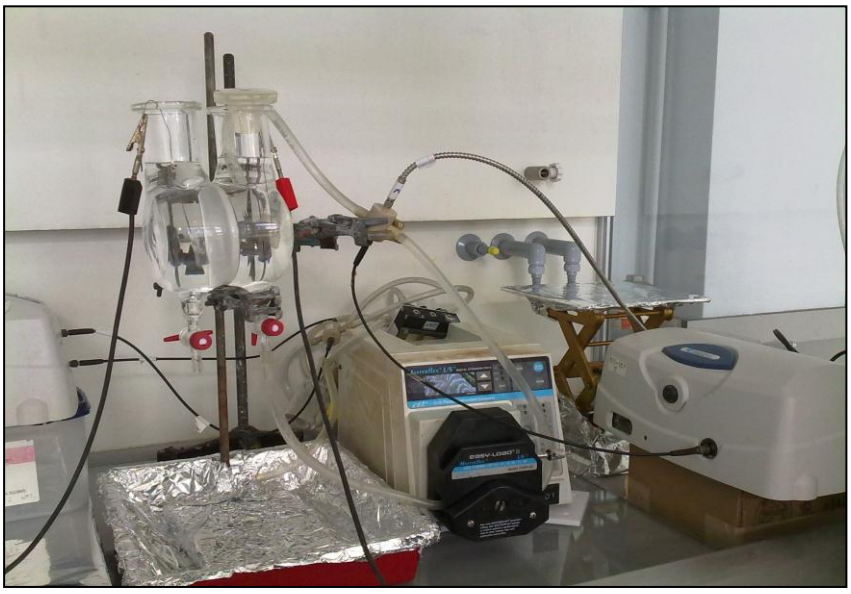

(a)

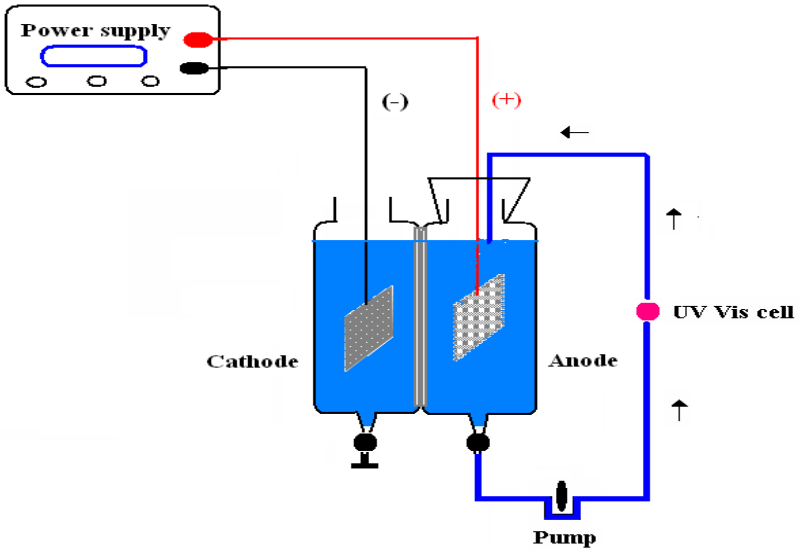

(b)

Figure 5.12 (a) Photograph and (b) Schematic of the electrochemical cell employed in the initial studies on the activation of Au-containing Ni/Sb-SnO_2 anodes. Anolyte and catholyte 350 cm^3 (each) 0.5 M H_2SO_4, anolyte flow rate 90 cm^3 min^{-1}, cell voltage 3.0 V.

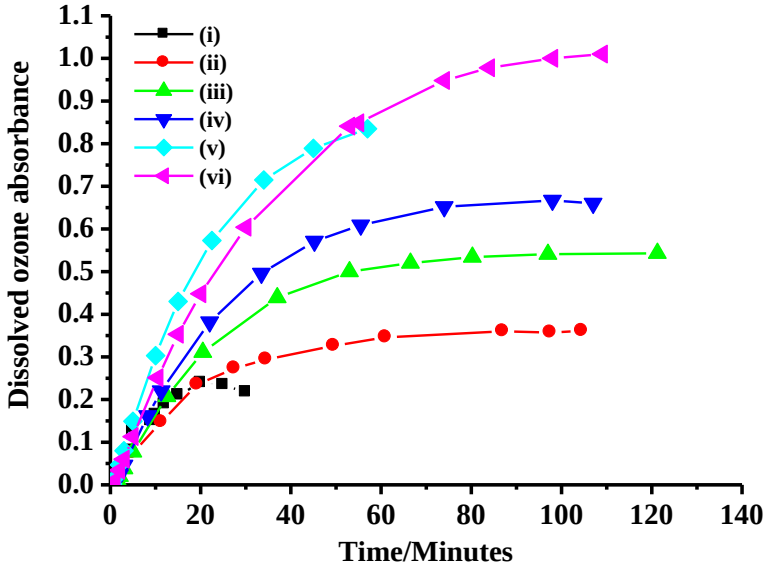

(a)

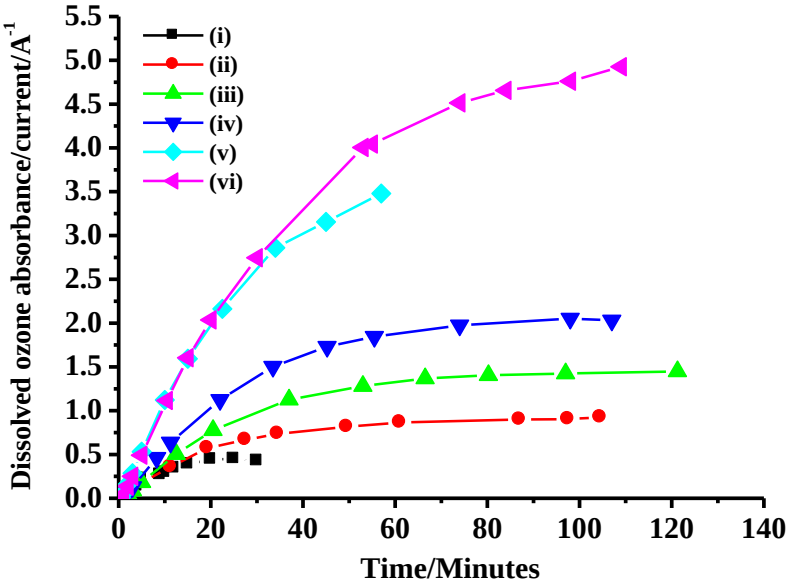

(b)

Figure 5.13 Plots of (a) ozone absorbance vs. time, and (b) ozone absorbance/current at wavelength 258 nm obtained in figs. 5.12 (a) and (b), a cell voltage was 3.0 V, 0.5 M H_2SO_4 anolyte and catholyte, at a flow rate of 90 cm^3 min^{-1} in recycle mode of (i) freshly prepared (■), (ii) after 2 days electrolysis at 3.0 V (●), (iii) after 4 days (▲), (iv) after 6 days (▼), (v) after 19 days (♦) and (vi) after 25 days (◄) anode PC6. See text for details.

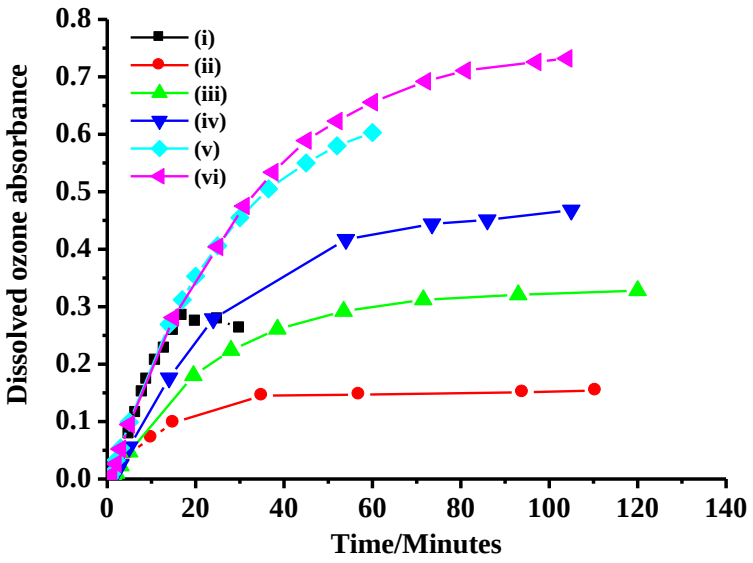

(c)

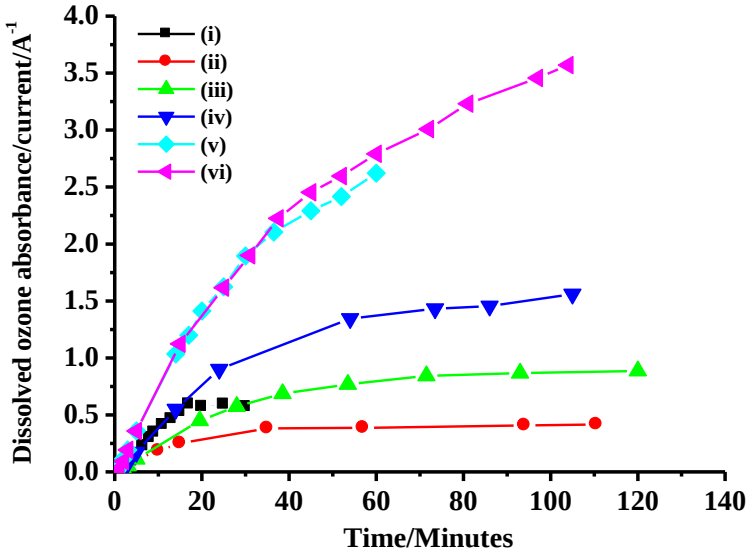

(d)

Figure 5.13 Plots of (c) ozone absorbance vs. time, and (d) ozone absorbance/current at wavelength 258 nm obtained in figs. 5.12 (a) and (b), at a cell voltage was 3.0 V, 0.5 M H_2SO_4 anolyte and catholyte, at a flow rate of 90 cm^3 min^{-1} in recycle mode of (i) freshly prepared (■), (ii) after 2 days electrolysis at 3.0 V (●), (iii) after 4 days (▲), (iv) after 6 days (▼), (v) after 19 days (◆) and (vi) after 25 days (◀) anode PC8. See text for details.

5.3.2 The "Purple of Cassius" problem

The work on the Au-containing anodes was carried out in collaboration with Dr. Henriette Christensen and was led by Clarizon.

It was soon found that the dip-coating solution containing $AuCl_3$ often turned purple over a relative short period after preparation. Dr. Christensen realised that if the dip-coating solution was prepared without $AuCl_3$ and allowed to stand overnight before adding the gold salt, the purple solution often did not form. Further investigation by Dr. Christensen indentified the purple solution as "Purple of Cassius", finely dispersed metallic Au adsorbed on insoluble SnO_2 [16]. This is produced by the reaction of $AuCl_3$ and $SnCl_2$, and is one of the earliest qualitative, colorimetric methods for the detection of small quantities of Au. The discovery of Purple of Cassius is wrongly credited to Dr. A. Cassius in Leyden in 1663; in fact a detailed method of preparing the compound had been published by 1659 [17]. Dr. Christensen reasoned that $SnCl_2$, present as an impurity in the $SnCl_4$, was reducing the $AuCl_3$. Various methods were employed to ensure oxidation of the $SnCl_2$ and it was found that either heating the dip-coating solution for 5 hours at 60 ºC or bubbling O_2 gas through the solution for 2-3 hours before adding the $AuCl_3$ gave solutions that did not turn purple, and one of these method were generally used in the preparation of the gold-containing anodes.

5.3.3 Overview of the studies on the Au-containing anodes

As may be seen from tables 4.1-4.3, AJED series 14, 15 and 17 all contained gold. However, all the coating solutions turned purple and the work was abandoned. The anodes were made before the pre-treatment to prevent the formation of the Purple of Cassius were devised.

Later in the project, the protocols to avoid the formation of the "Purple of Cassius" were developed. Hence, a project was initiated to identify a reproducible synthesis and it was decided to start with the synthetic procedure employed to make the most active and durable anodes to date, the anode AJED2F. The strategy was to start with the essentials of the etching, electrodeposition and catalyst coating methods employed to make the

anodes AJED2 series, modifying where necessary based on the experience since acquired. Particular attention would be paid to investigating the electrodeposition step with the aim of making it more reproducible in terms of the loading structure and morphology of the EDIL. The most effective method would then be employed to make electrodes coated with catalyst based on the series AJED2 process. If this resulted in active and selective anodes the effect of the addition of gold would then be investigated. The results so obtained are presented in the next section.

5.3.4 Anodes AJED25E and the anodes AJED27 series: investigating the effect of Au

The first stage of the strategy outlined above was to investigate the electrodeposition step. Thus, 8 x 6.25 cm^2 Ti meshes were flattened in the Chauffante Elcometer press, washed and etched in oxalic acid exactly as had been carried out for the anodes AJED2 series. Electrodeposition was carried out on anode AJED25A from a 10:1 Sn:Sb solution using a single Pt/Ti counter electrode at 6.4 mA cm^{-2} for 25 minutes, as per the anodes AJED2 series. However, based on the work in section 4.4.3, electrodeposition of the EDILs on the remaining meshes was from 10:2 Sn:Sb solutions. Electrodes AJED25C and AJED25D explored the effect of the area of the counter electrode (36.0 cm^2 and 6.25 cm^2, respectively) and anodes AJED25D-H investigated the effect of electrodeposition time (25, 20, 15, 10 and 5 minutes respectively, 6.25 cm^2 counter electrode). Based on the work in section 4.4.3, the EDIL-coated Ti meshes were heated at 520 ºC in the furnace.

Unfortunately, with the exception of anode AJED25E, electrodeposition resulted in very low and inhomogeneous coverage by Sb, see figs. 5.14 (a) and (b).

The EDIL loading of anodes AJED25A-D and AJED25F-H was 0.27 ± 0.13 mg cm^{-2}. In contrast, the loading on anode AJED25E was 0.99 mg cm^{-2}, and it was decided to proceed to the coating step with this electrode, despite the ongoing problems with the reproducibility of the electrodeposition step.

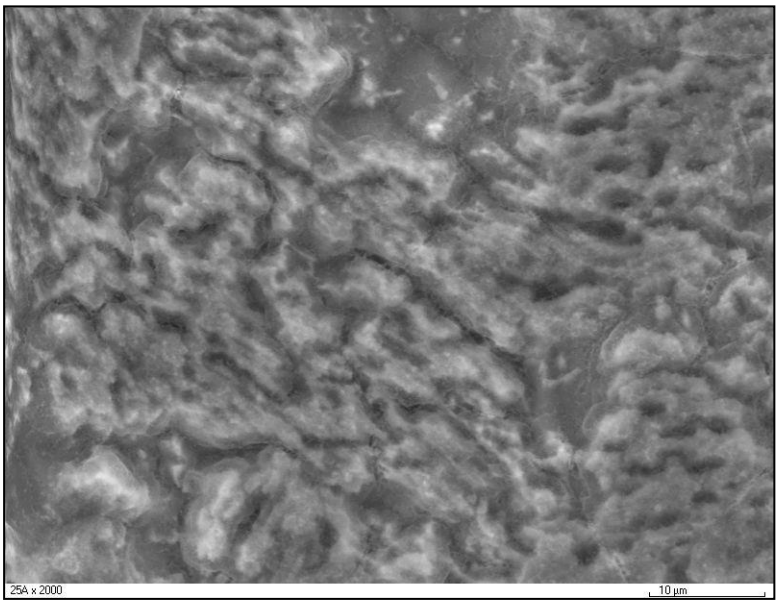

(a)

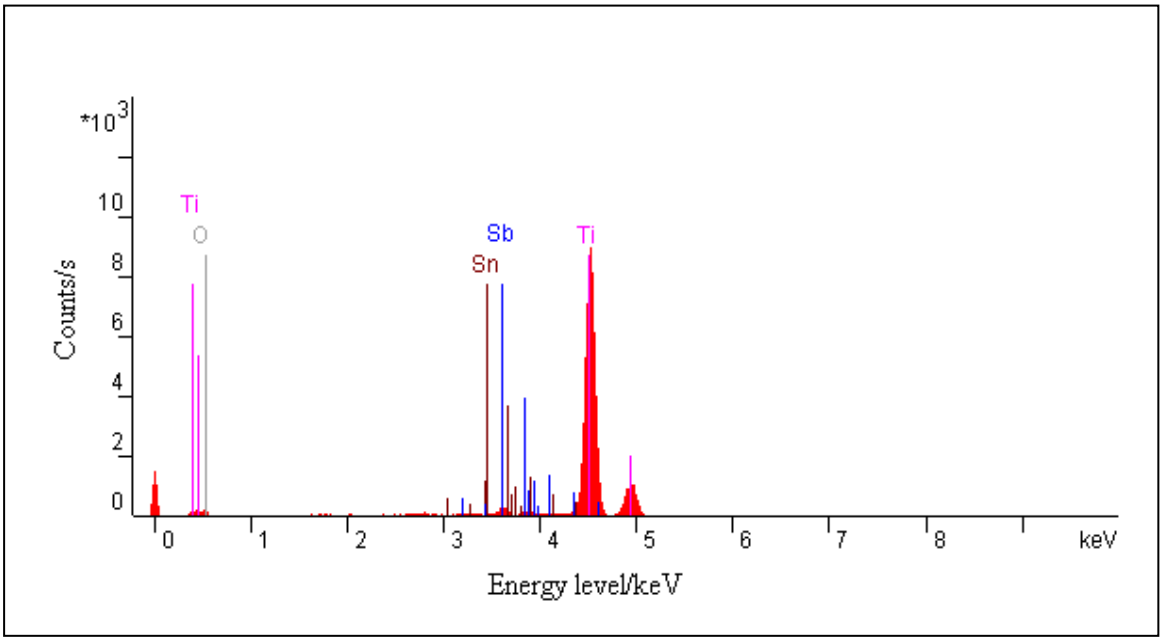

(b)

Figure 5.14 (a) Typical SEM image (x2000, bar = 10 µm) and (b) EDX spectra of anode AJED25A.

As with the anode AJED25E, the catalyst coating solution contained Sn, Sb and Ni in the ratio 500:8:3. The EDIL-coated Ti mesh was dip-coated 20 times and the catalyst uptake is shown in table 5.3. Based on the work in section 4.5.3, the dip-coated electrodes were pyrolysed at 460 ºC.

EDIL loading /mg cm^{-2}	**Catalyst uptake/mg after**				**Total catalyst /mg**	**Catalyst loading /mg cm^{-2}**
	5 cycles	**10 cycles**	**15 cycles**	**20 cycles**		
0.99	5.8	5.8	6.3	7.5	25.4	4.1

Table 5.3 EDIL and catalyst uptake by anode AJED25E.

Anode AJED25E was tested in the glass cell, in single pass and recycle systems, in 0.5 M H_2SO_4, then SEM and EDX measurements before and after testing. Typical data from a single pass system (experiment 2) are shown in figs. 5.15 (a) and (b).

In total, 15 experiments were carried out using anode AJED25E and these are summarized in table 5.4. All but experiment 3 were carried out in single pass system (experiment 3 was recycle system). Experiments 1-6, 8 and 15 were conducted at 2.7 V and experiments 7, 9-14 at a constant current of 0.625 A (100 mA cm^{-2}), the latter to provide some insight into durability. Each experiment lasted 20 minutes.

As can be seen from the figure, the first two experiments gave current efficiencies of *ca.* 41%. Following the recycle experiment (3, which gave the usual current efficiency of 6% when calculated from the gas phase ozone absorbance) the current efficiency, running at 0.625 A (*ca.* 2x the current determined at 2.7 V) did not seem to increase the decline in current efficiency, the latter stabilising at *ca.* 22-23% after experiment 11. Furthermore, in the constant current experiments, the cell voltage remained reasonably constant at *ca.* 3.03 ± 0.04 V, suggesting little change in the nature of the ozone-active sites. The current in the constant voltage experiments also remained fairly stable.

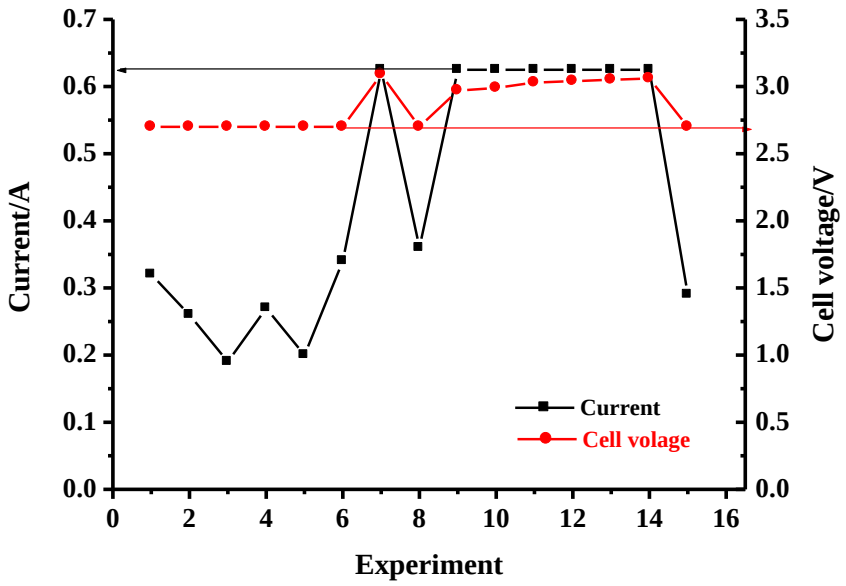

Figure 5.15 (a) Plots of current (■) and cell voltage (●) measured during the single pass (flow) experiments using anode AJED25E in 0.5 M H_2SO_4 in the glass cell. The experiments were conducted at 2.7 V (experiments 1-6, 8 and 15) or 0.625 A (experiments 7, 9-14).

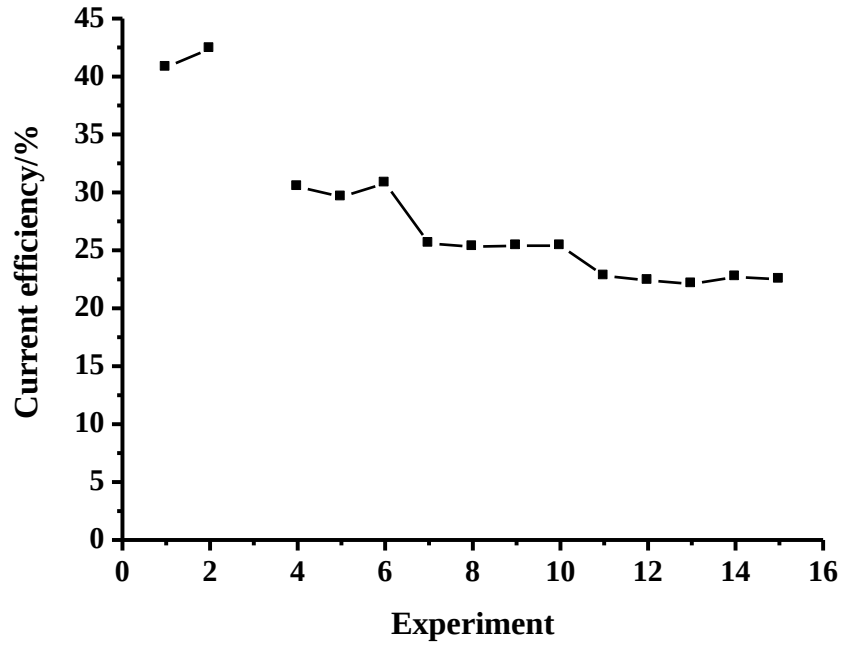

Figure 5.15 (b) Plot of the current efficiencies determined during the experiments in fig. 5.15 (a).

The mass of the anode was measured before experiment 1 and after experiments 5, 7 and 15, see table 5.4. As can be seen, *ca.* 25% of the catalyst coating had been lost by the end of experiment 5, perhaps accounting for the decrease in current efficiency from (and including) experiment 4. This does not correlate with a similar decrease in current, suggesting that the catalyst lost was rich in ozone-active sites perhaps due to etching of the surface during the recycle experiment. A further 3% of the remaining coating was lost by the end of experiment 7 and a total of 50% by the end of experiment 15. This latter loss was not reflected in the current.

Experiment No.	**Cell voltage /V**	**Current /A**	**Dissolved ozone absorbance**	Φ_{O3}^{e} **/%**	**Mass change after experiment/mg (mg cm^{-2})**
1	2.70	0.32	0.68	40.8	
2	2.70	0.26	0.59	42.4	
3	2.70	0.19	0.14 (gas)	6.0 (gas)	
4	2.70	0.27	0.44	30.5	
5	2.70	0.20	0.31	29.6	6.7 (1.7)
6	2.70	0.34	0.54	30.8	
7	3.09	0.625	0.83	25.6	0.7 (0.11)
8	2.70	0.36	0.48	25.3	
9	2.97	0.625	0.83	25.4	
10	2.99	0.625	0.83	25.4	
11	3.03	0.625	0.74	22.8	
12	3.04	0.625	0.73	22.4	
13	3.05	0.625	0.72	22.1	
14	3.06	0.625	0.74	22.7	
15	2.70	0.29	0.34	22.5	5.3 (0.85)

Table 5.4 Summary of the experiments carried out on anode AJED25E.

The SEM data supported the mass and efficiency data above to some extent. Thus, figs. 5.16 (a)-(c) show micrographs (x150) of anode AJED25E (a) before any testing and after (b) experiment 3 and (c) after experiment 5. Unfortunately, the images in the figures are all from different regions of the anode. If fig. 5.16 (a) is taken as representative, then the coating is free from any large defects. As usual, the coating on the crossing points of the wires shows a "cracked mud" morphology, significantly different to that on the strands, as was noted in section 5.2. This can be seen more clearly in figs. 5.17 (a) and (b) which show SEM images at a higher magnification (x5000) from the crosswire and strand regions, respectively of the image in fig. 5.16 (b). As can be seen from figs. 5.17 (a) and (b), the coating on the strands is more compact and lacks any of the crevices characteristic of the crosswire region. The "cracked mud" morphology could provide access to the underlying Ti substrate and hence be at risk of spallation. However, as may be seen from the EDX spectra in figs. 5.18 (a)-(g), the catalyst coating is sufficiency thick that no signal due to Ti is derived even after the 15th experiment.

Returning to the SEM images in figs. 5.16 (a)-(c), fig. 5.16 (c) clearly shows the loss of large areas of the coating from the upper and lower left strands and the upper right strand, consistent with the significant mass loss and decrease in efficiency (fig. 5.15 (b)) determined after experiment 5. Given the clear discontinuity between 1 and 2 on one hand, and experiments 3-5 on the other, it does not seem unreasonable to postulate that the damage and loss of efficiency occurred during the recycle experiment, experiment 3. Interestingly, physical loss of catalyst would be expected to be accompanied by a decrease in current; this was not the case as can be seen from fig. 5.15 (a).

From figure 5.16 (c), it can be seen that damage consistent with spalling occured in other areas of the anode. In addition, figs. 5.19 (a) and (b) show SEM images of the crosswire areas of anode AJED25E (x5000) after experiments 5 and 15, respectively, both of which suggest etching/erosion of the catalyst coating had taken place, as the large 'flakes' comprising the 'cracked mud' morphology evident in fig. 5.17 (a) have clearly been eroded in figs. 5.19 (a) and (b).

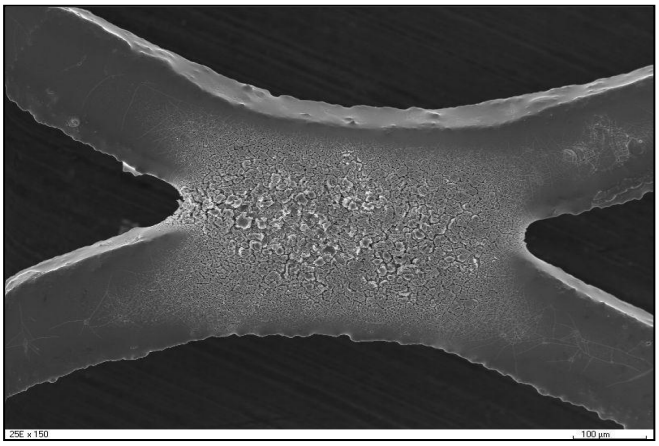

(a)

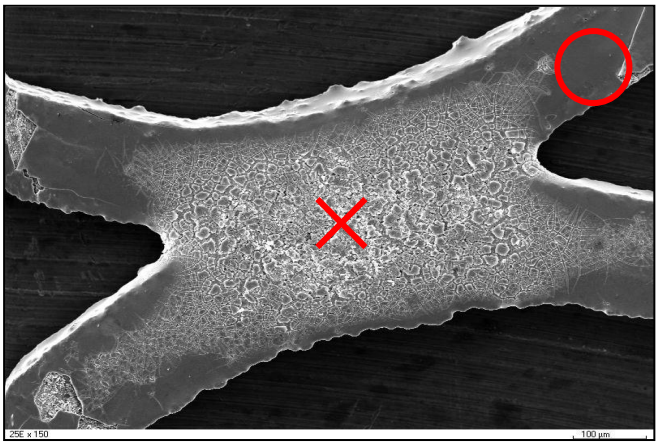

(b)

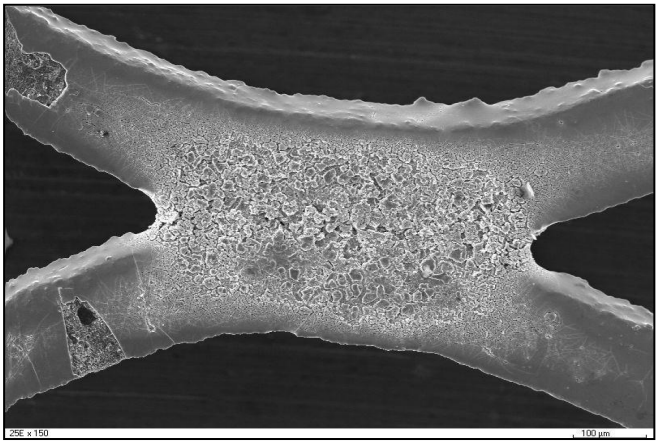

(c)

Figure 5.16 SEM images (x150) of anode AJED25E (a) before testing, (b) after experiment 3 and (c) after experiment 5. The image in (a) was taken at a different location to those in (b) and (c). The bar = 100 µm.

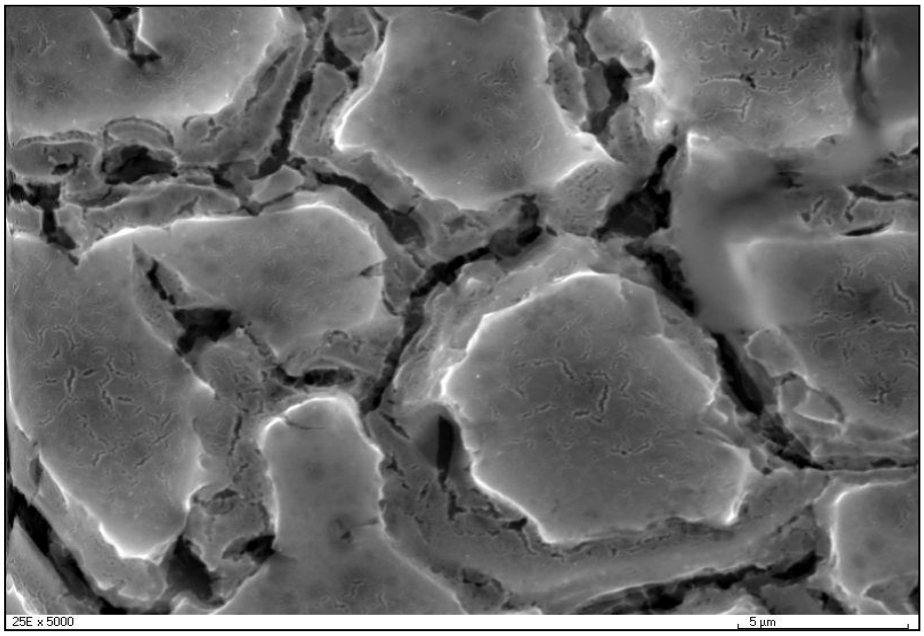

(a)

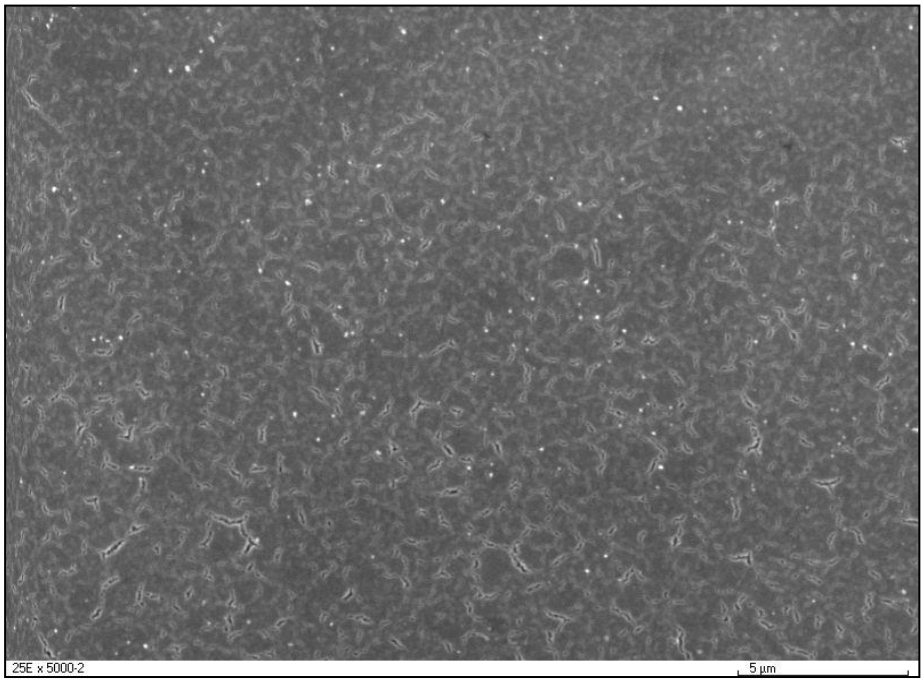

(b)

Figure 5.17 SEM images (x5000) taken from (a) the crosswire region and (b) the area marked by a red circle of anode AJED25E in fig 5.16 (b). The bar = 5 µm.

The EDX spectra in figs. 5.18 (a)-(g) suggest the coating had not spalled off or been eroded sufficiently to expose the Ti mesh. However, the SEM images in figs. 5.16 (a)-(c) and 5.19 (a) and (b) do suggest significant catalyst loss (as does the total mass loss of 50% after experiment 15) and spalling of the coating. Either the spalling of the coating was not complete or damage and loss of catalyst was not distributed evenly across the anode. This still leaves the fact that the current did not decrease in line with the mass loss unexplained. If it is accepted that high concentrations of ozone inhibit ozone evolution (see Chapter 3), then areas of anode will be deactivated by rising bubbles of ozone, and it may be that only the lowest regions of the (vertical) anodes are active. If it is accepted that these will also be the areas to suffer damage and catalyst loss, then the next lowest region would become active, and so on. However, this would have required the higher regions still to be active for O_2 evolution and hence loss of catalyst to cause a decrease in overall (O_2 + O_3) current.

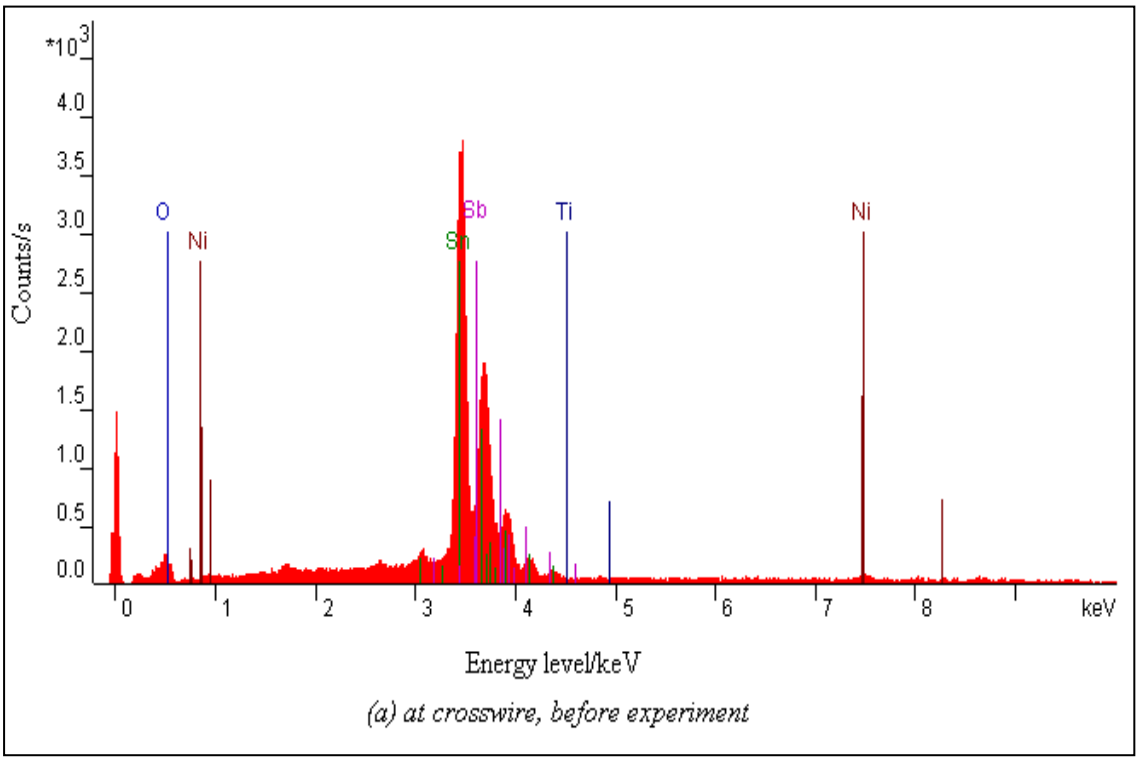

Figure 5.18 (a) EDX spectra of anode AJED25E before experiment at the crosswire region in fig. 5.16 (a).

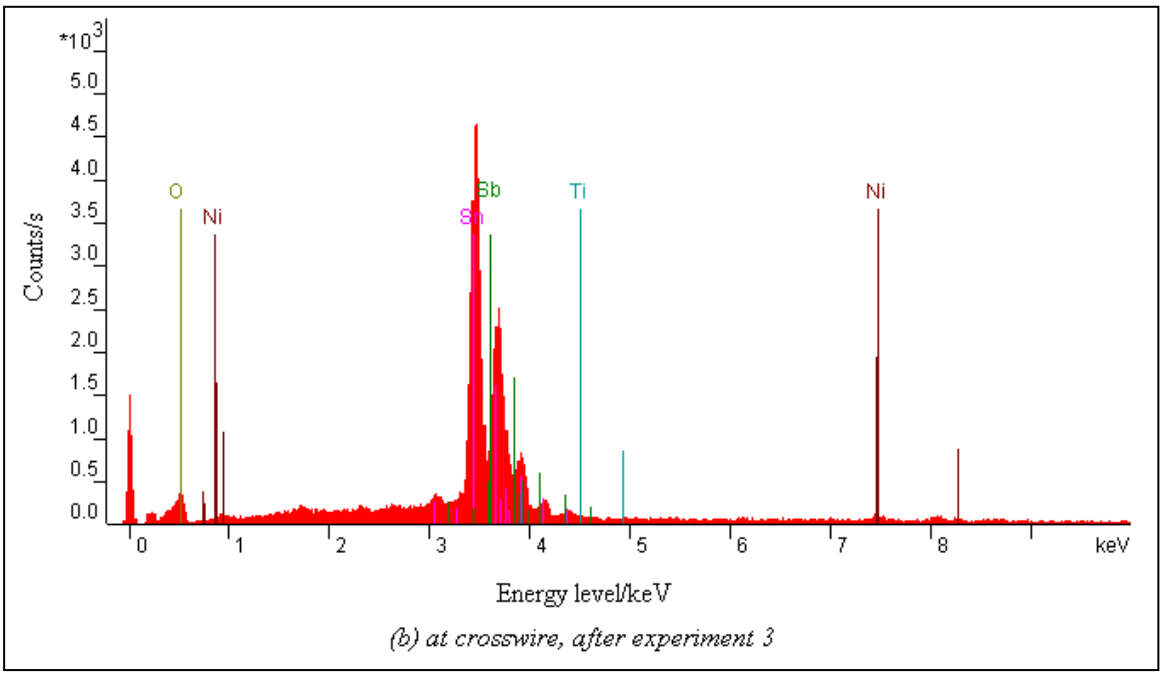

(b) at crosswire, after experiment 3

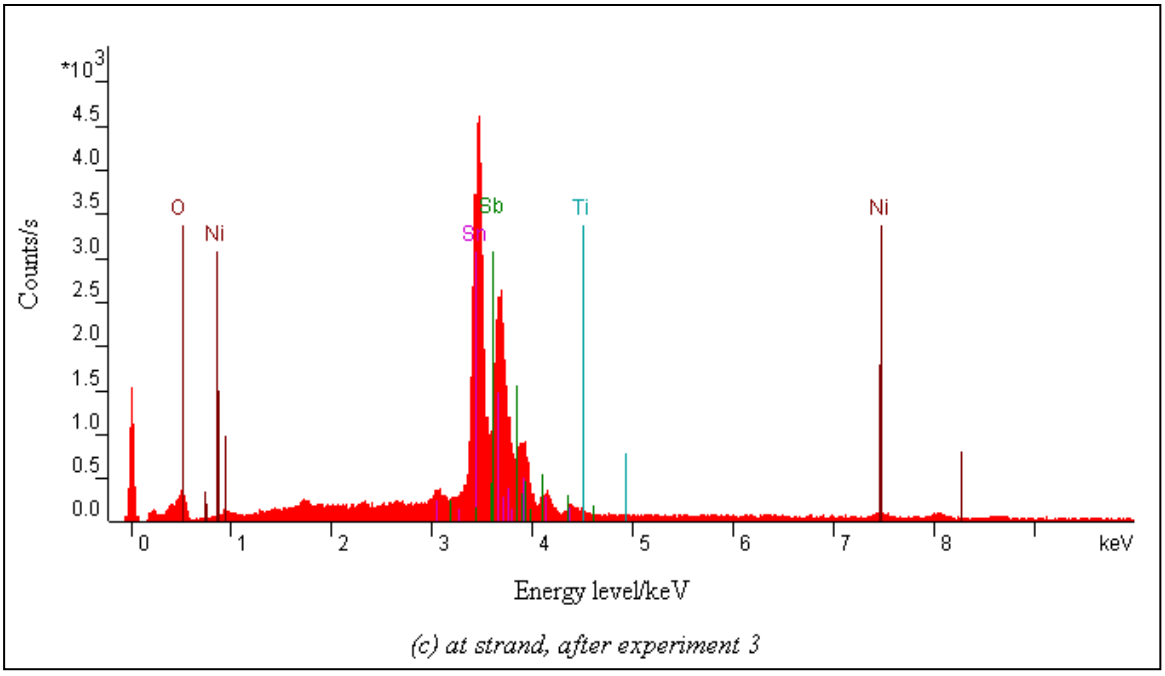

(c) at strand, after experiment 3

Figure 5.18 EDX spectra of anode AJED25E after experiment 3 at (b) the crosswire region and (c) the strand in fig. 5.16 (b).

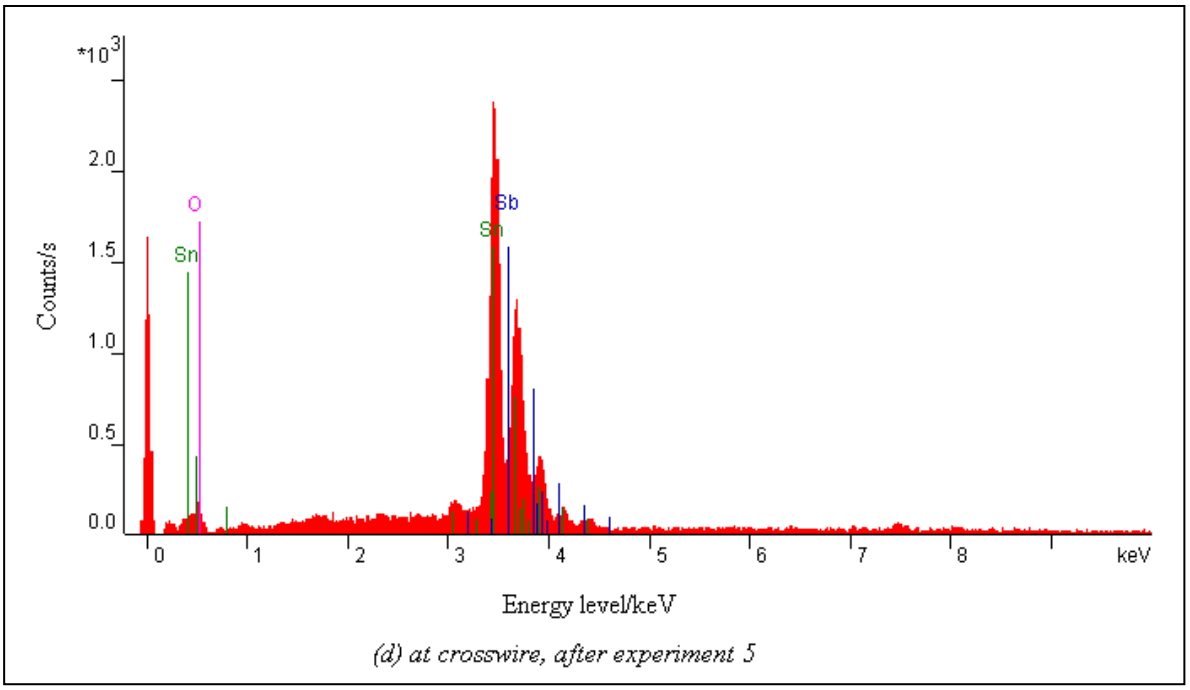

(d) at crosswire, after experiment 5

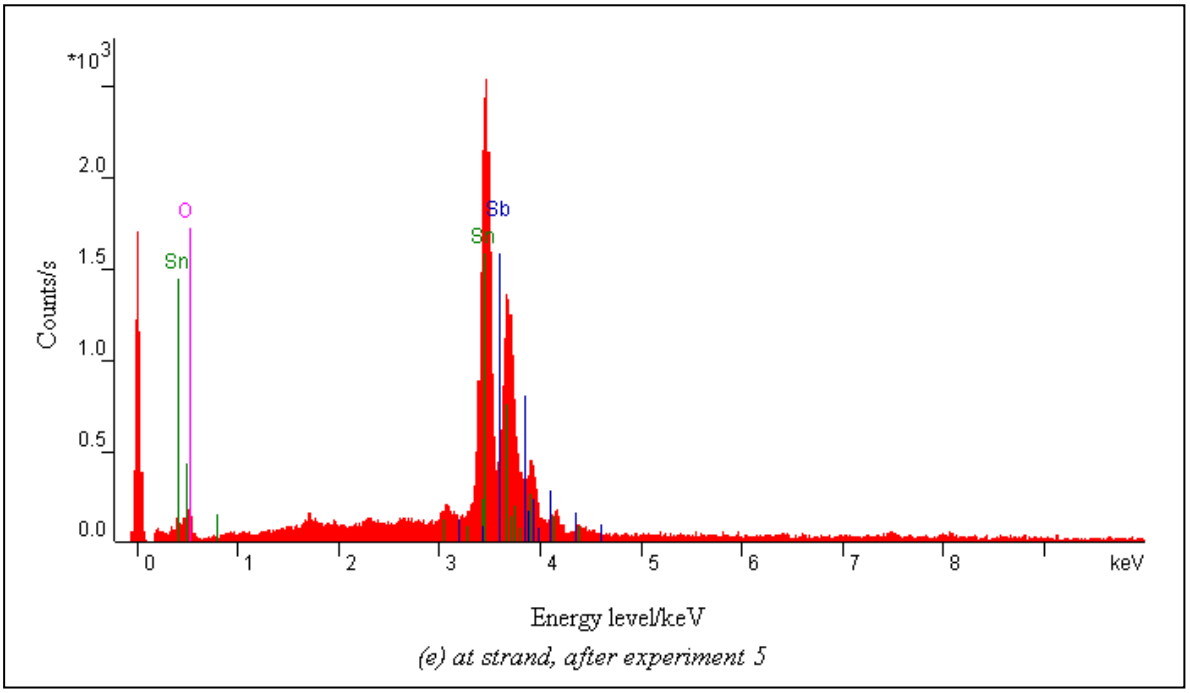

(e) at strand, after experiment 5

Figure 5.18 EDX spectra of anode AJED25E after experiment 5 at (d) the crosswire region and (e) the strand in fig. 5.16 (c).

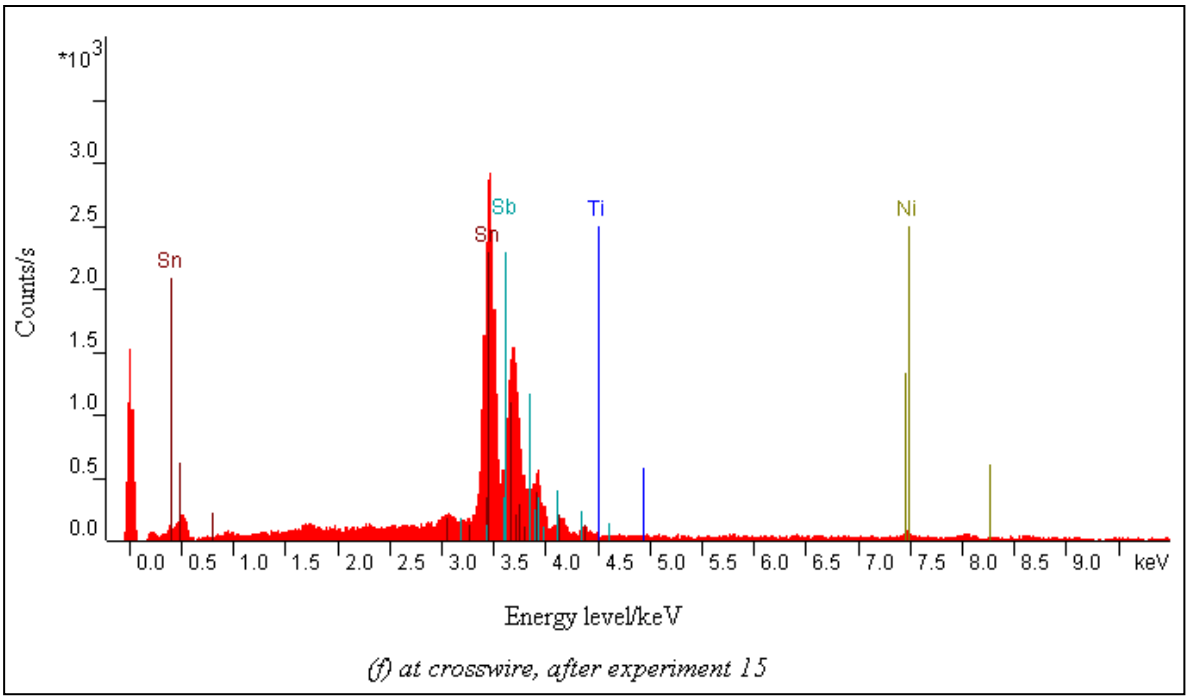

(f) at crosswire, after experiment 15

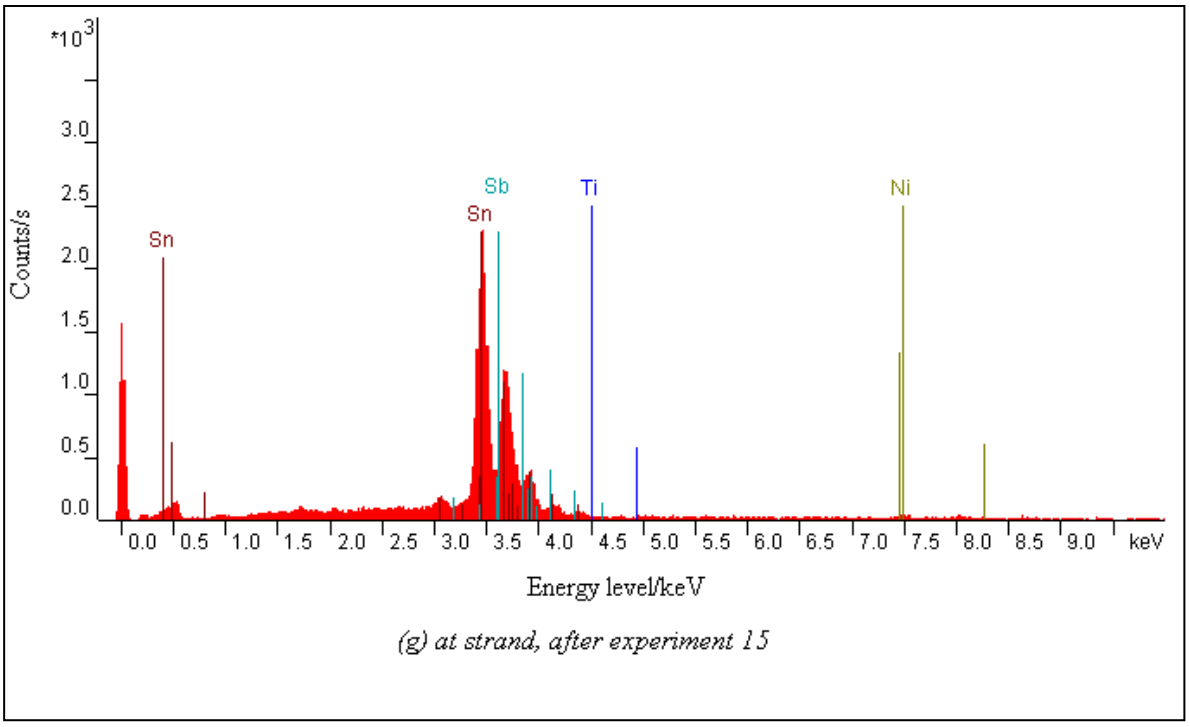

(g) at strand, after experiment 15

Figure 5.18 EDX spectra of anode AJED25E after experiment 15 at (f) the crosswire region and (g) the strand of anode.

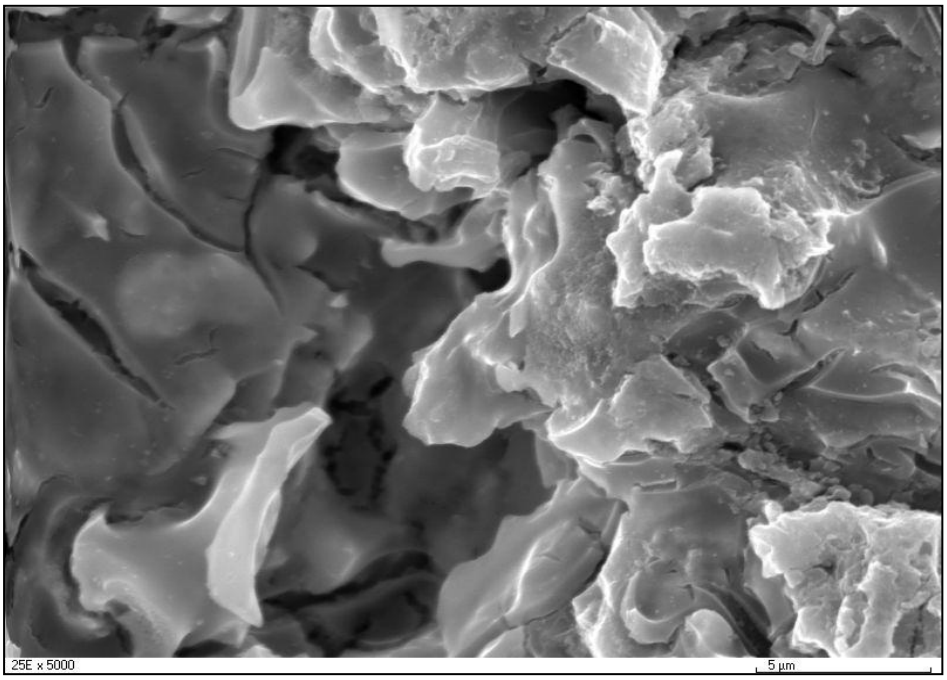

(a)

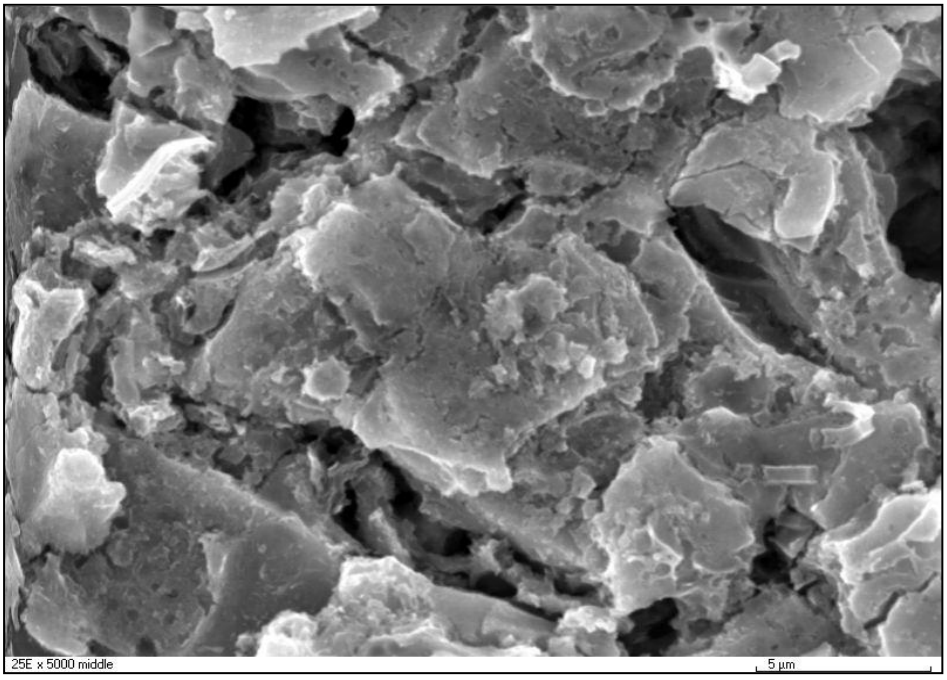

(b)

Figure 5.19 SEM images (x5000) of crosswire regions of anode AJED25E (a) after experiment 5 and (b) after experiment 15. Bar = 5 µm.

The results using anode AJED25E were extremely promising, and consistent with the activity, selectivity and durability of the anodes AJED2 series. Hence, it was decided to make a batch of anodes to explore the reproducibility of the synthesis and the effect of Au (*i.e.* to explore the "surface disruption strategy"). Thus, anodes AJED27A-L were made exactly as anode AJED25E, except that $HAuCl_4$ was added to the dip-coating solutions of anodes AJED27D-L after heating the latter at 55 ºC for 5 hours to ensure that all Sn^{II} was converted to Sn^{IV}, see section 5.3.2. Table 5.5 summarises the composition and the EDIL and catalyst uptake of the anodes AJED27 series. As may be seen from the table, the distribution of EDIL loading is, as usual, quite broad given this step was identical for all of the anodes prepared.

Anode AJED27	**500:8:3 :Au**	**EDIL loading /mgcm^{-2}**	**Catalyst uptake after 5 coats /mg**	**Catalyst uptake after 10 coats /mg**	**Catalyst uptake after 15 coats /mg**	**Catalyst uptake after 20 coats /mg**	**Total catalyst loading /mgcm^{-2}**
A	0	1.71	7.7	7.2	6.8	8.6	4.85
B	0	0.37	7.0	6.5	8.2	6.9	4.58
C	0	0.42	6.6	7.2	7.5	6.7	4.48
D	0.1	0.29	6.8	8.5	7.3	7.1	4.75
E	0.1	0.24	7.0	6.3	7.2	5.8	4.21
F	0.1	0.58	5.8	6.4	6.9	6.1	4.03
G	0.3	0.64	7.3	7.2	7.6	7.0	4.65
H	0.3	0.30	6.1	6.1	6.7	6.6	4.08
I	0.3	0.42	5.9	6.6	6.5	6.9	4.14
J	1.5	0.32	4.8	7.1	6.6	7.7	4.19
K	1.5	0.21	6.3	7.4	6.4	7.1	4.35
L	1.5	0.19	6.2	6.8	5.5	7.0	4.08

Table 5.5 The composition of the dip-coating solution and the uptake of EDIL and catalyst for the anodes AJED27 series.

The catalyst deposition is shown more clearly in figs. 5.20 and 5.21; figs. 5.20 (a)-(d) show the mass of catalyst deposited every five dip-coats and fig. 5.21 the total loading of catalyst across the anodes AJED27 series. As may be seen from figs. 5.20 (a)-(d) within each sub-series (*i.e.* A-C = 0 Au, D-F = 0.1 Au, G-H = 0.3 Au and I-L = 1.5 Au) the deposition process is reasonably reproducible, despite the very marked variation in EDIL ("0 dip-coats" on the figure). The total loading of catalyst was 4.37 ± 0.27 mg, *i.e.*

± 6% a very satisfactory range, suggesting good reproducibility. Figure 5.21 supports this.

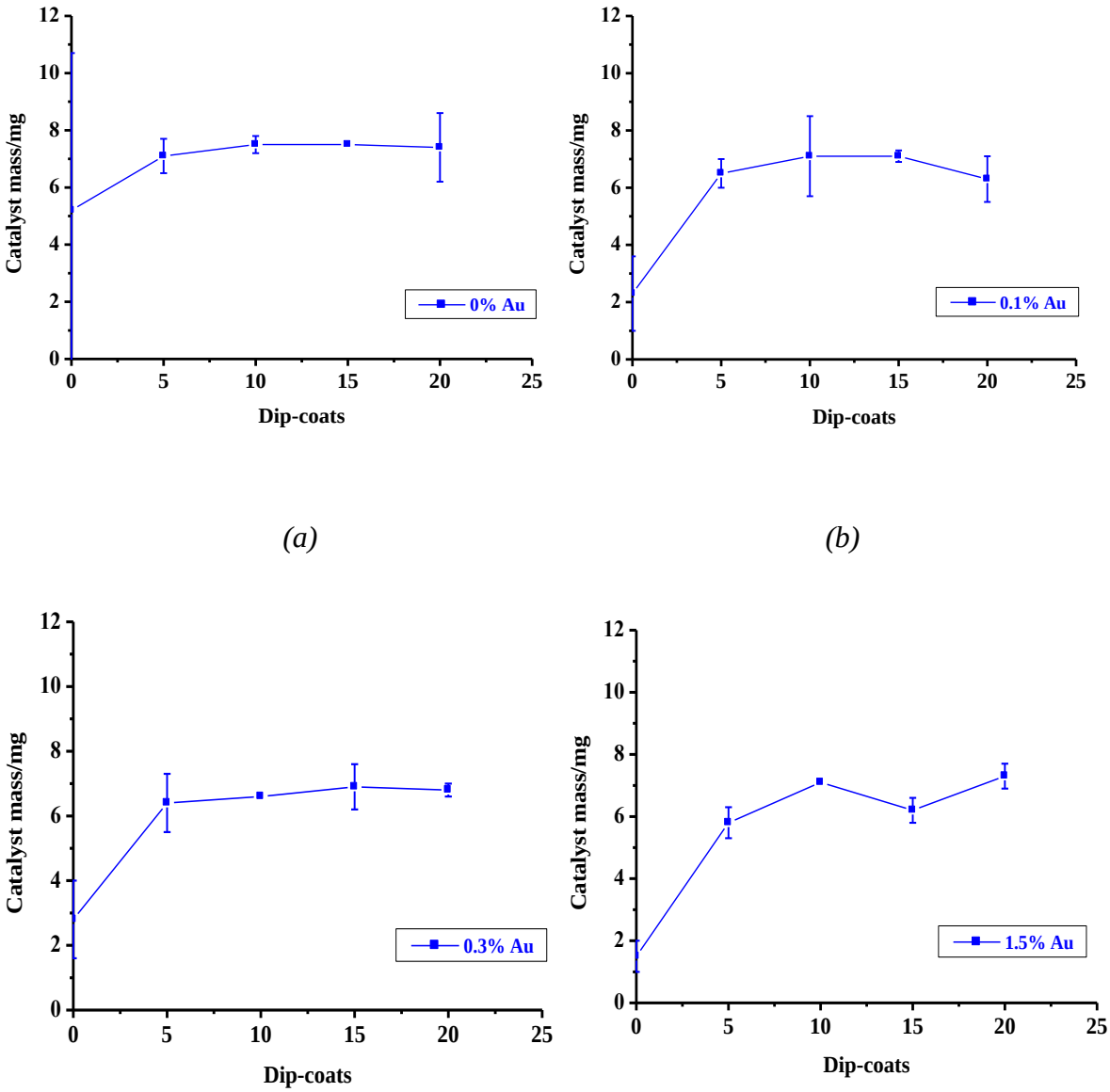

Figure 5.20 The variation in catalyst uptake with the number of dip-coats (0 = mass of EDIL) for anodes AJED27series at (a) 0, (b) 0.1, (c) 0.3 and (d) 1.5 wt% Au.

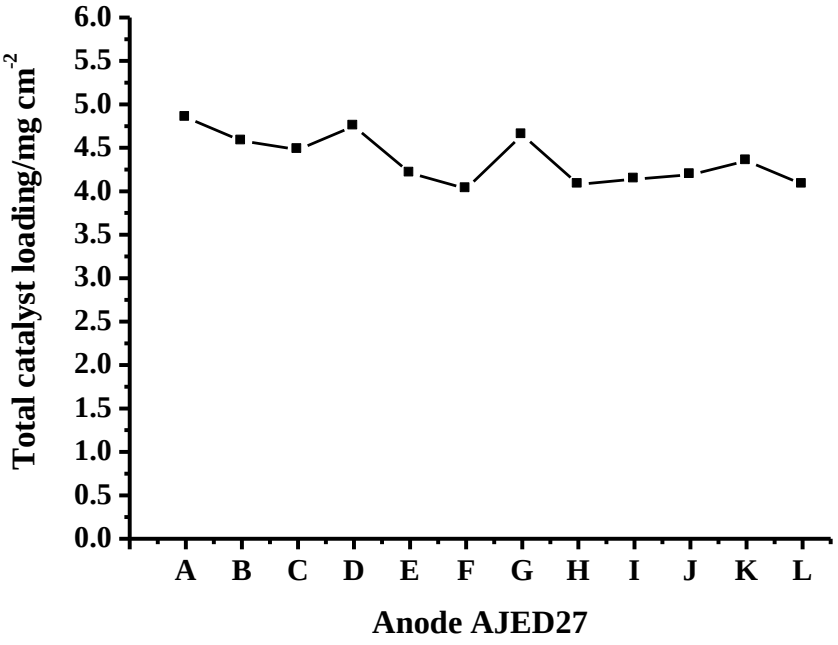

Figure 5.21 The total catalyst loading of the anodes AJED27 series.

The anodes were tested in single pass in the glass cell at 2.7 V and 0.625 A in 0.5 M H_2SO_4 at an anolyte flow rate of 60 cm^3 min^{-1} (static catholyte). Each anode was tested at least 3 times (at 2.7 V, 0.625 A and 2.7 V) and one anode from each batch was used to electrolyse for 8 hours in 0.5 M H_2SO_4 at 2.7 V, tested (experiment 4) then used in electrolysis again for 8 hours and retested (experiment 5). A typical set of data is shown in figs. 5.22 (a)-(c) and the results using all the anodes are summarised in table 5.6 and figs. 5.23-5.25.

The apparatus employed to test the anodes AJED27 series is shown in fig. 5.26; the use of the gas separator, whilst resulting in an underestimate of current efficiency where the gas phase ozone was not measured (usually due to demand on equipment), clearly resulted in stable absorbances, as may be seen from fig. 5.22 (b), which was typical of the series.

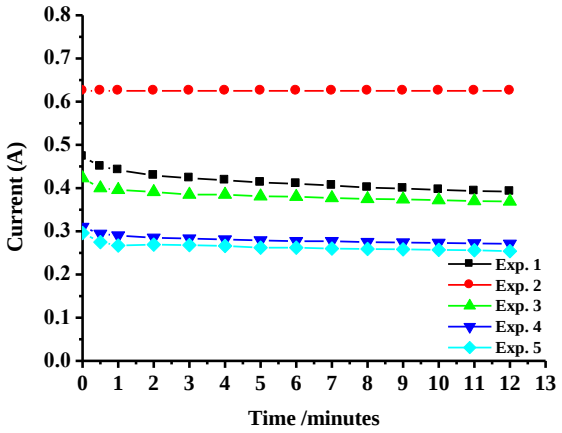

(a)

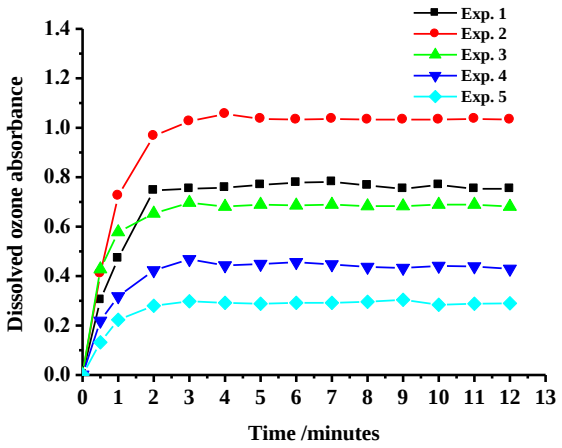

(b)

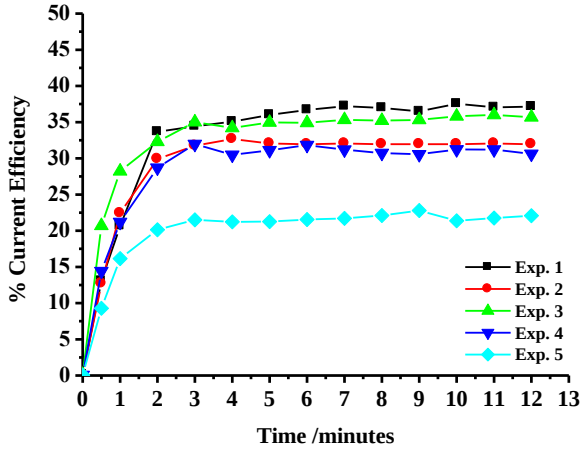

(c)

Figure 5.22 Plots of (a) current, (b) dissolved ozone absorbance and (c) current efficiency of anode AJED27A in 0.5 M H_2SO_4, static catholyte, anolyte flow 60 cm^3 min^{-1} in the glass cell; Pt/Ti mesh counter electrode; experiment 1 (■), experiment 2 (●) was carried out at constant current (0.625 A), experiments 3 (▲) and experiment 4 (▼) after the anode was employed to electrolyse 0.5 M H_2SO_4 for 8 hours and Experiment 5 (◆) at 2.7 V again. See table 5.6 detail.

Anode (Sn:Sb:Ni:Au)	Experiment No.	Current /A	Φ_{O3}^{e} /%	Mass before experiment	Mass After experiment	Δm /mg	Comments
AJED27A (500:8:3:0)	1	0.41	36.7	275.5	275.9		
	2	0.625	32.0				Fix current density 100 mA cm^{-2}
	3	0.38	34.9				
	4	0.27	31.3	275.7			0.33-0.23 A
	5	0.26	21.2		275.1	0.6	
AJED27B (500:8:3:0)	1	0.41	41.2	250.9	251.1		
	2	0.625	35.9				Fix current density 100 mA cm^{-2}
	3	0.38	41.2				
AJED27C (500:8:3:0)	1	0.48	39.9	251.2	251.8		
	2	0.625	33.2				Fix current density 100 mA cm^{-2}
	3	0.44	34.7				
AJED27D (500:8:3:0.1)	1	0.35	38.4	253.5	252.7	0.8	
	2	0.625	33.2				Fix current density 100 mA cm^{-2}
	3	0.32	37.7				
	4	0.24	34.4	253.0			0.31-0.20 A
	5	0.17	20.8		252.4	0.6	
AJED27E (500:8:3:0.1)	1	0.33	43.1	245.8	246.3		
	2	0.625	34.4				Fix current density 100 mA cm^{-2}
	3	0.30	43.4				
AJED27F (500:8:3:0.1)	1	0.34	41.7	247.4	248.1		
	2	0.625	32.6				Fix current density 100 mA cm^{-2}
	3	0.28	37.3				
AJED27G (500:8:3:0.3)	1	0.38	37.0	248.5	248.4	0.1	
	2	0.625	35.4				Fix current density 100 mA cm^{-2}
	3	0.35	37.3				
	4	0.31	33.4	248.3			0.24-0.11 A
	5	0.24	24.0		247.8	0.5	

Anode (Sn:Sb:Ni:Au)	Experiment No.	Current /A	Φ_{O3}^{e} /%	Mass before experiment	Mass After experiment	Δm /mg	Comments
AJED27H (500:8:3:0.3)	1	0.40	38.5	242.3	242.7		
	2	0.625	33.4				Fix current density 100 mA cm^{-2}
	3	0.36	35.6				
AJED27I (500:8:3:0.3)	1	0.36	38.2	248.3	248.9		
	2	0.625	33.7				Fix current density 100 mA cm^{-2}
	3	0.33	35.1				
AJED27J (500:8:3:1.5)	1	0.40	21.5	248.8	249.7		
	2	0.625	21.1				Fix current density 100 mA cm^{-2}
	3	0.37	21.6				
AJED27K (500:8:3:1.5)	1	0.41	19.4	250.9	251.8		
	2	0.625	20.4				Fix current density 100 mA cm^{-2}
	3	0.38	20.6				
	4	0.25	22.0	251.7			0.26-0.24 A
	5	0.21	5.5		250.5	1.2	
AJED27L (500:8:3:1.5)	1	0.38	23.9	239.9	240.9		
	2	0.625	16.5				Fix current density 100 mA cm^{-2}
	3	0.34	17.6				

Table 5.6 Summary of the experiments carried out using the anodes AJED27 series in the glass cell. Cell voltage 2.7 V or constant current (0.625 A, 100 mA cm^{-2}), 0.5 M H_2SO_4, static catholyte, anolyte flow 60 cm^3 min^{-1}. Pt/Ti counter electrode.

Figure 5.23 and 5.24 show the average current efficiencies determined for experiments 1 and 3 (at 2.7 V) and during experiment 2 (at 0.625 A) for each of the anodes AJED27 series. It is clear that very high current efficiencies were determined for the electrodes with 0, 0.1, and 0.3 mole ratio Au in the dip-coating solution, *ca.* 35-45% at 2.7 V and 30-35% at 0.625 A. However the presence of 1.5 Au in the dip-coating solution reduced the current efficiencies very significantly, to *ca.* 20% at 2.7 V and 15-20% at 0.625 A. In terms of the current, the addition of Au up to and including Sn:Sb:Ni:Au 500:8:3:0.3 had no effect (fig. 5.25 (a)). Thus, up to 0.3 Au, Au appears to have no detrimental effect, but (in terms of current and current efficiency *i.e.* ozone activity and selectivity), no beneficial effect either. As was discussed in section 5.3, the strategy behind the addition of Au was to improve durability; the preliminary experiments (see figs. 5.13 (a)-(d)) showed that gold-doped Ni/Sb-SnO_2 anodes initially showed low current efficiencies that improved with electrolysis time; this clearly was not derived with the anodes AJED27 series since the efficiencies calculated were very high from the start. In addition, all the anodes selected for the additional electrolysis experiments (anodes AJED27A, D, G and K, see figs. 5.25 (a) and (b)) behaved in the same manner. Thus the anodes (anodes AJED27D, G, K containing Au, A without Au) all showed a steady decrease in current in the constant voltage experiments, fig. 5.25 (a), whilst current efficiencies decreased slowly between experiments 1, 3 and 4 (*i.e.* including the first 8 hours electrolysis, experiment 4, see fig. 5.25 (b)) and then showed a large drop between experiments 4 and 5, *i.e.* following the second electrolysis. Thus, it appears that the addition of gold had no beneficial effect.

As an additional check on the validity of the comparison of the anodes AJED27 series given the concerns over the potential effect of the variation in EDIL loading on catalyst uptake, the current and current efficiencies determined in the first experiments employing anodes AJED27B, D, H and J are shown in fig. 5.27. These anodes were chosen as having similar EDIL loading (0.37, 0.29, 0.30 and 0.32 mg cm^{-2}, respectively). As may be seen from the figure, the results follow almost exactly the trends obtained in figs. 5.25 (a) and (b).

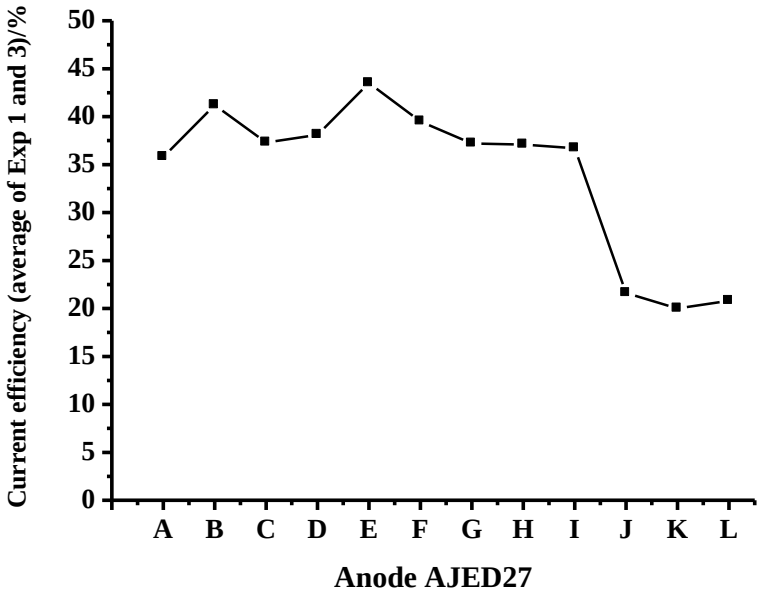

Figure 5.23 The average of the current efficiencies determined for experiments 1 and 3 across the anode AJED27 series. Experimental conditions as in fig. 5.26.

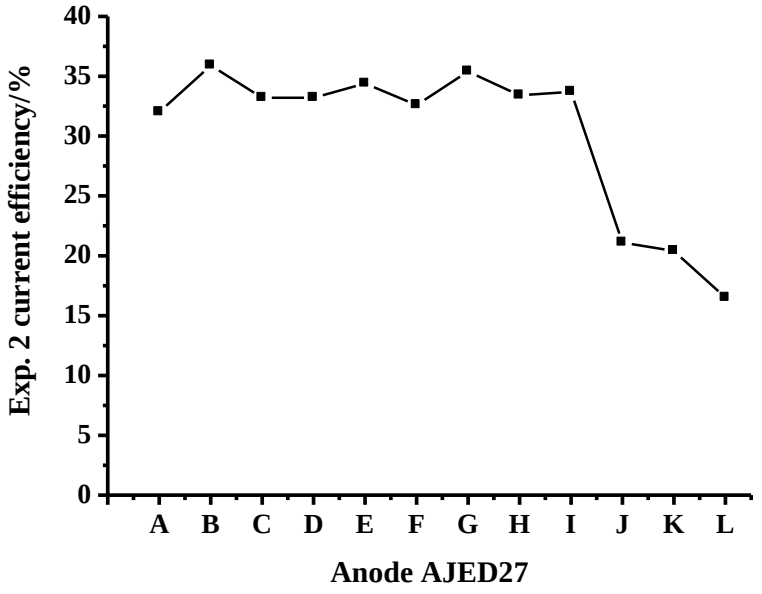

Figure 5.24 The current efficiencies determined for experiment 2 (constant current) across the anode AJED27 series. Experimental conditions as in fig. 5.26.

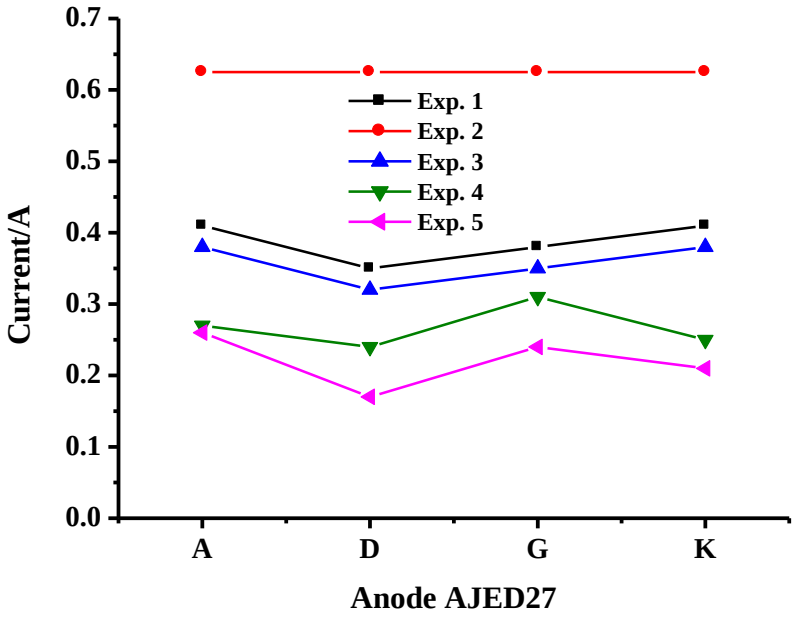

(a)

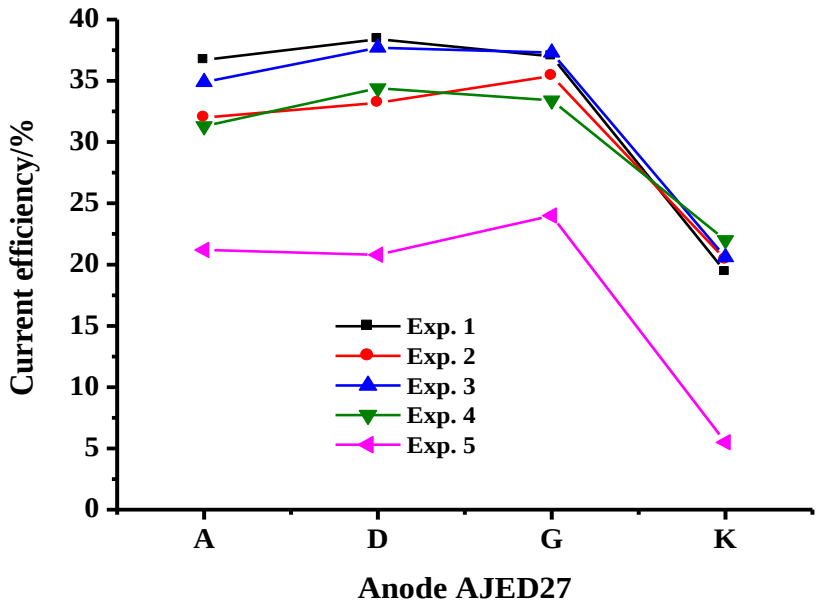

(b)

Figure 5.25 Plots of (a) current and (b) current efficiency determined for the experiments using the anodes AJED27 series. Experimental conditions as in fig. 5.26; experiment 1 (■), experiment 2 (●) was carried out at constant current (0.625 A), experiments 3 (▲), experiment 4 (▼) after the anode was employed to electrolyse 0.5 M H_2SO_4 for 8 hours and experiment 5 (◀) at 2.7 V. See table 5.6 detail.

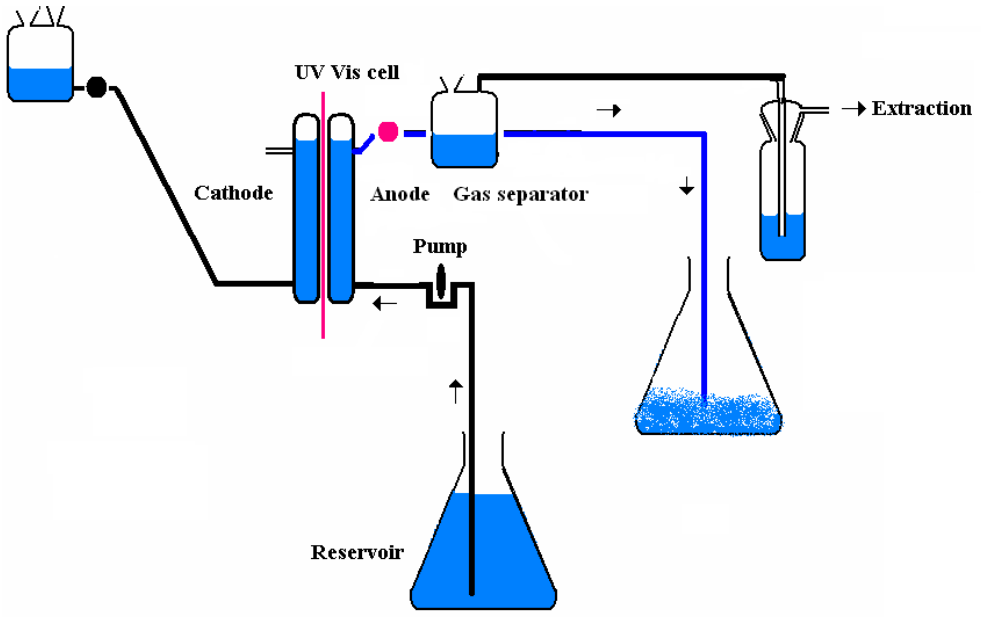

Figure 5.26 The apparatus employed in anodes AJED27 series.

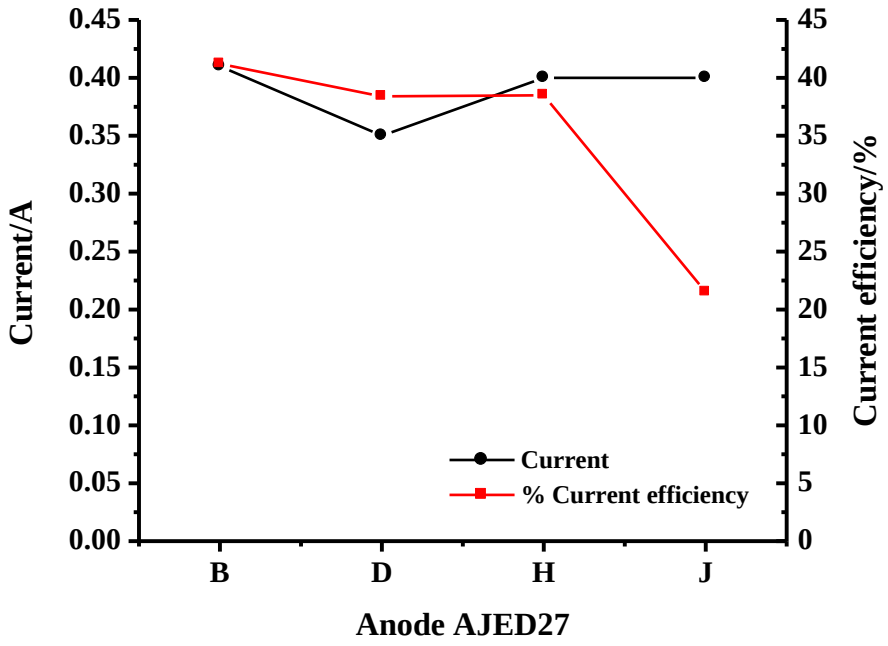

Figure 5.27 Plots of current (●) and current efficiency (■) determined for the first experiments using anodes AJED27B, AJED27D, AJEd27H and AJED27J. Experimental conditions as in fig. 5.26. The anodes had similar EDIL loadings.

5.4 Overview of the change in the reproducibility of the catalyst synthesis

Given the significant effort invested in the synthesis methodology to try and improve the reproducibility of the process (see tables 4.1-4.3), it is appropriate to review the progress made. Table 5.7 presents a summary of EDIL and catalyst loadings and current density and current efficiency for all the anodes AJED series including standard deviation.

Figure 5.28 (a) and (b) plot the essential data from the table. Thus fig. 5.28 (a) shows a plot of mean EDIL loading for the 6.25 cm^2 AJED anodes made using 500:8:3 mole ratio of Sn:Sb:Ni in the coating solution, ED1 cell 1 *i.e.* following the methods employed to make the anodes AJED2 series. The plot represents clearly the EDIL problem in that the electrodeposition proved irreproducible.

Figure 5.28 (b) shows mean values of the catalyst loading, current density and current efficiency for the 6.25 cm^2 anodes AJED series (500:8:3) which the catalyst 20 coats in total were pyrolysed at 460 ºC or 520 ºC. As may be seen from the figure, the reproducibility in terms of catalyst loading appears to improve, but the total loading declines by *ca.* 20% towards the end of the series. Both current and current efficiency improve across the series, but reproducibility did not show such a clear change.

Figure 5.29 shows analogous plots to those in fig. 5.28 (b) for the AJED anodes prepared using a 500:8:1 molar ratio of Sn:Sb:Ni in the coating solution and pyrolysis of the catalyst coats for 10 minutes at 460 ºC or 20 minutes at 520 ºC. As with the data in fig. 5.28 (b), there appeared to be a gain in current density as the synthesis was 'improved', but no real change in reproducibility. There appeared to be no change in catalyst loading or current efficiency, nor of reproducibility.

Series	Area /cm^2	Number of anodes	EDIL loading /mg cm^{-2}	500:8: Ni(Au)	Catalyst loading /mg cm^{-2}	Current density /mA cm^{-2}	Φ_{O3}^{e} /%	Comments
1	6.25	8	NED	1	-	50.60 ± 3.91	6.75 ± 1.09	NED and ED1 and 1, CC1
		4	-	1	-	51.20 ± 4.80	7.50 ± 0.50	NED, CC1
		4	-	1	-	50.00 ± 2.62	6.00 ± 1.00	ED1 and 1, CC1
2	6.25	2	-	1	-	44.80 ± 0.00	10.55 ± 0.25	ED1 and 1, CC1
		2	-	2	-	49.60 ± 3.20	15.55 ± 0.85	
		2	-	3	-	44.00 ± 0.80	16.60 ± 2.40	
		2	-	4	-	35.20 ± 1.60	16.50 ±1.50	
3	6.25	2	-	0.2	-	48.80 ± 0.80	4.10 ± 0.20	ED1 and 1, CC1
		2	-	2.5	-	62.40 ± 4.80	9.25 ± 0.25	
		2	-	5.0	-	-	-	
		2	-	10.0	-	-	-	
4	6.25	2	0.77 ± 0.26	2	6.14 ± 0.12	32.80 ± 0.80	22.60 ± 0.60	ED2 and 1, CC2 (paint brush)
		4		3	5.34 ± 1.00	25.60 ± 6.79	28.48 ± 9.78	
		3		4	4.63 ± 0.76	24.50 ± 20.50	20.80 ± 8.21	
5	6.25	2	0.13 ± 0.04	2	0.55 ± 0.03	67.20 ± 1.60	13.05 ± 0.35	ED3 and 1, CC3
6	4.0	8	NED	3	3.50 ± 0.25	67.50 ± 12.50	11.76 ± 3.45	NED, CC3
7	4.0	8	NED	3	3.15 ± 0.50	58.21 ± 8.84	6.49 ± 2.47	NED, CC3
8	4.0	8	NED	3	2.76 ± 0.41	54.38 ± 9.08	6.84 ± 4.21	NED, CC3
9	6.25	8	0.85 ± 0.17	1	5.98 ± 0.81	28.60 ± 3.53	30.23 ± 2.12	ED1 and 1, CC4 (HCl and no HCl)
		4	0.87 ± 0.15	1	6.78 ± 0.11	30.40 ± 3.39	30.59 ± 1.78	ED1 and 1, CC4 (no HCl)
		4	0.84 ± 0.19	1	5.19 ± 0.21	26.80 ± 2.62	29.86 ± 2.37	ED1 and 1, CC4 (HCl)
10	6.25	8	0.52 ± 0.11	1	4.67 ± 0.45	32.60 ± 3.99	21.99 ± 1.82	NED and ED1 and 1, CC4
		4	NED	1	4.46 ± 0.41	30.40 ± 3.58	22.44 ± 1.76	NED, CC4
		4	0.52 ± 0.10	1	4.89 ± 0.38	34.80 ± 3.07	21.54 ± 1.78	ED1 and 1, CC4
11	6.25	4	0.92 ± 0.35	3	5.33 ± 0.35	33.20 ± 4.98	23.47 ± 3.55	ED1 and 1, CC4
12	6.25	8	0.44 ± 0.28	1	4.85 ± 0.40	44.08 ± 2.80	31.19 ± 2.98	ED1 and 1, CC4
		2	0.19 ± 0.00	1	4.90 ± 0.35	42.88 ± 2.08	32.11 ± 1.48	ED1 and 1, CC4, 480 °C, 20 mins
		2	0.28 ± 0.24	1	4.56 ± 0.59	48.00 ± 1.60	27.72 ± 2.23	ED1and 1, CC4, 480 °C, 40 mins
		2	0.35 ± 0.11	1	4.80 ± 0.05	42.24 ± 0.96	32.37 ± 3.40	ED1and 1, CC4, 520 °C, 20 mins
		2	0.37 ± 0.00	1	5.13 ± 0.11	43.20 ± 1.60	32.57 ± 0.86	ED1and 1, CC4, 520 °C, 40 mins

Series	Area /cm^2	Number of anodes	EDIL loading /mg cm^{-2}	500:8: Ni(Au)	Catalyst loading /mg cm^{-2}	Current density /mA cm^{-2}	Φ_{O3}^{e}/%	Comments
13	6.25	8	0.50 ± 0.37	1	4.40 ± 1.59	42.54 ± 3.56	24.84 ± 4.30	ED1 and 1, CC4
		2		1	2.66 ± 0.12	37.20 ± 1.52	21.07 ± 0.28	ED1and1,CC4,10dips,460°C,10 mins
		2		1	5.75 ± 0.31	43.28 ± 2.00	31.19 ± 1.41	ED1and1,CC4,20dips,460°C,20 mins
		2		1	6.18 ± 0.18	44.00 ± 0.96	26.04 ± 0.76	ED1and1,CC4,20dips,520°C,10 mins
		2		1	3.01 ± 1.59	45.68 ± 3.56	21.05 ± 4.30	ED1and1,CC4,10dips,520°C,20 mins
14	35.0	8	NED	3	1.19 ± 0.32	11.86 ± 1.29	11.15 ± 0.35	NED, CC5, (7 coats and ramp)
		8	NED	3 (3)	1.46 ± 0.33	10.14 ± 0.14	12.40 ± 0.50	
15	35.0	1	NED	1 (1.5)	1.83	-	-	NED, CC6
		1	0.06		2.49	-	-	ED4 and 1, CC6
		1	NED	1(3)	1.79	-	-	NED, CC6
		1	0.08		2.05	-	-	ED4 and 1, CC6
		1	NED	3 (1.5)	2.35	-	-	NED, CC6
		1	0.07		2.20	-	-	ED4 and 1, CC6
		1	NED	3 (3)	2.17	-	-	NED, CC6
		1	0.09		2.68	-	-	ED4 and 1, CC6
16	35.0	8	0.42 ± 0.16	1	0.45 ± 0.08	4.46 ± 0.47	7.14 ± 1.33	ED4 and 1, CC6-8 (5 coats)
		2		1	0.46 ± 0.02	4.14 ± 0.14	6.96 ± 0.29	Uppermost in beaker
		2		1	0.49 ± 0.07	4.29 ± 0.29	7.01 ± 0.82	Uppermost beaker and hair drier
		2		1	0.36 ± 0.04	4.29 ± 0.29	7.12 ± 0.01	Pegged on line
		2		1	0.51 ± 0.08	5.14 ± 0.47	7.47 ± 3.52	Pegged on line and hair drier
17	35.0	4	NED	NCC	NCC	-	-	NED, NCC
		4	0.53 ± 0.16	NCC	NCC	-	-	ED4 and 1, NCC
18	35.0	3	0.62 ± 0.10	1	4.33 ± 0.15	11.71 ± 1.07	16.70 ± 3.69	ED5 and 1,CC9 (14 coats,390 °C)
		3		1	2.51 ± 0.30	17.81 ± 4.81	10.93 ± 2.42	ED5 and 1,CC9 (14 coats,460 °C)
		3		1	1.93 ± 0.13	23.33 ± 1.28	4.13 ± 1.76	ED5 and 1,CC9 (14 coats,520 °C)
19	6.25	2	0.60 ± 0.32	3	1.01 ± 0.19	45.60 ± 10.40	16.75 ± 2.15	ED7 and 1, CC10 (5 coats)
		2		3	2.97 ± 0.19	26.40 ± 8.80	19.75 ± 0.55	ED7 and 1, CC10 (10 coats)
		2		3	3.92 ± 0.48	35.20 ± 1.60	24.30 ± 0.30	ED7 and 1, CC10 (15 coats)
		2		3	6.27 ± 0.32	41.60 ± 3.20	19.50 ± 3.60	ED7 and 1, CC10 (20 coats)

Series	Area /cm^2	Number of anodes	EDIL loading /mg cm^{-2}	500:8: Ni(Au)	Catalyst loading /mg cm^{-2}	Current density /mA cm^{-2}	Φ_{O3}^{e}/%	Comments
19	6.25	1	0.29	3	2.19	33.60	17.20	ED9 and 1, CC10 (10 coats)
		2	0.16 ± 0.02	3	5.71 ± 0.05	36.00 ± 0.80	30.60 ± 0.70	ED9 and 1, CC10 (20 coats)
		2	0.43 ± 0.16	3	1.42 ± 0.11	23.20 ± 4.00	15.60 ± 0.20	ED8 and 1, CC10 (5 coats)
19	6.25	2	0.43 ± 0.16	3	2.88 ± 0.05	28.80 ± 4.80	23.40 ± 0.10	ED8 and 1, CC10 (10 coats)
		2		3	4.03 ± 0.56	35.20 ± 0.00	26.65 ± 0.35	ED8 and 1, CC10 (15 coats)
		3		3	5.71 ± 0.12	36.80 ± 3.46	25.40 ± 2.41	ED8 and 1, CC10 (20 coats)
		1	0.27	3	1.15	22.40	16.70	ED8 and 2, CC10 (5 coats)
		1	0.22	3	1.47	35.20	22.90	ED8 and 2, CC10 (10 coats)
		1	0.26	3	5.86	35.20	27.60	ED8 and 2, CC10 (15 coats)
		1	0.30	3	4..82	35.20	32.20	ED8 and 2, CC10 (20 coats)
	0.64	2	1.80 ± 0.71	3	8.44 ± 0.63	100.00 ± 0.00	23.52 ± 0.30	ED8 and 1,CC10
20	35.0	8	0.46 ± 0.10	3 (1.5)	4.07 ± 0.18	260.20 ± 29.13	23.38 ± 2.84	ED6 and 1, CC11
21	6.25	2	7.94 ± 1.33	3	0.94 ± 0.00	37.60 ± 8.80	28.60 ± 1.49	ED7 and 1 (10:1,40 mA)
		2	0.17 ± 0.06	3	0.55 ± 0.70	42.40 ± 4.00	15.40 ± 0.50	ED12 and 2 (10:2, 5 minutes)
		2	0.27 ± 0.05	NCC	NCC	-	-	ED12 and 2 (10:2, 10 minutes)
		2	0.45 ± 0.02	NCC	NCC	-	-	ED12 and 2 (10:2, 15 minutes)
		2	0.65 ± 0.05	NCC	NCC	-	-	ED11 and 2 (10:2, 20 minutes)
		2	0.16 ± 0.08	NCC	NCC	-	-	ED13 and 2 (no Sn, 5 minutes)
		2	0.32 ± 0.02	NCC	NCC	-	-	ED13 and 2 (no Sn, 10 minutes)
		2	0.38 ± 0.01	NCC	NCC	-	-	ED13 and 2 (no Sn, 15 minutes)
		2	0.45 ± 0.02	NCC	NCC	-	-	ED13 and 2 (no Sn, 20 minutes)
22	6.25	4	0.53 ± 0.08	3	2.95 ± 0.19	39.2 ± 7.02	28.60 ± 1.49	ED12 and 2, CC12, 15 coats
		4			3.71 ± 0.08	33.6 ± 1.96	25.48 ± 1.58	ED12 and 2, CC12, 20 coats
23	0.64	2	1.25 ± 0.45	NCC	NCC	-	-	ED14 and 2 (10:2, 5 minutes)
		2	0.70 ± 0.20	NCC	NCC	-	-	ED14 and 2 (10:2, 10 minutes)
		1	1.2	NCC	NCC	-	-	ED14 and 2 (10:2, 15 minutes)
		2	0.95 ± 0.45	NCC	NCC	-	-	ED14 and 2 (10:2, 20 minutes)
		2	0.55 ± 0.25	NCC	NCC	-	-	ED15 and 2 (no Sn, 5 minutes)
		2	0.50 ± 0.00	NCC	NCC	-	-	ED15 and 2 (no Sn, 10 minutes)
		1	0.9	NCC	NCC	-	-	ED15 and 2 (no Sn, 15 minutes)
		2	2.00 ± 0.30	NCC	NCC	-	-	ED15 and 2 (no Sn, 20 minutes)

Series	Area /cm^2	Number of anodes	EDIL loading /mg cm^{-2}	500:8: Ni(Au)	Catalyst loading /mg cm^{-2}	Current density /mA cm^{-2}	Φ_{O3}^{e}/%	Comments
24	6.25	2	10.71 ± 1.83	NCC	NCC	-	-	ED7 and 1 (10:1,40mA)
		1	0.08	NCC	NCC	-	-	ED12 and 2 (10:2 , 5 minutes)
		1	0.26	NCC	NCC	-	-	ED12 and 2 (10:2 , 10 minutes)
		1	0.46	NCC	NCC	-	-	ED12 and 2 (10:2 , 15 minutes)
24	6.25	2	0.45 ± 0.10	NCC	NCC	-	-	ED12 and 2 (10:2 , 20 minutes)
		1	0.80	NCC	NCC	-	-	ED12 and 2 (10:2 , 30 minutes)
		1	1.15	NCC	NCC	-	-	ED16 and 2 (10:2, 20 minutes)
25	6.25	1	0.21	NCC	NCC	-	-	ED17 and 1 (10:1), 6.25cm^2 Pt/Ti
		1	0.38	NCC	NCC	-	-	ED18 and 1 (no Sn,)
		1	0.54	NCC	NCC	-	-	ED19 and 1 (10:2, 36 cm^2 Pt/Ti)
		1	0.14	NCC	NCC	-	-	ED20 and 1 (10:2, 5 minutes)
		1	0.13	NCC	NCC	-	-	ED20 and 1 (10:2, 10 minutes)
		1	0.24	NCC	NCC	-	-	ED20 and 1 (10:2, 15 minutes)
		1	0.99	NCC	NCC	-	-	ED20 and 1 (10:2, 20 minutes)
		1	0.27	NCC	NCC	-	-	ED20 and 1 (10:2, 25 minutes)
25E	6.25	1	0.99	3	4.06	0.32	40.8	ED20 and 1, CC12
26	0.64	3	0.89 ± 0.45	0	6.41 ± 0.34	126.17 ± 58.83	2.12 ± 0.97	ED14 and 2, CC12
		4	1.25 ± 0.16	3	6.30 ± 0.41	78.63 ± 34.63	11.68 ± 6.72	NED, ED14 and 2, CC12
		2	NED	3	6.19 ± 0.54	81.95 ± 5.55	11.61 ± 9.06	NED, CC12
		2	1.25 ± 0.16	3	6.41 ± 0.16	75.31 ± 48.44	11.75 ± 2.86	ED14 and 2, CC12
		5	1.15 ± 0.41	3 (0.1)	5.84 ± 0.29	85.66 ± 80.18	23.63 ± 11.03	NED, ED14 and 2, CC12
		2	NED	3 (0.1)	5.94 ± 0.32	26.25 ± 0.63	24.92 ± 15.46	NED, CC12
		3	1.15 ± 0.41	3 (0.1)	5.78 ±0.25	145.08 ± 13.52	22.33 ± 0.99	ED14 and 2, CC12
27	6.25	3	0.83 ± 0.62	3	4.64 ± 0.16	69.30 ± 5.28	39.27 ± 1.89	ED20 and 1, CC12
		3	0.37 ± 0.15	3 (0.1)	4.33 ± 0.31	54.40 ± 1.31	41.07 ± 1.97	
		3	0.45 ± 0.14	3 (0.3)	4.29 ± 0.26	60.80 ± 2.61	37.90 ± 0.65	
		3	0.24 ± 0.06	3 (1.5)	4.21 ± 0.11	63.47 ± 2.00	21.60 ± 1.84	

Series	Area /cm^2	Number of anodes	EDIL loading /mg cm^{-2}	500:8: Ni(Au)	Catalyst loading /mg cm^{-2}	Current density /mA cm^{-2}	Φ_{O3}^{e}/%	Comments
27	0.64	1	0.05	3	6.72	-	-	ED21 and 1, CC12
		1	0.21	3 (0.1)	6.41	-	-	
		1	0.11	3 (0.3)	5.94	-	-	
		1	0.06	3 (1.5)	6.25	-	-	

Table 5.7 Overview of the EDIL loading, catalyst loading, current density and efficiency derived at the end of the first experiment for the anodes investigated during the work in this thesis. In each case, the anodes were employed to electrolyse 0.5 M H_2SO_4 in glass cell at a cell voltage of 2.7 V in single pass system.

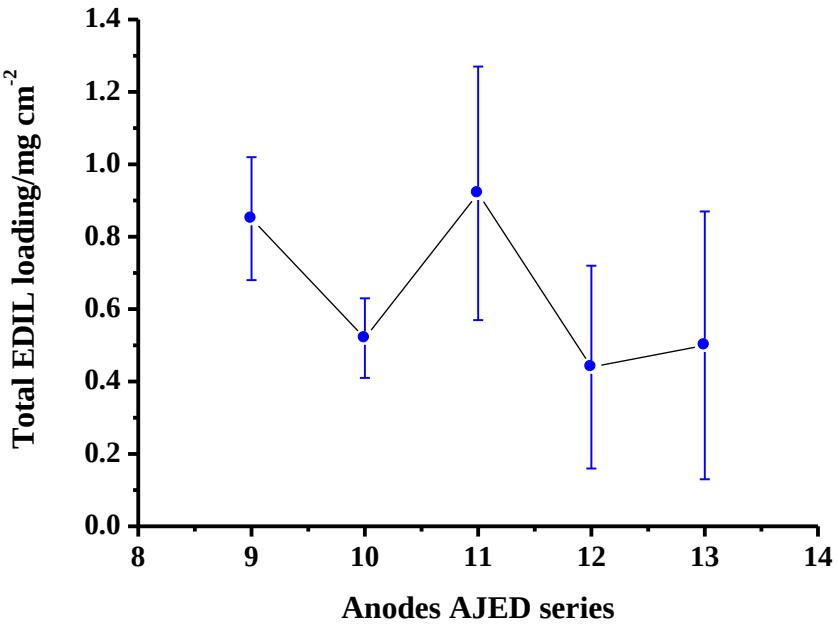

Figure 5.28 (a) A plot of the mean EDIL loadings of the anodes AJED series prepared at 520 ºC and utilising ED1 and cell configuration 1.

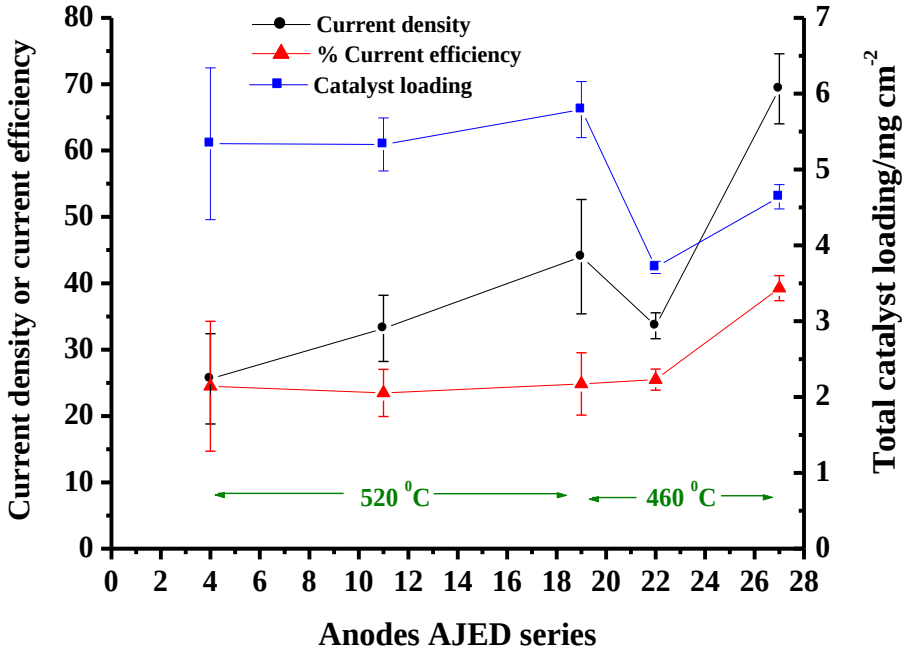

Figure 5.28 (b) Plots of current density (●), current efficiency (▲) and catalyst loading (■) of the 6.25 cm^2 anodes AJED series (500:8:3) anodes prepared by pyrolysis the catalyst coating for 10 minutes at 460 ºC or 20 minutes at 520 ºC.

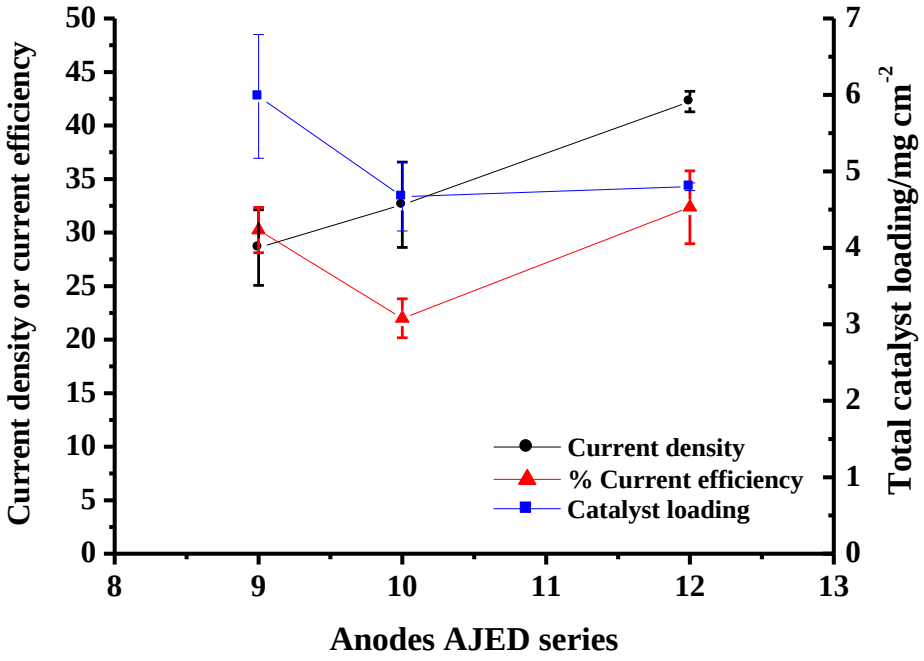

Figure 5.29 Plots of current density (●), current efficiency (▲) and catalyst loading (■) of the 6.25 cm^2 anodes AJED series (500:8:1) anodes prepared by pyrolysis of the catalyst coating for 20 minutes at 520 ºC.

5.5 Conclusions

The Ni/Sb-SnO_2 anodes deactivated by two primary mechanisms: (1) physical loss of bulk catalyst (*i.e.* spallation), possibly associated with defects in the coating, leading to a decrease in current and current efficiency, and (2) dissolution of Ni (and possibly Sb and Sn) leading to a switch from ozone to oxygen but no decrease in current. The latter can be ameliorated by heating the anode to promote diffusion of Ni from the bulk to replenish the surface.

The catalyst development represented by tables 4.1 to 4.3 did not result in an improvement of ozone selectivity or activity or in an improvement in the reproducibility of the synthetic procedure. However, modification of the synthesis employed to produce the anodes AJED2 series anodes did give highly active and selective anodes, and did give good reproducibility in terms of the catalyst loading, current and ozone current efficiency. However, the EDIL loading remained irreproducible, and the addition of Au to the catalyst resulted in no beneficial effect.

5.6 References

1. Lozano, B. C., Ch. Comninellis and A. De Battisti, "Service Life of Ti/SnO_2-Sb_2O_5 Anodes," *Journal of Applied Electrochemistry* 27(8):970-974 (1997).
2. Foller, P. C., and C. W. Tobias, "The Anodic Evolution of Ozone," *Journal of the Electrochemical Society* 129(3): 506-515 (1982).
3. Bard, A. J., R. Parsons and J. Jordan, *Standard Potentials in Aqueous Solution*. New York and Basel: International Union of Pure and Applied Chemistry, p. 321-339 (1985).
4. Chan, K. Y., and P. A. Christensen, *Personal Communication.* (2006).
5. Kelsall, G., and P. A. Christensen, *Personal Communication.*, January (2011).
6. Pourbaix, M., *Atlas of Electrochemical Equilibria in Aqueous Solutions.* Texas : National Association of Corrosion Engineering, p. 330-342 (1974).
7. Wagman, D. D., W. H. Evans, V. B. Parker, R. H. Schumm, I. Halow, S. M. Bailey, K. Churney and R. L. Nuttall, "The NBS Tables of Chemical Thermodynamic Properties," *Journal of Physical Chemistry Reference Data 11*, Supplement 2 (1982).
8. Cotton, F. A., and G. Wilkinson, C. A. Murillo and M. Bochmann, *Advanced Inorganic Chemistry*, 6th Edition, Toronto, p. 835-854 (1999).
9. Treasatti, S. and W. E. O'Grandy In: H Gerischer and CW Tobias, Editors, *Advances in Electrochemistry and Electrochemical Engineering*. Vol. 10, New York: Wiley Interscience p. 213-321 (1980).
10. Vicent, F., E. Morallón, C. Quijada, J. L. Vázquez and A. Aldaz, "Characterization and Stability of Doped SnO_2 Anodes," *Journal of Applied Electrochemistry* 28:607-612 (1998).
11. Kötz, R., S. Stucki and B. Carcer, "Electrochemical Waste Treatment using High Overvoltage Anodes. Part I: Physical and Electrochemical Properties of SnO_2 Anodes," *Journal of Applied Electrochemistry* 21(1): 14-20 (1991).
12. Montilla, F., E. Morallón, A. De Battisti and J. L. Vázquez, "Preparation and Characterization of Antimony-Doped Tin Dioxide Electrodes. Part 1. Electrochemical Characterization," *Journal of Physical Chemistry B* 108(16): 5036-5043 (2004).

13. Montilla, F., E. Morallón, A. De Battisti, A. Benedetti, H. Yamashita and J. L. Vázquez, "Preparation and Characterization of Antimony-Doped Tin Dioxide Electrodes. Part 2. XRD and EXAFS Characterization," *Journal of Physical Chemistry B* 108(16): 5044-5050 (2004).
14. Montilla, F., E. Morallón, A. De Battisti, S. Barison, S. Daolio and J. L. Vázquez, "Preparation and Characterization of Antimony-Doped Tin Dioxide Electrodes. Part 3. XPS and SIMS Characterization," *Journal of Physical Chemistry B* 108(41): 15976-15981 (2004).
15. Christensen, P. A., and W. F. Lin, *Electrode and Method of Manufacture and Use Thereof*. PCT/GB07/02299, 19 June (2007).
16. Brackenbury**,** K. F. G., L. Jones**,** I. Nel**,** K. R. Koch **a**nd J. M. Wyrley-Birch**,** "Tin(II) Chloride in the Analytical Chemistry of the Platinum Metals: From the "Purple of Cassius" to Polyurethane Foams," *Polyhedron* 6(1): 71-78 (1987).
17. Hunt, L. B., "The True Story of Purple of Cassius. The Birth of Gold-Based Glass and Enamel Colours," *Gold Bulletin* 9(4): 134-139 (1976).

Chapter 6 Scale up

6. Scale up

6.1 Introduction

This chapter reports data obtained using 24 cm^2 and 35 cm^2 Ni/Sb-SnO_2 electrodes in 0.5 M H_2SO_4 the glass and polycarbonate cells, respectively, in single pass system (see fig 3.8), and also in single pass system in the water/air cell. The first scale up was to 6.0 cm x 4.0 cm, and these anodes were tested in the glass cell as an intermediate step to the polycarbonate cell. Anodes for the latter (both for acid electrolyte and water/air tests) were usually > 35 cm^2 to allow for the removal of the wire contacts for deposition and then cut to 7.0 cm x 5.0 cm and spot-welded to a Ti frame (aperture 6.0 cm x 4.0 cm, see fig 2.4 (h)). The regions to be spot-welded were gently sanded to remove the catalyst coating.

The work reported in this chapter was carried out in collaboration with Dr. Henriette Christensen and employing primarily anodes made by her as part of the Clarizon development programme.

6.2 Fabrication and testing of 24-35 cm^2 anodes in acidic electrolyte

6.2.1 Anodes HCED2 series

The first, scaled-up batch of electrodes made by Dr. Christensen (6.0 cm x 4.0 cm, anodes HCED2 series prepared by ED1/CC4) were tested in the glass cell for ozone activity at a cell voltage 2.7 V using the experimental system shown in fig. 3.8. The characteristics of the anodes and the ozone activities derived in the first experiment on each electrode are shown in table 6.1.

As well as investigating the potential challenges of scaling up the preparation of the anodes, the series was also intended to confirm the effect of adding HCl to the electrodeposition and catalyst coating solutions. The results so obtained did confirm the findings in section 4.4.2 in that the addition of HCl reduced the average catalyst loading.

From table 6.1 it can be seen that the electrodeposition process resulted in a relatively wide variation in EDIL loading within the 'no HCl' and 'added HCl' sub-series. The catalyst loading also showed some irreproducibility, particularly in the case of anodes HCED2E-H. The current efficiencies determined in 0.5 M H_2SO_4 were fairly reproducible for anodes HCED2A-D, but less so for anodes HCED2E-H, possibly reflecting the variation in both EDIL and catalyst loadings of the latter anodes.

Anodes HCED2	**EDIL loading /mg cm^{-2}**	**Catalyst loading /mg cm^{-2}**	**Current at 2.7 V /A**	**Current efficiency /%**	**Comments**
A	0.55	3.1	0.40	25	No HCl
B	0.75	3.4	0.50	25	
C	0.74	3.4	0.45	24	
D	0.74	3.4	0.45	22	
E	1.25	2.8	0.40	24	HCl
F	1.55	3.0	0.50	22	
G	0.97	2.9	0.35	20	
H	0.92	2.4	0.45	15	

Table 6.1 The characteristics of the 6.0 cm x 4.0 cm anodes HCED2 series (500:8:1 Sn:Sb:Ni in the coating solution). The anodes were tested in the glass cell at a cell voltage of 2.7 V, anolyte and catholyte 0.5 M H_2SO_4.

6.2.2 Anodes HCED15 series

The anodes HCED15 series were the first attempt to make anodes for use in the polycarbonate water/air cell. The mole ratio in the catalyst coating solution was 500:8:1:1.5 Sn:Sb:Ni, and the electrodes were fabricated using ED1 and CC6. Electrodeposition and catalyst coating was carried out using 5.0 cm x 8.0 cm mesh substrates, after which the wires were cut off to leave 7.0 cm x 5.0 cm meshes which were then spot-welded into Ti frames for use in the polycarbonate cell, see section 2.2.2 and 2.4.

The work described in section 4.4 suggested that furnace temperatures < 400 ºC should be employed to avoid excessive EDIL loss during furnace treatment; this was supported by Prof. K. Y. Chan who stated the temperature monitoring system on his furnace during his early work [1][2][3] had been faulty, reading high. He reduced the post-ED furnace temperature to 390 ºC [4] in his subsequent work. Hence, the EDIL-coated series 15 Ti meshes were heated at 390 ºC. In addition, the catalyst-coated anodes HCED15A-D were pyrolysed at 520 ºC, whilst anodes HCED15E-H were pyrolysed at 460 ºC. Table 6.2 summarises the EDIL and catalyst loadings of the series 15 anodes. The mole ratio in the coating solution was 500:8:1:1.5 Sn:Sb:Ni:Au.

Anodes HCED15	**EDIL loading /mg cm^{-2}**	**Catalyst loading /mg cm^{-2}**	**Comments**
A	1.1	3.0	Catalyst coating pyrolysed at 520 ºC
B	1.1	2.8	
C	1.1	2.8	
D	1.1	2.8	
E*	0.4	3.1	Catalyst coating pyrolysed at 460 ºC
F	1.1	3.0	
G	1.0	2.8	
H	0.9	2.8	

*Table 6.2 The EDIL and catalyst loading of the anodes HCED15 series. The EDIL was heated at 390 ºC in the furnace. The geometric area of the Ti mesh used to calculate the EDIL and catalyst loadings was 40.0 cm^2. The area of the mesh in the Ti frame was 35.0 cm^2. (*During the electrodeposition of the EDIL on anode E, the electrodes touched)*

As may be seen from the table, the lower furnace temperature resulted in a more reproducible EDIL loading of *ca.* 1.1 mg cm^{-2}. In addition, the catalyst loadings only varied to within ± 10%. However, there was no discernible difference between the anodes pyrolysed at 520 ºC and those pyrolysed at 460 ºC (anodes HCED15A-D and HCED15E-H, respectively). Despite the more reproducible EDIL loading derived with the anodes series 15, the coverage of the Ti substrate was poor, as may be seen from the

typical SEM images of anode HCED15F in figs. 6.1 (a) and (b), and the corresponding EDX spectrum in fig. 6.1 (c).

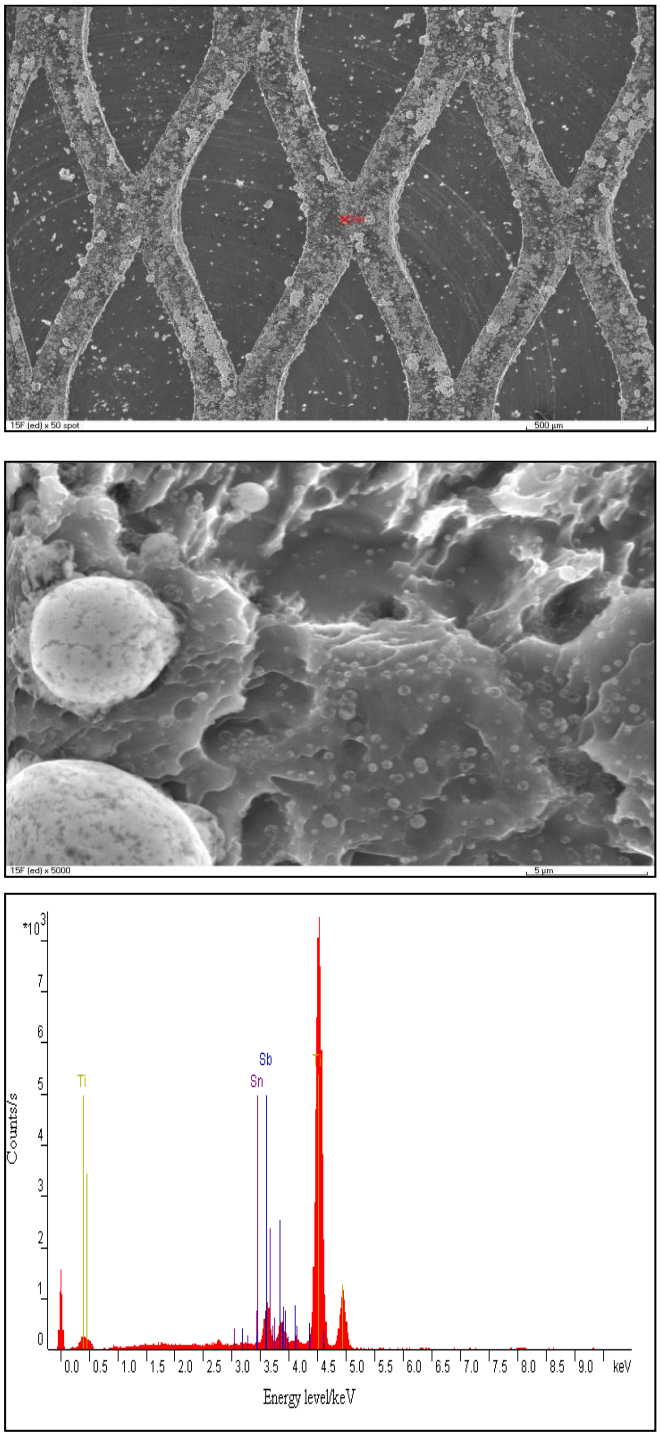

(a)

(b)

(c)

Figure 6.1 SEM micrographs of anode HCED15F (a) x50 and (b) x5000, and (c) an EDX spectrum of the anode, taken from the spot marked with an "X" in (a).

This poor coverage by the EDIL did not seem to affect the catalyst coating process, as may be seen from figs. 6.2 (a)-(c) which show plots of the catalyst mass after 5, 10 ,15 and 18 cycles for (a) anodes HCED15A-D and (b) anodes HCED15E-H, and (c) the total catalyst mass. The plots for anodes HCED15A-D show remarkable reproducibility, whilst those for anodes HCED15E-H still show good reproducibility when allowance is made for the electrodeposition problem with anode HCED15E.

The anodes HCED15 series were tested for activity with respect to ozone generation in the polycarbonate cell using aqueous 0.5 M H_2SO_4 as the anolyte and catholyte. Initial experiments showed low currents, typically *ca.* 0.6 A, suggesting the current was scaling with perimeter rather than area. Typical data are shown in fig. 6.3 for the current (a) and current efficiency (b) observed during an electrolysis experiment employing anode HCED15B.

The design of the polycarbonate cell was such that the geometric areas of cathode and anode are ≤ 35 cm^2 in total, with the aperture of the Ti frames employed (see fig. 2.4 (h)) being 24 cm^2. The maximum anode area of 35 cm^2 was employed by Clarizon meaning that the maximum counter electrode area was also 35 cm^2. Hence, unless the Pt/Ti counter electrode had a significantly higher surface roughness than the ozone anode, the electrolysis could be counter electrode limited. In order to test this, a new, freshly prepared Pt/Ti counter electrode was employed, the electrolysis repeated and the data plotted also in figs. 6.3 (a) and (b).

As may be seen, the replacement of the counter electrode had a marked effect, and one that was observed with all the anodes HCED15 series, upon both the current and current efficiency. Typically, at a cell voltage of 2.7 V, currents around *ca.* 2.0 A were determined (greater than would be expected on scaling the currents typically derived with the 6.25 cm^2 anodes in the glass cell), but some of this enhancement was almost certainly due to the uniform and smaller electrode separation in the polycarbonate cell compared to the glass (cell). In addition, very much higher current efficiencies were determined, particularly with anodes HCED15E-H. The significantly higher currents and

ozone current efficiencies required much higher anolyte flow rates, and the former led to significant instabilities in the ozone UV absorbance due to vigorous bubble formation, as may be seen in the plots of current and efficiency obtained.

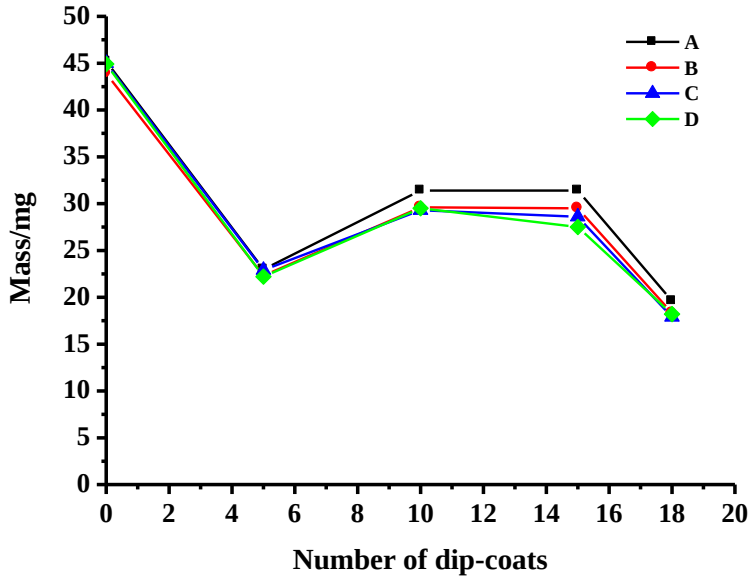

(a)

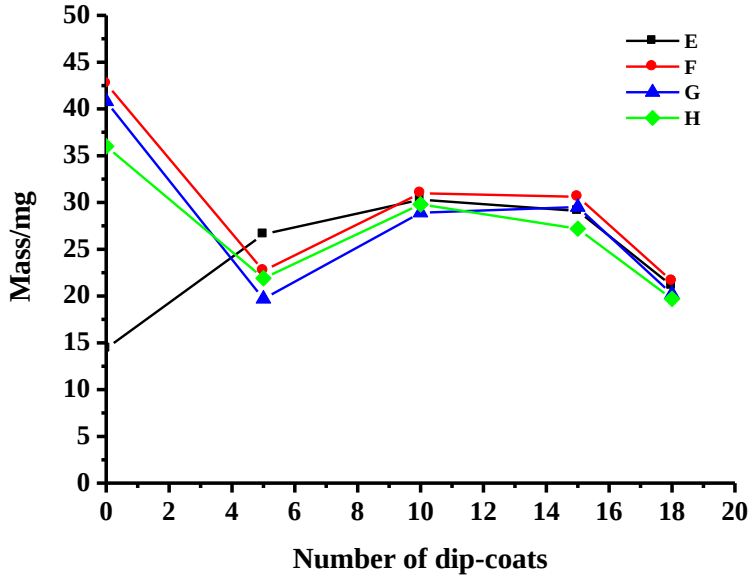

(b)

Figure 6.2 Plots of the catalyst mass deposited after 5, 10, 15 and 18 dip-coats for the (a) anodes HCED15A-D and (b) anodes HCED15E-H. The mass at 0 dip-coats is the mass of the EDIL.

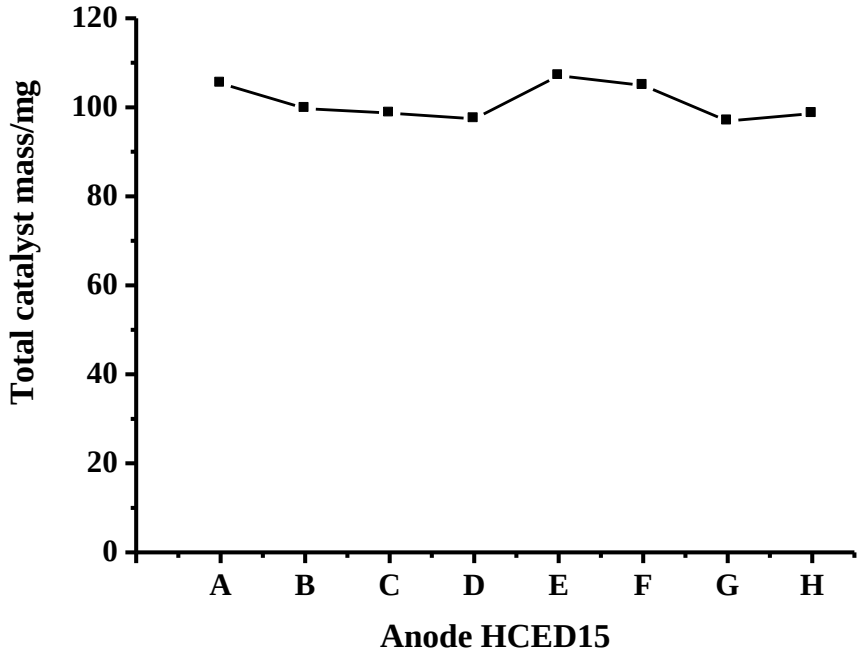

Figure 6.2 (c) Plot of the total catalyst mass deposited for the anodes HCED15 series.

The problem of gas bubbles occurred despite using a gas separator, see fig. 6.4. The ozone gas was not measured; hence the current efficiencies so obtained are very likely to be underestimates. The currents and current efficiencies derived for the anodes HCED15 series are summarised in table 6.3.

In general, the anodes HCED15 series did not show degradation after *ca.* 2 days electrolysis in 0.5 M H_2SO_4 at 3.0 V, see figs. 6.5 (a) and (b). As may be seen from the figure, electrolysis did not affect the current, *ca.* 2.0 A at 2.7 V. Gas evolution was vigorous, suggesting that the 10% current efficiency measured from the dissolved ozone was a significant underestimate.

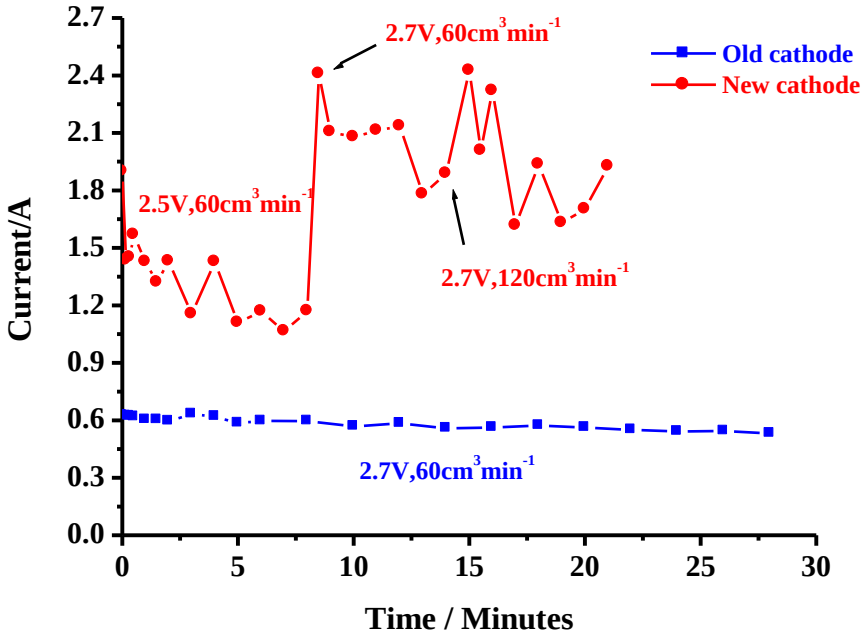

(a)

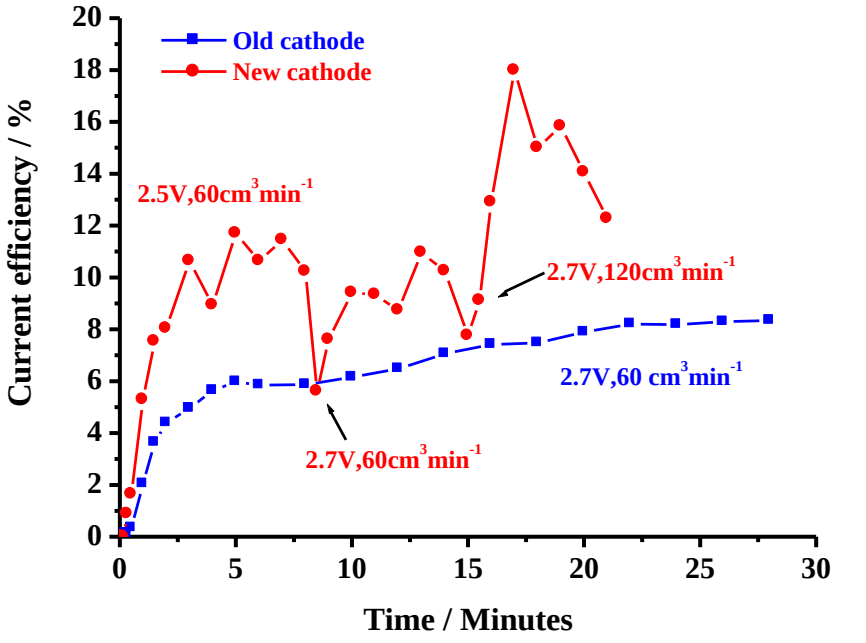

(b)

Figure 6.3 Plots of (a) current and (b) current efficiency obtained during the electrolysis of 0.5 M H_2SO_4 in the polycarbonate cell at a cell voltage of 2.7 V using anode HCED15B. The anode was tested twice: once using an old 5.0 cm x 7.0 cm Ti frame-mounted Pt/Ti counter electrode, (aperture 6.0 cm x 4.0 cm) (■) and then again using a freshly prepared counter electrode (●).

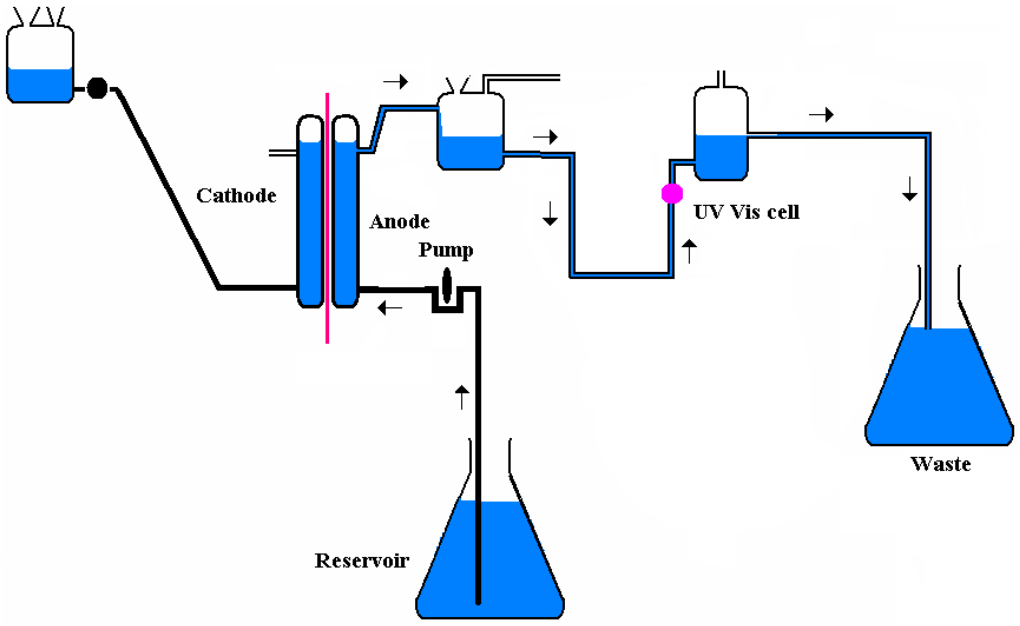

Figure 6.4 The experimental system employed to measure the ozone activity of the anodes HCED15 series. The anti-siphon device was employed to prevent the sucking back of electrolyte from the reservoir.

Anode HCED15	Current at 2.7 V /A	Current efficiency /%
A	1.9	25
B	2.1	15
C	2.4	12
D (1)	1.4	6
D (2)	2.0	10
E	1.7	30
F	2.0	30
G	2.0	30
H	2.0	40

Table 6.3 The currents and current efficiencies for ozone determined using the anodes HCED15 series in the polycarbonate cell and the system in fig. 6.4 cell voltage 2.7 V, flow rate 240 cm^3 min^{-1} 0.5 M H_2SO_4 (static catholyte).

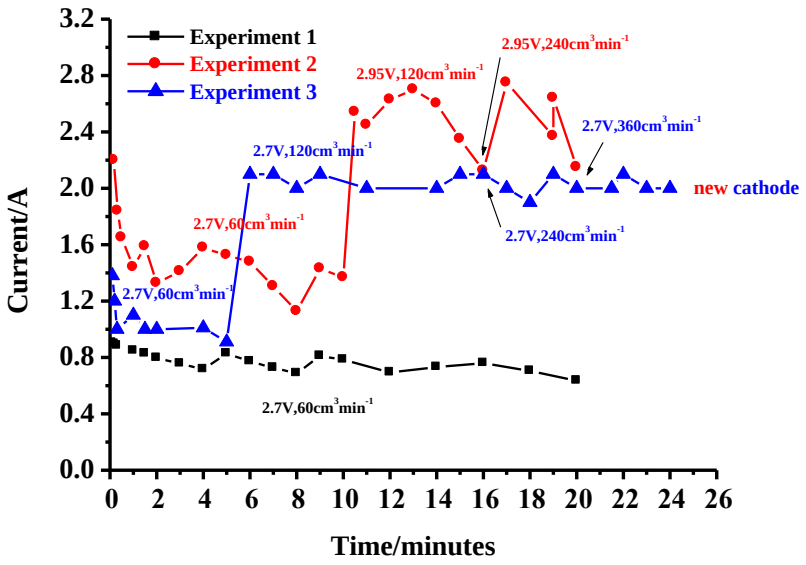

(a)

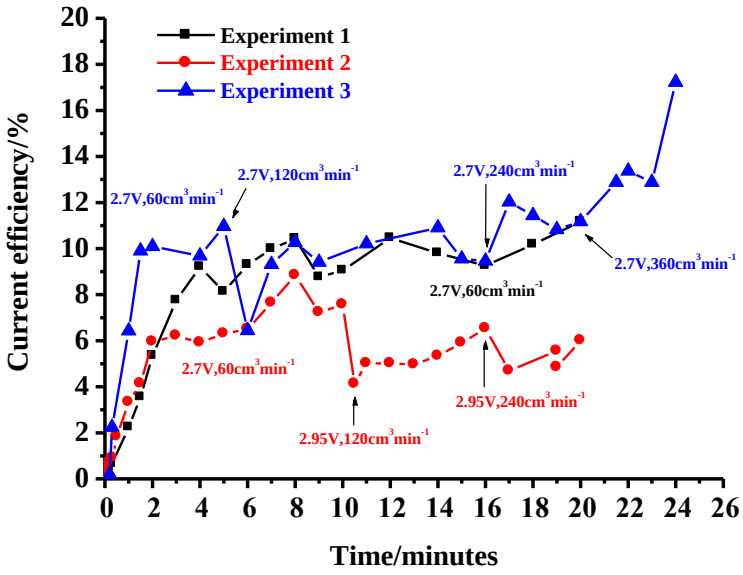

(b)

Figure 6.5 Plots of (a) current and (b) current efficiency during three experiments using anode HCED15D to electrolyse 0.5 M H_2SO_4 in the glass cell. Experimental conditions as shown on the figure. Experiment 1 (■), experiment 2 (●) and experiment 3 (▲); between experiments 1 and experiment 2 the anode was employed to electrolyse 0.5 M H_2SO_4 in a beaker for 48 hours at 3.0 V. Counter electrode was Pt/Ti mesh.

6.2.3 The anode Magneto series

Clarizon approached Magneto, a specialist electrode company located in The Netherlands [5], to manufacture a batch of anodes according to the methodology developed in Newcastle. The primary aims of this were to gain access to the company's expertise and to see if the technology developed in Newcastle could be transferred.

Twenty 7.7 cm x 6.0 cm etched and EDIL-coated Ti meshes were sent to Magneto (cleaned and etched in Newcastle as per the procedures in Chapter 2), along with the metal salts and instructions. In essence, the Magneto (MAGED1-20) anodes were prepared *via* ED1/CC3; however, the catalyst coating was brushed on and the Sn^{II} was oxidised to Sn^{IV} prior to adding the $AuCl_3$ by bubbling oxygen through the catalyst coating solution for 2 hours. The target catalyst loading was 125 ± 0.5 mg, before removing the Ti wires and hence trimming the mesh to 7.0 cm x 5.0 cm ready for spot-welding to the Ti frame. The characteristics of the anodes are shown in table 6.4.

Magneto anodes	**EDIL loading / mg cm^{-2}**	**Mass of catalyst / mg**
1	0.79	126
2	0.75	127
3	1.06	125
4	0.84	127
5	0.98	128
6	0.72	125
7	0.78	127
8	0.70	126
9	1.02	126
10	0.95	124
11	1.04	129
12	1.03	125
13	1.08	128
14	1.03	128
15	1.05	128
16	0.94	126
17	1.17	128
18	1.17	129
19	1.23	125
20	1.12	126

Table 6.4 The EDIL and catalyst loading of the anodes Au/Ni/Sb-SnO_2 (MAGED series) prepared by Magneto.

Despite employing the lower furnace temperature, as may be seen from the table, the EDIL loading showed a wide variation, *i.e.* from 0.70 to 1.23 mg cm^{-2}. However, the distribution of the catalyst mass was very narrow indeed 124-129 mg, an excellent result.

SEM and EDX were employed to characterize representative anodes from the Magneto series, and compared to similar data obtained using HCED18N (prepared *via* ED1/CC4).

Figures 6.6 (a) and (b) show typical SEM images of anode HCED18N at x50 and x5000 magnification, respectively. The morphology was of the usual 'cracked earth' form, see fig. 6.6 (b). As may be seen from fig. 6.6 (a), there seems to be significant difference between the coating where the strands cross and on the strands themselves. This was confirmed by EDX spectra taken where the crosses are in fig. 6.6 (a); see figs. 6.7 (a) and (b).

Given the assignments of the EDX peaks of Ti, Sn and Sb (see table 4.5 and discussion) it was clear that the catalyst coating was significantly thinner on the strands compared to the crossing points since, at the former the peak due to Ti at 4.52 keV is clear, and the Sb peaks due to the underlying EDIL dominate (3.62 keV, 3.88 keV, 4.11 keV and 4.37 keV). This was quite often found to be the case, irrespective of who made the anodes in Newcastle.

For comparisons, figs. 6.8 and 6.9 show analogous data to those in figs. 6.6 and 6.7 for anode MAGED3 which were typical of the series. As may be seen from fig. 6.8 (a), the anode presents a more uniform topography than anode HCED18N, with no difference between strands and crossing points. This was supported by the EDX spectra in figs. 6.9 (a) and (b). Figure 6.8 (a), however, suggests a more granular structure of the catalyst than anode HCED18N. The layer appears to be continuous, with no cracks or crevices and hence may provide a more effective barrier to electrolyte penetration. The EDX spectra apparently show a 30% thicker catalyst layer on the crossway in agreement with the SEM image in fig. 6.9 (a), but the relative intensities of the Sn and (Sn+Sb) peaks

are 2.0:1 at the crossway and 1.8:1 on the strand, which were relatively close (especially when compared to fig. 6.7 (b) where the ratio is 1:1). There were no significant Au features. Thus it appears that the catalyst layer was more uniformly distributed across the mesh, and more homogeneous in composition than was routinely obtained with the Newcastle anodes.

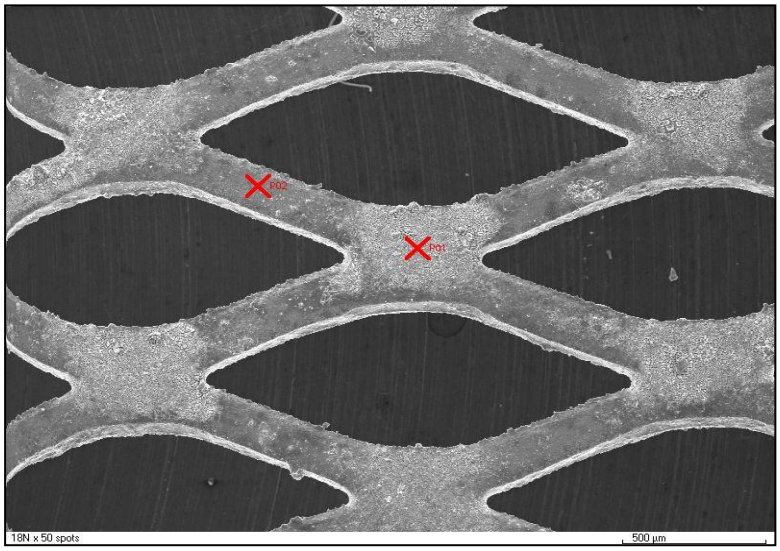

(a)

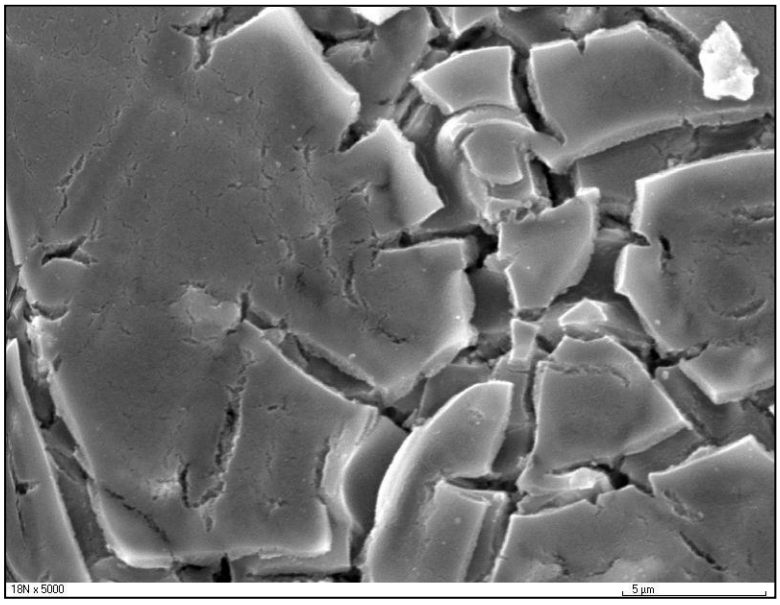

(b)

Figure 6.6 Typical SEM images of anode HCED18N (a) x50 and (b) x5000. The bars = (a) 500 µm and (b) 5 µm.

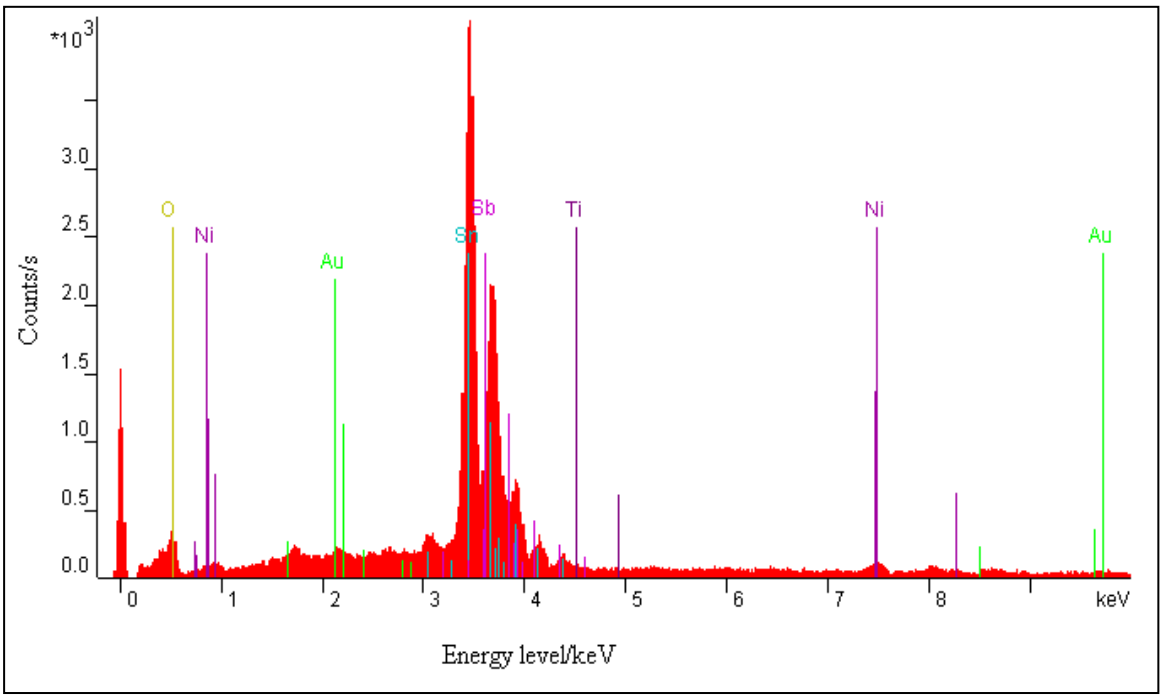

(a)

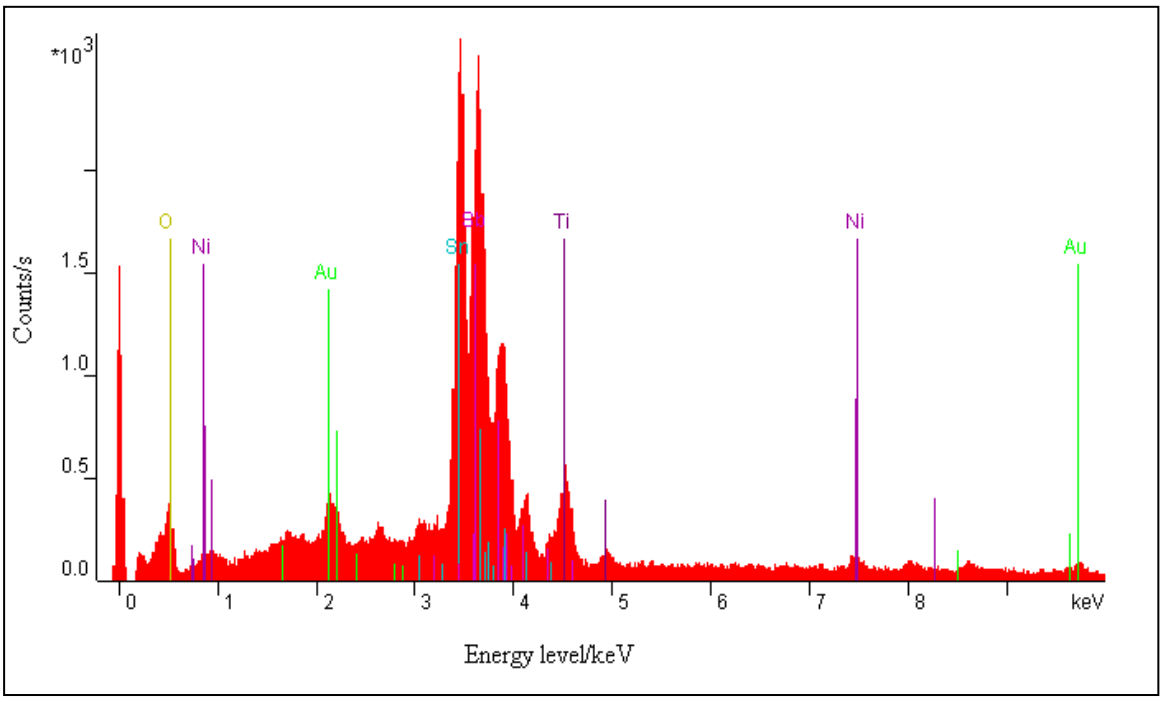

(b)

Figure 6.7 EDX spectra of anode HCED18N on (a) crosswire and (b) strand from the locations marked with the X's in fig. 6.6 (a).

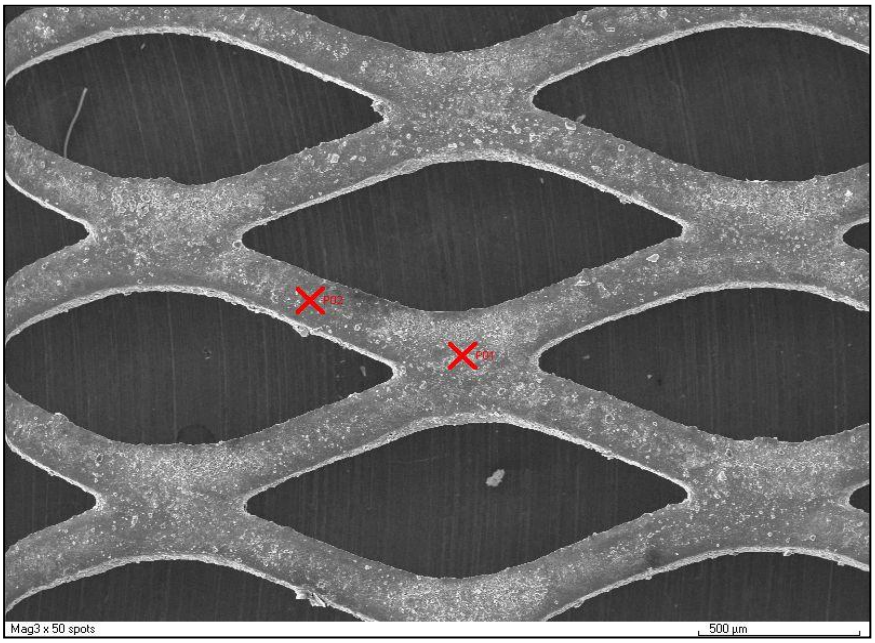

(a)

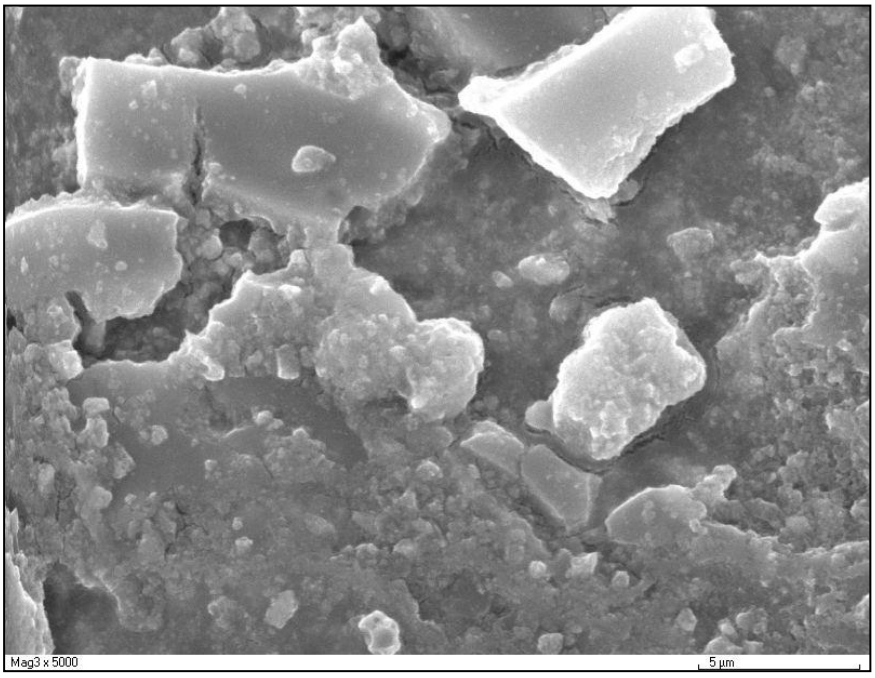

(b)

Figure 6.8 Typical SEM images of anode MAGED3 (a) x50 and (b) x5000. The bars = (a) 500 µm and (b) 5 µm.

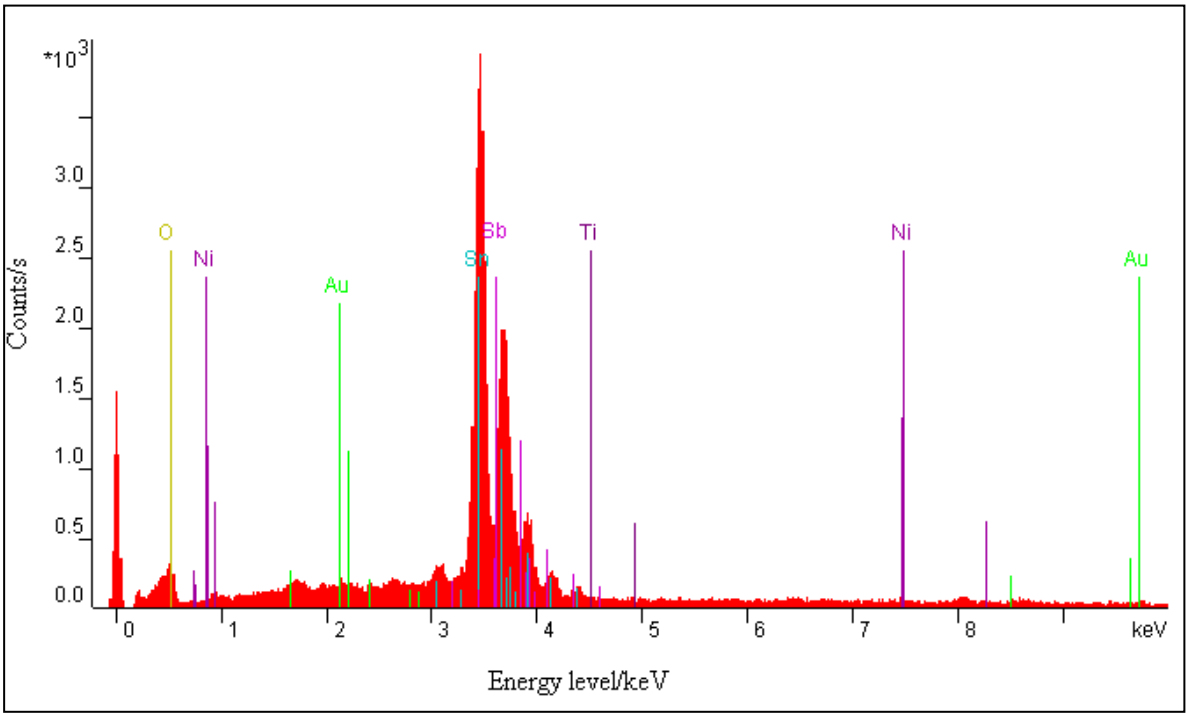

(a)

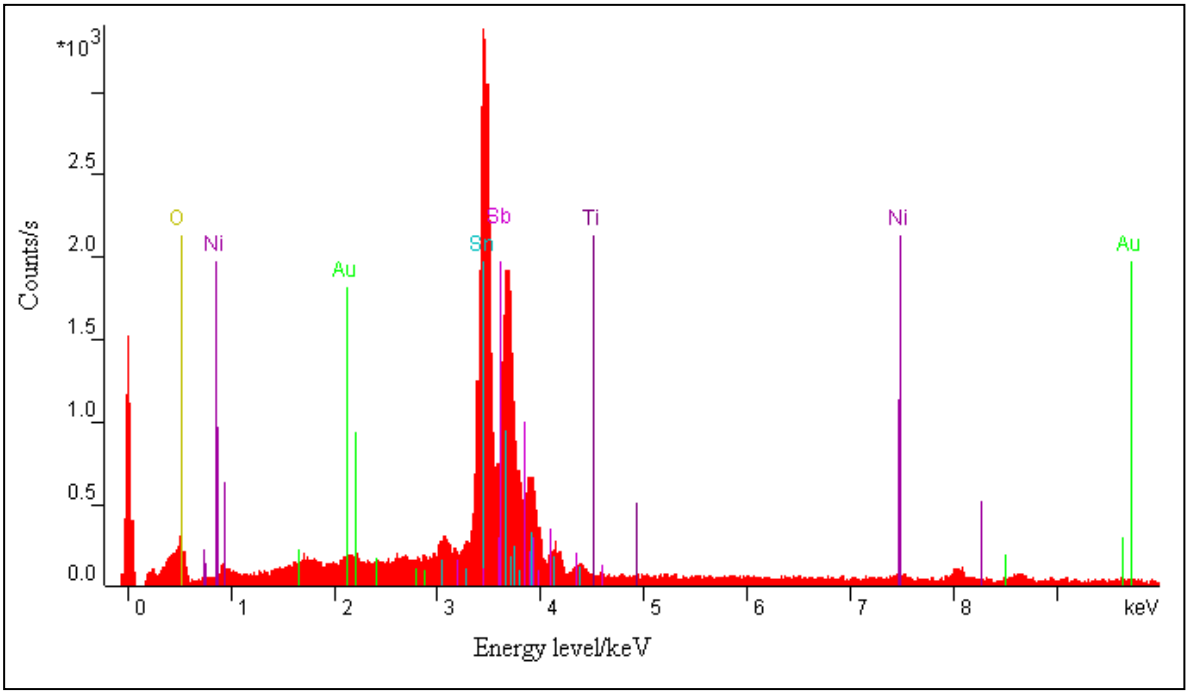

(b)

Figure 6.9 EDX spectra of anode MAGED3 on (a) crosswire and (b) strand from the locations marked with the X's in fig. 6.8 (a).

Time did not allow all the nodes MAGED series to be tested for ozone activity; those that were investigated were tested in the polycarbonate cell in the system depicted in fig. 6.10, which allowed both gas phase and liquid phase ozone to be monitored. Data typical of those anodes that were investigated are shown in figs. 6.11 (a) and (b), which show plots of current, solution absorbance and gas absorbance, fig. 6.11 (a), and efficiencies, fig. 6.11 (b), obtained with anode MAGED13. The data were obtained using new prototype software developed by Clarizon for controlling both the Hameg power supply and the Astranet spectrometer.

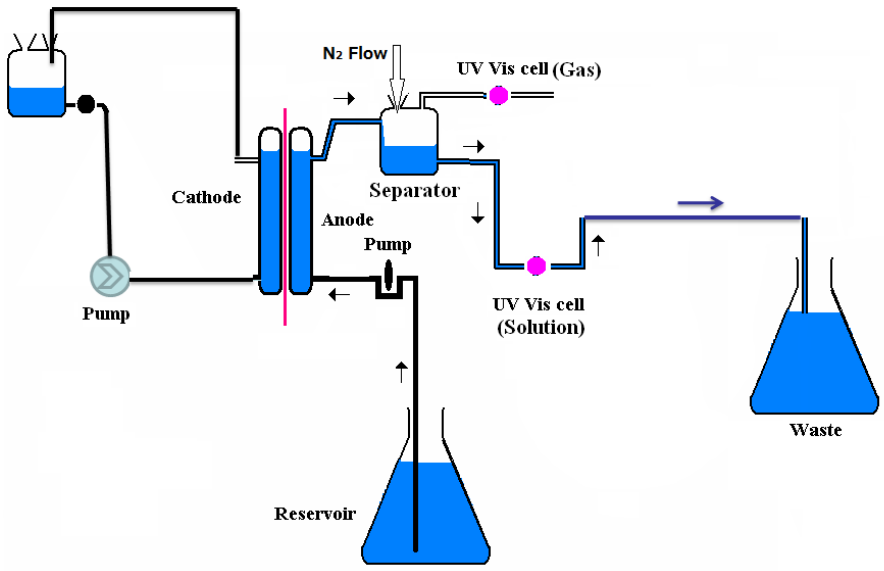

Figure 6.10 The experimental system employed to measure the ozone activity of the anodes MAGED series.

As can be seen form figs. 6.11 (a) and (b), the current observed at the cell voltage of 2.7 V falls from *ca.* 2.9 to 1.8 A over the 12 minutes of the experiment, and was fairly unstable. Such high currents clearly generate very high volumes of gas, 11.0 cm^3 per minute (assuming 100% current efficiencies for O_2 evolution, for convenience) in a solution volume of 200 cm^3. The presence of such bubbles will cause fluctuations in the solution resistance, as shown by the variation in the current; accumulation of bubbles in the cell can cause blockage of the anode, which may be the reason for the fall in current over the timescale of the experiment. Bubbles bursting will cause fluctuations in the gas

phase O_3 absorbance and light scattering by bubbles in solution will similarly cause fluctuations in the solution phase measurements, hence the variations in the relevant plots in fig. 6.11 (a).

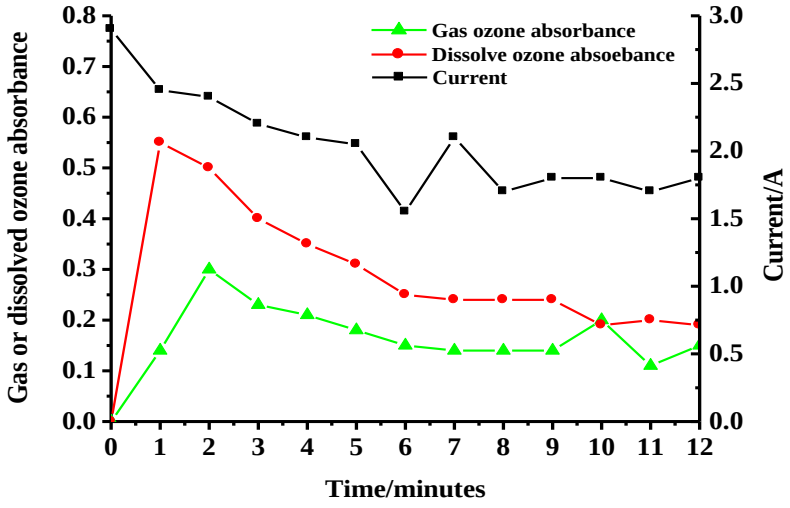

(a)

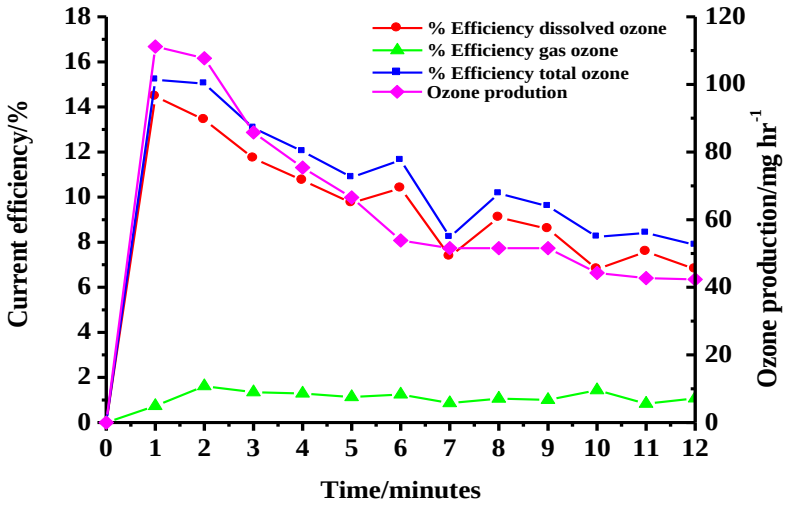

(b)

Figure 6.11 Plots of (a) current, dissolved and gas phase absorbance. (b) Dissolved, gas and total ozone current efficiencies measured during the electrolysis of 0.5 M H_2SO_4 by anode MAGED13 at 2.7 V in the system in fig. 6.10. The anolyte flow rate was 200 cm^3 min^{-1} and the N_2 flow rate 40 cm^3 min^{-1} (to dilute the gas phase, see Chapter 3). The counter electrode was a Ti frame-mounted 7.0 cm x 5.0 cm Pt/Ti mesh, frame aperture 6.0 cm x 4.0 cm.

Figure 6.12 show plots of current and total ozone current efficiency *vs.* the number of experiments, such as that depicted in figs. 6.11 (a) and (b), measured at the end of the experiments.

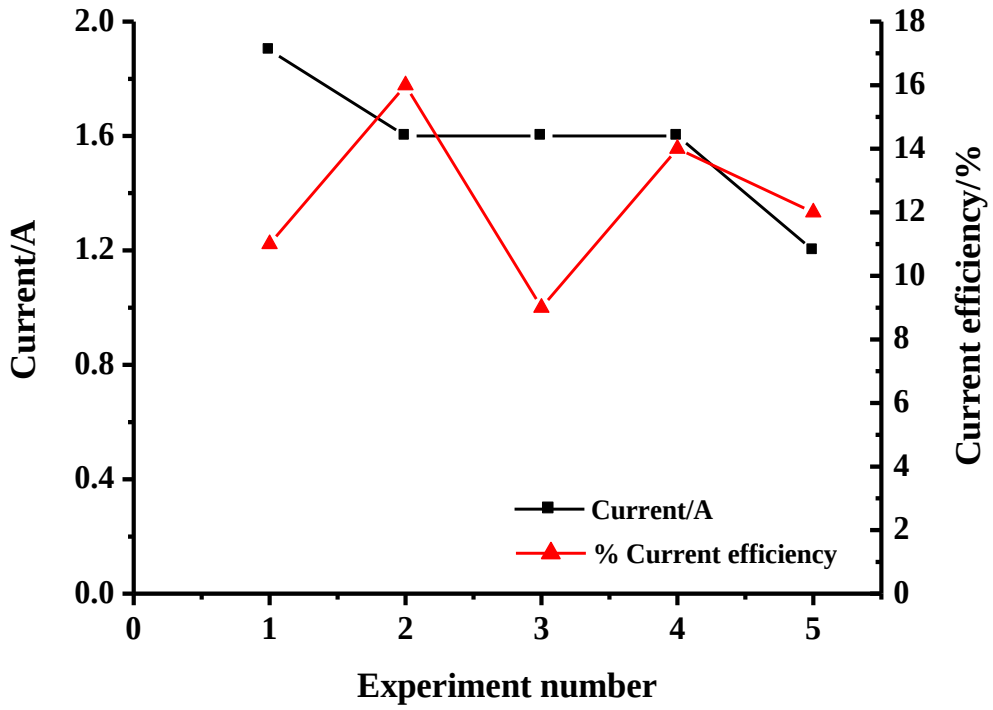

Figure 6.12 The current (■) and total (gas + solution) current efficiency (▲) measured during five successive electrolyses analogous to the experiment depicted in figs 6.11 (a) and (b), except employing anode MAGED13. The current and current efficiency was measured at the end of each experiment.

The data are promising, but incomplete. The currents are very high (at 2.7 V cell voltage) and efficiencies around *ca.* 10% at such currents yield large amounts of ozone. However, whilst the data in fig. 6.12 are encouraging in terms of the durability of the anodes, significantly more characterisation of the anodes is required.

6.3 Preliminary studies on water/air cells

6.3.1 Previous work on polymer electrolyte membrane zero gap cells

The use of Nafion as the polymer electrolyte membrane in a zero-gap cell for electrolysing water without added electrolyte was first reported by Stucki and co-workers in 1985 [6]. In essence, ionic contact between the electrodes of such cells was maintained by pressing the mesh or otherwise porous electrodes tightly either side of the Nafion membrane. Studies using such zero gap cells to generate ozone have been reported by Babak and co-workers [7], Katoh et al. [8], Onda et al. [9], Wang and co-workers[3], Han et al. [10], Arihara and co-workers [11][12], Kraft et al. [13], Franco et al. [14] and Cui et al. [4]. Most reports concern work using the configuration employed in the Membrel Ozoniser reported by Stucki [6][15] and Babak [7] where a substrate (typically porous Ti plate or mesh) coated with β-PbO_2 is employed as the ozone anode and Pt directly deposited on the Nafion membrane or on carbon cloth or Ti mesh as cathode [9][10]. Boron doped diamond (BDD) electrodes have also been employed in such zero gap cells to produce ozone directly into water [11][12][13] as have Ni/Sb-SnO_2 anodes by the Hong Kong group [3][4].

The 'Membrel' type zero gap cells, using β-PbO_2 and Pt electrodes pressed firmly either side of the Nafion, generally give current efficiencies of 12-18% at room temperature, at cell voltages of *ca.* 3.0 V [6][9][15]. The same cell configuration employing BDD anodes give 24-47% current efficiency, but require significantly higher cell voltages, up to 25 V [11][12][13]; all these systems employ high water flow rates through the anode compartments of up to 24 $dm^3\ min^{-1}$.

In the zero gap cells reported in references [3-15], oxygen and ozone are produced *via* the electrolysis of water at the anode:

$$2H_2O \rightarrow O_2 + 4H^+ + 4e^- \qquad (6.1)$$

$$3H_2O \rightarrow O_3 + 6H^+ + 6e^- \qquad (6.2)$$

and the protons pass through the Nafion to the cathode where they are reduced to hydrogen gas:

$$2H^+ + 2e^- \rightarrow H_2 \qquad (6.3)$$

Such gas evolution may not be desirable in, for example, domestic applications. Thus, Katoh and co-workers [8] were the first to report the use of an air, gas diffusion electrode (GDE) as the cathode, as routinely employed in low temperature fuel cells [16], where the cathode reaction is the reduction of oxygen to water:

$$O_2 + 4H^+ + 4e^- \rightarrow 2H_2O \qquad (6.4)$$

This has the added advantage of decreasing the cell voltage, and hence reducing the power consumption, as E^o for (6.4) is +1.23 V compared to 0 V for reaction (6.3). Again, the anode and cathode were pressed firmly either side of the Nafion membrane to ensure ionic contact between the electrodes and membrane. The authors achieved a current efficiency of *ca.* 19% at a cell voltage of 2.2 V, although no details of the water flow rate were provided.

A common factor of all the above studies is high current densities, up to 2.0 A cm^{-2}.

Professor Chan reported studies using a 6.0 cm x 4.0 cm Ni/Sb-SnO_2/Ti anode in an air breathing cell (*i.e.* passive air rather than flowing oxygen fed to the cathode as in the work by Katoh et al. [8]) and using static water in the anode compartment [3]. He obtained a maximum current efficiency of 15.2% at a cell voltage of 2.0 V. In a later paper [4], Chan and co-workers reported work using 104 cm^2 Ni/Sb-SnO_2/Ti anodes and air breathing, porous carbon/Pt cathode which were hot-pressed either side of the Nafion membrane to form a Membrane Electrode Assembly, prior to assembling the electrolysis cell. 5% Nafion solution in alcohol was employed to facilitate good ionic contact between the electrocatalysts and the Nafion membrane. In addition, Prof. Chan's group were the first to report studies on a cell stack (of 4 individual cells), each comprising 104

cm^2 anodes. With a single cell, at a cell voltage of 3.0 V and water flow of 4.0 $dm^3 min^{-1}$, Chan obtained an ozone current efficiency of 17%. Using the 4 cell stack at 3.0 V and 5.4 dm^3 min^{-1}, obtained 21%.

6.3.2 The fabrication of the first Membrane Electrode Assembly

The methods employed by Dr. Henriette Christensen to make the first MEA were adapted from those developed in Newcastle to make MEAs for the Direct Methanol Fuel Cell.

The air breathing cathode was prepared as follows: 1.2 g of XC-72R porous carbon was added to 80-100 cm^3 of isopropanol in a 250 cm^3 beaker and stirred for 2 minutes, after which it was sonicated for 15 minutes. 20 g of 60 wt% PTFE emulsion (equivalent to 1.2 g of dry PTFE) was added with stirring for 2 minutes, followed by sonication for 30 minutes. One side of a 5.2 cm x 7.2 cm piece of Toray 90 (20 wt% PTFE) carbon paper was coated with the carbon/PTFE slurry and left to dry in air for 1 hour. The loading of carbon in this the Gas Diffusion Layer (GDL) was calculated by weighing the carbon paper before and after addition. More slurry was added (and left to dry) as necessary to attain a loading of 4.0 mg cm^{-2}.

The coated carbon paper was placed in a pre-heated furnace at 360 ºC under N_2 for 15 minutes after which the furnace was turned off and allowed to cool to room temperature before the carbon paper was removed.

Platinized carbon ink was prepared by adding a few drops of Millipore water to wet 1.5 g of 60 wt% Pt on porous carbon in a 100 cm^3 beaker, after which 60 cm^3 of ethanol was added and the slurry stirred for 15 minutes. 5% Nafion solution was added slowly to give a weight ratio of Nafion: Pt/C of 1:4 (*ca.* 45-50 cm^3) with stirring. When the addition was complete, the mixture was stirred for a further 2 minutes and then sonicated for 30 minutes.

The GDL was painted with catalyst ink and allowed to dry in air, after which it was weighted. More catalyst ink was added until the target loading of *ca.* 3-5 mg cm^{-2} Pt was attained. The actual Pt loading was 3.7 mg cm^{-2}.

The Gas Diffusion Electrode (GDE, *i.e.* the cathode) and ozone anode were pressed onto a Nafion membrane to form an MEA as follows. A 8.0 cm x 5.0 cm piece of Nafion 117 membrane was soaked in 5% H_2O_2 solution for 60 minutes, washed thoroughly in Millipore water and then boiled in 0.5 M H_2SO_4 for 30 minutes, after which it was washed again. The Nafion was blotted dry using Whatman filter paper and then placed between anode HCED5A (mounted in a Ti frame) and the GDE; the catalyst coated Ti mesh contacted one face of the Nafion membrane and the platinized carbon of the GDE the other face. The anode/Nafion/cathode sandwich was then placed between the plates of the Chauffante Elcometer press: to prevent adhesion to the plates of the press they were covered with silicone-coated grease proof paper. The MEA was prepared by pressing at 1000 kg and 130 ºC for 3 minutes, after which it was removed from the press and allowed to cool.

6.3.3 Testing of the first MEA and subsequent experiments

The apparatus employed to test the HCED5A MEA in single pass system is shown in figs. 6.13 (a) and (b). The polycarbonate cell was laid flat, cathode uppermost, on the Masterflex pump with the UV-Vis cell placed (vertically) immediately after the outlet from the anode compartment. Figure 6.13 (b) shows the cell placed on its side to reveal the ventilation holes to the air breathing cathode.

As may be seen from the fig. 6.13 (c), the onset potential for anodic current was *ca.* 1.0 V, *ca.* 1.0 V lower than observed in anodic electrolyte with hydrogen evolution as the counter electrode reaction. This is somewhat more anodic than would be expected on the basis of an Eº of 1.23 V *vs.* NHE for oxygen reduction. Taking *ca.* 1.5 V as equivalent to the usual cell voltage of 2.7 V employed in acid/acid experiments, it can be seen from fig 6.14 that the current obtained at this cell voltage is only *ca.* 0.2 A; significantly less than observed using the anode HCED15A in the acid/acid experiments (see section

6.2.2), and very much smaller indeed than the ~2.0 A expected with an effective Pt/Ti counter electrode. This suggests a high resistance somewhere in the cell, possibly due to in sufficient compression.

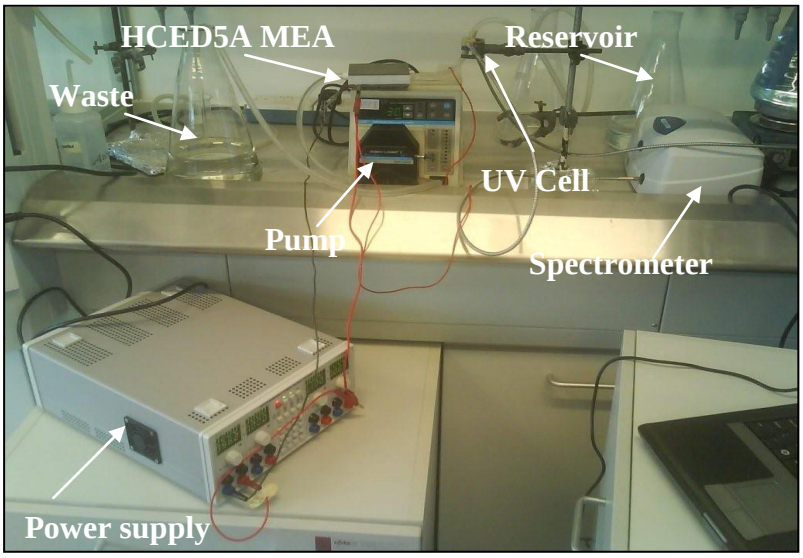

(a)

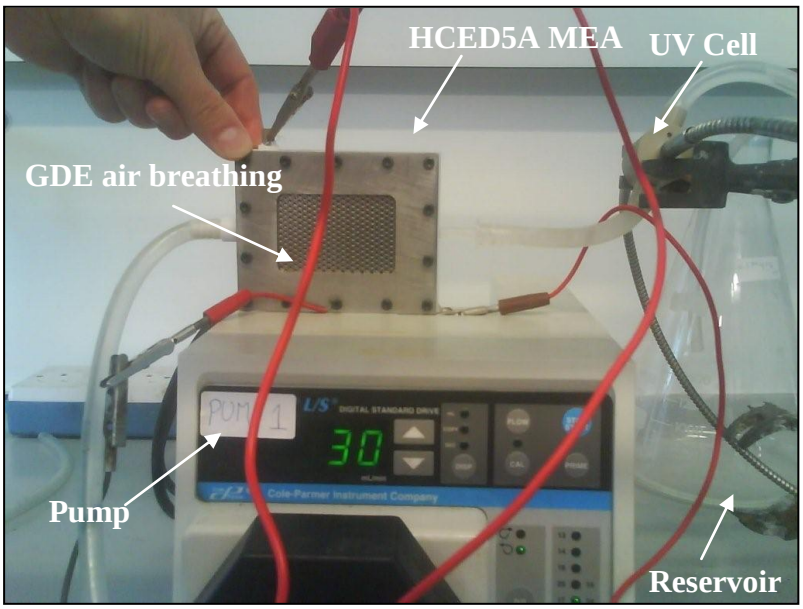

(b)

Figure 6.13 Photographs of the apparatus employed to test the first Membrane Electrode Assembly (MEA, employing anode HCED5A); (a) showing all the equipment employed and (b) with the cell placed on its side to show the ventilation holes to the air breathing cathode.

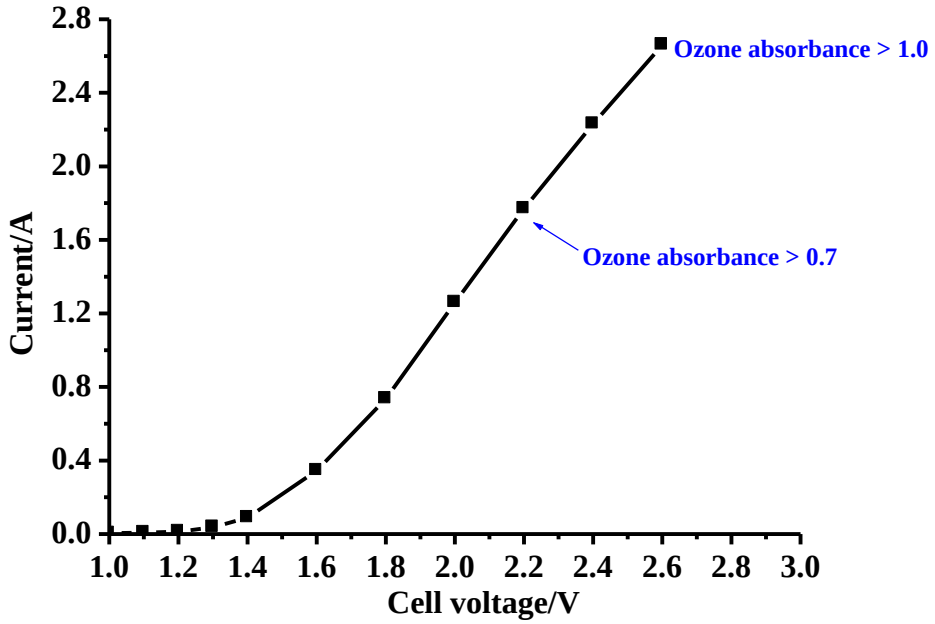

Figure 6.13 (c) Current/voltage plot obtained using the water/air cell and system shown in figs. 6.13 (a) and (b). Millipore water was pumped through the anode compartment at 30 cm^3 min^{-1}.

Millipore water was pumped through the anode compartment at 30 cm^3 min^{-1}, and a current/voltage plot obtained by changing the cell voltage on the Hameg power supply and noting the current, see fig 6.14.

Figure 6.14 shows plots of (a) the current and absorbance, and (b) the current efficiency observed during the single pass experiment using the HCED5A MEA. As may be seen from the figures, the current efficiency at 1.6 V looked to be >10%; unfortunately, the cell voltage was increased to 2.0 V and then 2.2 V, at both of which the efficiency was *ca.* 5%, before steady state was reached. A second experiment showed very little current, suggesting damage to the MEA had occurred, possibly delamination. To test this, a single pass experiment was carried out using 0.05 M H_2SO_4 as the anolyte. If the anode alone had delaminated, the use of a conducting electrolyte should restore activity. The results are shown in figs. 6.15 (a) and (b).

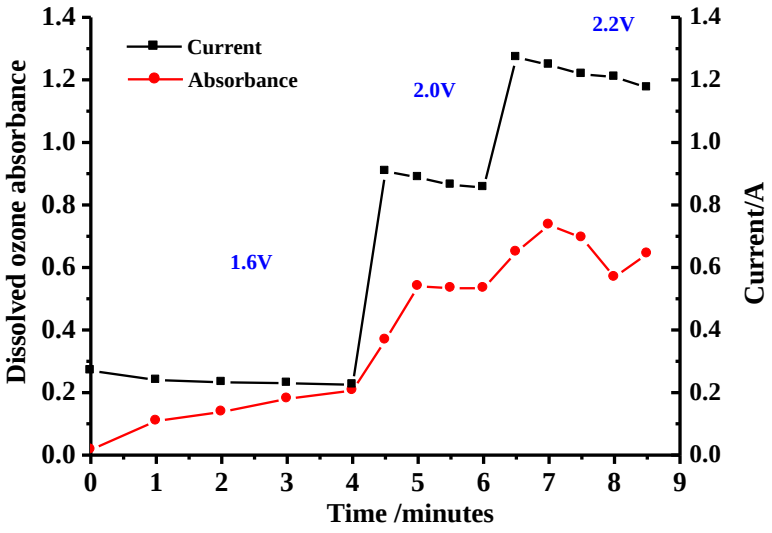

(a)

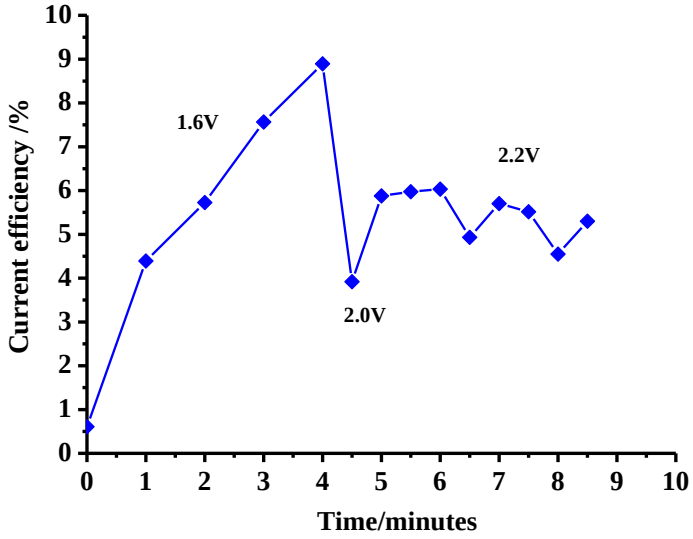

(b)

Figure 6.14 Plots of (a) current (■) and dissolved ozone absorbance (●) and (b) the corresponding current efficiency (◆) derived during the experiment employing the HCED5A MEA. Millipore water was pumped through the anode compartment at 30 cm^3 min^{-1} and the cell voltages employed are as shown in the figures.

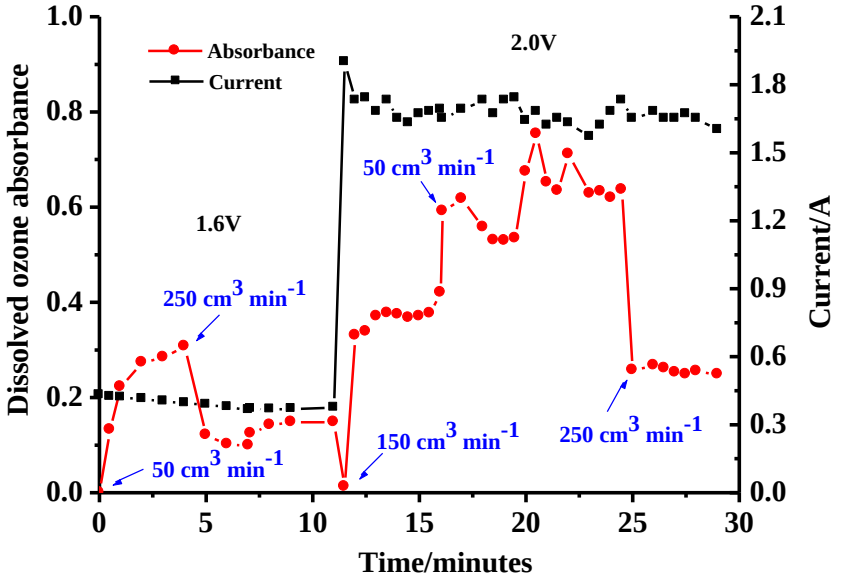

(a)

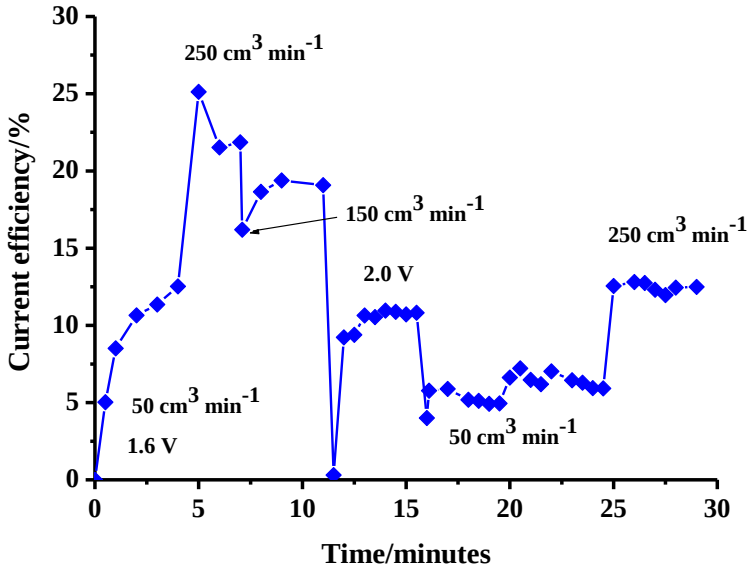

(b)

Figure 6.15 Plots of (a) current (■) and dissolved ozone absorbance (●) and (b) the corresponding current efficiency (◆) measured during a second experiment employing the HCED5A MEA. 0.05 M H_2SO_4 was pumped through the anode compartment and the cell voltages and anolyte flow rates employed are as shown in the figures.

As may be seen, the current measured using the acid electrolyte (note: 10x more dilute than normally employed in acid/acid experiments) was *ca.* 0.4 A at 1.6 V. The current efficiency increased with anolyte flow rate (as was discussed in section 3.2.3) presumably due to the entraining of more ozone into solution. At a flow rate of 250 cm^3 min^{-1}, a perfectly acceptable efficiency of *ca.* 22% was calculated. This fell to *ca.* 13% at 2.0 V.

The data in figs. 6.14 and 6.15 support the postulate that delamination of the anode has taken place. There may have been some delamination of the cathode, but this would have required 0.5 M H_2SO_4 to have been employed in the experiment in fig. 6.15 to allow direct comparison with the current typically observed in acid/acid runs, and this experiment was not carried out. However, when the cell was disassembled, delamination of both the anode and cathode was observed, as shown in figs. 6.16 (a) and (b). Delamination is evident from the pale areas indicating detachment had taken place.

Delamination remained a problem, and this appears to be inherent in the prototype water/air cell design. A number of MEAs were made using AJ, MAG and HC series anodes. In each case, initial experiments showed currents up to 1.5 A at 1.6 V and efficiencies up to *ca.* 15%. However, with each subsequent experiment, the current decreased, as did efficiency. Figures 6.17 to 6.19 show typical data; the figures show results from, three sequential runs using an MEA fabricated using anode HCED22 series (ED1/CC4) and air breathing cathode supplied by Johnson Matthey. The anode and membrane were sent to Dr. Martin Hogarth at Johnson Matthey, and they were laminated with the JM cathode at the company. This was carried out as part of Clarizon's strategy to identify potential sub-contractors to manufacture the components of the Clarizon cells.

Figures 6.17 to 6.19 (a) show plots of current and dissolved ozone absorbance with time and (b) the corresponding plots of current efficiency. The first two experiments (figs. 6.17 and 6.18) were carried out using Millipore water and the third (fig. 6.19) using tap water passed through a domestic 'Brita' filter unit (see fig. 6.20).

(a)

(b)

Figure 6.16 Photographs of (a) the anode and (b) the cathode side of the HCED5A MEA after the completion of the tests on its activity.

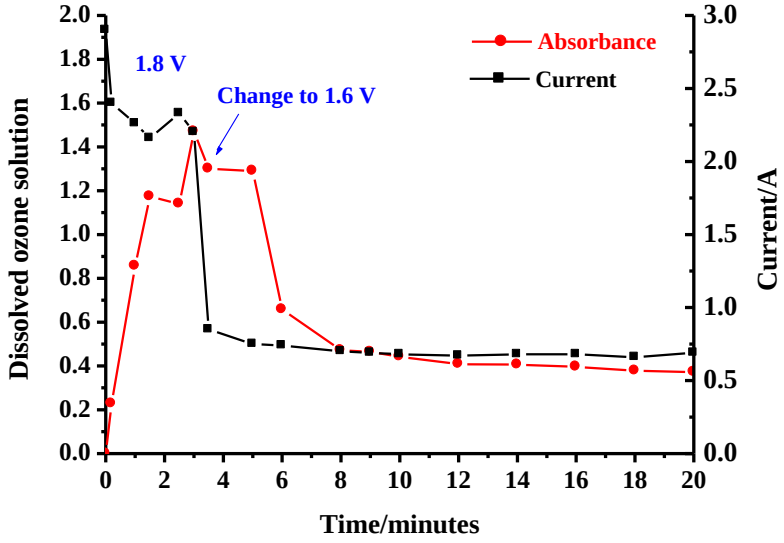

(a)

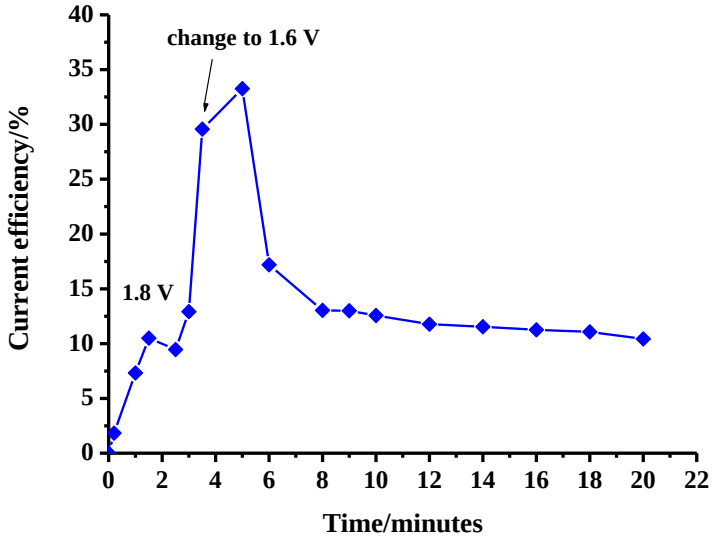

(b)

Figure 6.17 (a) Plots of current (■) and dissolved ozone absorbance (●) and (b) the current efficiencies (♦) on the successive experiment 1 carried out using a polycarbonate cell employing an MEA comprising anode HCED22 (7.0 cm x 5.0 cm in Ti frame), Nafion and a Johnson Matthey air breathing cathode. The experiments were carried out in single pass experiment at 60 cm^3 min^{-1} using Millipore water. Cell voltages were as shown.

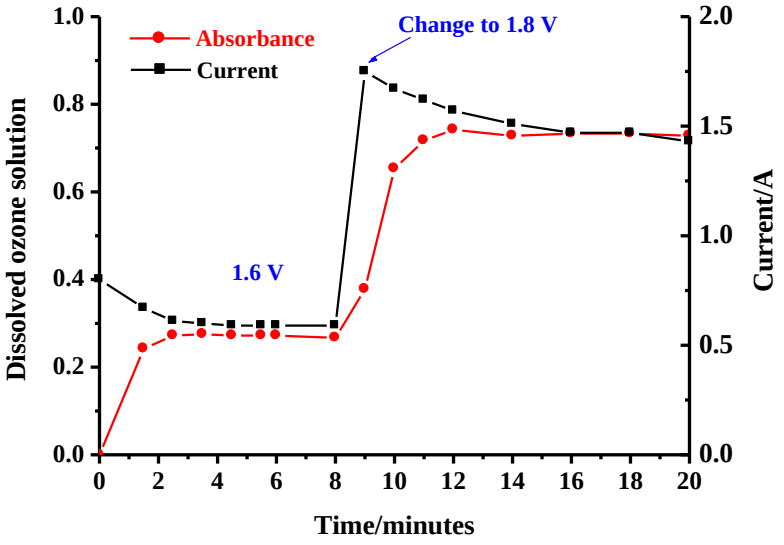

(a)

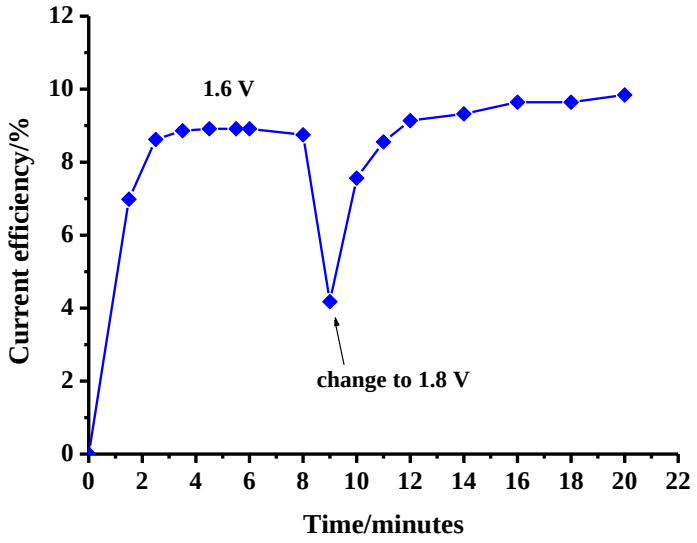

(b)

Figure 6.18 (a) Plots of current (■) and dissolved ozone absorbance (●) and (b) the current efficiencies (♦) on the successive experiment 2 carried out using a polycarbonate cell employing an MEA comprising anode HCED22 (7.0 cm x 5.0 cm in Ti frame), Nafion and a Johnson Matthey air breathing cathode. The experiments were carried out in single pass experiment at 60 cm^3 min^{-1} using Millipore water. Cell voltages were as shown.

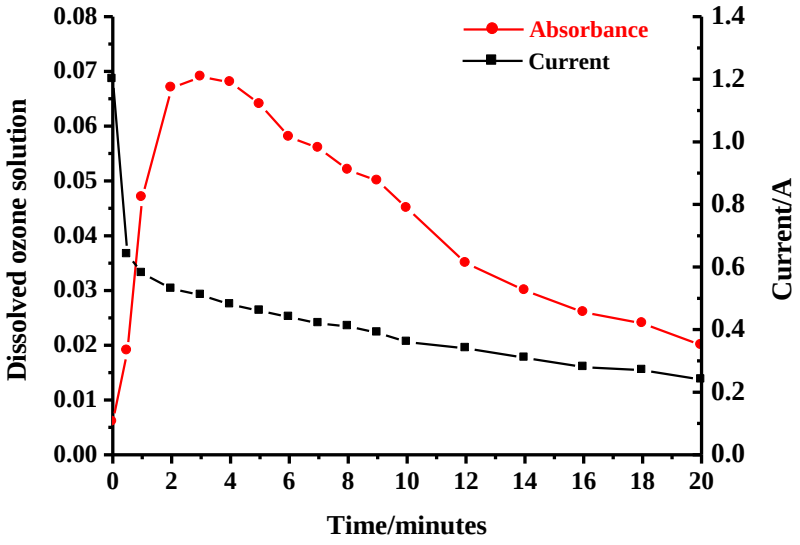

(a)

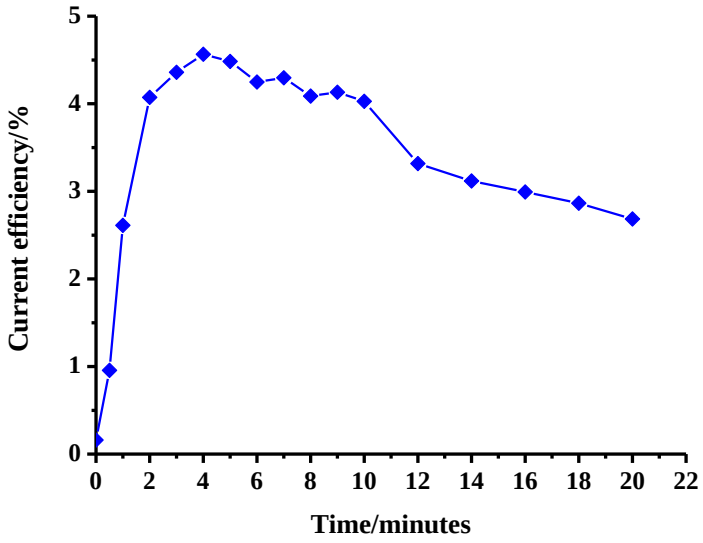

(b)

Figure 6.19 (a) Plots of current (■) and dissolved ozone absorbance (●) and (b) the current efficiencies (♦) on the successive experiment 3 carried out using a polycarbonate cell employing an MEA comprising anode HCED22 (7.0 cm x 5.0 cm in Ti frame), Nafion and a Johnson Matthey air breathing cathode. The experiments were carried out in single pass experiment at 60 cm^3 min^{-1} using tap water passed through a Brita filter. Cell voltages were as shown.

Figure 6.20 Photograph of the domestic Brita filter unit [18][19].

A Brita filter was employed to provide water typical of the quality that would be treated by a domestic ozoniser. Such water would require treatment to remove Ca^{2+}, Mg^{2+} and other polyvalent cations (which cause 'hard water' responsible for deposits that block plumbing) as these will reduce the conductivity of the Nafion membrane [16][17]. The application of such a pretreatment system would not add significant complexity or cost to the ozone unit.

As shown in figs. 6.17 to 6.19, for example from the regions of the plots where the cell voltage was 1.6 V, there was a marked decrease in current over the experiments, from *ca.* 0.75 A in experiment 1 to 0.3 A in experiment 3, and a concomitant decrease in current efficiency from *ca.* 12% to *ca.* 3%. The decline appears to be more marked in experiment 3 using Brita filtered water. This may be due to incomplete removal of polyvalent ions or to delamination. Unfortunately, time did not allow this to be investigated further.

It is interesting to note that the majority of the studies on electrochemical ozone generation using zero gap cells employ very high water flow rates *e.g.* up to: 1 dm^3 min^{-1} [5], 33 dm^3 min^{-1} [8], 2 dm^3 min^{-1} [11], 667 cm^3 min^{-1} [12] and 4 dm^3 min^{-1} [4]. Given that the solubility of ozone decreases as pH increases (see section 3.2.6), and β-PbO_2 and BBD anodes demand high current densities (>1.0 A cm^{-2}) [5][6][7][8][9][10][11][14], such high flow rates may be necessary simply to dissolve/entrain the ozone. However, Kraft [12] suggests that high flow rates are necessary to minimize local heating effects and the concomitant thermal decay of ozone. Cui et al. [4], who employ Ni/Sb-SnO_2 anodes and current densities <60 mA cm^{-2} [4], state that high flow rates ensure good mass transport and the removal of products, particularly bubbles of O_2 and O_3 which would otherwise block active sites.

6.4 Conclusion

The data reported in this chapter are preliminary and it is clear that there is a significant design flaw in the prototype water/air cell, in that there appears to be insufficient compression of the MEA. This leads to high internal resistance, and hence low current densities, and delamination. However, current efficiencies up to 22% were determined, which is very encouraging and compares favorably to the 21% reported by Prof. Chan using the same type of anode and cell [4]. This performance is generally superior to that observed using β-PbO_2 in water/water and water/air cells, of 18%, although the current densities employed in the latter systems are significantly higher [5][6][7][8][9][14]. It is clear that higher current densities are possible with the Clarizon/Newcastle cell (see fig. 6.17 (a)), and hence higher ozone production rates should be possible once the design flaws are remedied.

The current efficiency derived by Fujishima et al. [11] using a BDD anode, 47%, cannot be matched (as yet) by the prototype cell developed in Newcastle. However, BDD anodes in general require much higher cell voltages than Ni/Sb-SnO_2 electrodes and this leads to significantly higher energy consumption; *e.g.* 140 kWh kg^{-1} compared to 24 kWh kg^{-1} for the data in fig. 6.15 (b). Furthermore, with the exception of the reports by

Fujishima and co-workers, such high efficiencies have not been obtained using BDD anodes.

6.5 References

1. Cheng, S. A., and K. Y. Chan, "Electrolytic Generation of Ozone on an Antimony-Doped Tin Dioxide Coated Electrode," *Electrochemical and Solid State Letter* 7(3): D4-D6 (2004).
2. Wang, Y. H., S. Cheng, K. Y. Chan and X. Y. Li, "Electrolytic Generation of Ozone on Antimony and Nickel-Doped Tin Oxide Electrodes," *Journal of the Electrochemical Society* 152(11): D197-D200 (2005).
3. Wang, Y. H., S. Cheng and K. Y. Chan, "Synthesis of Ozone from Air *via* a Polymer-Electrolyte-Membrane Cell with a Doped Tin Oxide Anode," *Green Chemistry* 8: 568-572 (2006).
4. Cui, Y. H, Y. H. Wang, B. Wang, H. H. Zhou, K. Y. Chan and X. Y. Li, "Electrochemical Generation of Ozone in a Membrane Electrode Assembly Cell with Convective Flow," *Journal of the Electrochemical Society* 156(4): E75-E80 (2009).
5. Retrieved 5th April 2011, from World Wide Web http://www.magneto.nl/home.en_US.html
6. Stucki, S., G. Theis, R. Kötz, H. Devantay and H. J. Christen, "In Situ Production of Ozone in Water Using a Membrel Electrolyzer," *Journal of the Electrochemical Society* 132(2): 367-371 (1985).
7. Babak, A. A., R. Amadelli, A. De Battisti and V. N. Fateev, "Influence of Anions on Oxygen/Ozone Evolution on PbO_2/*spe* and PbO_2/Ti Electrodes in Neutral pH Media," *Electrochimica Acta* 39(11-12): 1597-1602 (1994).
8. Katoh, M., Y. Nishiki and S. Nakamatsu, "Polymer Electrolyte-Type Electrochemical Ozone Generator with an Oxygen Cathode," *Journal of Applied Electrochemistry* 24(6): 489-494 (1994).
9. Onda, K., T. Ohba, H. Kusunoki, S. Takezawa, D. Sunakawa and T. Araki, "Improving Characteristics of Ozone Water Production With Multilayer

Electrodes and Operating Conditions in a Polymer Electrolyte Water Electrolysis Cell," *Journal of the Electrochemical Society* 152(10): D177-D183 (2005).

10. Han, S. D., J. D. Kim, K. S. Myung, R. Kumar and K. C. Singh, "Electro-Chemical Production of Ozone Using Water Electrolysis Cell of Solid Polymer Electrolyte (SPE)," *Indian Journal of Chemical Technology* 13: 156-161 (2006).
11. Arihara, K., C. Terashima and A. Fujishima, "Application of Freestanding Perforated Diamond Electrodes for Efficient Ozone-Water Production," *Electrochemical and Solid-State Letters* 9(8): D17-D20 (2006).
12. Arihara, K., C. Terashima and A. Fujishima, "Electrochemical Production of High-Concentration Ozone-Water Using Freestanding Perforated Diamond Electrodes," *Journal of the Electrochemical Society* 154(4): E71-E75 (2007).
13. Kraft, A., M. Stadelmann, M. Wünsche and M. Blaschke, "Electrochemical Ozone Production Using Diamond Anodes and a Solid Polymer Electrolyte," *Electrochemistry Communications* 8: 883-886 (2006).
14. Franco, D. V. W. F. Jardim, J. F. C. Boodts and L. M. Da Silva, "Electrochemical Ozone Production as an Environmentally Friendly Technology for Water Treatment," *Clean* 36(1): 34-44 (2008).
15. Stucki, S., H. Baumann, H. J. Christen and R. Kötz, "Performance of a Pressurized Electrochemical Ozone Generator," *Journal of Applied Electrochemistry* 17: 773-778 (1987).
16. Larminie, J., and A. Dicks, *Fuel cell systems explained*. 2nd Editions, West Sussex: John Wiley and Sons Inc. (2003).
17. Retrieved 5th April 2011, from World Wide Web http://www2.dupont.com/FuelCells/en_US/assets/downloads/dfc101.pdf.
18. Peron, J., A. Mani, X. Zhao, D. Edwards, M. Adachi, T. Soboleva, Z. Shi, Z. Xie, T. Navessin and S. Holdcroft, "Properties of Nafion NR-211 membranes for PEMFCs," *Journal of Membrane Science* 356: 44-51 (2010).
19. Retrieved 5th April 2011, from World Wide Web http://www.brita.net/uk/index.html.
20. Dean, K., K. Gaffney, J. Bergman, B. Post and A. Anrtsen, "Sustainability Assessment of Brita Water Filters", December 6 (2010).

Chapter 7

Conclusions and future work

7. Conclusions and future work

7.1 Conclusions

The objective of this chapter was to explore the conclusions shown previously in each chapter into one coherent argument and also to suggest the further work that would be worth conducting on the basis of the results presented here.

A value of 3000 dm^3 mol^{-1} cm^{-1} was chosen as the most appropriate for dissolved ozone and gas phase ozone at 255 nm and 258 nm, respectively, as recommended by the International Ozone Association.

Cells and systems were commissioned successfully to allow the measurement of ozone evolved in both single pass and recycle systems using Ni/Sb-SnO_2 anodes. In the latter, it was found that ozone at the inlet of the electrochemical cell inhibits the evolution of ozone. Thus, ozone current efficiencies of 30-40% could be routinely achieved in aqueous sulfuric acid in single pass system at a cell voltage of 2.7 V, with efficiencies up to 50% also determined. The optimum catalyst composition was found to be that resulting from a 500:8:3 mole ratio of Sn:Sb:Ni in the catalyst coating solution. In batch recycle system, current efficiencies were typically <10%; this was attributed to the removal of key intermediates (O_{2ads}, $O^{\cdot}_{ads}$) from the anode surface as the components of the electrochemical system (*e.g.* the membrane, cell material etc.) did not have an effect with respect to the possible decay of ozone. Celgard 2400 cell separator was found to be a promising alternative to Nafion when operating with aqueous acid anolyte and catholyte.

When operating in single pass system, it was generally found that increasing the anolyte flow rate resulted in a larger fraction of the evolved ozone dissolving in the anolyte, as opposed to the gas phase.

After detailed investigation of the anode synthesis, it was found that the electrodeposition step, to form the protective Electro Deposited Inter Layer (EDIL)

around the Ti mesh substrate was a significant source of irreproducibility. However, the remaining steps in the synthesis were refined successfully resulting in a reproducible specify here (in terms of current, current efficiency and catalyst loading).

The Ni/Sb-SnO_2 anodes showed marked variations in durability, even within a particular series; some anodes showed a stable performance over many experiments, others were inactivated in hours. The deactivation appeared to be due to one or more of three principle mechanisms: physical loss of catalyst (spalling); dissolution of Ni and switching of ozone sites to oxygen evolution. In some cases, the anodes could be reactivated by heating, presumably due to Ni diffusing to the surface from the bulk. In-depth study of the active sites responsible for ozone generation was hampered by the very low Ni content of the catalyst; this meant that the Ni content could not be investigated by EDX or even XPS. Towards the end of the project it was found that ToF-SIMS was sensitive enough to detect Ni, but time did not allow the approach to be investigated in any detail. The use of Au as a means of improving durability was investigated, based on reports in the literature that showed that adding Pt to Sb-SnO_2 anodes improved durability by disrupting the surface and hence preventing passivation. However, no beneficial effect was derived with additions of Au.

The synthesis of the Ni/Sb-SnO_2 anodes was scaled up successfully from 6.25 cm^2 to 35.0 cm^2 and the latter anodes were employed in preliminary experiments using membrane electrode assemblies, or MEAs. The MEAs consisted of a Ni/Sb-SnO_2 anode and Pt/porous carbon, air breathing cathode hot-pressed either side of a Nafion membrane. These allow ozone to be injected directly into water (with no added electrolyte) with oxygen reduction, rather than hydrogen evolution, taking place at the cathode. Promising current efficiencies of up to 22% were derived, but the cell required significant redesign to overcome problems associated with poor compression, and hence a high internal resistance.

7.2 Future work

In terms of future work, the nature of the active site requires urgent investigation using ToF-SIMS, and a structure/composition-activity correlation established. A detailed, mechanistic study of the effect of ozone on ozone generation should be carried out using a rotating disk, or rotating ring disc, electrode, looking at Tafel slopes etc. as a function of the dissolved ozone concentration. Similarly, a detailed study of the failure/deactivation of the Ni/Sb-SnO_2 anodes should be carried out and hence the reason why some anodes are durable established and exploited. Finally, MEA fabrication and the water/air cell design should both be optimized.

Appendix

Appendix

Calculation of the Inner Galvani potential difference, $\delta\phi_a$, across the anode/electrolyte interface.

From Section 3.3, the Inner Galvani potential difference [1] at the anode $\delta\phi_a$ is given by:

$$\delta\phi_a = |V_{cell}| - jR_{elec}' - jR_{Nafion}' - |\eta_c| \quad (1)$$

Where the resistance R' (Ω cm^2) of a medium of thickness x and conductivity κ (Ω^{-1}cm^{-1}) is given by [2]:

$$R' = x/\kappa \quad (2)$$

In order to determine the overpotential at the cathode, η_c, it is necessary to calculate the current density at the cathode, j_{Cath}, for a set of typical experimental parameters; this is obtained from a consideration of equation (5) and the limiting current density, $j_{L,Cath}$:

$$j = \frac{j_0\left(e^{(\beta_A \eta f)} - e^{(-\beta_C \eta f)}\right)}{1 + \left[\left(\frac{j_0 e^{(\beta_A \eta f)}}{j_{L,An}}\right) - \left(\frac{j_0 e^{(-\beta_C \eta f)}}{j_{L,Cath}}\right)\right]} \quad (3)$$

Equation (3) is derived in order to remove the indeterminate concentration terms in the Butler-Volmer equation (see equation (8) below), and this is achieved as follows (for simplicity, micro-convection effects due to bubble evolution are neglected).

Taking the limiting current density first, a typical electrolysis reaction involves the transfer of charge between an electrode and a species in solution. Consider a current density *j* passing through the glass cell where O is being reduced to R at the cathode in a 1-electron process:

$$\text{Reactant (O)} + e^- \underset{k_r}{\overset{k_f}{\leftrightarrow}} \text{Product (R)} \qquad (4)$$

At a sufficiently high cathodic potential to neglect the reverse reaction, a diffusion gradient will be set up between the bulk and surface concentration of O, $C_{Ox}^{\ 0}$ and $C_{Ox}^{\ S}$, respectively, see fig. A1. The diffusion layer thickness δ_N is the distance from the electrode beyond which convection maintains the concentration of O at the bulk value.

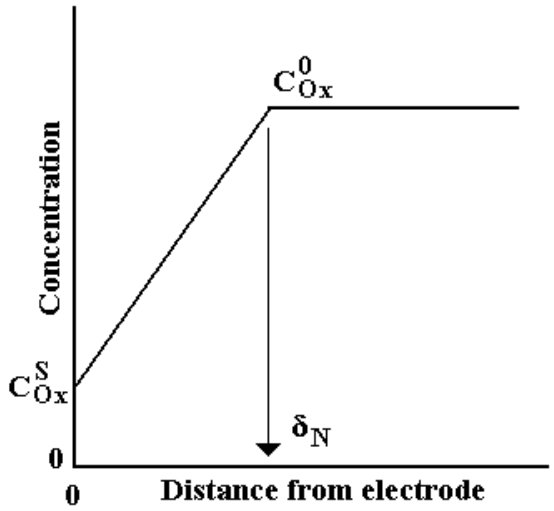

Figure A1 The diffusion layer.

The cathodic current density for the reduction of O to R will be given by

$$j_{Cath} = \frac{-F\ D_{Ox}\left(C_{ox}^{o} - C_{ox}^{s}\right)}{\delta_N} \qquad (5)$$

Where D_{Ox} is the diffusion coefficient of Ox. The highest, or limiting, cathodic current density obtainable, $j_{L,Cath}$, will be when $C_{Ox}^{\ S} = 0$, hence:

$$j_{L,Cath} = \frac{-F\ D_{Ox} C_{Ox}^{O}}{\delta_N} \tag{6}$$

At a Pt/Ti cathode:

$$H^+ + e- \rightarrow \tfrac{1}{2}H_2 \tag{7}$$

δ_N is rather indeterminate, and a number of values are quoted in the literature, see for example [3]. An intermediate value of δ_N was chosen of 5 x 10^{-3} cm; using $C_{Ox}{}^{O}$ = 0.5 x 10^{-3} mol cm^{-3}, F = 96485 C mol^{-1} and the diffusion coefficient of the proton, $D_{Ox} = D_{H+}$ = 7.80 x 10^{-5} cm^2 s^{-1} [4] gives $j_{L,cath}$ = -0.75 A cm^{-2}.

The equation relating current density (j) to the forward and reverse reactions of a redox couple under mass transport control is the Butler Volmer equation [5]:

$$j = \left[k_f C_{Red}^{S} e^{(\beta_A \eta f)}\right] - \left[k_r C_{Ox}^{S} e^{(-\beta_c \eta f)}\right] \tag{8}$$

Where k_f and k_r are the forward and reverse rate constants, $C_{Red}{}^{S}$, $C_{Ox}{}^{S}$ are the surface concentration of reactant and product, respectively. β_A and β_B are the anodic and cathodic transfer coefficients, which can be approximated to 0.5. η is overpotential (η = E - E_{eq} where E is the electrode potential and E_{eq} the potential defined by the Nernst equation at zero net current) and $f = F/RT$ = 38.9 V^{-1}.

At equilibrium, j = 0, and hence:

$$j = 0 = \left[k_f C_{Red}^{S} e^{(\beta_A \eta f)}\right] - \left[k_r C_{Ox}^{S} e^{(-\beta_c \eta f)}\right] \tag{9}$$

Also at equilibrium, $C_{Red}{}^{S} = C_{Red}{}^{O}$ and $C_{Ox}{}^{S} = C_{Ox}{}^{O}$, hence;

$$k_f C^O_{\mathrm{Red}} = j_O = k_r C^O_{Ox} \tag{10}$$

Taking the ratio of (5) and (6):

$$\frac{j_{Cath}}{j_{L,Cath}} = \frac{\left[\frac{FD_{Ox}\left(C^O_{Ox} - C^S_{Ox}\right)}{\delta_N}\right]}{\left[\frac{FD_{Ox}C^O_{Ox}}{\delta_N}\right]} \tag{11}$$

and re-arranging:

$$\frac{j}{j_{L,Cath}} = \frac{\left(C^O_{Ox} - C^S_{Ox}\right)}{C^O_{Ox}} \tag{12}$$

In terms of the net current density, the electrochemical process at the surface will be the algebraic sum of the anodic and cathodic current densities j_{Cath} and j_{An}.

From (12):

$$C^S_{Ox} = \frac{C^O_{Ox}\left(j_{L,Cath} - j\right)}{j_{L,cath}} \tag{13}$$

Similarly:

$$C^S_{\mathrm{Red}} = \frac{C^O_{\mathrm{Red}}\left(j_{L,An} - j\right)}{j_{L,An}} \tag{14}$$

Replace (13) and (14) into (8) and remembering that j_{Cath} is a negative number.

$$j = \left[k_f C^O_{\mathrm{Red}} \frac{\left(j_{L,An} - j\right)}{j_{L,An}} e^{\left(\beta_A \eta f\right)}\right] - \left[k_r C^O_{Ox} \frac{\left(j_{L,Cath} - j\right)}{j_{L,Cath}} e^{\left(-\beta_c \eta f\right)}\right] \tag{15}$$

From equation (12):

$$k_f C_{\mathrm{Red}}^{O} = j_O = k_r C_{Ox}^{O} \tag{10}$$

(15) becomes:

$$j = \left[j_O \frac{\left(j_{L,An} - j\right)}{j_{L,An}} e^{\left(\beta_A \eta f\right)} \right] - \left[j_O \frac{\left(j_{L,Cath} - j\right)}{j_{L,Cath}} e^{\left(-\beta_C \eta f\right)} \right] \tag{16}$$

$$\frac{j}{j_o} = \left[\left(\frac{j_{L,An}}{j_{L,An}} - \frac{j}{j_{L,An}} \right) e^{\left(\beta_A \eta f\right)} \right] - \left[\left(\frac{j_{L,Cath}}{j_{L,Cat}} - \frac{j}{j_{L,Cath}} \right) e^{\left(-\beta_C \eta f\right)} \right] \tag{17}$$

$$\frac{j}{j_o} = e^{\left(\beta_A \eta f\right)} - \left(\frac{j e^{\left(\beta_A \eta f\right)}}{j_{L,An}} \right) - e^{\left(-\beta_C \eta f\right)} + \left(\frac{j e^{\left(-\beta_C \eta f\right)}}{j_{L,Cath}} \right) \tag{18}$$

$$\frac{j}{j_o} + \left(\frac{j e^{\left(\beta_A \eta f\right)}}{j_{L,An}} \right) - \left(\frac{j e^{\left(-\beta_C \eta f\right)}}{j_{L,Cath}} \right) = e^{\left(\beta_A \eta f\right)} - e^{\left(-\beta_C \eta f\right)} \tag{19}$$

$$j \left(\frac{1}{j_o} + \frac{e^{\left(\beta_A \eta f\right)}}{j_{L,An}} - \frac{e^{\left(-\beta_C \eta f\right)}}{j_{L,Cath}} \right) = e^{\left(\beta_A \eta f\right)} - e^{\left(-\beta_C \eta f\right)} \tag{20}$$

$$j \left(\frac{1}{j_o} + \frac{j_o e^{\left(\beta_A \eta f\right)}}{j_o j_{L,An}} - \frac{j_o e^{\left(-\beta_C \eta f\right)}}{j_o j_{L,Cath}} \right) = e^{\left(\beta_A \eta f\right)} - e^{\left(-\beta_C \eta f\right)} \tag{21}$$

$$j \left(1 + \frac{j_o e^{\left(\beta_A \eta f\right)}}{j_{L,An}} - \frac{j_o e^{\left(-\beta_C \eta f\right)}}{j_{L,Cath}} \right) = j_o \left(e^{\left(\beta_A \eta f\right)} - e^{\left(-\beta_C \eta f\right)} \right) \tag{22}$$

$$j = \frac{j_0\left(e^{\left(\beta_A \eta f\right)} - e^{\left(-\beta_C \eta f\right)}\right)}{1 + \left[\left(\frac{j_0 e^{\left(\beta_A \eta f\right)}}{j_{L,An}}\right) - \left(\frac{j_0 e^{\left(-\beta_C \eta f\right)}}{j_{L,Cath}}\right)\right]} \tag{3}$$

Assuming that the cathode is operating at sufficient overpotential such that $|exp(-\beta_C \eta f)|$ >> $|exp(\beta_A \eta f)|$, *i.e.* the reverse reaction ($1/2H_2 \rightarrow H^+ + e$) can be neglected:

$$j = \frac{-j_0\left(e^{\left(-\beta_C \eta f\right)}\right)}{1 + \left(\frac{j_0 e^{\left(-\beta_C \eta f\right)}}{j_{L,Cath}}\right)} \tag{23}$$

Using equation (23) with the exchange current density for H_2 evolution at Pt =7.94 x 10^{-4} A cm^{-2} in 1 M H_2SO_4 [6], approximating β_C as equal to 0.5, f = 38.9 V^{-1} and $j_{L,Cat}$ = -0.75 A cm^{-2}, a plot of current density was obtained as function of hydrogen overpotential, see fig. A2:

Figure 2 was then employed to calculate the hydrogen overpotential at each current density measured in the experiment in fig. 3.25 on page 108 of the thesis. The remaining terms in equation (1) were determined as follows: from equation (2) the IR drop across an electrolyte of thickness x due to a current density j is:

$$IRdrop = \Delta V = \frac{jx}{\kappa} \tag{24}$$

R_{elec}' can be calculated from the conductivity of 0.5 M H_2SO_4 at 20 ºC = 0.21 Ω^{-1} cm^{-1} [7] with x the total electrolyte thickness; two values of x were employed, of 0.4 cm and 1.0 cm, as representative of the typical and 'worst case' separation of the electrodes either side of the Nafion membrane. R_{Nafion}' can be calculated from the conductivity of

Nafion 117 membrane, 0.16 Ω^{-1} cm^{-1} [8] and the thickness of the membrane, 0.0183 cm [9]. Thus, $\delta\phi_a$ was calculated as a function of current density from equation (1) see fig. A3. A typical current at a cell voltage of 2.7 V was 0.24 A, equivalent to a current density of 38.0 mA cm^{-2}; from fig. A3, taking a total electrolyte thickness of 4.0 mm as a typical value gives $\delta\phi_a$ = 2.3 V at this current density.

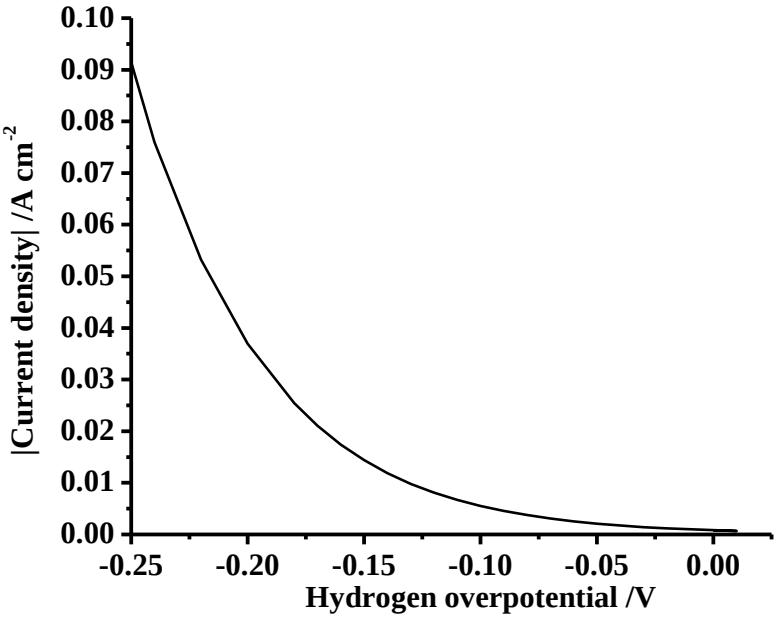

Figure A2 Plot of the magnitude of the cathodic current density as a function of the overpotential at the hydrogen-evolving cathode, calculated from equation (23).

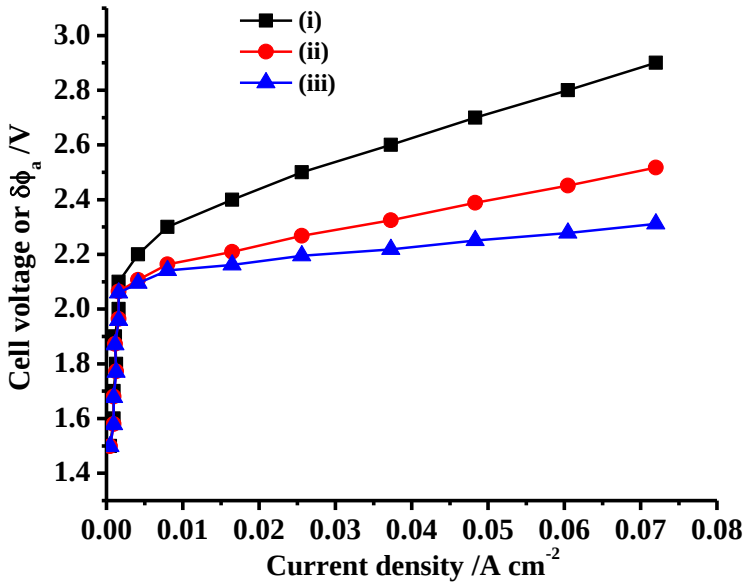

Figure A3 (i) The cell voltage vs. current density plot from fig. 3.25, uncorrected (■) for IR drops etc., and the Inner Galvani potential difference across the anode, $\delta\phi_a$, vs. current density calculated for a total electrolyte thickness of (ii) 0.4 cm (●) and (iii) 1.0 cm (▲).

References

1. Hamman, C. H., A. Hamnett and W. Vielstich, *Electrochemistry*, 2nd Edition, Weinheim: Wiley-VCH Verlag GmbH & Co. KGaA, p.77-81 (2007).
2. Atkins, P. W., *Physical Chemistry.* 5th Edition, Oxford: Oxford University Press, p. 834-839 (1994).
3. Hamman, C. H., A. Hamnett and W. Vielstich, *Electrochemistry*, 2nd Edition, Weinheim: Wiley-VCH Verlag GmbH & Co. KGaA, p.188 (2007).
4. Julie, V. M. and P. R. Unwin, "Determination of the Diffusion Coefficient of Hydrogen in Aqueous Solution Using Single and Double Potential Step Chronoamperometry at a Disk Ultramicroelectrode," *Analytical Chemistry* 69(11): 2063-2069 (1997).
5. Hamman, C. H., A. Hamnett and W. Vielstich, *Electrochemistry*, 2nd Edition, Weinheim: Wiley-VCH Verlag GmbH and Co. KGaA, p.166 (2007).
6. Sawyer, D. T., A. Sobkowiak and J. L. Roberts, *Electrochemistry for Chemists.* New York: John Wiley (1995).
7. Darling, H. E., "Conductivity of Sulfuric Acid Solution," *Journal of Chemical and Engineering Data* 9(3): 421-426 (1964).
8. Slade, S., S. A. Campbell, T. R. Ralph and F. C. Walsh, "Ionic Conductivity of an Extruded Nafion 1100 EW Series of Membranes" *Journal of The Electrochemical Society* 149(12): A1556-A1564 (2002).
9. http://www2.dupont.com/FuelCells/en_US/assets/downloads/dfc101.pdf.